Humboldt-Universität zu Berlin

Dissertation

Performance-oriented strategies for integration and wiring of the photosystem I inside 2D and 3D architectures and coupling photocatalysis with enzymatic catalysis

Zur Erlangung des akademischen Grades

„Doctor rerum naturalium“ (Dr. rer. nat.) in der Wissenschaftsdisziplin Biophysik

eingereicht an der Lebenswissenschaftlichen Fakultät

der Humboldt-Universität zu Berlin

von:

Dipl.-Biochemiker Dmitri Ciornii

Präsidentin der Humboldt-Universität zu Berlin:

Prof. Dr.-Ing. Dr. Sabine Kunst

Dekan der Lebenswissenschaftlichen Fakultät

der Humboldt-Universität zu Berlin:

Prof. Dr. Bernhard Grimm

Gutachter/in: 1. Prof. Dr. Athina Zouni

2. Prof. Dr. Franz Bartl

3. Prof. Dr. Thomas Friedrich

Datum der Einreichung: 08.10.2019

Datum der Verteidigung: 10.06.2020

Zusammenfassung

In der vorliegenden Arbeit sind unterschiedliche Kopplungsstrategien des natürlichen Photosystems I (PSI) aus Cyanobakterium *Thermosynechococcus elongatus* mit verschiedenen Elektrodenoberflächen sowie Interaktion mit Nanomaterialien und Enzymen bearbeitet worden. Zum einen wurde gezeigt, dass die Immobilisierung des PSI auf modifizierten mehr-wandigen Kohlenstoffnanoröhrchen zur funktionalen Photobiohybridelektrode führt. Dabei wurde das PSI mit der Elektrode elektrisch mit Hilfe eines Redoxproteins, Cytochrom *c* (cyt *c*), verknüpft.

Das System (PSI-cyt *c*) wurde auch auf eine dreidimensionale Elektrodenoberfläche des Metaloxids Indiumzinnoxid (eng. ITO) übertragen. Hierbei wurde zusätzlich die Transparenz-Eigenschaft solcher Oberflächen ausgenutzt. Die Präparation solcher transparenter Elektroden wurde optimiert, um höhere Photoströme zu generieren.

Weiterhin wurde eine neue Methode der elektrischen Kontaktierung des PSI mit der Elektrode etabliert. Hierfür wurden Fullerene eingesetzt. Durch erhöhte molekulare Effizienz wurde gezeigt, dass Fullerene effektivere Elektronvermittler zwischen PSI und der Elektrode sind als das cyt *c*.

Zusätzlich wurden im Rahmen dieser Doktorarbeit die photokatalytischen Eigenschaften von PSI mit den biokatalytischen Eigenschaften des Enzyms humane Sulphit Oxidase (hSOx) kombiniert. Hierbei wurde das Enzym als ein alternativer und effizienter Elektronzulieferer für PSI eingesetzt. Ein drittes Protein, das cyt *c*, fungierte als elektrisches Bindeglied und sicherte die elektrische Kommunikation zwischen den katalytischen Proteinen im System und der Elektrode.

Die Komplexität des PSI sowie seine Kommunikation mit anorganischen Nanomaterialien und anderen komplexen Biomolekülen, wie z.B. Enzymen, zeigt ein großes Potential des Einsatzes von PSI-basierter Biohybriden in den Biotechnologien der Zukunft.

Schlagwörter: Photosystem I, Kohlenstoffnanoröhren, Cytochrom *c*, 3D ITO Elektroden, Fullerene, Sulphit Oxidase

Abstract

In this thesis, different strategies for coupling of the natural complex photosystem I from the cyanobacterium *Thermosynechococcus elongatus* with different electrode surfaces, and the interaction of PSI with nanomaterials and enzymes has been investigated. First, it was shown that immobilization of PSI on modified multi-walled carbon nanotubes (MWNT) leads to a functional photobiohybrid electrode. Here, PSI has been electrically wired to the electrode via a redox-active protein, cytochrome *c* (cyt *c*).

The system (PSI-cyt *c*) has been scaled up to the three-dimensional surface of a metal-oxide, indium tin oxide (ITO). Here, additionally the high transparency property of this material has been exploited. The new preparation procedure of such transparent electrodes has been optimized in order to achieve high pohotocurrents.

Furthermore, a new method of electric wiring of the PSI with the electrode has been established. Here, fullerenes have been employed. The high molecular efficiency of such a system proves that fullerenes are more effective wiring agents between the PSI and the electrode as compared to the cyt *c*.

Additionally, in this thesis the photocatalytic property of the PSI has been combined with the biocatalytic property of the enzyme human sulphite oxidase, hSOx. Here, the enzyme has been employed as an alternative electron supplier for PSI. The third protein, cyt *c*, acted as an electric wiring agent and ensured electric communication between both catalytic proteins of the system and the electrode.

The versatility of the PSI as well as its communication with anorganic nanomaterials and biological molecules, e.g. such as enzymes, shows a great potential for use of PSI-based bio-hybrids in the future biotechnological applications.

Keywords: Photosystem I, Carbon Nanotubes, Cytochrome *c*, 3D ITO electrodes, Fullerenes, Sulfite Oxidase

Table of Contents

List of Abbreviations

A_0	Modified chlorophyll A_0
A_1	Phylloquinone A_1
AFM	Atomic force microscopy
Ag/AgCl	Silver/Silver chloride reference electrode
AgNP	Silver nanopyramids
ATO	Antimony tin oxide
ATP	Adenosintriphosphate
BOD	Bilirubin oxidase
BPPG	Basal plane pyrolytic graphite
bpy	Bis-bipyridyl
bRC	Bacterial reaction centre
C_{60}	Fullerene C_{60}
Chl *a*	Chlorophyll *a*
CNT	Carbon nanotubes
cyt *c6*	Cytochrome *c6*
CV	Cyclic voltammetry
Cys	Cysteine
cyt *b6f*	Cytochrome *b6f*
cyt *c*	Cytochrome *c*
DCPIP	2,6-Dichlorophenolindophenol
DET	Direct electron transfer
DF	Dendrofullerenes
DMPC	Dimyristoylphosphatidylcholine
DNA	Deoxyribonucleic acid
EDC	1-Ethyl-3-(3-dimethylaminopropyl)carbodiimid
EPPG	Edge plane pyrolytic graphite
EQE	External quantum efficiency
ET	Electron transfer
ETC	Electron transfer chain
$FADH_2$	Flavinadenindinucleotide
Fdx	Ferredoxin

FNR	Ferredoxin-NAD-reductase
FTO	Fluorine-doped tin oxide
F_X, F_A, F_B	4Fe-4S clusters: F_X, F_A, F_B
GaAs	Gallium arsenide
GCE	Glassy carbon electrode
GDH	Glucose dehydrogenase
GO	Graphene oxide
GOx	Glucose oxidase
HET	Heterogeneous electron transfer
HOMO	Highest occupied molecular orbital
Ipa	Anodic peak current
Ipc	Cathodic peak current
IQE	Internal quantum efficiency
ITO	Tin-doped indium oxide
$K_3[Fe(CN)_6]$	Kaliumhexacyanoferrate
Km	Michaelis-Menten constant
Ks	Heterogeneous electron transfer constant
LB	Latex beads
LUMO	Lowest occupied molecular orbital
MET	Mediated electron transfer
Moco	Molybdenum cofactor
MV^{2+}	Methyl Viologen
MW	Molecular wire
MWNT	Multi-walled carbon nanotubes
NADPH	Nicotinamide adenine dinucleotide phosphate
ND	Nanodisc
NHS	*N*-Hydroxysuccinimid
OCP	Open-circuit potential
ORR	Oxygen reduction reaction
P_{700}	Special pair Chlorophyll *a/a'*
PASA	Sulfonated polyaniinie
PBV^{2+}	Polybenzylviologen
PC	Plastocyanin

PDB	Protein data bank
PEG	Polyethyleneglycol
PEI	Polyethyleneimine
PG	Pyrolytic graphite
Pheo	Pheophytin
PQQ	Pyrroloquinoline quinone
PsaC-PsaX	Subunits from photosystem I
PSI	Photosystem I
PSII	Photosystem II
PTAA	Poly(3)-thiophene acetic acid
PVI	Polyvinylimidazole
PVP	Polyvinyl pyrrolidone
Qa	Plastoquinone A
Qb	Plastoquinone B
QD	Quantum dots
RC	Reaction center
RGO	Reduced graphene oxide
ROS	Reactive oxygen species
rps	Rotations per second
SAM	Self-assembled monolayer
SEM	Scanning electron microscope
SHE	Standard hydrogen electrode
SOX	Sulfite oxidase
SWNT	Single-walled carbon nanotubes
TCO	Transparent conducting oxide
Te	Turnover frequency
TW	Terrawatt
UV/Vis	Ultraviolet/visible
vaCNT	Vertically aligned carbon nanotubes
WET	Wired electron transfer
β-DM	n-dodecyl-β-D-maltoside

1. Introduction

Since the very beginning of life on earth living organisms have learned to make use of energy coming from sun, the sunlight. The sunlight energy converts H_2O and CO_2 by an intricate machinery of cells into energy-rich biomolecules for sustaining of life processes. This simple and at the same time complex chemical reactions led to rise of higher life forms, including us, mankind. Since humanity develops very quickly, there is an ever growing demand of energy source. Until now, canonical fuels such as oil, coal, natural gas, but also sophisticated nuclear energy have been exploited. Not only that these resources are of finite extent, they cause tremendous pollution and are dangerous in terms of devastating damages if an accident happens (1986, Chernobyl, Ukraine; 2011, Fukushima, Japan). This is why the search for renewable, green and carbon-neutral energy resources has become such an indispensable ecological, industrial and political issue in the last decades. Here we return back to nature, since mankind is still learning to harvest more and more of "green" resources. Besides harvesting hydrothermal energy or wind energy, an interesting possibility represents solar energy. This ubiquitous energy source can be transformed into electrical energy and used for performing useful work, like powering household or industrial electric devices, cars and light bulbs. Another possibility of harvesting sunlight arises when turning the high-energy electrons, which are generated in the process of light absorption, into chemical energy. This could be relevant in terms of synthesis of otherwise expensive chemicals, e.g. pharmaceuticals, or expensive reduction equivalents such as H_2, NADPH, $FADH_2$, or energy-rich compounds like EtOH a.o. However, light-harvesting is far from efficient. The extraordinary amount of sunlight energy delivered in just one hour (4.6×10^{20} J h^{-1}) could be enough to satisfy the world energy demand for a year, if efficiently used.[1] This illustrates how inefficient the sunlight harvesting technology is today. Despite the fact that electricity production from solar energy records just 0.015% of the worlds' electricity production it holds a great potential in the future, when traditional fuel resources will be vanishing, and the energy demand will be ever growing.[1] In the most optimistic scenario, the global energy consumption is expected to rise up to 27 TW by 2050 and 43 TW by 2100 (compared to 13.5 in 2001).[2] Therefore, it is necessary to develop more efficient technologies of photon-to-current conversion. Until now, some progress in this field has been achieved by employing versatile inorganic and organic materials for harvesting sunlight. However, often rare metals or environmentally unfriendly compounds are used and poisonous waste is generated. Here, the use of natural photoactive molecules, such as photosystems, which perform

photosynthesis, has quickly evolved and many promising implementation strategies have been successfully exploited. There are several publications on long-term stability of photosystem-based devices and some first attempts for solid-state implementation have already been reported. These findings have directed our attention towards natural photoactive compounds and to further development of the photobiotechnology for a more efficient sunlight use.

2. Objectives of the Thesis

The scope of this thesis is to make a contribution to the further development of photobioelectrochemistry and photobiotechnology. Therefore, three aspects were put into the focus of the present research: a) construction of three-dimensional (3D) photobioelectrodes for high performance b) realization of efficient electric wiring of PSI to the electrode and c) combination of photocatalysis with the biocatalytic reaction of an enzyme.

For the first objective the intention was to test a conductive nanomaterial, multi-walled carbon nanotubes (MWNT), for the use as conductive support for PSI. The three-dimensional character of these nanostructures ensures high surface area and, hence, should allow for the immobilization of a large amount of PSI molecules. The rather small size could provide conditions for a fast electron exchange between the electrode and the PSI. Besides carbon-based material also transparent metal oxide material (tin-doped indium oxide, ITO) has been employed for construction of 3D photobioelectrodes, since here the 3D surface structure can be better controlled.

The second objective has been realized by employing fullerene C_{70} as carbon nanoparticles. Here, the small size of such a compound (ca. 1 nm) and its ability to participate in electron transfer reactions might improve the electric communication between PSI and electrode.

The third objective was to investigate the coupling of the photocatalytic activity of the PSI with the enzymatic activity of an enzyme, the human sulphite oxidase (hSOx), as well as the ability of hSOx to supply electrons for PSI independently of the electrode. For this, both proteins have been integrated in a 3D architecture and wired with each other and with the electrode *via* a third protein, cyt *c*.

3. Theoretical Background

3.1 Photosynthesis – powering the planet

The ancient process of photosynthesis has arisen almost 3.5 billion years ago and can be considered as one of the best conserved and elegant biological conversions in the history of this planet. The beauty of photosynthesis is in its simplicity. This process, which is at the base of each phototrophic organism, can be summarized in the following general formula:[3]

$$\mathbf{2\ H_2A + CO_2 + h\nu \rightarrow CH_2O + 2\ A + H_2O} \qquad \mathbf{(1)}$$

In which $\mathbf{H_2A}$ – is an electron donor, e.g. H_2O, $\mathbf{CH_2O}$ – carbohydrate, and **A** – an oxidized electron donor, e.g. O_2 or S, and hν represents a photon.

As presented in the above mentioned photochemical reaction, the low-energy carbon dioxide is converted into reduced, energetically loaded species, carbohydrates. Talking about photosynthetic organisms, these can be divided into anoxygenic and oxygenic. To the first group belong green sulphur bacteria, purple bacteria and green gliding bacteria. These organisms use other molecules than water for the oxidation, and thus, no oxygen is generated. The photosynthetic machinery of the anoxygenic phototrophic organisms relies on specialized light-harvesting reaction centres (RC), which contain bacteriochlorophylls and carotenoids for light absorption in the range 700 - 1000 nm. To the second group of photosynthetic organisms, the oxygenic group, belong cyanobacteria, algae and plants. These organisms, in contrast to the anoxygenic organisms, oxidize water and liberate oxygen. Interestingly, the side-product of photosynthetic reaction in these organisms, oxygen, accumulated in the lower atmosphere and enabled aerobic higher organisms to emerge, including humans. The photosynthetic process is generally divided into two reactions: the light-dependent reaction and the "dark-reaction". As the name implies, the light reaction occurs upon irradiation of the photosynthetic machinery. In this reaction, water splitting into oxygen, protons and excited electrons occurs, followed by transfer of electrons in the electron transfer chain (ETC). The "dark-reaction", also called Calvin cycle, takes place independently of light: here, carbohydrates are synthesized. Summarizing these events, a photosynthetic net reaction for oxygenic organisms can be written as follows:

$$\mathbf{6\ CO_2 + 12\ H_2O \rightarrow C_6H_{12}O_6 + 6\ H_2O + 6\ O_2} \qquad \mathbf{(2)}$$

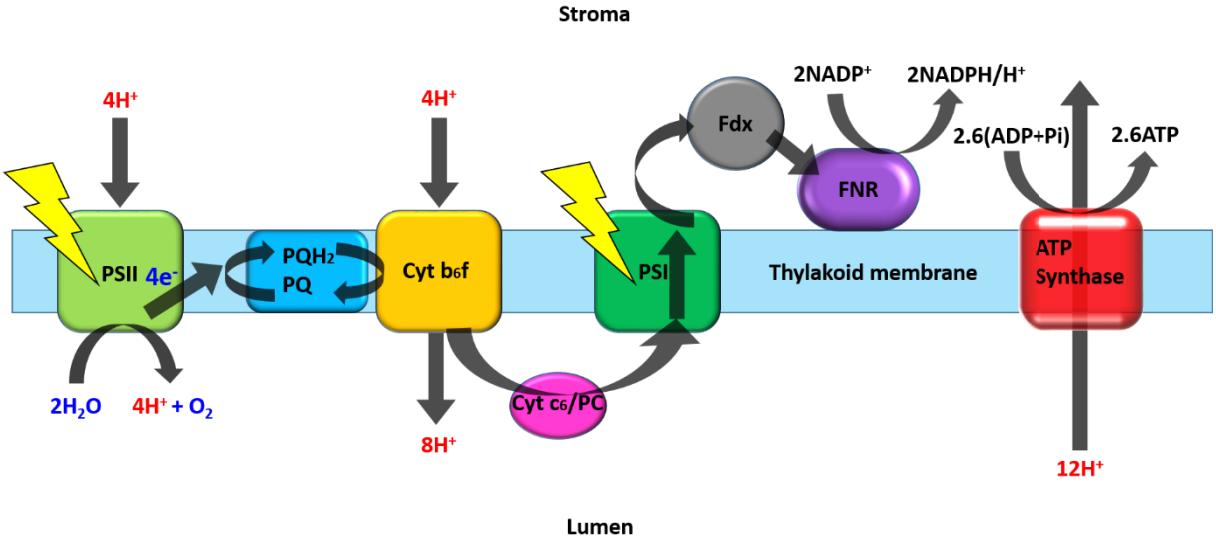

Figure 1. Schematic illustration of photosynthesis and reaction pathways inside the thylakoid membrane. First step in the reaction cascade is the absorption of light by photosystem II (PSII), followed by oxidation of two molecules of water. Further, the resulting electrons are transferred via plastoquinone (PQ) to the cytochrome *b6f* (cyt *b6f*) complex, which reduces either cytochrome *c6* (cyt *c6*) or plastocyanin (PC) (in bacteria or plants, respectively). From there, electrons are further transferred to the oxidized centre of photosystem I (PSI), called the P_{700} centre. Upon light absorption by PSI, also an excited electron is generated and transferred intramolecularly to ferredoxin (Fdx) on the stromal side of the thylakoid membrane. Fdx reduces ferredoxin-$NADP^+$-reductase (FNR), which, in turn, produces NADPH from $NADP^+$. The accumulated protons at the luminal side of the thylakoid membrane are used for synthesis of ATP by the ATP-Synthase.

In plants, the reaction takes place in chloroplasts, which are believed to have evolved from a symbiotic process between plant cells and cyanobacteria. These chloroplasts incorporate stacked thylakoids, which accommodate photoactive protein complexes, photosystem I (PSI) and photosystem II (PSII). Both photosystems and other proteins, such as cytochrome *b6/f* (cyt *b6/f*) and ATP synthase, which belong to the photosynthetic apparatus, are integrated in the thylakoid membrane. Two compartments can be discriminated, the luminal side of the thylakoid membrane and the stromal side. The photosynthetic ETC and proteins involved in the photosynthesis are graphically represented in Fig. 1.

Photosystems are composed of several units: i) the light-capturing unit is represented by antennae chlorophylls. These molecules are able to absorb photons and transfer the excitation energy to the next unit ii) the specialized reaction centres, called P_{700} in PSI and P_{680} in PSII, respectively, where the actual charge separation takes place, iii) the third unit is represented by the redox centres in PSI and PSII specialized in electron transfer chain (ETC).

First, upon absorption of 4 photons, the photosystem II splits two molecules of water into 4 protons, 4 electrons and molecular oxygen, a process catalysed by an intricate integrated complex, the Mn_4CaO_5 cluster. Water serves here as an electron donor for the photosynthesis

process.[4] Further, 2 electrons are collected in two one-electron steps by the plastoquinone (PQ + 2 e^- → PQH_2). Due to its lypophilic character, PQH_2 can easily diffuse in the membrane and from there it reduces the cyt *b6/f*.[5-7] It is at this stage, in which the protons are transferred from the stromal side to the luminal side of the membrane to contribute to the proton gradient, which is responsible for ATP synthesis.[8, 9] Next, at the luminal side of the cyt *b6/f* complex, the electrons are collected by cytochrome *c6* (cyt *c6*) or plastocyanin (PC), if in higher plants.[10-12] The light absorption by PSI leads also to charge separation and an oxidized reaction centre, P_{700}^+ (the hole), and an excited electron are generated. The hole can now be refilled with an electron by cyt c*6* (or PC). *Via* an intramolecular electron transfer inside PSI[13] the photo-excited electrons find their way downstream the energy valley to F_B cluster. From here it is transferred to ferredoxin, which transiently docks the stromal side of PSI.[14, 15] Ferredoxin shuttles the electrons to the ferredoxin-$NADP^+$ oxidoreductase (FNR), which, as the name already implies, reduces $NADP^+$ to NADPH.[16, 17] For the synthesis of one NADPH molecule two electrons are needed. NADPH is then used for synthesis of sugars in the Calvin cycle.[18] The light-induced transfer of electrons drives protons from the stromal side to the luminal side. Due to the impermeability of the thylakoid membrane towards protons the pH gradient across the membrane is maintained. This creates the driving force which is responsible for proton transfer along the proton gradient through a specialized channel in ATP synthase.[19-21] This energy is used for synthesis of the biological currency, ATP.[9, 22, 23] For the synthesis of sugars, however, both the ATP and NADPH are needed. The overall reaction including ATP synthesis can be summarized as follows:[24, 25]

$$\mathbf{2\ NADP^+ + 2\ H_2O + 3\ ADP + 3\ Pi + h\nu \rightarrow 2\ NADPH + 3\ ATP + 2\ H^+ + O_2} \qquad \mathbf{(3)}$$

3.2 Structure of Photosystem I

The protein used in experimental part of the present thesis is a trimeric photosystem I from the cyanobacterium *Thermosynechococcus elongatus* and is of about 1 MDa molecular weight, measuring 21 nm in length and 9 nm in height. It consists of 127 compounds (96 chlorophylls, 2 phyloquinones, 22 carotenoids, 3 4Fe-4S clusters and 4 lipids) and 12 different protein-subunits (PsaA-PsaX), each of them responsible for different tasks.[26] PsaA and PsaB represent the largest subunits, each of them ca. 80 kDa, they span across the thylakoid membrane and harbour the elements of the electron transfer chain (ETC), which

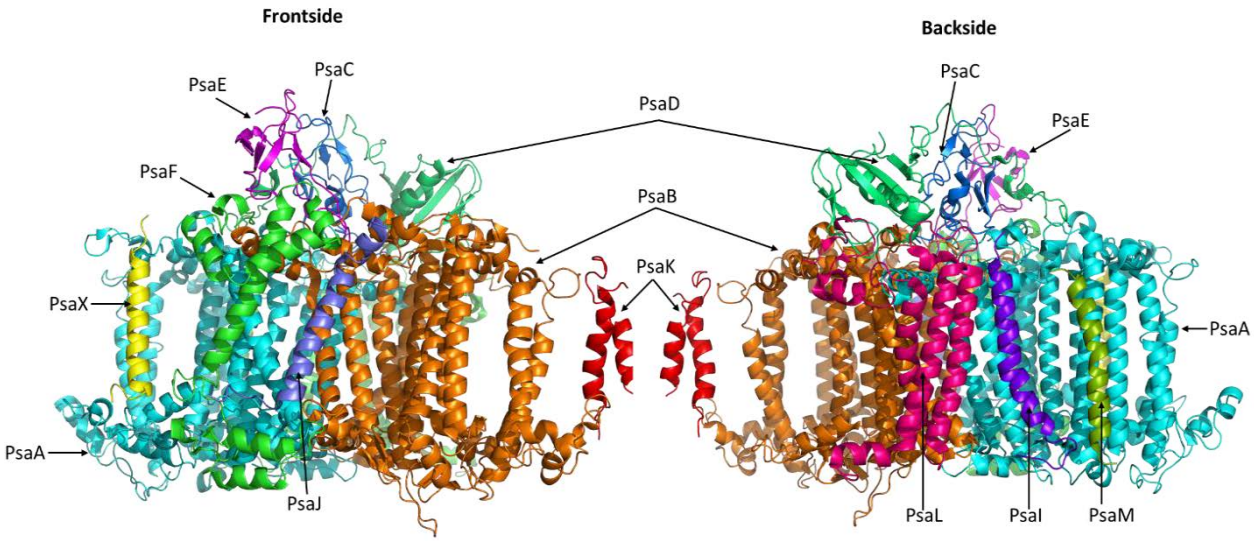

Figure 2. Crystal structure of subunits in PSI monomer (front- and backside). Subunits are represented in their secondary structure: PsaA (A, cyan), PsaB (B, golden), PsaC (C, blue), PsaD (D, light green), PsaE (E, magenta), PsaF (F, green), PsaI (I, dark violet), PsaJ (J, light violet), PsaK (K, red), PsaL (L, rose), PsaM (M, green-yellowish), PsaX (X, yellow). Structural information used form Jordan et al. 4FE1.

consists of: a) the primary electron donor, also called the special pair of chlorophylls, P_{700}, b) the primary electron acceptor, A_0, c) the phylloquionone A_1 and d) the three 4Fe-4S clusters, Fx, F_A and F_B.[27, 28] Other subunits, PsaF, PsaJ, PsaK, PsaX, are facing with its hydrophobic helices the lipid membrane whereas carotenoids are participating in stabilization of the antennae system.[26, 29] PsaL and PsaI are responsible for holding a trimer together.[30, 31] PsaM is placed between the two monomers and is involved in coordination of Chl *a* molecule.[30, 32, 33] PsaC, PsaD, PsaE, located at the stromal side of thylakoid membrane, are involved in docking of ferredoxin or flavodoxin. PsaC, a 8.9 kDa subunit, coordinates the two terminal 4Fe-4S clusters, F_A and F_B.[32, 34, 35] PsaD has been demonstrated to be involved directly in the docking of ferredoxin.[36-38] PsaE has been shown to participate in the docking process of ferredoxin, too.[39-41] Furthermore, it has been suggested, that a Ca^{2+} ion might be coordinated by PsaL and PsaA subunits, playing role in stabilization of PSI.[26] Fig. 2 shows a monomeric PSI in cartoon representation where each polypeptide chain is differently coloured. Computational analysis of the charge distribution on the surface of PSI has revealed a dipole character. Vacuum electrostatic calculations at pH7 show that stromal side of PSI, the donor side, is preferably positively charged, whereas the luminal side, the acceptor side, is mostly negative charged. It has to be mentioned, however, that both sides of PSI contain both acidic and basic amino acids, the dipole character is therefore a smooth transition. It is possible, though, to adjust the surface charge by placing photosystem in a strongly basic or strongly acidic medium. Fig. 3 depicts monomeric PSI from different views.

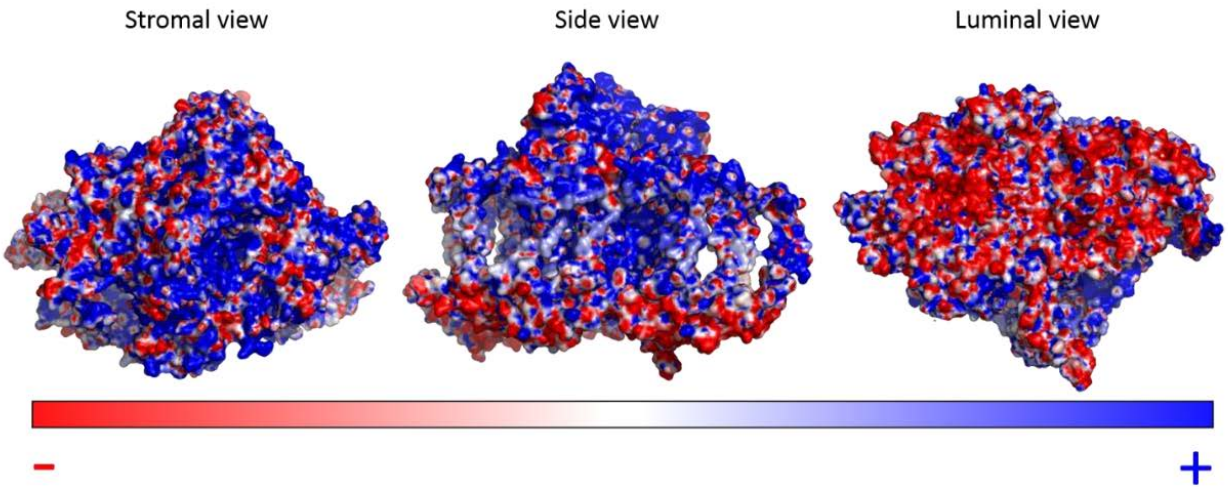

Figure 3. Surface electrostatics of the PSI monomer generated with PyMol. The stromal side of PSI (left) shows a more pronounced positive charge (blue) due to larger amount of basic Lys residues. The luminal side of PSI (right) is characterized by a larger amount of acidic amino acids, contributing to the more pronounced negative charge (red).

3.3 Electron transfer in photosynthesis: energetic view

The efficiency and accuracy of electron transfer reactions in the process of photosynthesis is astonishing. The pathway of the electrons from water to the NADPH stretches over several redox-active components which exchange electrons with loss of energy. The maintaining of the flow in the electron transfer chain (ETC) is due to the redox potential gradient which is built between the initial highly energetic species (P_{680}^{*}, E_0 = - 0.62 V vs. SHE) and the final, lower energy species ($NADP^+$, E_0= - 0.37 vs. SHE). Initially, light is captured by the specialized antennae chlorophyll *a* molecules, which surround the reaction centre in a way that allows for "focussing" of the photon-coupled energy, similarly to the mirror telescopes, in which all light is focussed in the centre. The coherent energy transfer represents a wave-like transfer mechanism, in which the exciton wavefunction is preserved over a relatively prolonged period of time (in the range of 300 fs)[42] allowing for special transfer without wavefunction collapse (without quantum decoherence). Once the excitation has found its target chromophore - the P_{680} - the electrons are elevated to the higher energy levels and hence, the redox potential of the absorber is elevated. This excited state represents the reductive driving force of the molecule and is equivalent to - 0.62 V vs. SHE for P_{680}. From here, electrons are transferred to the pheophytin (Pheo, E_0 = - 0.5 V vs. SHE) and subsequently to the plastoquinone A (Q_A, E_0 = - 0.14 V vs. SHE). Next, the electron is transferred to the stromally situated quinone B (Q_B/Q_BH_2, E_0 = - 0.06 V vs. SHE). However, this is a two-electron step, in which also two protons are "imported" from the stromal side of

the thylakoid membrane. Completely reduced Q_BH_2 is then oxidized by the plastoquinone pool, situated in the membrane space. During the following sequential electron transfer steps down the chemical potential gradient (PQ → cyt *b6f* → cyt *c6*) electrons reach the photo-excited and oxidized special pair of PSI, the P_{700}. At this stage, some reasonable amount of the nominal reductive force ($E_{initial}(P_{680}^*)$ = - 0.62 V vs. SHE) has been dissipated and the redox potential of electrons ("cold electrons") in cyt *c6* is E_0 = + 0.36 vs. SHE, which is roughly enough to reduce the hole P_{700}^+ (E_0 = + 0.42 V vs. SHE). At the PSI module a second "energetic boost" in form of photoexcitation occurs. The 92 antennae chlorophylls capture and transport the exciton in a wave-like fashion, as previously described for PSII, taking simultaneously all possible pathways, which are in superposition, until an energetical trap captures the excitation at the level of the special pair of chlorophylls, Chl *a*, also known as primary donor (P_{700}). This process, similarly to that in PSII, leads to charge separation. The photo-excited electron ("hot electron") in PSI is elevated to the highest reductive potential known in nature, E_0 = -1.3 V vs. SHE.[43, 44,45] Millions years of evolution have transformed the charge separation mechanism to an astonishingly efficient process with quantum efficiency of nearly 100 %.[46] The stabilization of the excited state in PSI occurs due to a capturing of the excited electron by the primary electron acceptor, a chlorophyll A_0 (E_0 = -1.1 V vs. SHE). From here, electrons are shuttled to phylloquinone A_1 (E_0 = - 0.71 V vs. SHE) and three 4Fe-4S clusters, F_X (E_0 = - 0.7 V vs. SHE), F_A, F_B (E_0 = - 0.53 V and E_0 = - 0.58 V vs. SHE, respectively).[32] The electron transfer is thermodynamically favourable and occurs due to the lower reduction potentials of each following compound, creating an energy gradient along which electrons "flow" with some loss in reducing force. Further, electrons are transferred to the soluble electron shuttle, ferredoxin (Fdx), which transiently docks at the PsaC and PsaD subunits to ensure electron transfer from F_B to the Fdx. The terminal cluster, F_B, however, has E_0= - 0.58 V vs. SHE and thus has a more negative redox potential than the F_A cluster, E_0= - 0.53 vs. SHE. This fact has been intensively discussed and several studies have been struggling to clarify the electron transfer steps between F_A-F_B-Fdx.[47-52] The generally accepted mechanism suggests, that upon transient docking of Fdx to the PsaC subunit of the stromal side of PSI, the redox potential of F_B is shifted to a more positive value, so that electron tunnelling from F_A to F_B becomes feasible.[53, 54] For each forward electron transfer step in the PSI there is also a certain probability of the backward reaction or recombination to the ground state, P_{700}. The half-life times of forward and recombination reactions have been estimated based on the fluorescence decay, as can be extracted from Fig. 4, right.[55, 56]

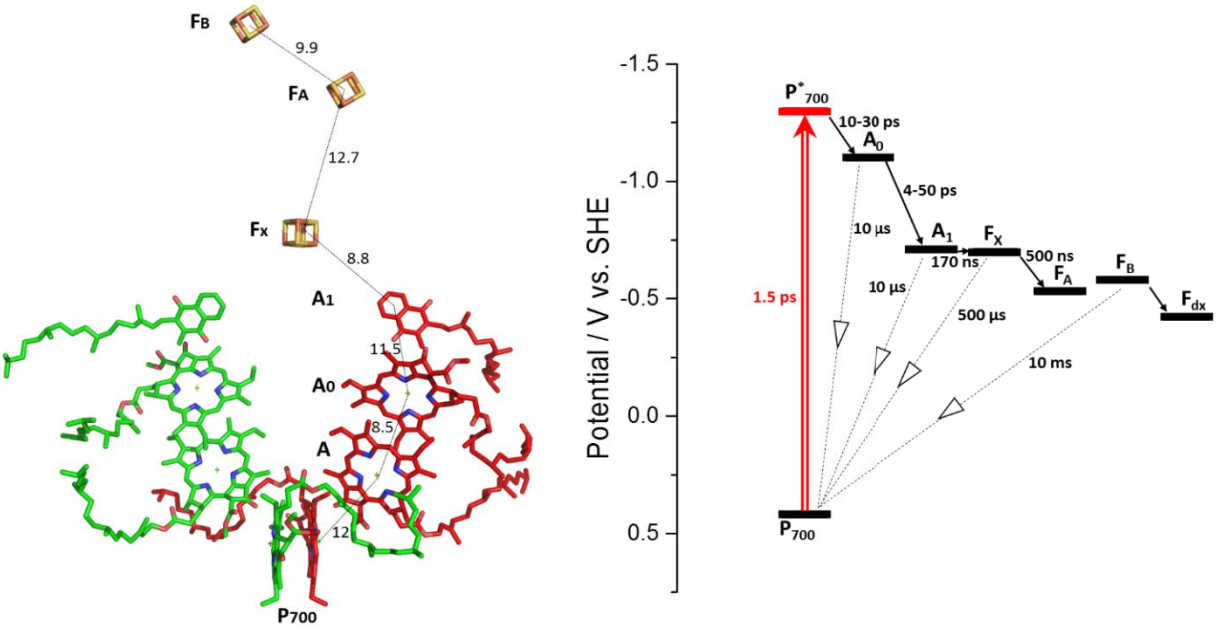

Figure 4. Left – 3D visualization of intramolecular ETC in PSI (A branch – green and B branch – red). Both branches participate in electron transfer, however, in the branch B the electron transfer is faster than in the branch A. Lines only denote distances in Angström between cofactors. **Right** - energy diagram representing redox potentials of ETC cofactors in PSI vs. SHE. Black arrows with dashed lines represent half-life times of the electron transfer steps during relaxation into the ground state P_{700}. Structure has been used from Jordan *et al.* PDB: 4FE1.

3.4 Electrochemistry of redox-active proteins

In nature, electron transfer reactions between and within redox-active proteins are at the heart of life processes such as cellular respiration or photosynthesis and play an important role in energy transduction. Understanding and harnessing of these inter- and intramolecular electron transfer processes represents a great challenge in bioelectronics, voltaics, bioelectrochemistry, bioanalytics and sensorics. Electrochemical techniques serve as a powerful tool for investigating electron transfer properties of the electroactive species. Here, biomolecules such as enzymes and redox-active proteins (e.g. metalloproteins) are of particular interest. For the study on electrocatalytic properties of proteins it is essential to electrically address their redox centre and explore how to transduce the chemical signal into an electrical signal, e.g. by means of an electrode, which can serve as transducing element. Here, transformation of the substrate into the product by an enzyme is associated with an electron transfer process, in which the enzyme is acting as an electrocatalyst and facilitates electron transfer between the substrate and the electrode. During this electrochemical transformation, the catalytic current is generated and detected at the electrode.

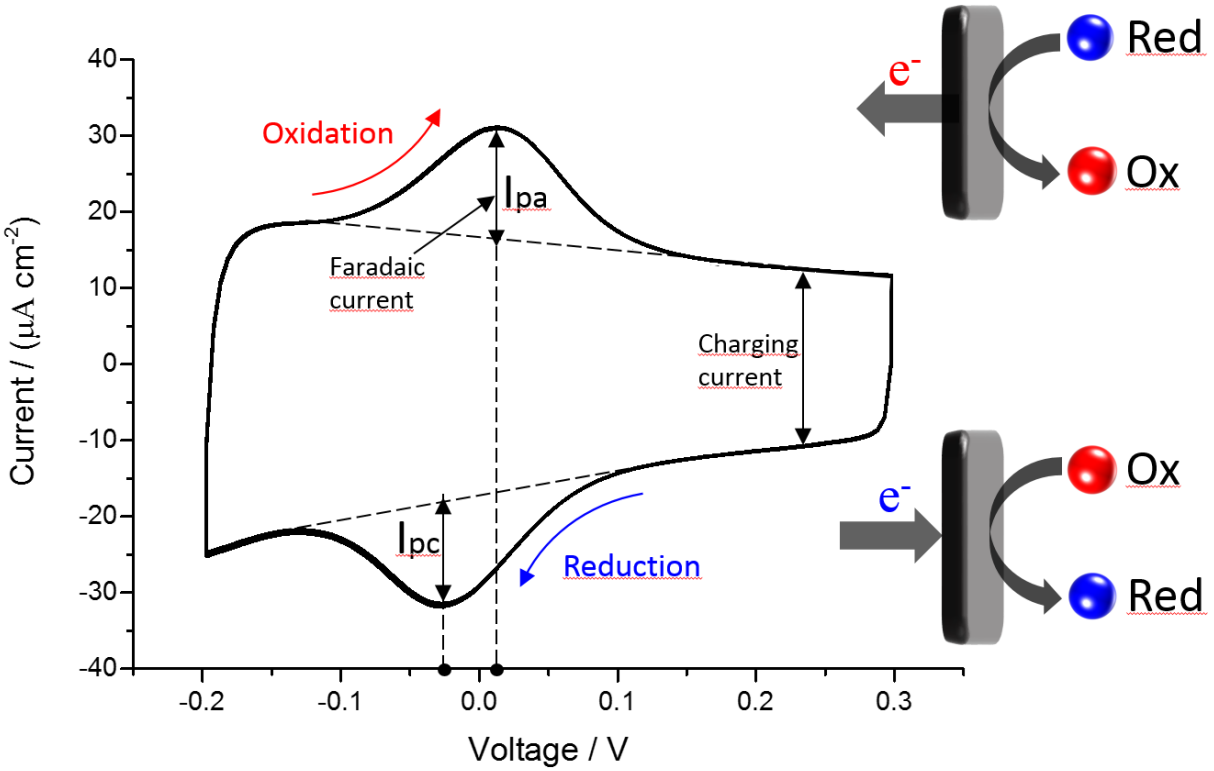

Figure 5 Example of a cyclic voltammogram. Catalytic and charging current can be distinguished. Ipa – anodic peak current, Ipc – cathodic peak current.

Current represents the amount of charge (electrons) which has been transferred per unit time. The SI unit of current is Ampere (A), 1 A = 1 Coulomb s^{-1}. In electrochemical experiments current can have different source and thus two types of current should be distinguished: the faradaic current and the charging current (capacitive current). The faradaic current is generated when species from solution or fixed at the electrode surface are converted, either oxidized (anodic faradaic current) or reduced (cathodic faradaic current) and is proportional to the rate of converted substrate according to the relation:

$$I = nF \frac{d[Ox]}{dt} = - nF \frac{d[Red]}{dt} \quad \textbf{(4)}$$

In which I is the current, n – the number of electrons participating in conversion event, F – the Faraday constant (96.485 C mol^{-1}). The capacitive current, in contrast, is not related to the conversion of electroactive species. Also called charging current, this current originates from the rearrangement of ions in the double layer at the electrode-solution interface, an event which can be compared to the charging of a capacitor. During charging, the electrons are not transferred through the solution-electrode interface, whereas during redox reactions, electrons cross the electrode-solution interface. The applied potential (E) defines the concentration ratio

between oxidized and reduced species at the electrode surface. The relation between E, the redox potential of the species (E_0), and the ratio between oxidized and reduced form of the electroactive species has been developed by Nernst:

$$E = E^\circ + \frac{RT}{nF} \ln \frac{[Ox]}{[Red]} \quad \textbf{(5)}$$

In Fig. 5, a cyclic voltammogram is depicted. The charging current can be clearly differentiated from faradaic current. Two cases can be differentiated: I) the redox compound is dissolved in solution, II) the redox compound is immobilized on the electrode surface. If the redox-active compound is in an immobilized state on the electrode (case II), the faradaic peaks can be integrated and the amount of charge can be calculated and thus, related to the coverage of the electroactive species on the electrode surface (e.g. a redox protein).

For efficient electrochemical characterization of an electroactive species, fast kinetics and unhindered electron exchange with the electrode should be guaranteed. However, the direct electrochemistry of many proteins is hindered by the fact that the redox groups are often buried by the protein shell and thus are not accessible for direct electron exchange reactions. In order to overcome this hurdle, redox-active, freely diffusible electron-shuttle molecules, mediators, can be employed with the aim to wire the redox group electrochemistry with the electrode. Another possibility to establish electric coupling of the protein with the electrode is wiring, which provides a molecular wire between the electrode and the protein. Here, the wire serves as conductor of electric charge. Three possibilities to address electro-active properties of molecules as well as emerging applications will be elucidated in more details in the following subchapter.

3.4.1 *Direct electron transfer* (DET)

Direct protein electrochemistry is a method of choice for investigation of bioelectrocatalytic properties of redox proteins and enzymes. It allows to establish a direct electrical communication with the redox centre of the biomolecule and recording of accurate faradaic responses. Depending on the enzymatic reaction type, the substrate can be either reduced or oxidized by the enzyme, followed by reduction or oxidation of the redox centre of the enzyme by the electrode. In nature, the design of the biological molecule is programmed in such a way, that electrochemical transformation reaction proceeds without any impediment. At the electrode-electrolyte interface, however, sometimes conformational changes of the protein

might impede the natural electron flow rate in the biomolecule. Several barriers concerning direct electrochemistry of proteins at electrodes are: i) slow diffusion rate of the biomolecule, which leads to small faradaic responses, ii) the limited accessibility of the redox centre, which prohibits communication with the electrode and iii) some proteins denature at the electrode-electrolyte interface (rapid and irreversible adsorption).[57, 58] For this reasons, it has been suggested that for a reversible direct electrochemistry several sequential events have to occur successfully and fast: a) fast diffusion of the biomolecule towards the electrode; b) successful association of the biomolecule with the electrode surface, in an orientation suitable for rapid electron transfer; c) fast heterogeneous electron transfer; d) dissociation and diffusion of the protein away from the electrode. First attempts to study electrochemistry of redox active proteins have been performed at unmodified electrodes, e.g. cytochrome *c* electrochemistry has been evaluated at gold,[59] platinum,[60] mercury,[61] silver[62] and p-type silicon electrodes.[63] Here, the electron transfer reactions occurred at very slow rates, thus making the electrochemical study of cyt *c* prohibitive.[57] This is why for many years it has been considered that direct electron transfer between redox proteins and electrodes was not feasible. Later, it has been suggested that if an appropriate design of the electrode surface is used, direct protein electrochemistry can be improved. The presence of functional groups on the electrode surface is beneficial for rapid and reversible binding of the protein to the electrode, thus preventing irreversible degradative protein adsorption. Besides, it is considered, that such functionalities might resemble the physiological partners of proteins. Indeed, first reversible direct electrochemistry between cyt *c* and a modified electrode has been shown in 1977 on 4,4′-bipyridyl-modified gold. Here, the compound attached to the gold surface cannot be regarded as mediator, since it remains electro-inactive in the potential range in which catalytic electron transfer has been observed.[64] In the same year 1977 it has been also demonstrated that cyt *c* "behaved well" at the ITO electrode, since its hydrophilicity facilitates association and dissociation rates of the protein.[65] In another study over 50 surface-modifiers of metal electrodes have been investigated for the study of electrochemistry of cyt *c*,[66] enlightening the large impact of electrode modifications on direct electrochemistry of proteins at electrode interfaces. For surface-bound proteins the distance between the redox active centre of the protein and the electrode becomes a crucial parameter. Here, electron tunnelling events are decisive and the distance towards the electrode surface becomes a rate-limiting factor.[67, 68] According to Marcus theory, the electron transfer rate decays exponentially with increasing distance and decreases with smaller potential difference

between reactant and an electrode (but also btw. two redox-active reactants).[69, 70] It has been demonstrated, that at distances below 1 nm tunnelling between electroactive species becomes highly probable.[70-74] Moreover, the reorganization energy of the participating molecules is crucial and reflects structural rigidity of the two species and thus, the eagerness to exchange electrons: the lower the reorganization energy of participants in an electrochemical event is, the higher is k_{ET}. Until now, many other redox-active proteins and enzymes have been demonstrated to exchange electrons directly at modified electrodes: a) Cu-redox proteins: azurin,[75, 76] hemocyanin,[76, 77] plastocyanin,[78] b) Fe-redox proteins: cytochrome *c*,[79-85] ferredoxin,[86, 87] myoglobin,[88, 89] hemoglobin[90, 91] c) Heme-enzymes: sulphite oxidase,[92] peroxidase,[93, 94] d) Cu-enzymes: bilirubin oxidase,[95, 96] Laccase,[97] e) Fe-S/Fe-Fe/Ni-Fe enzymes: hydrogenases,[98, 99] fumarate reductase,[100, 101, 102] f) PQQ-dependent enzyme: glucose dehydrogenase[103-105] g) FAD-dependent enzymes: glucose oxidase,[106, 107] cellobiose dehydrogenase[108, 109] a.o.

3.4.2 *Mediated electron transfer (MET)*

As the name already implies, is realized *via* a mediator. The mediator can be a low-molecular weight compound, which can be oxidized and reduced. In mediated electrochemistry, during biocatalytic reactions, the enzyme converts not only the substrate, but also the mediator. The reverse process, i.e. regeneration of the mediator proceeds at the electrode. The mediator needs to function as a second substrate for the enzyme and the regeneration process at the electrode site has to be a fast process.[110] The electrode process (mediator regeneration) can be regarded as non-catalytic process, in contrast to the transformation of the substrate, which is a catalytic process. Mediators can be different – from small organic or inorganic molecules up to redox proteins. Some examples of the compounds which are often used as mediators are: ferrocene and its derivatives,[111] methyl viologen (MV^{2+}), quinones, metal chelates, such as ruthenium hexammine (ruhex) and other hexaammine metal compounds, kalium hexacyanoferrate ($K_3[Fe(CN)_6]$). Small redox proteins, such as cyt *c*, azurin, ferredoxin, flavodoxin etc. are examples of proteins which can acts as mediators. The advantages and disadvantages of using one particular mediator type over another result from their diffusion rate, size, substitutionality, availability, ET rate, redox potential a.o. Inorganic and organic mediators have generally faster diffusion rates, since these compounds are very small. Redox proteins, in contrast, are usually larger and propagate more sluggish in a solution. Besides, availability and ease of use make non-biological mediators more attractive for electrochemical

purposes. Furthermore, desired substituents can be introduced (e.g. ferrocene derivatives), classifying it as a versatile and tunable mediator. On the other hand, biological mediators have been effectively employed in electron transfer reactions with relevant enzymes. A redox protein allows for specially controlled electron flow, selectivity and directionality towards its partner, a feature, which obviously is lacking by small unspecific non-biological redox compounds. Besides, the auto-oxidation rates of the redox proteins usually are lower than for the exposed non-biological compounds. The choice of an appropriate mediator is, therefore, dependent on the requirements which have to be met in an electrochemical system.

3.4.3 *Wired electron transfer (WET)*

This type of electron exchange necessitates a molecular "wire" between the active centre of the molecule and the electrode surface. The requirement on "molecular wire" is its conductivity, which enables electron passage through it. A molecular wire can be a redox polymer (e.g. Os polymers, conductive polyanilines, polypyrroles) or a small molecule, e.g. π-conjugated systems (e.g. unsaturated alkyl-spacers, aromatic pyrenes, anthracenes, naphthalenes, pyrroloquinoline quinones) or even nanostructures such as carbon nanotubes. Usually, such molecular wires are bound to the electrode at one side and hold the molecule of interest at the other side. Here, diffusion does not play any role, since the electron exchange partners – the electrode and the electro-active molecules - are bound together. Thus, this type of ET is considered to proceed faster than the mediated approach, in which dissolved molecules have to diffuse to the electrode. For example, if a redox protein is "wired" to the electrode by means of a conductive π-conjugated compound, ET occurs through the π-system.[112, 113] In a redox polymer, however, the electrons are transferred by a "hopping" mechanism, in which multiple redox-units, such as metal ions, can receive and donate an electron, thus changing the redox-state (Fe^{II}/Fe^{III}, Os^{II}/Os^{III}, Ru^{II}/Ru^{III} etc.). The binding of an enzyme to such a polymer can occur electrostatically (e.g. a polyanionic enzyme can be bound to a polycationic polymer) or covalently. The main difference between DET and WET, however, is that in DET just one electron transfer step is required for a direct electron exchange with the electrode, whereas in a wired approach additional electron transfer steps are necessary. One great advantage of using the redox polymers instead of small π-conjugated compounds is that an enzyme bound to the polymer is contacted in multiple ways and no certain orientation is required, i.e. due to multiple redox-sites in such a polymer all redox centres of the enzyme are connected and transfer electrons to the electrode, whereas in a

monolayer-modified electrode, the proper orientation of an enzyme on the surface is needed, such that redox centre is oriented towards the electrode surface. This situation is highly unlikely, thus ET efficiency is drastically reduced in such systems. Another variability to the polymer approach represents the use of a redox hydrogel. Here, the advantageous features of a hydrogel (swelling/collapsing feature, stability against water, water-retaining capacity at ca. 90 %, intrinsic 3D framework) are synergized with conductive properties of a polymer, e.g. a redox polymer.[114] In redox hydrogels the enzymes are also contacted abundantly and the electrons are shuttled towards the electrode, without the need for oriented accommodation of the enzyme. Moreover, redox hydrogels are unique for the ability to transport ions, electrons and small molecules.[115] Some successful attempts to attach enzymes at the electrode *via* a molecular wire are listed below: electrostatic complexation of glucose oxidase to a polycationic redox-Os-polymer,[116] poly(1-vinylimidazole)[117] or a redox hydrogel;[118] laccase and glucose oxidase wiring *via* carbon nanotubes in a biofuel cell;[119] horseradish peroxidase wired *via* ferrocene derivative with a long poly(oxyethylene);[120] wiring glucose oxidase by reconstitution of FAD-modified thiol monolayer etc.[121]

3.5 Enzyme attachment strategies

Physical adsorption - represents perhaps one of the most facile ways to integrate a molecule on the electrode surface. This type of adsorption is realized by hydrophobic interactions and the Van der Waals forces. This technique is not optimal for dealing with complex proteins which can quickly denature and lose their native function. These interactions are weak, and thus the stability of the bonds is not expected to resist mechanical stress (e.g. when the electrode is dipped in the buffer) or chemical stress (if pH or molarity of the working buffer are beyond mild).

Electrostatic approach - this approach is based on electrostatic forces between the molecule of interest and the electrode. If the electrode surface possesses a net charge, then an oppositely charged compound can be assembled on such a surface *via* Coulomb forces. For example, gold electrodes can be modified with organothiol-based self-assembled monolayers (SAM). These SAMs are known for building ordered monolayers on gold surface *via* chemisorptive sulfur-gold interaction (this type of interaction has energy of 40 kcal mol^{-1}).[122, 123] For comparison, a C-C covalent bond is estimated to be around 86.6 kcal mol^{-1} [124, 125] and the affinity of sulfur atoms to gold makes the orientation of such molecules preferably with its SH-group oriented towards gold and the other end of molecule, which can bear any functional

groups. This allows for chemical modifications and attachments of other molecules on top of such thiol-functionalized layers. Furthermore, by choosing the appropriate length of a thiol, also the electron tunnelling distance can be adjusted. It has to be mentioned here, however, that the electron tunneling rate is higher for shorter SAMs ($<C_3$) but the SAM layer is more disordered, and allows undesired cross-reactions at the electrode, whereas longer SAMs ($>C_6$) build stable layers which are not permittive for such side-reactions. On the other hand, the tunneling rate decreases exponentially with increase of SAM lengths, this is why there is a trade-off between tunneling rate and an ordered isolating SAM layer. Other promoters which carry charge, e.g. functionalized π-conjugated molecules such as carboxy- and amino-pyrene, functionalized naphthalene or anthracene compounds, pyrroloquinoline quinone (PQQ, with its' caraboxyl-group) can be used for functionalizing CNTs or graphene electrodes, enabling electrostatic interactions.

Covalent approach - is characterized by realization of a strong covalent bond between two partners. Such attachment can hold molecules stably together and is regarded as the preferable integration strategy. However, the binding does not necessarily occur at a defined site. Often, lysine residues of the molecules, which need to be integrated, are employed in this type of bonding. Here, for example, if a mutation is engineered exactly near the region of active center, such an attachment strategy can become very successful and the coupling can be considered specific. Basically, covalent chemistry is possible if the modification of the electrode carries carboxylic groups.

In the focus of the present thesis, however, is PSI and in the following subchapter detailed insights into direct photoelectrochemistry (I) and strategies for coupling PSI to electrodes (II) will be given.

3.6 Photoelectrochemistry of PSI: general considerations

Photosystem I can be considered as a photodiode in which the electron transfer has a defined vector, i.e. from luminal side (P_{700} - electron donor site) towards the stromal side (terminal electron acceptor site - F_B). To make use of the photo-excited electrons, they have to be efficiently extracted on one side and efficiently supplied on the other side. In nature, as mentioned before, these processes are realized by the Fdx – electron extraction, and by cyt *c6*/PC – indirect electron supply from PSII. However, in order to make use of the photogenerated electrons from PSI, first, it has to be extracted from its natural ambient and then transferred on to a conducting support and efficiently wired to it. There are several

possibilities for PSI to be arranged on the electrode. If the PSI is assembled with its stromal side towards the electrode (Fig. 6, B), it works as a photoanode and the electrons from PSI can be used as power source, e.g. in solar cells. If now a load is applied, then upon illumination electrons would flow from solution (where an electron donor should be present) *via* PSI and from there into the electrode, performing work on the load attached. Here, the presence of an electron donor in the solution is a prerequisite for functioning, since the PSI needs to be continuously reduced in order to maintain electron flow. If PSI's direction of electron transfer is pointing away from the electrode (Fig. 6, C) then the electrode functions as an electron supplier for PSI. In such an arrangement, the electron scavenger function is accomplished often by the dissolved oxygen, since electrodes are placed in a buffered solution. In this case the electrode-PSI system is acting as a photocathode: the electrons flow from the electrode towards the PSI and from the terminal F_B cluster into the solution. This configuration allows for extraction of high-energy electrons which might be turned into chemical energy. Other arrangements of PSI on the electrode are considered non-productive, since none of its redox centres is properly wired to the electrode. The use of PSI as a photoactive material is particularly interesting because of the high output voltage equal to ca. 1V. Another major advantage of PSI is its biocompatibility with other biomolecules, opening possibilities for combination with enzymes and thus coupling photocatalysis with enzymatic conversions of interest. Since PSI is also a photoactive enzyme the enzyme electrochemistry discussed in the previous chapter is also applicable regarding PSI. For a fast electron flow, electrons have to be quickly supplied and extracted from PSI.

3.6.1 *Direct Electron Transfer (DET) between PSI and electrodes*

A better fundamental understanding of photosynthetic redox cofactors and their electro- and photoelectrochemistry is a desired issue in modern photobiotechnology. Directly addressing of PSI, PSII and other photosynthetic proteins might be helpful herein. The difficulty of such investigations, however, arises from the fact that the redox active centres are shielded by the protein shell of the photosynthetic complex, as is often the case with many other enzymes. Nevertheless, until now many efforts have been made to achieve DET between photosynthetic proteins and electrodes, and several studies have reported direct electrochemistry of either bacterial reaction centres (bRCs), PSII or PSI on electrodes. Kievit *et al.* revealed in their study on P_{700} (PSI) and P_{870} (bRCs) centres that it is possible to perform direct electrochemistry on a solubilized protein.[126] In the study of Munge *et al*. the redox cofactors

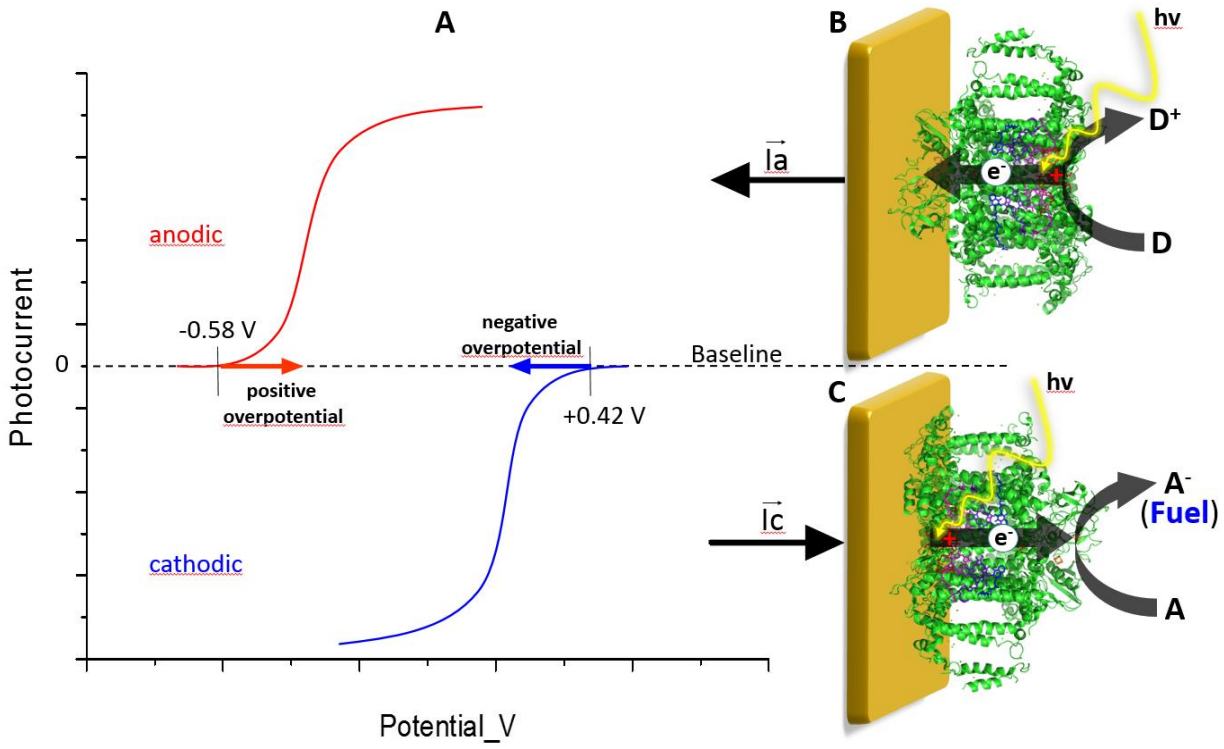

Figure 6. A - Anodic photocurrent can theoretically start at applied potentials more positive than the redox potential of F_B cluster (E_0 = - 0.58 V vs. SHE) (the prerequisite for this situation is that 100% of PSI molecules are assembled in anodic configuration), whereas cathodic photocurrent sets in theoretically at overpotentials more negative than the redox potential of P_{700} (E_0 = + 0.420 V vs. SHE) (also here is prerequisite that all PSI molecules are oriented in cathodic configuration). **B -** anodic configuration, **C** – cathodic configuration. In the anodic configuration, an electron donor should be present in solution. In the cathodic configuration, an electron acceptor should be present, this can be, for example, oxygen or another oxidized species.

of PSI have been addressed directly by means of voltammetry. Here, electrochemistry of the F_A/F_B and phylloquinone A_1 could be investigated in the dark; however, upon illumination no photocurrents could detected, indicating probable protein denaturation processes.[127]

Direct electrochemistry and photoelectrochemistry of the PSI has been investigated on thiol-modified gold electrodes in the study of Ciobanu *et al*., in which self-assembled monolayers (SAM) of hydroxyl-thiols with varying backbone lengths (C_2-C_{11}) have been compared. The study clearly revealed that C_6 and C_8 hydroxyl-thiols where most appropriate for productive PSI assembly and, thus, photocurrent generation of about 6.6 nA cm^{-2}. Additionally, electrochemical signals assigned to P_{700} and F_A/F_B could also be detected.[128] In another study, a pyrene-modified graphene electrode has been employed for covalent attachment of PSI. In this study, a direct photoelectrochemistry at P_{700} site has been achieved.[129] Here, good electrical communication between PSI and electrode has been achieved due to close proximity

of P_{700} to the electrode surface and good intrinsic electric conductivity of graphene and resulted in enhanced cathodic photocurrent production, of more than 100 μA cm^{-2}.

Direct photoelectrochemistry of PSI on metal oxide and semiconductor electrodes has been demonstrated in the work of Mershin *et al.*, in which a PsaE has been genetically engineered in such a way, that it showed high affinity towards metal oxide surfaces.[130] This allowed for selective binding of PSI with its stromal side towards the electrode surface, and hence, direct electron injection from F_B cluster into the electrode. The electrode materials tested in this study where ZnO and TiO_2.[130] Here, rather high photocurrent of about 362 μA cm^{-2} could be generated. However, it has to be mentioned here that TiO_2 being a high bandgap semiconductor can absorb light in the UV-region, so the calculated photocurrent contribution from TiO_2 was ca. 20%. Also in the work of LeBlanc *et al.*, direct photoelectrochemistry at the P_{700} site has been reported for PSI assembled on p-doped silicon, resulting in rather high cathodic photocurrents (ca. 875 μA cm^{-2}); however, also here, the semiconducting electrode alone generated over 250 μA cm^{-2}.[131] The largest reported photocurrents so far (anodic photocurrents) have been achieved from PSI electro-sprayed at nanostructured TiO_2, ca. 4.15 mA cm^{-2}. Also in this approach, the electrode material itself produced a considerable amount of photocurrent, ca. 1.5 mA cm^{-2}. Photocurrents under visible light were 780 μA cm^{-2}, still remaining the largest ever reported for PSI-based electrodes.[132]

3.6.2 *Mediated Electron Transfer (MET) between PSI and electrodes*

3.6.2.1 *Soluble mediators*

An alternative to the DET approach represents the mediated approach, where redox centres of PSI are addressed by a mediator. In many cases, it turns out to be very helpful in establishing a good electrical wiring between PSI and the electrode. Until now, many researchers have been employing mediated photoelectrochemistry on photosynthetic proteins. This approach is quite simple, since the precise orientation of such a super-complex as PSI is not a pivotal issue and good electron transfer rates can be achieved easily, depending on the concentration of the mediator and on its redox properties. Typical mediators used for addressing the P_{700} centre are, e.g. e^- donors for PSI: $Os(bpy)_2Cl_2$, cytochrome *c* (cyt *c*), ferrocenylmethyl-trimethylammonium hexaflorophosphate (FcTMA), sodium ascorbate/2,6-dichloroindophenol, ferrocyanide. Usually, the presence of dissolved oxygen in working solution is an advantageous fact for a photocathode configuration, since oxygen is able to oxidize the F_B cluster directly. The solution concentration of oxygen is around 250 μM.

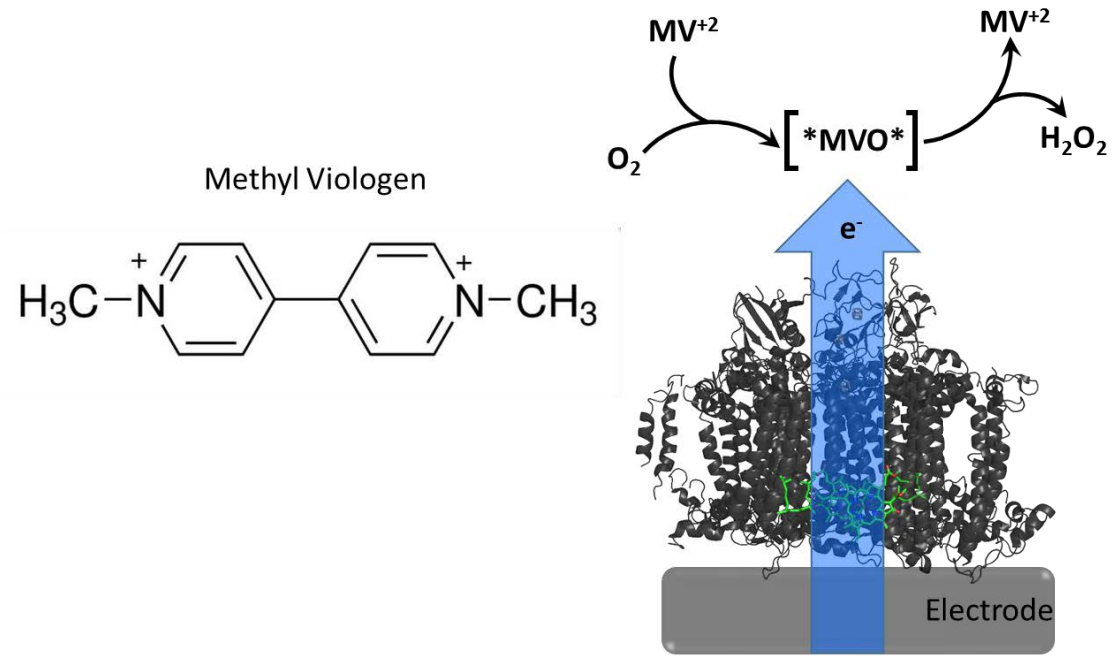

Figure 7. Left – structure of methyl viologen. Right – proposed **e**lectron transfer mechanism from photo-excited PSI to methyl viologen (MV^{2+}). Upon interaction of MV^{2+} with oxygen, a transition complex can be formed (*MVO*), which can decay quickly to the O_2^- and recover to MV^{2+}. In the last step, O_2^- can be further reduced to H_2O_2.

However, there are many other synthetic traditional electron scavengers that can be used for electron uptake from the terminal F_B cluster: methyl viologen, ferredoxin, anthraquinone-2-sulfonate, 2-hydroxy-1,4-naphthoquinone, methylene blue, hexaammineruthenium (III) ($Ru^{III}(NH_3)_6$), ferricyanide.[133] Here, the problem of cross-reaction between the electron acceptor and other species or at the electrode should be taken into account and circumvented. Noteworthy, methyl viologen (MV^{2+}) has been demonstrated to enhance the oxidation rate of the F_B cluster, but only in the presence of oxygen in solution. Several mechanisms of electron uptake by the MV^{2+} have been proposed. One of them postulates that MV^{2+} can form a short-living intermediate complexes with oxygen (MVO*) (Fig. 7), which further can oxidize the F_B cluster and subsequently regenerate to MV^{2+} by producing H_2O_2.[134] Another terminal electron acceptor can be even an enzyme (e.g. hydrogenase)[135-137] or a noble metal particle (e.g. Pt).[138, 139] This would be an aim for hydrogen production, which is of high commercial interest.

Many publications have been reported, in which MET between PSI and electrode has been achieved via soluble mediators. In the study of Faulkner *et al.*, PSI has been assembled by a vacuum-assisted approach on thiol-modified gold (-COOH, $-NH_2$ and $-CH_3$ functionalized thiols). Here, 100 nA cm^{-2} of cathodic photocurrent has been achieved by employing

mediators, Asc and DCPIP.[140] In the study of Ciesielski *et al.*, a similar electrode modification has been applied, however, on a 3D nanoporous gold leaf electrode. Also here, mediators have been used for establishing electrical coupling of PSI with the electrode. Photocurrents of 1 μA cm^{-2} have been reported.[141] In another work of Ciesielski *et al.*, densely packed PSI multilayers have been assembled on bare gold electrode, cathodic photocurrents of 2 μA cm^{-2} have been achieved.[142] In the study of Manocchi *et al.*, PSI assembled on charged (carboxylic thiols), hydrophobic (methyl thiols) and polar (hydroxyl thiols) thiols generated photocurrents upon addition of mediator Os-bis-bipyridyl ($Os(bpy)_2Cl_2$) and an electron acceptor MV^{2+} into working solution.[143] Photocurrents generated in this study were 75 nA cm^{-2}. A comprehensive study of various mediators has been done in the work of Chen *et al.*, where both, e^- acceptors and e^- donors for PSI, have been tested. Best results for anodic photocurrents have been achieved with FcTMA (200 μM) compounds showing average magnitude of ca. 1.2 μA cm^{-2}, and for the cathodic photocurrents with $Fe(CN)_6^{3-/4-}$, ca. 1 μA cm^{-2}.[144] Recently, Niroomand *et al.* published a study on assembly of PSI on different thiol-modified substrates, ITO, Ag, AgNP-ITO. A photocurrent of 90 nA cm^{-2} has been measured.[145] In the same year 2018 Pamu *et al.* published an interesting study on coupling PSI onto plasmonic Ag nanopyramids. Here, an 8-fold photocurrent enhancement has been achieved when comparing photocurrents on planar Ag with those on AgNPs, and yielded 75 nA cm^{-2}.[146]

3.6.2.2 *Molecular wires*

For improvement of the photoelectrochemistry of PSI the ultimate goal is to achieve direct non-interrupted wiring of the PSI with the electrode. One of the possibilities for such wiring can arise from the extraction of a cofactor from PSI (e.g. the phylloquinone A_1) and replacement of it with another compound for the direct wiring to the electrode. Such a strategy has been implemented in the work of Terasaki *et al.*, in which the natural ET chain has been by-passed by wiring of the vacant site of the A_1 cofactor with a phylloquinone analogue.[147] Here, mediators have been used as electron donors for P_{700}. Anodic photocurrents of 40 nA cm^{-2} have been reported. In 2010, Yehezkeli *et al.*[148] has wired PSI to the gold electrode *via* bis-aniline cross-linking approach. Here, anodic photocurrents have been generated (2 μA cm^{-2}). In the work of Efrati *et al.*, PSI has been covalently attached to the gold electrodes via a pyrroloquinoline quinone (PQQ) molecular wire. In this study, both, anodic (ca. 240 nA cm^{-2}) and cathodic (ca. 80 nA cm^{-2}) photocurrents have been reported.[149] Cytochrome *c* has been extensively investigated as electron mediator for PSI in the studies of

Stieger *et al.* Here, not only beneficial charge effect of cyt *c* on the directionality of PSI immobilization has been demonstrated, but also effective electrical wiring of P_{700} with the electrode *via* cyt *c*. The good functionality of PSI-cyt *c* system has been demonstrated by means of its vast applicability, stability, magnitude of the photocurrent and scalability. Not only a monolayer of PSI could be electrically addressed by a monolayer of cyt *c*, but a multilayer approach could be achieved as well.[85, 150] Besides thiol-modified gold, this system could be transferred also on other conductive support, 3D micro-ITO electrodes.[84] In these systems, the following cathodic photocurrents have been achieved: 1.6 μA cm^{-2}, 25 μA cm^{-2} and 150 μA cm^{-2}, respectively.[84, 85, 151] An intriguing study on the shuttle ability of di-hemic cyt *c4* has been performed in the same work group by Feifel *et al*. in 2018. Here, PSI has been electrically wired by a rather uncanonical redox di-hemic protein, cyt *c4*. The photocurrent output was in the range of 25 μA cm^{-2}.[152]

3.6.2.3 *Redox/conductive polymers/redox-hydrogels*

Next improvement step in wiring of PSI to electrodes represents the entrapment of PSI in a redox/conductive polymer or a redox hydrogel. Such an approach allows for multiple contacts between redox-sites of a polymer with redox centers of PSI, therefore, ET can be established even without proper orientation of PSI towards the electrode and represents an advantage over a PSI monolayer approach. A rather spread technique in this direction represents wiring of PSI onto or entrapping into the redox active polymer, e.g. an Os-based conductive polymer. This approach is based on the finding that Os redox potential can be aligned perfectly with respect to P_{700} in such a way, that a maximum gain from photovoltage becomes feasible. Furthermore, such redox polymer acts simultaneously as ET mediator and immobilization matrix for PSI. Badura *et al.* used Os-Polymer-PSI assembly and reported 29 μA cm^{-2} cathodic photocurrent.[153] In the work of Baker *et al.* PSI has been entrapped in polyvinylimidazole (PVI) polymer modified with $Os(bpy)_2Cl_2$. Cathodic photocurrent densities of 1.2 μA cm^{-2} have been achieved.[154] In a similar approach, Zhao *et al.* adjusted the hydrophobicity of Os-complex and an enhanced cathodic photocurrent 70 μA cm^{-2} could be achieved.[155] In the study of Kothe *et al.*, further improvements in an Os-complex-polymer-PSI system could be achieved by pH-induced collapse of the hydrogel structure, where PSI has been entrapped. Here, high cathodic photocurrents of about 322 μA cm^{-2} have been reported.[156] Baker *et al.* exploited also another polymer backbone, the well-known Nafion, which was enriched with $Os(bpy)_2Cl_2$.[157] Here photocurrents of 4 μA cm^2 have been reported. In the study of Gizzie *et*

al., a PSI-polyaniline mixture has been electro-copolymerized, resulting in photocurrent of ca. 5.7 μA cm^{-2}.[158] Finally, Zhao *et al.* reported the establishment of an efficient entrapment of PSI into an Os-polymer, a technique which has become very popular in last years. Here, ca. 25 μA cm^{-2} photocurrent has been reported at rather high light intensity, 280 mW cm^{-2}.[159]

3.7 Immobilization strategies

Since PSI is a large complex protein and also a membrane protein, several aspects have to be taken into account when designing an appropriate electrode surface for photoelectrochemistry on this protein. The requirements on the electrode are following: i) the electrodes should provide a protein-friendly environment. It has been previously mentioned, that surface modifications are beneficial for contacting proteins with electrodes and can significantly improve electrochemistry of proteins (e.g. cyt *c*). The same rules apply also to PSI, ii) electrodes should provide large surface area, which would allow higher loadings with proteins, e.g. 3D electrodes can be used, iii) electrodes should have high conductivity. Based on these principles, many strategies on coupling proteins and also PSI have been developed. In the following subchapter, some of these strategies are presented and compared in terms of photocurrent production by PSI.

3.7.1 PSI on gold electrodes

The most widespread electrode material is gold. However, for electrochemical investigations on proteins, as mentioned before, some modifications are desirable. For this reason thiols have largely been employed as surface promoters for attachment of biomolecules. These molecules are known for building self-assembled monolayers (SAM) by hydrophobic interactions between the backbones of the alkyl chains. The thiol group shows affinity towards gold and thus chemisorption of a thiol occurs between –SH and Au. Since the backbones of such thiols can pack densely, such thiol layers can prevent undesired cross-reactions between the redox species from electrolyte and the electrode. Furthermore, the solution-exposed thiol end can carry a functional group, which favors electrostatic interactions, or even enables covalent chemistry. PSI, for example, is a charged biomolecule and has both, positive and negative patches. The luminal side of PSI has an overall negative charge and the stromal side has a net positive charge, at pH 7, although both, the stromal and the luminal sides have positive and negative patches. Due to its dipole character, PSI can be adsorbed on a charged electrode in a specific way, either with its luminal side facing the

electrode, or with its stromal side. For these reasons, the deposition of photosystem I (PSI) on gold, modified with organothiol-based self-assembled monolayers (SAM), has been investigated. In the work of Lee *et al.* different functionalities of such SAMs have been tested: $-COO^-$, -OH and $-NH^+(CH_3)_2$. It has been demonstrated, that 70 % of assembled PSI molecules with the direction of electron flow pointing away from the electrode could be realized on hydroxyl-terminated thiols.[160] The estimation has been derived from the shape of I-V curves for 100 random PSI molecules on the electrode surface. The I-V curve is dependent on the orientation of the PSI on the electrode: if electron transfer vector is oriented parallel to the surface, then a semiconductor-like I-V curve is obtained, if, on the other hand, the PSI (and respectively the electron transfer vector) is oriented perpendicular to the surface, then a diode-like I-V curve is registered. In this study, however, the aim was just to clarify the orientation of PSI on the electrode, and therefore, no photocurrent has been measured. In the study of Mukherjee *et al.* hydroxyl-terminated thiols have been tested for oriented assembly of PSI by comparing the gravity-assisted method vs. the electric field-assisted assembly technique. It has been found out that uniform orientation of PSI layer could be obtained and that the electric field could promote a formation of a denser PSI-layer.[161] Also Manocchi *et al.* showed that electrophoretically assembled PSI molecules on top of mercaptohexanol and mercaptohexanoic acid could be obtained and thus proved again that there are some interactions between the charged thiol-layer and the surface charge of PSI, which are responsible for electrostatic attachment.[143] Frolov *et al.* realized a covalent attachment of Cys-mutant PSI directly on the gold electrode, however, here a photovoltage of ca. 1 V but no photocurrents have been reported.[162] In the study of Kincaid *et al.*, PSI has been assembled on C_6-thiols carrying –OH groups after which C_{22}-thiols have been introduced by back-filling, thus mimicking the thylakoid membrane (here, the long hydrophobic backbones of the C_{22}-thiol can interact with the hydrophobic membrane region of the PSI).[163] In this study, PSI has been stably trapped on the thiol layer and could be exposed to organic solvents without loss of function. In the study of Ciobanu *et al.*, as mentioned before in the previous section, a 6.6 nA cm^{-2} cathodic photocurrent could be generated on C_6-hydroxythiols. Several covalent approaches have been employed to bind PSI to the gold electrode *via* an activated promoter: PSI on Au-SAM with terminal aldehyde group (100 nA cm^{-2}),[140] PSI on 3D nanoporous gold leaf electrode using the same coupling as Faulkner *et al.*(1 μA cm^{-2}). Another approach has been employed by Terasaki *et al.*, where PSI has been attached to the gold electrode via a molecular wire (vitamin K), which replaced the phylloquinone A_1 and bridged the A_1 pocket

with the gold electrode. Here, an anodic photocurrent of about 1.6 μA cm^{-2} has been reported.[164] Even though the modification of metal electrodes is often required for creating a protein-compatible microenvironment, there are also several studies on attachment of PSI at unmodified gold electrodes: in the work of Ciesielski *et al.* PSI multilayers have been deposited in a container and upon addition of mediators photocurrents of 2 μA cm^{-2} could be generated. Tapia *et al.* published a system in which a hydrogenase has been tethered to the stromal side of PSI. Here, cathodic photocurrents were 12 μA cm^{-2}, however, after 10 minutes continuous illumination 50 % of activity of PSI was lost.[165]

3.7.2 PSI on carbon-based materials

Among different types of employed electrode materials for PSI immobilization carbon-based electrodes have gained some attention among researchers. This particular class of electrodes is distinguishable by high conductivity, biocompatibility, low prize, high resistance against chemical agents, light weight, 0-to-3 dimensionality and many other outstanding features which carbon is bearing inside these structures. Some of the usual and most simple carbon-based electrodes are glassy carbon and pyrolytic graphite electrodes. In the work of Munge *et al.*, PSI has been assembled on pyrolytic graphite electrodes in the following way: a mixture of PSI and dimyristoylphosphatidylcholine (DMPC) has been spread over PG electrode and dried overnight.[127] Here, only electrochemical investigation of redox cofactors has been performed, however, no photocurrents have been reported. Kothe *et al.* immobilized PSI on Os-polymer modified glassy carbon electrodes (GCE), resulting in a well-performing photocathode (322 μA cm^{-2}).[116] Other carbon nanomaterials which can act as conductive support are carbon nanotubes and graphene. Carbon nanotubes provide high surface area, due to their advantageously high surface/volume ratio. Besides, this material is known for its outstanding conductivity. Graphene sheets are ultra-flat and optically transparent and show also enhanced conductivity. The above-mentioned features make CNTs and graphene promising electrode materials. A break-through has been achieved by using transparent electrodes for PSI assembly. In the group of Gunther *et al.* such transparent graphene-based electrodes have been employed for the first time, resulting in photocurrent generation from PSI and allowing for the use of opaque mediators.[166] The reported cathodic photocurrents were 550 nA cm^{-2}. LeBlanc *et al.* reported immobilization of PSI on graphene oxide (GO) and reduced graphene oxide (RGO). Here, photocurrents were rather high: for PSI-GO-Si 80 μA cm^{-2}, and for PSI-RGO-Si 95 μA cm^{-2}.[167] Later, Feifel *et al.* developed modified-graphene

electrodes (π-π-based modification with a NHS-pyrene ester) for PSI attachment, which resulted in a well-performing PSI-based photobioelectrode, here 135 μA cm^{-2} have been reported.[129] CNTs, in contrast, might be even better materials for high performance of a PSI-based photobioelectrode, since they provide much higher surface area than a flat graphene. Several approaches are known so far from the literature, in which PSI was immobilized on CNTs. Carmeli *et al.* immobilized Cys-mutant PSI on SWNTs and recorded a photocurrent of 100 nA, however, the electrode area was not reported.[168] Kaniber *et al.* published three studies on covalent attachment of Cys-mutant PSI onto maleimide-functionalized SWNTs. However, no photocurrent has been measured in these works.[111, 169, 170] Nii *et al.* 2017, reported specially designed, genetically engineered variant of PSI, which has affinity towards carbon nanotubes. Such PSI has been attached specifically to the SWNTs, however, the photocurrents produced were very tiny: anodic photocurrent 0.08 μA cm^{-2}.[171]

3.7.3 PSI on other conductive and semiconductive electrodes

Besides gold- and carbon-based electrodes many groups have investigated non-metal materials as electrode supports for assembly of various biomolecules, including PSI. Here, Frolov *et al.* showed that Cys-mutant PSI can be attached on maleimide-modified p- and n-type GaAs electrodes.[172] Photocurrents have been reported, but the generated photovoltage was equivalent to 0.3 V and - 0.47 V vs. SHE respectively. Nikandrov *et al.* succeeded in immobilization of PSI on TiO_2 semiconductive matrix, in which high loadings of protein have been achieved due to mesoporous structure of such electrode.[173] Anodic photocurrents of 1μA cm^{-2} have been reported. LeBlanc *et al.* made use of p- and n-doped silicon for PSI attachment. Here, photocurrent generation has been investigated, and it has been demnonstrated that p-doped silicon is a better candidate as compared to n-doped silicon.[131] Highest cathodic photocurrents have been achieved on p-type Si, 875 μA cm^{-2}, light intensity 190 mW cm^{-2}, U = -0.5 V vs SHE, 115 mM MV^{2+} (however, ca. 625 μA cm^{-2} can be attributed to the PSI activity, the rest is coming from p-doped Silicon). Here, however, it must be taken into account, that such experimental conditions are extreme and the reported photocurrent values refer to the transient photocurrent peaks and not steady-state photocurrent. In this system, the photocurrent decays to 20 % of the nominal value after 20 seconds. ITO electrodes have been widely used as conductive supports for PSI attachment. In the study of Yehezkeli *et al.*, 2013, PSI has been assembled on ITO pre-modified with cyanopropyl triethoxysilane, followed by adsorption of poly-benzyl viologen, PBV^{2+}. On top

of this conductive polymer PSI layer has been attached, this procedure has been repeated several times for construction of multilayers. The highest reported photocurrents in this system were 2.2 μA cm^{-2}.[174] In 2013 Ocakoglu *et al.* published deposition of PSI on hematite (α-Fe_2O_3)-coated FTO by electrostatic forces (hematite positive, PSI negative). An anodic photocurrent 57 μA cm^{-2} has been reported.[175] In 2015 Gizzie *et al.* reported a solid state solar cell based on PSI-Pani (PSI-polyaniline) deposited on TiO_2-FTO. The photoanode produced I_{SC} 72 μA cm^{-2}.[176] Shah *et al.* reported anodic photocurrents from PSI electro-sprayed on nanostructured TiO_2. Under visible light 780 μA cm^{-2}, the highest anodic photocurrent ever reported for PSI-based electrodes.[132] In 2016, Efrati *et al.* has published a PSI linked to PQQ-modified ITO. Here, anodic photocurrents of 2.25 μA cm^{-2} have been reported.[177] Other interesting study on PSI on transparent conductive oxides has been recently published by Peters *et al*. Here, PSI has been assembled on 3D macroATO (antimony tin oxide) and cathodic photocurrents have been measured, 7 μA cm^{-2}.[178] Figure 8 depicts several most popular immobilization approaches used for attachment of photoactive proteins on electrodes.

3.7.4 PSI multilayers

Since one of the prerequisites for high output performance of any system is high loading of active converting molecules, a large amount of studies investigated multilayer arrangements of PSI. In the study of Ciesielski *et al.* a vacuum-assisted deposition of PSI on glass and gold has been performed, resulting in 2 μA cm^{-2} photocurrent generation.[179] Entrapment of PSI molecules in the redox-active polymers has been shown in the work of Yehezkeli *et al.*,[174] where polymer was consisted of poly-benzyl viologen (PBV^{2+}) mojeties $(PBV^{2+}\text{-PSI})_n$, 2.2 μA cm^{-2} and 1.8 μA cm^{-2} have been generated. Large amounts of PSI have been entrapped also in a conductive Nafion filled with $Os(bpy)_2Cl_2$ as hole scavenging compound[157] and resulted in generation of 4 μA cm^{-2} photocurrents. In the work of Stieger *et al.*, a promising cyt *c*-PSI tandem has led to possibilities for multilayer assembly on 2D gold electrode with considerably larger cathodic photocurrents, 25 μA cm^{-2}.[85]

3.8 Carbon Nanotubes: structure and properties

Carbon nanotubes or CNTs have been discovered in 1991 by Sumio Iijima and represent graphene sheets rolled in a tube. A pure graphene is a monoatomic sheet of carbon atoms bound to each other in a hexagon-like fashion, representing a conjugated π-system, in which

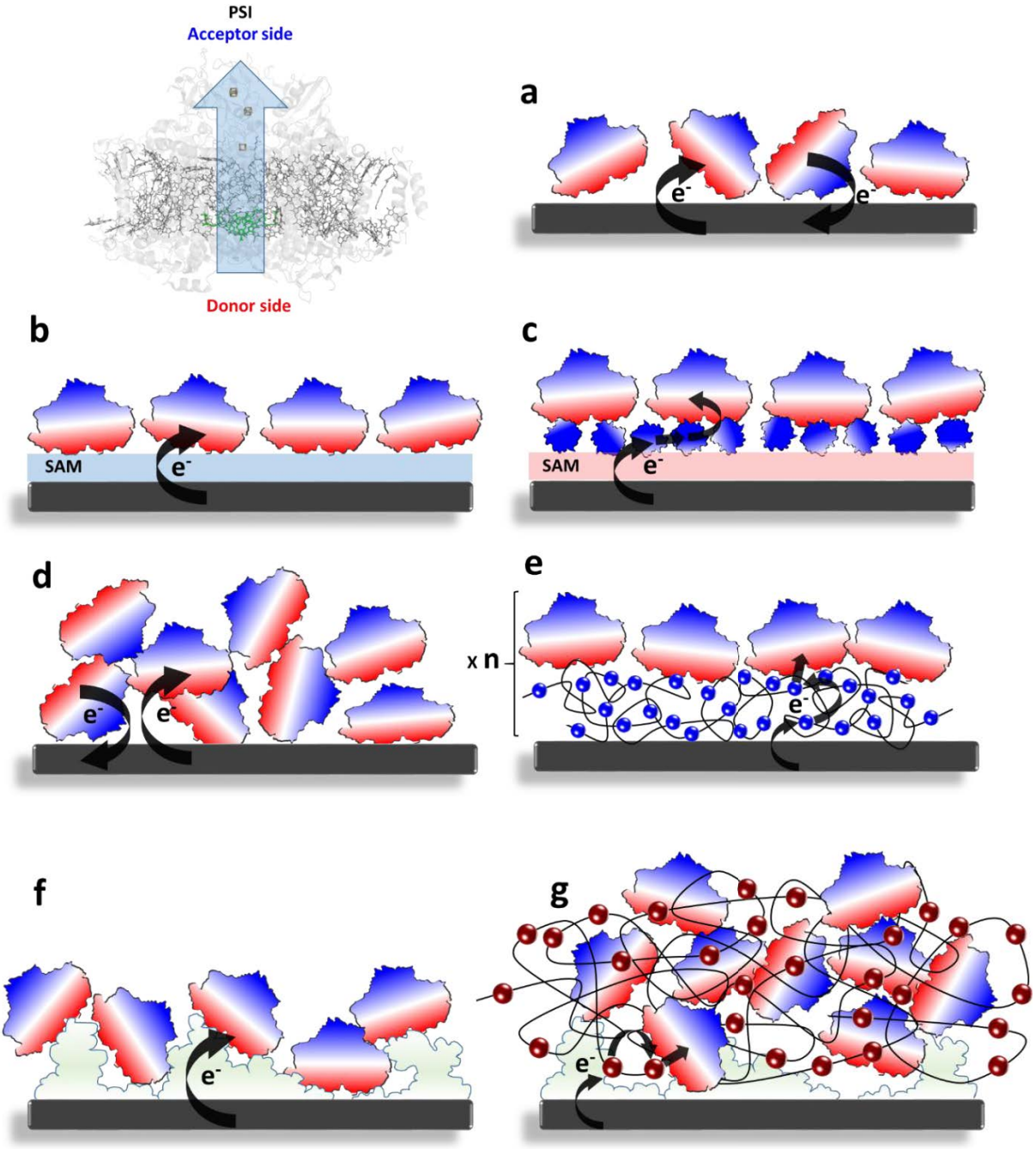

Figure 8 PSI-based photobioelectrode configurations. Red – donor side, blue – acceptor side of PSI. a) Bare electrode, DET (but short-circuits are possible). b) modified electrode surface (e.g. self-assembled monolayer, SAM), a more directed assembly is possible, short-circuits might be reduced. c) Additional modification of SAM-electrode with cyt c, preferred orientation of PSI can be achieved. d) Vacuum-assisted deposition of thick layers of PSI, here, short-circuits are often encountered. e) Layer-by-Layer deposition by alternating charged polymer-PSI. f) 3D nanostructured/mesoporous electrode configuration, higher protein loadings become feasible. g) Redox-polymer hydrogel entrapment (in this example on a 3D electrode).

each of the carbon atoms is in its sp^2 hybridization state. CNTs can be classified into single-walled carbon nanotubes (SWNTs)[180, 181] and multi-walled carbon nanotubes (MWNTs), the latter having 2 - 50 walls.[182] The SWNTs have a diameter of ca. 0.4 - 3 nm and length of several µm, and are hardly found isolated,[183] forming bundles, whereas the MWNTs can achieve ca. 3 to several hundreds of nm in width and up to 0.5 m in length. Outstanding mechanical, thermal, chemical, optical, electronic properties of CNTs arise from their structure. Astonishingly, CNTs are exceptionally hard in terms of tensile strength and elastic modulus (harder than steel), but at the same time are very soft in the radial direction, have light-weight and are flexible, thus outperforming steel at all accounts.[184, 185] They can be semiconductive or conductive, which is determined by the orientation of chiral vectors (n, m) of the lattice structure.[186, 187] Therefore, three types of CNT are defined: m = 0 → "zigzag" (semiconductor), m = n → "armchair" (metallic), other → "chiral" (semiconductor), (see Fig. 9). In Fig. 10 scanning electron microscope images are shown in order to create an impression of how these structures look under magnification. The delocalized π-conjugated character of these nanomaterial and extremely small size allow for fast ballistic electron transfer, in which no scattering of electrons is present to impede the electron flow, however, this condition may

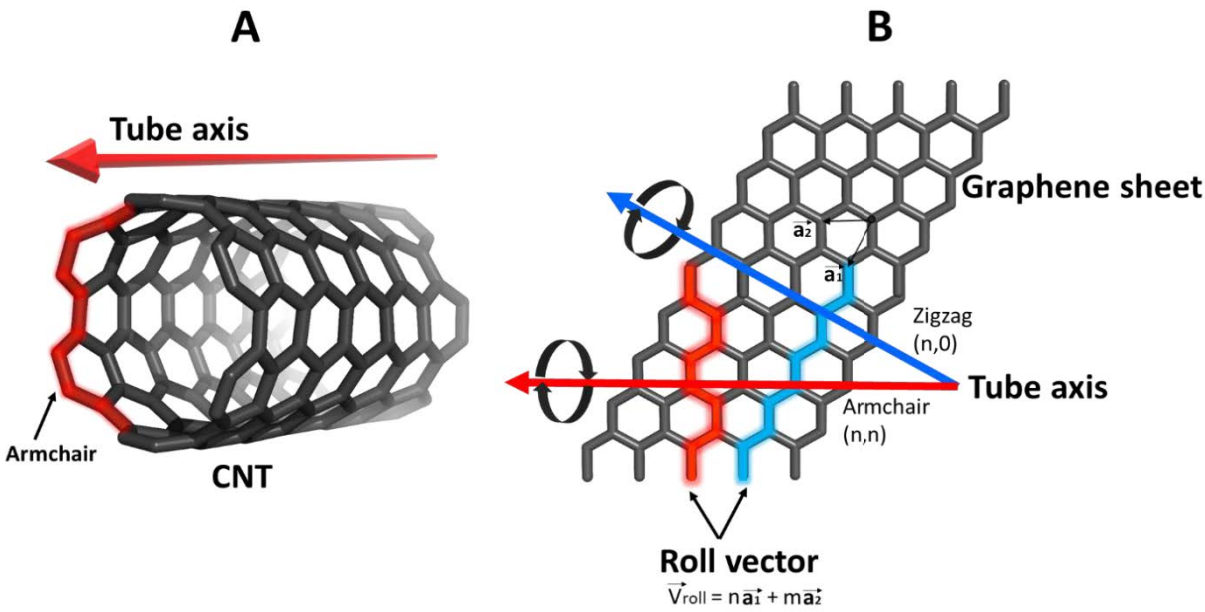

Figure 9. Schematic representation of structure of carbon nanotubes (CNT) and visualization of lattice vectors. **A**- a rolled graphene sheet, a CNT, in its "armchair" rolling. **B** – graphene sheet, a_1 and a_2 – lattice vectors (unit vectors), tube axis is perpendicular to the roll vector V_{roll}. Blue - zigzag rolling (semiconductor character), red – armchair rolling (metallic character).

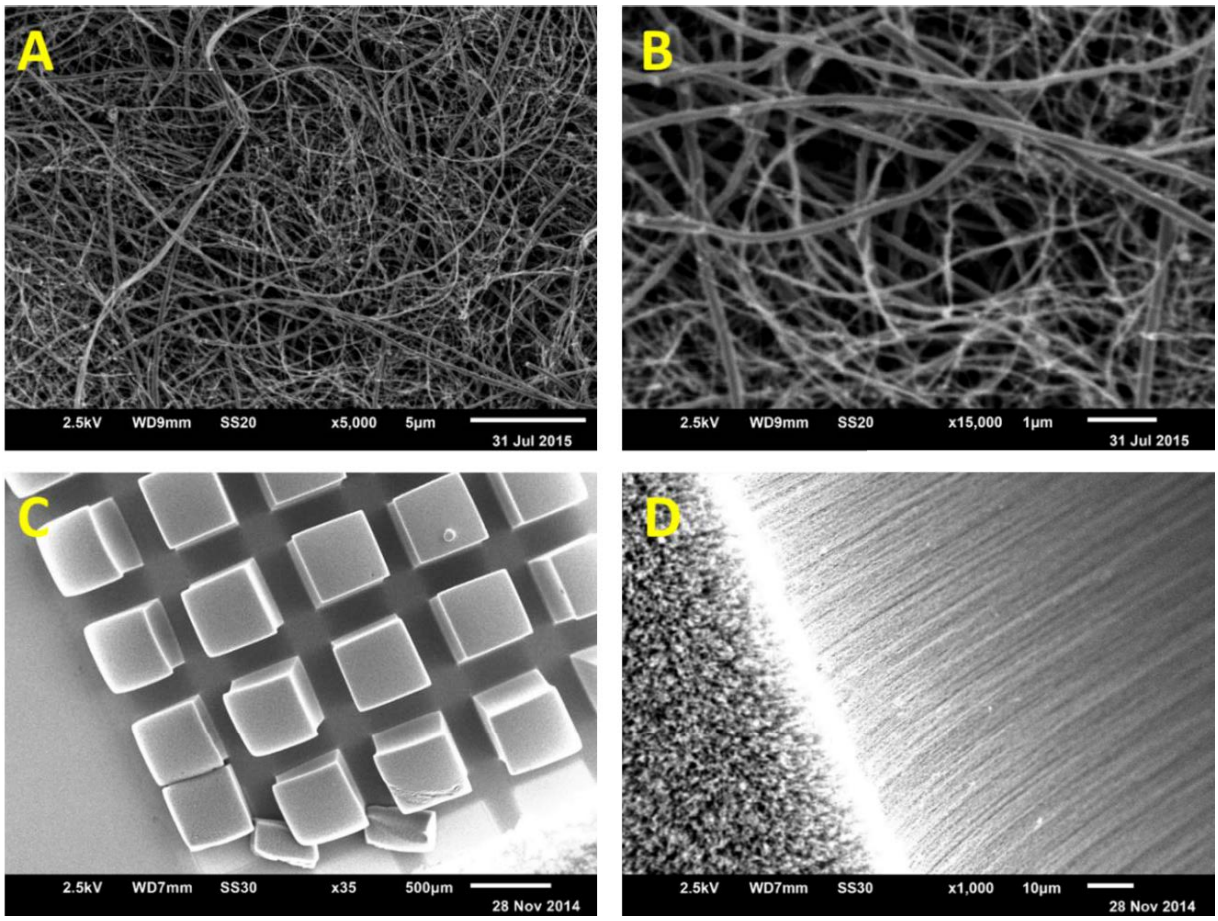

Figure 10. Typical image of multi-walled carbon nanotubes (MWNTs). **A –** randomly distributed MWNTs, **B** – magnification of **A**. **C** - vertically aligned carbon nanotubes (vaCNTs). **D -** magnification of **C**. Images have been taken with scanning electron microscope (SEM). Acceleration voltage 2.5 kV.

be achieved only if no impurities and defects in the structure are present.[188, 189] CNTs can transport up to 4 x 10^9 A cm^{-2} current densities, overcoming copper 1000-fold.[190] Since CNTs, especially SWNTs, have a very tiny cross-section, electrons propagate only along the longitudinal axis and hence, CNTs can be described as one-dimensional quantum wires. Particularly electric properties are of interest in the field of nano-engineering. CNTs show absorption and photoluminescence behaviour. Besides, these structures are known for exceptional thermoconductivity, almost 10-fold as compared to that of copper. In the following section the applications emerging from these exceptional properties of CNTs are presented.

3.8.1 Electrochemistry of CNTs

Besides the above-mentioned properties of CNTs, such as high electrical conductivity, a high surface/volume ratio, biocompatibility, other, electrochemical properties, gained much attention. These are: enhanced voltammetric current, increased heterogeneous electron transfer rates and insignificant fouling of CNT-based materials. Therefore, they have been employed for electrochemical investigations of small redox molecules and also larger ones, such as redox proteins and enzymes. Generally, it is considered that such small diameters of CNTs (e.g. in SWNTs or DWNTs, 1.2-5 nm) exhibit different electronic properties when compared to graphite.[191] Banks *et al.* showed that electrochemistry of some small redox active compounds, e.g. epinephrine, norepinephrine, NADH, is enhanced at the edges and defect sites of CNTs and at the edge planes of pyrolytic graphite (EPPG), whereas at the basal plane of pyrolytic graphite (BPPG) and at the pristine (pure/clean) wall of CNT less electrochemistry occurs, the electron transfer rates are limiting almost to zero. This phenomenon can be explained by the fact that edges act as microelectrodes, whereby the diffusion of electroactive species is radial, and not planar, as in the case of macroelectrodes. The faradaic current at such sites is enhanced compared to the charging background current, thus the signal-to-noise ratio is increased, and due to higher mass transport the electrochemical signal becomes larger per area as compared to typical planar electrodes (e.g. pyrolytic graphite electrodes). Another point is, that in the production process some metallic impurities like (Fe, Ni, Co, Mo, Cu) are present in CNT (1-10 %) and therefore they influence the electrocatalytic protperties of CNTs. These impurities can dominate the electrochemistry of entire CNTs since they behave like metallic nanoeletcrodes – the diffusion layers of these impurities can heavily overlap, which would make their behaviour similar to a macroelectrode. At the pristine, defect-free wall of CNTs, only poor electrochemistry has been shown and can be considered similar to the basal plane graphite electrochemistry.[192, 193] Besides, some groups have demonstrated, that introduction of functional groups into the CNT structure, e.g. oxidation of CNT, which inherently lead to the presence of oxygen-containing sites, also enhances the electrochemical properties of CNTs. Other groups, in contrast, have shown exactly the opposite: the heterogeneous ET is decreased when multiple oxidation sites are introduced. Here, one has to discriminate between strong oxidation by a violent acid, or by light electrochemical oxidation, where also to some degree a few oxygen groups are introduced; however, not as many as by treatment with HNO_3.

3.8.2 Applications of CNTs

There is a tremendous number of applications of carbon nanotubes almost in every field of science and industry. But only the most relevant for this thesis will be mentioned:

3.8.2.1 *Capacitor applications* – due to their high accessible surface area and high electric conductivity CNTs are very attractive for use as electrode materials. One particular direction can be the use as a supercapacitor or an actuator (in robotics). The small separation distance between the charge on the CNT and the countercharge in the electrolyte, is about nm as compared to μm in ordinary dielectric capacitors. Reaching capacitances of up to 200 F g^{-1}, the CNT-based devices allow for high charge injection and respectively energy storage.[194]

3.8.2.2 *Sensing and biosensing* – unique electrochemical properties of CNTs enable construction of improved sensing and biosensing devices, e.g. amperometric enzyme electrodes, nucleic-acid sensing or immunosensors. However, for optimal functionality of CNT-based biosensors not only a proper control of their physical and chemical properties is required but also surface functionalization. When functionalized, CNTs' properties can be modulated for low detection limit and high selectivity against certain compounds. A special case are the ink-jet-printed strips for progesterone and oestrogen detection, but also for protein and DNA sensorics, troponin or NO_2 are feasible.[195] Enhanced sensitivity can be achieved if the CNTs are vertically aligned, vaCNTs, a feature which is arising from different electrochemistry at the sidewall of CNT as compared to the edges. In vaCNT configuration, more edges are exposed to the solution as compared to randomly distributed CNTs, whereas the hydrophobic walls align together due to π-π interactions. vaCNTs are usually employed for detection of biomarkers, such as DNA,[196] glucose,[197, 198] cholesterol,[199, 200] cysteine,[201, 202] morphine,[203] dopamine[204, 205] etc.

3.8.2.3 *Hydrogen storage* – CNTs are well known for ability to store H_2. The hydrogen uptake proceeds by compresing of the gas at high densities inside CNTs walls by chemisorption between hydrogen atoms and carbon atoms. Such high loadings are due to high pore volume of CNTs and high surface area. Several studies have been dealing with hydrogen storage in SWNTs.[206-209]

3.8.2.4 *Fuel- and Biofuel cells* – CNTs have been successfully used in fuel-cell production replacing the use of Pt. Here, N_2-doped vaCNTs have been employed for oxygen reduction reactions (ORR) and generated four times more current than a Pt catalyst.[210] There are large number of publications on CNT-based biofuel cells, in which enzymes such as: glucose oxidase/glucose dehydrogenase/fructose dehydrogenase are attached at the anode and bilirubin oxidase or laccase are attached at the cathode.[211] An interesting electrode material here represents the so-called buckypaper, which in itself is an electrode and can be connected to the cell directly. Besides its properties such as high conductivity and possibility to be twisted, these carbon papers allow for high loadings of enzymes. Power densities of ca. 107 $\mu W\ cm^{-2}$ have been reported for a biofuel cell based on PQQ-modified buckypaper-glucose dehydrogenase-based anode and bilirubin oxidase-based cathode. In the same work, vertically aligned CNTs have been compared to the buckypaper and the power densities of 122 $\mu W\ cm^{-2}$.[212] There are several other studies where an enzyme has been employed for construction of a buckypaper-based biofuel cell: bilirubin oxidase-based cathode,[213, 214] glucose oxidase-horseradish peroxidase as biocathode,[215] laccase-based biocathode.[216]

3.8.3 Hybrid systems with biological molecules

Due to their versatile functions and outstanding features, CNTs have gained enormous scientific attention and there are plenty of studies on their use in hybrid systems. Combination of such structures with other nanomaterials can lead to new interesting composites with improved properties. Special interest represent hybrids with biomolecules (DNA, proteins or even enzymes). In such hybrid systems conductive properties of CNTs are combined with catalytic or recognition properties of the biomolecule. However, for a productive combination of two such different materials it is necessary to ensure their compatibility with each other. The pronounced hydrophobic character of CNTs not only hinders their transport in aqueous media but also suggests limiting biological implications, since hydrophobicity may act in a denaturating way on some biomolecules. This is why such structures can be previously functionalized with a hydrophilic promoter monolayer which can provide the optimal alignment of the protein for binding or even efficient electron transfer.[217] The mildest modification, i.e. without affecting conductivity, is "non-invasive" modification with a π-compound, by making use of π-π interactions.[218] These interactions are known as weak interactions, however, when many of them operate together, the binding strength is large enough for keeping even "heavy" molecules attached. As a π-modifier, different aromatic

mojeties like phenols, naphthalenes, anthracenes, pyrenes or pyrroloquinoline quinones (PQQ) have been reported so far. A different type of "non-invasive" modification of CNTs represents the wrapping procedure, in which CNTs can be wrapped in a polymer. Often the polymer is functionalized with hydrophilic groups, thus enhancing the solubility of CNTs and ensuring attachment sites for other biomolecules. Polymers which have been already successfully employed in modification of CNTs are: Nafion,[219] polyvinyl pyrrolidone (PVP) or polystyrene sulfonate,[220] polyethylene glycol (PEG), polyethylene imine (PEI),[221, 222] poly(metaphenylenevinylene),[223] sulfonated polyanilines.[224, 225] The composition of the polymer can be tunable, e.g. if a monomer mixture is electropolymerized on the CNT surface. In the work of Fusco *et al.*, it has been demonstrated that polythiophenes can be electropolymerized on MWNTs and different composition of the resulting polymer could be achieved, depending on the monomer mixture composition.[226, 227] Another possibility of modification of CNTs can be an "invasive" method, where double bonds are broken and covalently bound functional groups are introduced. Here, however, the modification degree has to be monitored, since each modification implies loss of conductivity by breaking the conjugated character of a pristine nanotube. This modification can be achieved by several methods: electrochemically by cycling CNTs, physically by sonication procedure or chemically by treatment with strong acids (e.g. HNO_3). These techniques introduce defects and oxygen functionalities into CNT structure, thus contributing to the hydrophilic character. Once the modification of CNT is achieved and its hydrophilic character is improved, these structures can be used for attachment of biomolecules. Proteins can be attached to CNTs in an electrostatic or covalent way, depending on the type of modification and the functional groups on the CNTs. In this way, enzymes like glucose oxidase, laccase, bilirubin oxidase, acetylcholine-esterase, choline oxidase, horseradish peroxidase, microperoxidase, or redox proteins such as cytochrome *c* or myoglobin have been contacted with CNTs. Some biomolecules, however, can interact with an unmodified hydrophobic CNTs, e.g. DNA, which has been shown to interact with CNTs by simple hydrophobic interactions, which DNA wraps the tube along its axis. Interestingly, MWNTs and SWNTs have already been combined with bacterial reaction centres (bRC), photosystem I molecules and even with complete thylakoid membranes to result in functional photobioelectrodes (see Table 1, Discussion chapter).

3.9 Fullerenes - *the "interstellar dust"*

3.9.1 Structure and properties

Since carbon is formed in the cores of stars by the fusion process and in the later stages is spread into the interstellar space it is not excluded that these carbon atoms may form different carbon allotropes, including fullerenes. Indeed, the presence of C_{60} and C_{70} in the interstellar dust has been detected by infrared Spectroscopy.[228, 229] On earth, fullerenes cannot be found in the rocks or elsewhere. These intricate structures have to be synthesized in the laboratory under certain experimental conditions. Fullerenes, thus, have been officially discovered by H. Kroto and R. Smalley in 1985, although other scientists (Eiji Osawa, R. W. Henson) have previously (in 1970) predicted their existence theoretically. These unusual new carbon allotropes have been named after the american architect Buckminster Fuller due to their "soccer-ball"-like structure. Being less than 1 nm (for C_{60}) in size fullerenes represent an icosahedron with alternating pentagons and hexagons (for C_{60} the structure contains 12 pentagons and 20 hexagons).[230] In this carbon allotrope all carbon atoms have all valences satisfied by two single- and one double-bond and hence, the structure is aromatic. Fullerenes may have different number of C-atoms: C_{20}, C_{60}, C_{70}, C_{76}, C_{80} – C_{1500} to name just few of them.[231] Fig. 11 depicts two examples of fullerenes C_{60} and C_{70}.

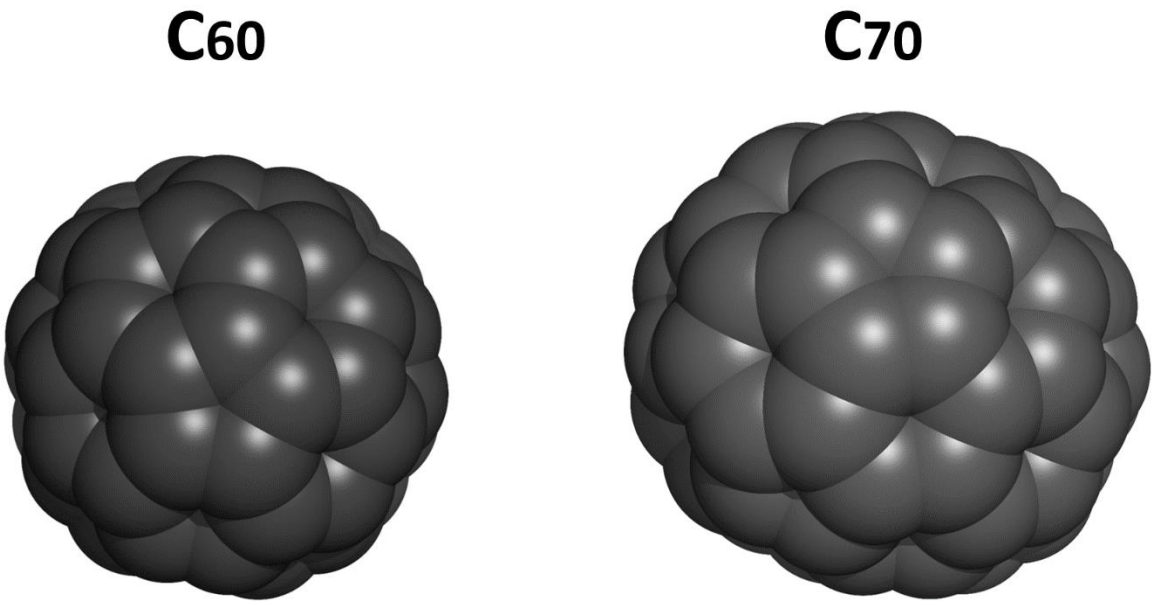

Figure 11. Fullerene C_{60} (left) and Fullerene C_{70} (right). Fullerene C_{60} appears more round and symmetrical, whereas in C_{70}, the additional carbon atoms confer a slightly ellipsoidal shape. Structures generated with PyMol.

Fullerenes are similar in behaviour with electron-deficient alkenes and thus, react willingly with electron-rich compounds being able to uptake up to six electrons per molecule of fullerene.[232] Fullerenes absorb both, in UV region and in visible region, and have a relatively small optical bandgap (1.6 eV for C_{60}[233, 234] and 1.65-1.76 eV for C_{70}[235-237]). The curvature of the fullerene allows for easy functionalization of such structures. The functionalization of fullerenes, similarly to the CNTs functionalization, allows fullerenes to undergo productive interactions with biomolecules, which are mostly hydrophilic molecules.

3.9.2 Electrochemistry of Fullerenes

The high affinity for electrons has been predicted even before the electrochemical experiments on fullerenes have been carried out. These structures have a triply degenerate and low-lying LUMO and this allows for easy uptake and donating of up to 6 electrons.

$C_{60}^{n-} + e^- \leftrightarrow C_{60}^{(n+1)-}$, n = 0, 1,…5

This feature is responsible for rich electrochemistry of fullerenes. In cyclic voltammetry six clear reversible redox peaks corresponding to one-electron transfer reactions could be identified as reported in many studies.[238, 239] The behaviour of C_{60} and C_{70}, thereby, is very similar.

3.9.2.1 *Electrochemistry of dissolved fullerenes in solution*

Since fullerenes are almost insoluble in polar and aqueous solvents, many electrochemical studies have been performed in non-polar media (e.g. benzene, toluene, *o*-dichlorobenzene). These media are suitable for basic investigations of fullerene properties, since their reduction window is very large as compared to other solvents. A diffusion-controlled reduction of fullerenes has also been demonstrated in mixed non-polar media (acetonitrile/toluene, 1:5). Here, all six one-electron reduction waves could be observed and the corresponding midpoint potentials ($E_{1/2}$) for the reduction peaks identified: -0.97, -1.34, -1.78, -2.21, -2.7, -3.07 V vs Fc/Fc^+).[240] The oxidation of fullerene, in contrast, is irreversible and can lead to a degradation of the fullerene molecules (both for dissolved fullerenes and the fullerene films).[238] In other media, e.g. in 1,1,2,2-tetrachloroethane (TCE), the first oxidation peaks of C_{60} and C_{70} have been identified to lie at +1.26 V and +1.2 V respectively and thus the HOMO-LUMO gap has been estimated to be 2.32 V for C_{60} and 2.22 V for C_{70}.[238] It has to be mentioned here, that midpoint potentials of the redox events, however, are depending on the solvent and supporting electrolyte used in the experiment.[241]

3.9.2.2 *Electrochemistry of fullerene films*

Electrochemistry on fullerene films usually is performed in solvents where fullerenes are insoluble or show negligible solubility (e.g. acetonitrile)[242] and has turned out to be far more complicated as for dissolved fullerenes. Usually, a supporting electrolyte is added for improving solvent ionic conductibility. The cations from the supporting electrolyte have been shown to have a large influence on fullerene films electrochemistry. The so-called "doping" with cations becomes feasible, since the cations can penetrate the film and neutralize the fullerene-anions generated in reduction processes (mono-, di-, tri-, tert-, penta- und hexaanions), thus changing drastically the conductivity and electrochemistry. Anions, however, have been shown to have little or no effect on fullerene electrochemistry. The cations from supporting electrolyte can be differentiated in large and small cations. The large cations, such as tetrabutylammonium (TBA^+), tetrahexylammonium (THA^+), tetraoctylammonium (TOA^+) act beneficially on fullerene film electrochemistry, since these induce reorganization in the interstitial space of the C_{60} lattice, such that the cations can intercalate and neutralize the excess of anionic charge. These events lead to less dissolution, thus, electrochemical activity of the film is signed by more stability even after several cycles. The small cations, such as tetraetylammonium (TEA^+), alkali metal or alkali earth metal cations (Na^+, K^+, Cs^+, Ba^{2+}), are known to cause dissolution of the fullerene film, and thus, electrochemical activity of the film becomes unstable.[242] For example the study on conductivity of partially reduced fullerenes by Szucs *et al.* investigated fullerene C_{60} and C_{70} films by means of cyclic voltammetry and in aqueous solutions. Here, the influence of the Li^+, K^+, Na^+, Ba^{2+} cation doping has been analysed. The study resulted in the conclusion that triply reduced K_3C_{60} salt is conductive, whereas Na^+, Ba^{2+}, Li^+ form only transiently C_{60}^{3-} which disproportionate to semiconductive C_{60}^- and C_{60}^{6-}.[243, 244] A completely reduced film, i.e. C_{60}^{6-} can be semiconducting or insulating, depending on the cation. Fig. 12 shows a C_{60}-fullerene film, in which K^+ ions have been integrated.

3.9.3 Hybrid systems with biomolecules

Generally, hybrids between fullerenes and biomacromolecules can be achieved by various approaches, some of them are based on connecting both molecules covalently to each other. Other approaches are based on adsorption process (e.g. wrapping) or by making use of electrostatic forces between functionalized fullerene and a biomolecule. Since fullerenes are very similar with CNTs, also here arises the problem of their intrinsic hydrophobicity, and

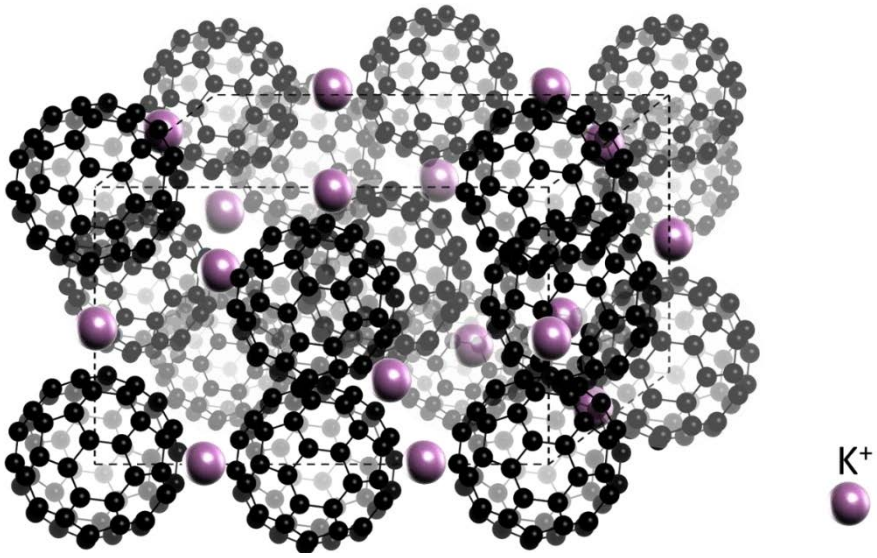

Figure 12 Schematic visualization of the intercalation of K^+-ions (magenta) into fullerene film (black). K_3C_{60} has been demonstrated to be conductive, while K_6C_{60} an insulator.

hence, these structures can be functionalized for enhancing solubility and compatibility with biological structures. Introducing of such functionalities inherently allows for productive connection of the fullerenes' properties with the properties of biomolecules, however, also unmodified fullerenes can undergo productive interactions with some biomolecules.

3.9.3.1 *Interactions between pristine fullerenes and biomolecules*

Many biologic systems have been shown to exchange electrons with fullerenes, among these are enzymes, DNA, cytochrome *c*, photosystem II. In these conjugates fullerenes can provide an ordered three-dimensional architecture and unique electronic and optical properties. The biological compound provides structural diversity, secondary structure, recognition, charge flexibility and biocatalytic capacity. There are only few examples on combination of pristine C_{60} with biomolecules, however it shows that also unmodified fullerenes can productively interact with some biomolecules: C_{60} has been combined with a lipase for construction of a biosensor, here the enzyme has been chemisorbed on pristine C_{60}-layer and showed catalytic activity (stereospecific hydrolysis of L-amino acid esters).[245] In another study, glucose oxidase (GOx) has been contacted with C_{60} resulting in a biosensor, here, GOx has been attached with its amino groups directly at the C_{60}-mojety (since the affinity of the nucleophilic NH_2-groups towards electron deficient systems has been already demonstrated). In this system, the enzyme was catalytically active and could oxidize glucose.[246, 247] In several

studies it has also been shown that hydrophobic interactions between DNA and fullerenes can occur.

3.9.3.2 *Interactions between functionalized fullerenes and biomolecules*

There is a tremendous number of possible chemical modifications and strategies for introduction of functional groups in a fullerene. The most used functional groups are -NH_2 and -COOH, and these play an important role in establishment of functional connection between fullerene and other molecules. Other spread fullerene modifications include different substituents of fullerene-pyrrolidines, polyhydroxyfullerenes, amino-acid like fullerenes etc. The presence of such functionalities improves solubility in aqueous media, which is good for preparation of homogeneous fullerene solutions, but also permits electrostatic interactions with other molecules or covalent chemistry (amino-, or carboxy-fullerenes).

1) *Interactions with DNA*

For example, in the study of Cassell *et al.* C_{60}-*N*,*N*-Dimethylpyrrolidinium has been employed for studies on complexation between DNA and fullerenes *via* electrostatic forces (between phosphate groups of the DNA backbone and the positively-charged tertiary N atom of the fullerene compound).[248] Other studies revealed that C_{60}-derivatives ($H_{10}C_{60}(NHCH_2CH_2OH)_{10}$) could interact with the major groove of the double-stranded DNA by means of π-π interactions with delocalized π-system of the DNA bases.[249]

2) *Interactions with enzymes*

Several studies have been reported on the combination of enzymes with functionalized fullerenes. In the study of Saeedfar *et al.*, a carboxylated fullerene C_{60} has been modified with urease by EDC-NHS covalent approach. Here, a carboxyl group of the fullerene first has been activated by the EDC-NHS compound, followed by replacement of EDC-NHS-ester by amino groups of the enzyme.[250] The immobilized enzyme showed catalytic activity in conversion of urea. The authors stated that fullerenes can increase sensitivity of the analyte detection due to the high surface-to-volume ratio.

In another study the combination between hydroxylated fullerenes and glucose oxidase (GOD) resulted in a functional high sensitivity and selectivity glucose biohybrid-sensor. The fullerene-chitosan matrix could preserve the conformational structure of the enzyme GOD.[251]

Other studies reported electrical communication between fullerenes and GOx as well.[252-254] The use of fullerenes in these studies leads to long life of the biohybrid sensor, no interferences from biological species such as ascorbate, galactose, uric acid or cysteine, high reproducibility.

3) *Interactions with redox proteins*

Kurz *et al.* published a paper on successful electrochemical interaction between fullerene C_{60} and azurin.[255] Csiszar *et al.* demonstrated that cyt *c* can be electrochemically addressed at the partially and fully reduced fullerene films. Here, CV experiments showed clear cyt *c* redox peaks only at partially reduced fullerne film (C_{60}^{3-}) but not at a fully reduced one (C_{60}^{6-}).[256] Photo-induced electron transfer between mitochondrial cyt *c* and dendrofullerene (DF) (i.e. fullerenes modified with long branches of aliphatic chains, often carrying functional groups, e.g. carboxylic groups) has been shown in the study of Braun *et al.*[257] Another study has been dealing with investigation of electrochemistry of cyt *c* on a Pd-fullerene-modified electrode.[258] Here, electric communication between Pd-functionalized fullerenes and cyt *c* has been achieved.

4) *Interactions with photoactive proteins*

A very interesting study on fullerenes in combination with photosystem II has been reported in 2016. Here, electron exchange between antennae chlorophylls of PSII and functionalized fullerenes C_{60} (C_{60}-(N,N-dimethyl pyrrolidinium) iodide) has been shown, helping to clarify alternative electron pathways in this highly complex biomolecule. It has been clarified that the source of H_2O_2 formation by the PSII are the side antenna chlorophyll molecules.[259]

All these publications demonstrate that electrical communication between an enzyme and fullerene can be realized. This fact enriches applicability of these small nanoparticles in bioelectrochemistry and photobioelectrochemistry.

3.10 Sulfite Oxidase

3.10.1 Structure and function

Sulphite Oxidase (SOx) is a homodimeric metalloprotein and belongs to the family of molybdenum-containing enzymes. The enzyme is situated in the mitochondrial intermembrane space and has a molecular weight of ca. 110 kDa. The active site of the enzyme is constituted of a Mo ion coordinated by three sulphur ligands, an oxo-group and one

water/hydroxo-group.[260] Each of the monomers of the enzyme has two domains – the catalytic domain, also called Moco-domain and cytochrome *b5* domain (the electron transfer domain).[261-264] It has been shown, that both domains in SOx are connected via a flexible loop region, and thus can change their conformation for a better electron exchange. The reaction of SOx is the oxidation of sulphite to sulphate (Reaction 3), a process which takes place in oxidative degradation pathway of sulphur-containing amino acids such as cysteine and methionine:

$$H_2O + SO_3^{2-} \rightarrow SO_4^{2-} + 2\,H^+ + 2\,e^- \qquad (3)$$

The reaction is catalyzed by the Moco-domain and the electrons are further transferred intramolecularly from the Moco-domain to the cyt *b5*-domain. From here, electrons are transferred to cytochrome *c*.[265] The role of the cyt *b5* domain in the intramolecular electron transfer mechanism has been elucidated voltammetrically in the study of Elliot *et al.*, which has shown that mobility of the heme domain represents a limitation in SOx activity.[266] Since the electron transfer to cyt *c* takes place *in vivo*, it has been explored whether an electron exchange between SOx and the electrode by means of direct electron transfer or mediated electron transfer via cyt *c* is feasible. Fig. 13 depicts structure of chicken sulfite oxidase (*human sulphite oxidase structure is currently not available*).

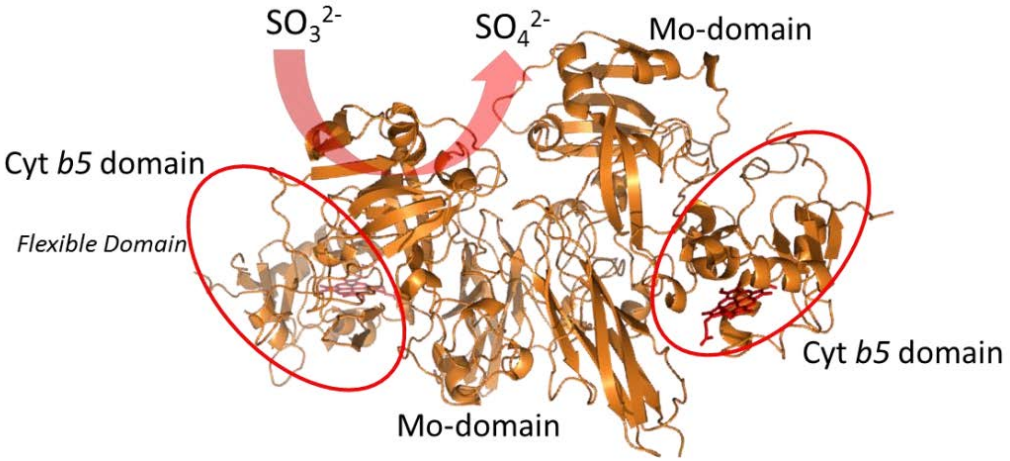

Figure 13. Crystal Structure of chicken sulfite oxidase. A homodimer of Sox is composed of a Molybdenum domain (Mo-domain), responsible for catalytic oxidation of sulfite to sulfate, and cyt *b5* domain, responsible for the intramolecular electron transfer. Structural information has been used from Kisker *et al.*PDB:1SOX.[363]

3.10.2 Electrochemistry on electrodes

Studies on the immobilized SOx have shown the possibility of direct and mediated electron transfer between SOx and the electrode.

3.10.2.1 *Direct electron transfer between SOx and electrodes*

One of the best platforms for studying catalytic properties of complex enzymes on electrodes represent thiol-modified gold electrodes. These provide large variability of functionalities and protein-friendly microenvironment. This is why first studies on electrodes have been performed on thiol-modified gold electrodes, and namely cysteamine, mercapto-ethanol, 11-mercapto-1-undecanol and 11-mercapto-1-undecamine.[92, 267] Here, direct heterogeneous electron transfer between cyt *b5*-domain of the SOx and the thiol-modified electrode has been demonstrated and an apparent catalytic rate constant of 18 - 24 s^{-1} has been reported. In the work of Frasca *et al.*, SOx has been immobilized on amine-gold nanoparticles-modified electrode. Here, the functionality of the enzyme could be achieved even at lower applied potential as compared to canonical DET-based sulphite sensors.[268] Another interesting approach, in which SOx has been assembled on a semiconductive quantum dots (QDs)-modified ITO electrode. Here a photobiosensor has been successfully constructed resulting in direct electrochemistry of SOx on the electrode and an enhanced generation of bioelectrocatalytic currents. In this system the oxidation onset potential started already at the redox potential of the electron transfer domain of SOx.[269]

3.10.2.2 *Mediated electron transfer between SOx and electrodes*

In contrast to direct electron transfer, which is problematic due to lack of accessibility of the catalytic centre arises, in the mediated approach, electrons can be transferred to a mediator, and from there to the electrode. Different synthetic and organic mediators have been tested.[270, 271] Since cyt *c* is a physiological partner for oxidation of cyt *b5*-domain of SOx, the use of cyt *c* as mediator becomes obvious. In the study of Dronov *et al.*, cyt *c* has been immobilized on the thiol-modified gold electrode, followed by assembly of SOx on top of the cyt *c* layer. In this way a layer-by-layer deposition of cyt *c*-SOx has been achieved.[272] In other approaches, a mixture SOx-cyt *c* has been directly applied on the electrode, e.g. a thiol-modified gold electrode. Such co-assembly of the cyt *c* and SOx, in which immobilization was based on direct protein-protein interactions, resulted in both high sensitivity and selectivity towards sulphite.[273] Another approach was based on cyt *c* and SOx incorporated into carbon-ink,

followed by transfer onto screen-printed electrodes. This biosensor also resulted in high sensitivity.[274] In other multilayer approaches, an anionic polyelectrolyte PASA (Poly-Aniline Sulfonic Acid) has been employed as a "glue" between cyt *c* molecules and SOx, resulting in productive sulphite biosensors.[275-277] Bahmani *et al.* immobilized SOx on the electrode by an electropolymerization approach, in which aniline monomers and SOx have been electropolymerized to result in a SOx-polyaniline construct which functioned as sulphite biosensor.[278]

3.11 Cytochrome *c*

Cyt *c* is a small Fe-heme protein of 12.3[279] kDa MW and ca. 3 nm in diameter[280] with pronounced positive net charge, which allows for strong electrostatic interactions with negatively charged species.[281] The heme of cyt *c* consists of porphyrin ring and an iron ion in the centre (Fe^{II}/Fe^{III})[281] and is relatively accessible - a fact that makes cyt *c* such remarkable electro-active partner. This protein is found ubiquitously in living organisms in the inner mitochondrial membrane, where it acts as electron shuttle between different proteins, such as cytochrome *c* reductase and cytochrome *c* oxidase. In photosynthesis, a relative of cyt *c*, cytochrome *c6*, acts as an electron shuttle between the cytochrome *b6/f* –complex and the P_{700} centre of photosystem I. Cyt *c* is one of the best-studied redox proteins. It can exchange electrons with many enzymes or redox-active species, with itself (self-exchange) and with electrodes of almost every type. Besides its outstanding redox properties, charge distribution and appropriate small size, an astonishing stability of this protein makes it even more attractive for electrochemical applications. Electrochemistry of cyt *c* has been reported on thiol-modified gold,[282-284] silver,[81, 285, 286] glassy carbon,[287, 288] carbon nanotubes-modified electrodes[289, 290] and even fullerene-modified electrodes,[256, 291] ITO and FTO electrodes,[84, 292, 293] the behaviour of cyt *c* on negatively charged thiols suggested a good and reproducible quasi-reversible electrochemistry and a good surface coverage by this protein on 11-mercapto-1-undecanoic acid/11-mercapto-1-undecanol (1:3) surfaces.[294] Fig. 14 depicts the structure of cyt *c* from horse heart.

3.11.1 Electrical communication with biomolecules

The most interesting aspect besides electrochemistry on cyt *c* itself, however, represents its ability to electrically communicate with a large number of biomolecules and enzymes and biocompatibility with other biomolecules. In several studies on combination between DNA-

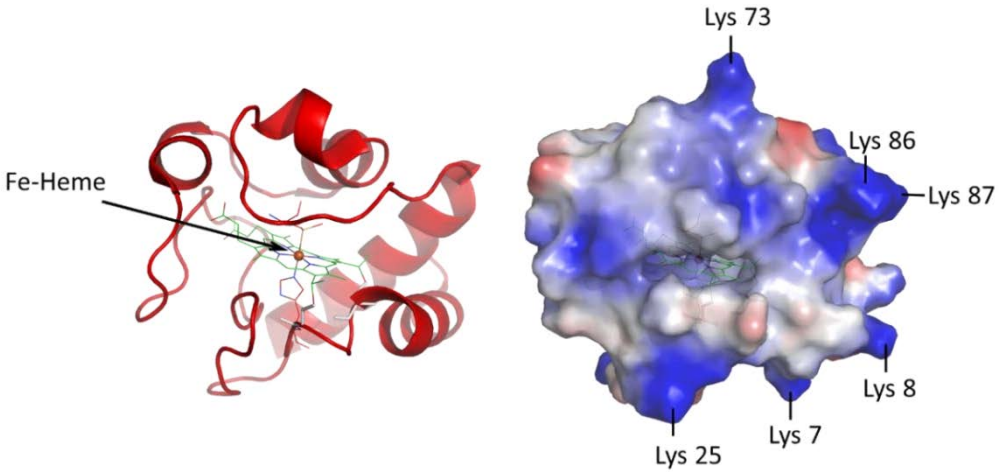

Figure 14. Crystal Structure of cytochrome *c* from horse heart. Left – representation of the secondary structure including the heme (cartoon), right – representation of the surface potential (calculated with vacuum electrostatics) of cyt *c*. Blue colours represent positive charge, red – negative charge. Structural information has been used from Bushnell *et al.*, PDB:1HRC.[281]

cyt *c* it has been demonstrated that electron exchange between cyt *c*-cyt *c* can be realized.[295, 296] An intensive study by Stieger *et al.* on cyt *c* in combination with such a super-complex molecule like PSI has resulted in three publications, in which several aspects of PSI-cyt *c* conjugates have been addressed: a) direct interaction between cyt *c* and PSI. Here, not only electrostatic interaction between cyt *c* and PSI has been achieved, but also electrical communication between these two proteins,[151] b) co-assembly of cyt *c* and PSI from solution. Here, combination with the third biomolecule, DNA, has been employed and stable photoactive multilayers (PSI-cyt *c*-DNA)$_n$ have been achieved.[85] c) integration of PSI-cyt *c* inside a 3D electrode architecture. Here, PSI-cyt *c* system could be transferred onto 3D inverse opal micro-ITO electrodes, in which high photocurrents could be achieved due to high loadings; however, the heterogeneous electron transfer constant was smaller than for the gold electrodes.[84]

Insights into interactions between cyt *c* and PSI have been also provided in the study of Kölsch *et al.*[297] In the study of Feifel *et al.*, cyt *c* combination with enzymes has been investigated, and two enzymes, cellobiose dehydrogenase and laccase have been immobilized in combination with cyt *c* on electrodes, creating two electron transfer pathways on the same electrode.[298] Here, electrical communication between both enzymes and the electrode has been realized via cyt *c*, serving as conductive matrix. In the workgroup of Wollenberger, quite a few studies have been dealing with construction of SOx- cyt *c*-based sulphite biosensors. It has been demonstrated, that SOx can also electrically exchange electrons with cyt *c* also in an

immobilized state on the electrode.[272, 273, 299, 300] Other studies have also demonstrated electrical compatibility on electrodes of cyt *c* with enzymes like bilirubin oxidase,[301] fructose dehydrogenase.[302]

In the present thesis different electrode materials have been employed: glassy carbon (P4.1), tin-doped indium oxide (ITO) in P4.2, gold (P4.3), fluorine-doped tin oxide (FTO) in P4.4. Furthermore, different electrode modifications have been applied: CNT (more specifically MWNTs) decorated over GC (P4.1), thiol-modified gold in combination with a metal chelate ruthenium hexamine (P4.3). Moreover, different wiring compounds between PSI and the electrode have been employed: cyt c in P4.1, P4.2 and P4.4, fullerenes in P4.3. An alternative way of electron supply towards PSI has been established in P4.2. Electron collection from PSI has been assured by oxygen, methyl viologen and ubiquinone Q_0.

In the following the results achieved in this thesis will be presented in the form of attached publications on each of the topics mentioned in "The objectives of the thesis".

Published in: physica status solidi (a) (PSSA). Dmitri Ciornii, Sven Christian Feifel, Mahdi Hejazi, Adrian Kölsch, Heiko Lokstein, Athina Zouni, Fred Lisdat. Construction of photobiocathodes using multi-walled carbon nanotubes and photosystem I. *physica status solidi (a)* **2017**, 214, 1700017-n/a. **DOI**: 10.1002/pssa.201700017.

4. Results

4.1 Construction of photobiocathodes using multi-walled carbon nanotubes and photosystem I

Authors: Dmitri Ciornii, Sven Christian Feifel, Mahdi Hejazi, Adrian Kölsch, Heiko Lokstein, Athina Zouni, Fred Lisdat

Abstract

In this work, we report on the successful assembly of cyanobacterial photosystem I (PSI) on carbon nanotubes for light-to-current conversion applications. For this purpose, glassy carbon electrodes (GCE) have been modified with multi-walled carbon nanotubes (MWCNTs). The surface of the MWCNTs has been adjusted in a non-invasive way by the use of a carboxylated pyrene derivative to achieve a covalent fixation of PSI. Our results show a cathodic photocurrent response and functionality of the biohybrid electrode upon illumination. The experiments verify that the photocurrent generation can clearly be attributed to a functional PSI on the electrode interface. An additional implementation of cytochrome *c* (cyt *c*) into this

electrode architecture results in a 25-fold enhancement of cathodic photocurrent response (0.8 to 18 $\mu A\,cm^{-2}$ at $-100\,mV$ and $100\,mW\,cm^{-2}$), which can be attributed to an improved connection of PSI with the underlying electrode.

Introduction

Solar energy represents the most abundant and accessible energy source available on earth. In nature it enables photosynthesis, which produces energy-rich compounds by harnessing photons. On this account exploiting the properties of photobiosynthetic proteins has become an interesting and challenging research topic in recent years. For this purpose both, photosystem I (PSI) and photosystem II (PSII) have been employed.[84, 85, 158, 303-305] In our study PSI from *Thermosynecchococcus elongatus (T. elongatus)* has been chosen due to its high stability. This protein is a trimeric supercomplex of ca. 1068 kDa integrated into the thylakoid membrane.[32] It consists of 12 protein subunits, 96 chlorophyll *a* molecules, 22 carotenoids, two phylloquinones and three [4Fe-4S]-cluster[29, 32, 306] and bears unique properties, such as reliable charge separation (with nearly 100% efficiency),[116, 307-310] fast photoelectron transfer (generating relatively long-living exciton) and a center of lowest reductive potential known in nature, P_{700}^{*} (-1.3 V).[174, 311] Upon illumination, photons are absorbed by the 96 antennae chlorophylls. This excitation energy is then transferred to the reaction center constituted of a special pair of chlorophylls allowing charge separation. The electron is almost instantaneously transferred to the next molecules in the electron transfer chain, via chlorophyll *a* to a phylloquinone. Subsequently, the electron is transferred to the F_X, F_A, F_B iron-sulfur clusters. This allows for reduction of ferredoxin in photosynthesis. The structure of a monomer of PSI is shown in Figure 1. The charges are distributed over entire surface of the protein complex, but with a pronounced concentration of negative charges on the luminal side. As suitable platform for attachment of PSI on the electrode we have selected carbon nanotubes. These nanostructures might be considered as rolled graphene sheets, which can be single- or multi-walled. Carbon nanotubes (CNTs) can have either semiconductive, conductive or even superconductive properties, depending on the arrangement of (n,m) unit vectors in the lattice of the graphene sheet. Conductive CNTs are particularly interesting in combination with electrodes.[194, 314-316] Depending on their diameter, multi-walled CNTs (MWCNTs) can have different specific surface areas, from ca. 800 $m^2\,g^{-1}$ for 2 nm diameter to 50 $m^2\,g^{-1}$ for 35 nm diameter,[317] which makes this material particularly interesting in catalysis and biosensorial applications because of the possibility of harboring large amounts of cata-

lysts, such as enzymes.[318-320]

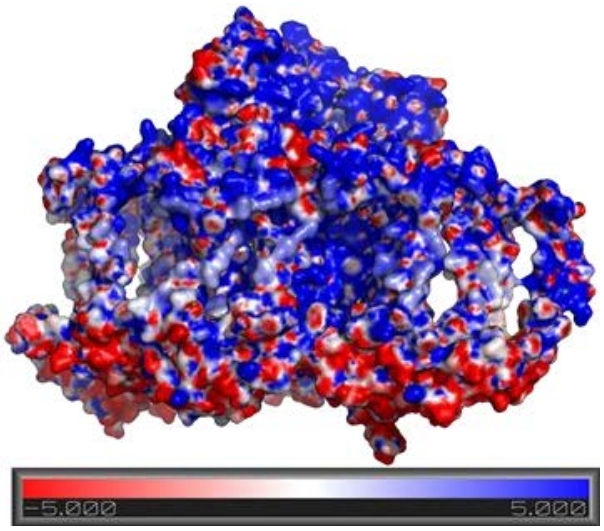

Figure 1. Electrostatic modulation of PSI in 5 mM KPP buffer, pH 7. Top – stromal side, bottom – luminal side, blue – positive net charge, red – negative net charge. Simulation was performed with PyMOL, V. 1.7. For the simulations crystal structure of PSI PDB:4FE1[312] has been chosen. pKa values were calculated by PROPKA at pH 7 and PARSE as force field.[313]

It has been shown that a CNT modification can act as an electrochemical platform[198, 321-324] because of its advantageous electrocatalytic properties. Other advantages for using CNTs represent high conductivity, robustness, and biocompatibility, which make this material an excellent candidate for the construction of photoenzymatic electrodes.

To date, only few studies on the combination of CNTs with photosynthetic protein complexes have been reported (see Table 1). First attempts were performed with PSI mutants (with cysteine side chains) to use the thiol group for covalent coupling with maleimid-modified CNTs[169, 170] Moreover, entire thylakoid membranes with all multi-protein complexes, including both photosystems (PSI and PSII) have been combined with MWCNTs. However, in this study the primary focus was on the photoelectrochemical properties of PSII.[307] Strano

Table 1. Overview on publications on electrode systems combining CNTs and PSI.

J(µA cm^{-2})	e-Donor	e-Acceptor	U(vs. Ag/AgCl)	Assembly	Reference
0.9	KHCF(II)	UQ-2	OCP	RC-NanoDisc-SWNT	[288]
1.4	*Cyt c*	Q2	-170 mV	MWNT	[290]
0.1	n.a.	n.a.	-600 mV	SWNT-COOH	[139]
7	n.a.	UQ-0	n.a.	ITO-MWNT-NH-PTAA	[289]

et al. immobilized the bacterial reaction center (RC) from *Rhodobacter sphaeroides* on phospholipid-modified single-walled carbon nanotubes (SWNTs) and demonstrated extended photoelectrochemical activity.[325] The study of Nagy *et al.* demonstrated a combination of RCs from *Rhodobacter sphaeroides* with SWNTs via a PTAA polymer.[326] Furthermore, encapsulation of the RC from *Rhodobacter sp*. inside MWCNTs was reported.[327]
In this study we focus on the construction of a photoactive bioelectrode by combination of PSI and MWCNTs and the characterization of this biohybrid system.

Materials and methods

Photosystem I preparation. PSI was isolated in its trimeric form from *T. elongatus*, as described by Kern *et al*. 2005.[328] PSI Trimer was crystalized by dilution with a buffer containing 5 mM MES-NaOH, pH 6.0 and 0.02 % n-Dodecyl-β-maltoside (β-DM) at 4 °C until a concentrationof 5 mM $MgSO_4$ was reached. The crystals were collected by centrifugation (5 min, 4°C, 4000 g), washed with the same buffer, resolubilized by adding 5 mM MES-NaOH, pH 6.0, 0.02 β-DM and 30 mM $MgSO_4$ and recrystalized as described above. For assembly experiments on electrodes PSI was solubilzed in 100 mM KPP buffer, pH 8 containing 0.02 % β-DM and dialyzed against 5 mM KPP buffer, pH 8 overnight.

Assay of PSI activity. Activity of PSI was measured as oxygen consumption using a Clark-type electrode (Hansatech, Germany) under saturating light conditions of 1000 µmol photons m^{-2} s^{-1} at 20 °C. In a final volume of 1 ml, the reaction mixture contained 20 mM Tricine buffer, pH 8.0, 0.2 mg ml^{-1} sodium ascorbate, 0.05 mg ml^{-1} methyl viologen, 16 µM cytochrome *c* from horse heart (Sigma-Aldrich) and 0.02 % β-DM. The reaction was started by addition PSI (final amount of 5 µg Chlorophyll).

Mass Spectrometry (MS) analysis of PSI. Aliquots (0.5 µl each containg 2 µM PSI) were mixed on the target with 0.5 µl of sinapinic acid matrix solution (dissolved in 40 % (w/v) acetonitrile and 0.1 % (v/v) TFA). The analyte-matrix mixtures were dried under a gentle stream of air. MALDI-TOF mass spectra were recorded on a Bruker Microflex spectrometer (Karlsruhe, Germany) in positive-ion mode. All spectra were measured in linear mode.

Preparation of multi-walled carbon nanotubes. Short thin carboxylated MWCNTs were purchased from Nanocyl, Belgium. Diameter of the MWCNTs was in the range 10-30 nm,

with lengths of a few hundred nm. 0.5 mg ml^{-1} of MWCNTs were suspended in a mixture 1:1 EtOH and deionized H_2O and sonicated for 60 seconds.

Preparation of PSI/π-pyrene/CNT/GCE electrodes. 30 µl of a suspension of MWCNTs were drop-casted on a freshly polished glassy carbon electrode (GCE). After drying, the CNT/GCE electrodes were further modified by incubation in 0.5 mM 1-pyrenecarboxylic acid (π-pyrene) in ethanolic solution overnight. This was followed by an EDC/NHS activation of the carboxylic groups (π-pyrene) for 30 min. In the final step, the electrode was incubated in PSI solution (2 µM protein in 5 mM potassium phosphate buffer at pH 8 (KPP8)) overnight.

Photoelectrochemical experiments. All experiments were performed in 5 ml electrochemical cells, filled with 5 mM KPP buffer at pH 7 with or/without methyl viologen (MV^{2+}) using a Pt-wire as counter electrode, an Ag/AgCl (1 M) as reference electrode and GCE as working electrode. Incident light intensity was varied in the range from 1 to 100 mW cm^{-2} at constant applied potential (U = -100mV vs Ag/AgCl (1 M)). In order to obtain the photo-action spectrum, the incident wavelengths were varied. Photocurrent production was also measured under variation of the applied potential (chopped light voltammetry). A potential scan was performed in the cathodic direction. During the measurement light was switched on and off with durations of 10 seconds, with a potential scan rate of 1 mV s^{-1} and illumination power of 100 mW cm^{-2}.

Scanning electron microscopy (SEM). SEM measurements have been performed for direct visualization of the assembly of MWCNTs on GCE and PSI attachment on the MWCNT surface. CNT/GCE and PSI/π-pyrene/CNT/GCE electrodes were transferred on the SEM (JSM-6510, JEOL) support and measurements were performed under vacuum at 30 kV acceleration voltage. Magnification of 50 000 x was achieved and MWCNT with/without PSI could be visualized.

UV-Vis spectroscopy. Absorption spectra of a 2 µM PSI solution (5 mM KPP pH 7) were measured using an UV-Vis Spectrophotometer (Evolution 201, Thermo Fisher Scientific - Shanghai). Chlorophyll concentrations were measured with the Nanodrop 2000 (Thermo Scientific) in an 80 % (v/v) acetone/water mixture and calculated according to the method described in.[329]

Results and discussion

Analysis of photosystem I. The oligomeric state and purity of trimeric PSI was analysed by blue-native PAGE and showed a single protein band of trimeric PSI with high purity and homogeneity (data not shown). The subunit composition of PS I has been analysed by MALDI-TOF using a linear positive mode. 10 of 12 subunits of PSI known from the 3D crystal structure were found by MALDI-TOF analysis. Moreover, subunits PsaA and PsaB could only be identified by SDS-PAGE because of their high molecular mass (data not shown). Thus, all known subunits have been identified in the PSI samples. Furthermore, the oxygen consumption rate for trimeric PSI in KPP buffer, pH 8, has been assessed to be 1740 ± 100 µmol O_2 h^{-1} mg Chl^{-1}.

Assembly of Photosystem I on Multi-walled Carbon Nanotubes. In this study we employed carboxylated multi-walled carbon nanotubes due to the few carboxylic acid groups. This type of carbon nanotubes has a better solubility in water as compared with pure MWCNTs and thus it can be expected to achieve a rather homogeneous coverage on the gla-

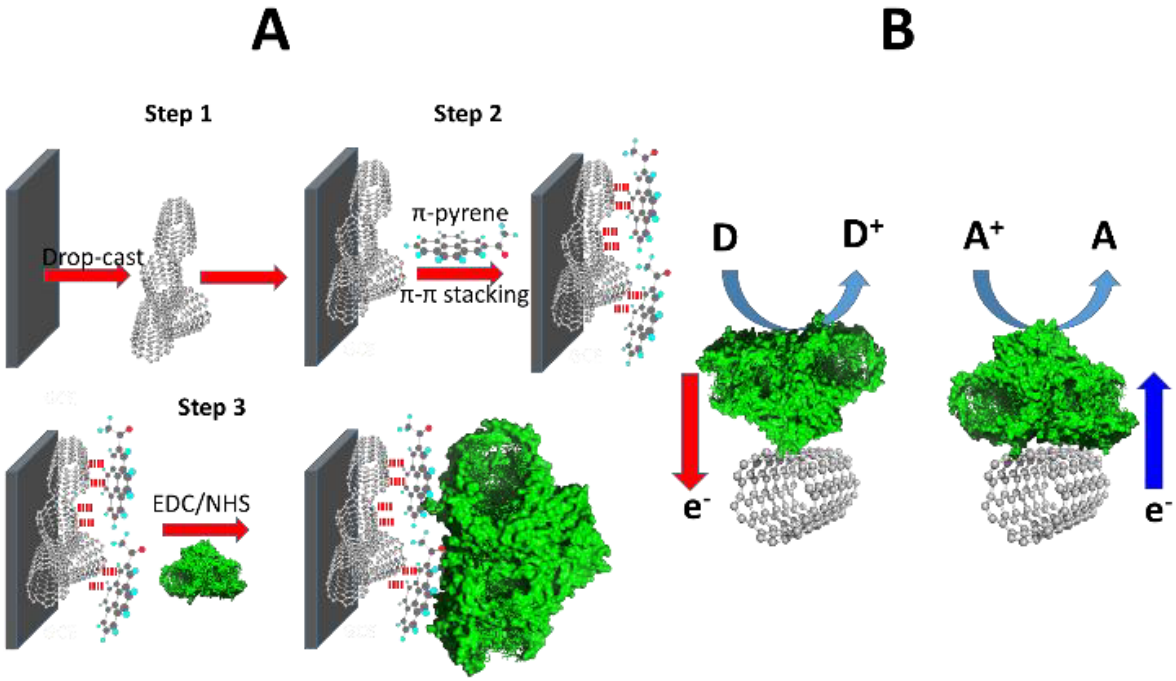

Figure 2. A: schematic representation of the electrode assembly, **B:** possible orientations of PSI on the electrode surface (in this picture PSI is shown as monomer) on the surface of a MWCNT. On the left - orientation with stromal side to the electrode (red arrow pointing towards the electrode, i.e. anodic current flow), on the right – orientation with luminal side to the electrode (blue arrow pointing towards the solution, i.e. cathodic current flow). For simplicity MWCNTs are represented as SWCNT. The elements are not represented in their real sizes.

ssy carbon surface. For two reasons the MWCNTs were additionally modified with 1-pyrenecarboxylic acid (π-pyrene): firstly, it can form *π-π* interactions with the MWCNTs. Secondly, the carboxylic acid groups of the π-pyrene allows for covalent chemistry, which is beneficial for PSI attachment. The complete assembly strategy is schematically represented in Figure 2A. The covalent approach was preferred because it can be expected to be more stable as compared to physisorption or electrostatic interactions. Generally, the assembly of PSI on the electrode surface can occur in different orientations. If the stromal side is oriented towards the working electrode, then electrons from F_B^- -cluster can be directly injected into the MWCNT (in this scenario anodic photocurrent is favored, see Figure 2B, left). If, on the other hand, PSI is oriented with its luminal side towards the working electrode, reduction of P_{700} by the electrode becomes feasible and a cathodic photocurrent is obtained (see Figure 2B, right). None-productive orientations of the PSI with no functional connection to the electrode need to be minimized for efficient photocurrent generation. After the assembly of the whole electrode we first characterized the functionality of the system by photoelectrochemical measurements. Electrodes were also tested without PSI, CNTs or π-pyrene in order to demonstrate the necessity of the individual components. For this purpose photocurrent measurements at a fixed potential have been performed; the results are summarized in Figure 3.The electrodes lacking PSI (see Figure 3, black line) showed no net photocurrent. If MWCNTs were absent

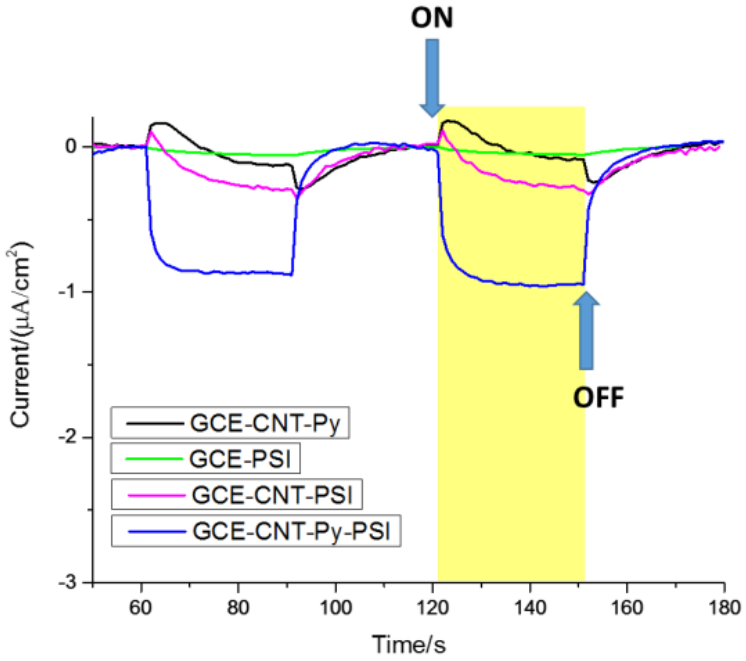

Figure 3. Photochronoamperometric experiment for comparison of biohybrid systems lacking one of the components. Black – π-pyrene/CNT/GCE, green- PSI/GCE, magenta – PSI/CNT/GCE, blue – PSI/π-pyrene/CNT/GCE. Experimental conditions: U= -100 mV vs. Ag/AgCl (1M), light intensity: 100mW cm^{-2}, 5 mM KPP, pH 7.

in the system, a very small photoresponse was recorded, 0.1 μA cm^{-2} (see Figure 3, green line). Further, when π-pyrene was absent, a moderate photocurrent was measured, 0.3 μA cm^{-2} (see Figure 3, magenta line), but much smaller than with the complete biohybrid system with all compounds included, 0.8 μA cm^{-2} (see Figure 3, blue line).

These observations lead to the conclusion that all employed components for the construction of the electrode are necessary and reasonable. The obtained photocurrent in the presence of PSI is an indirect proof of the successful immobilization of the large membrane protein on the CNT surface. In order to obtain a direct verification, SEM measurements have been performed with the hybrid electrode in comparison to a CNT-modified electrode only. The results shown in Figure 4 demonstrate clearly the coverage of the CNT-based electrode with a protein layer.

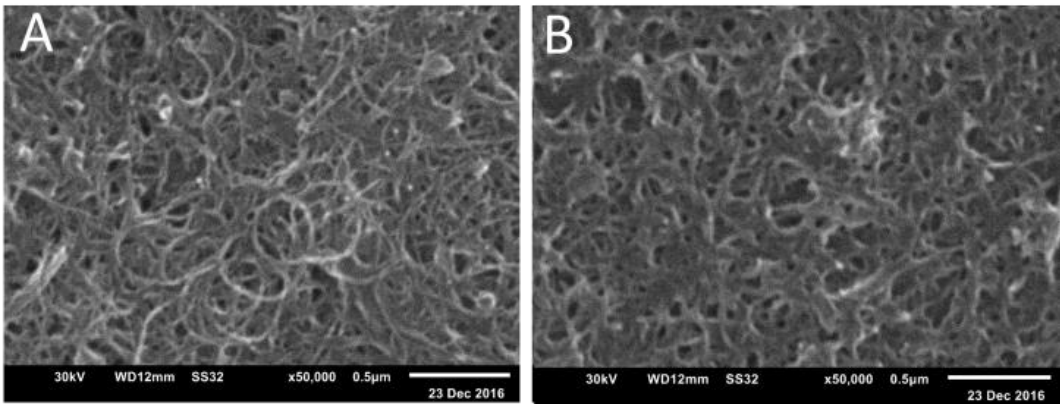

Figure 4. Scanning electron microscopy (SEM) of CNT/GCE electrode (A) and PSI/π-pyrene/CNT/GCE electrode (B). Magnification x50 000, scale bar 0.5 μm, acceleration voltage 30 kV.

For further characterization of the biohybrid electrode, measurements at different potentials but constant light intensity have been carried out. The result of a chopped light voltammetry experiment is shown in Figure 5. The observed photocurrent behavior indicates that under these experimental conditions electrons are delivered from the electrode to the oxidized reaction center (P_{700}^{+}) under illumination. The flow of electrons can thus be summarized as illustrated in the inset of Figure 5. Here the electron-flow is represented schematically for the system under illumination. Since electron transfer (ET) inside the PSI is strictly unidirectional the electrons are transferred to the terminal F_B-cluster. From here, under natural conditions, ferredoxin acts as the natural electron acceptor. However, under experimental conditions, also oxygen can act as electron-acceptor molecule. For study of the incident light power dependence we performed photochronoamperometry at constant potential by varying the

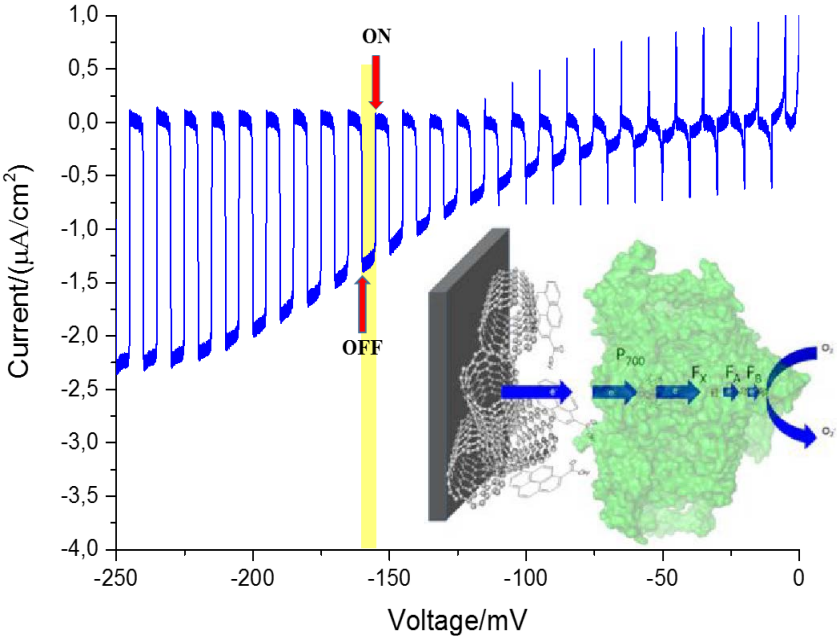

Figure 5. Chopped-light voltammetry of a PSI/π-pyrene/CNT/GCE in the potential range 0 → -250mV vs. Ag/AgCl (1M), illumination power 100 mW cm^{-2}, 5 mM KPP, pH 7, 1 mM MV^{2+}.

illumination intensity in the range from 1 to 100 mW cm^{-2}. Results show that the photocurrent can be enhanced upon increasing light intensity (see Figure 6).

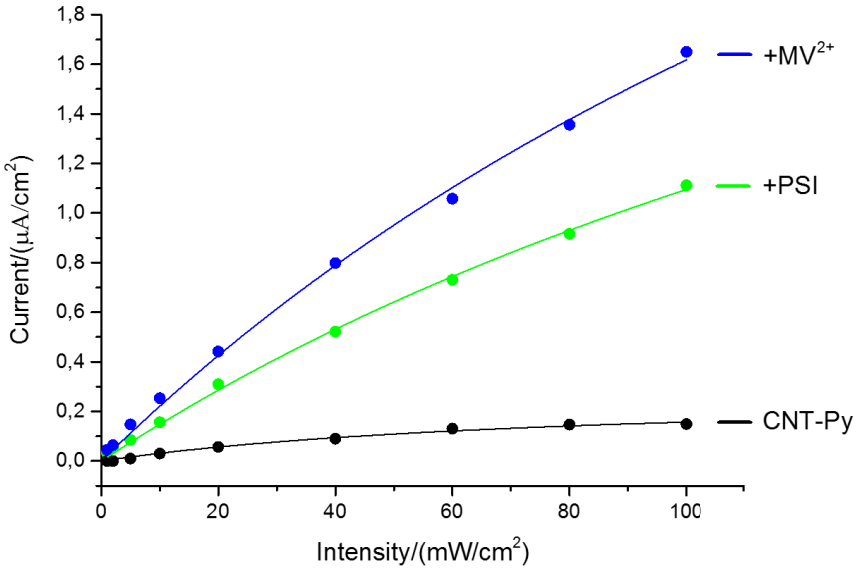

Figure 6. Photochronoamperometric experiment under constant applied potential, U = -100mV vs. Ag/AgCl (1M). π-pyrene/CNT/GCE (black), PSI/π-pyrene/CNT/GCE (green), PSI/π-pyrene/CNT/GCE + 1 mMV^{2+}. Experimental conditions: U= -100 mV vs. Ag/AgCl (1M), 5 mM KPP buffer, pH 7.

However, we could not observe saturation of the photo-response under our experimental conditions. This could suggest that our system is not limited by the light intensity. Production of the photocurrent can be limited by different factors, such as inefficient connection between PSI and electrode, limited availability and/or hampered diffusion of the acceptor compound as well as slow reaction kinetics with the acceptor (e.g. O_2). As the reaction with molecular oxygen is rather slow and diffusion of oxygen represents a limiting factor in the process of electron scavenging from the F_B-cluster we investigated the photocurrent behavior upon addition of methyl viologen (MV^{2+}) since it is known that MV^{2+} can enhance the rate of electron withdrawal from the reduced F_B-cluster [134]. The measurements shown in Figure 6 verify that the photocurrent can be increased in the presence of MV^{2+}, but also show that the enhancement is rather moderate pointing to limitations in the connection of PSI with the modified CNT surface. In order to confirm that the photoresponse of the electrode is determined by the photocatalytic properties of PSI and not by the MWCNTs we have varied the wavelength of the incident light in the range from 400 to 694 nm while measuring the photocurrent at constant potential (photo-action spectrum, Figure 7).

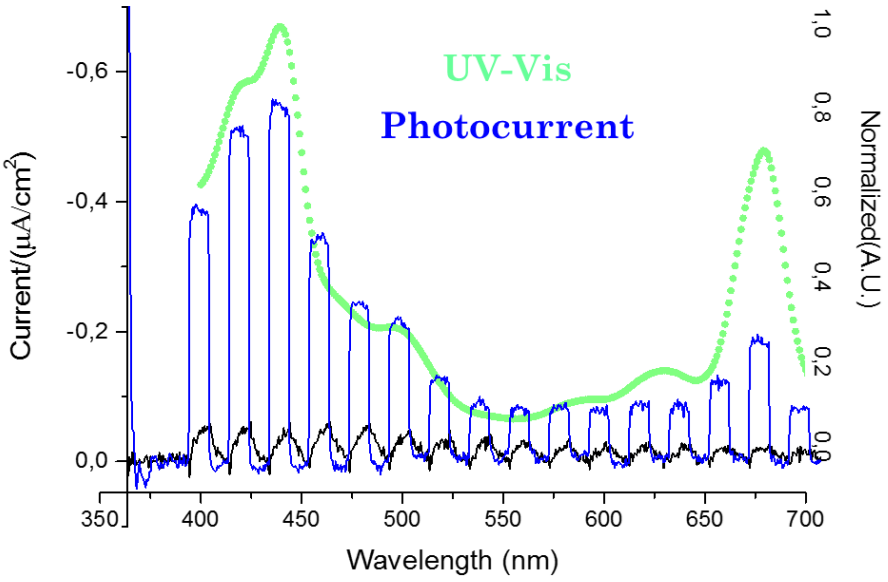

Figure 7. Photo-chronoamperometric experiment at different wavelengths. Photoaction spectrum of PSI/π-pyrene/CNT/GCE (blue curve) and π-pyrene/CNT/GCE (black curve) in the wavelength range from 400-694 nm. Green dots - UV-Vis absorbtion spectrum of PSI in solution. Experimental conditions: U= -200 mV vs. Ag/AgCl, light intensity: 100 mW cm^{-2}, 5 mM KPP, pH 7, 1 mM MV^{2+}.

Our results show that the electrode lacking PSI (π-pyrene/CNT/GCE) generates rudimental photocurrent (ca. 10-15 % compared to the PSI-electrode) upon illumination for each of tested

wavelengths (see Figure 7, black line). In contrast, PSI/π-pyrene/CNT/GCE electrode generates a much higher photocurrent (see Figure 7, blue line). A prominent photocurrent can be observed in the region of the Soret band (approximately 440 nm) and Q_y-band (680 nm), which is not the case for the electrode without PSI. There is a strong correlation between the photocurrent and the absorbed light at different wavelengths. This correlation can be visualized if the photoaction spectrum is overlayed with UV-Vis absorption spectrum (see Figure 7, green dots). This directly indicates that most of the photocurrent can be attributed to PSI.

In further experiments we assessed the stability of the photocurrent of the PSI/π-pyrene/MWCNT/GCE electrode (see Figure 8). Upon continuous illumination of the sample for 30 min (100 mW cm^{-2}) photocurrent stabilization was achieved within a few minutes after switching the light on. By comparing the photocurrent at the beginning and at the end ofillumination period only a slight decay (about 10 %) in the photocurrent has been found. This can be seen as a first hint for a rather stable situation on the electrode surface.

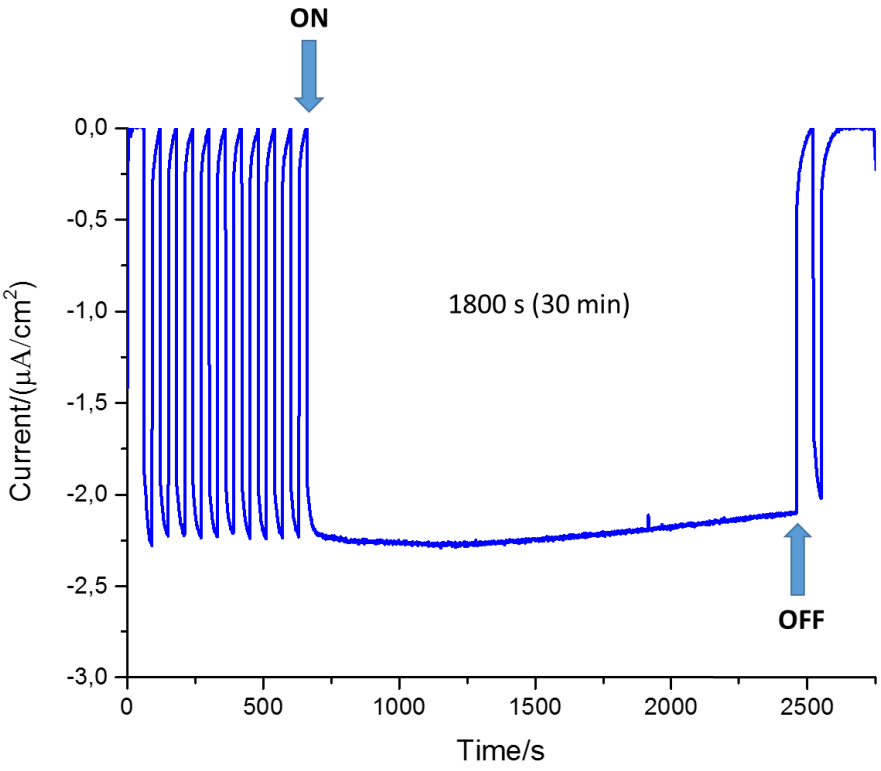

Figure 8. Photocurrent behavior of a PSI/π-pyrene/CNT/GC electrode at constant potential for 10 repeated light pulses (30 s) and a 30 min continuous illumination. Experimental conditions: U= -200 mV vs. Ag/AgCl (1M), light intensity: 100 mW cm^{-2}, 5 mM KPP, pH 7, 1 mM MV^{2+}.

Next, we investigated whether the productivity of our hybrid-electrode is limited by the inefficient or incomplete electrical connection between the electrode and PSI. In order to test this we have exploited the fast reaction of the redox protein cytochrome *c* (cyt *c*) with PSI, which can be used for the creation of efficient photocathodes since cyt *c* can effectively donate electrons to the excited reaction center.[84, 85, 150] When all PSI complexes are well connected to the electrode, the addition of cyt *c* would not much influence the photoresponse, as all electrons coming from the electrode would be collected by PSI. On the other hand, if some PSI molecules are not connected to the CNT electrode, the addition of cyt *c* would be expected to improve the photocurrent output. We analyzed the photoresponse of the biohybrid electrode (PSI/π-pyrene/CNT/GCE) in comparison to an electrode which was additionally incubated in cyt *c* solution overnight. We observed a 25-fold increase in photoresponse from 0.8 μA cm^{-2} to 18 μA cm^{-2} (see Figure 9).

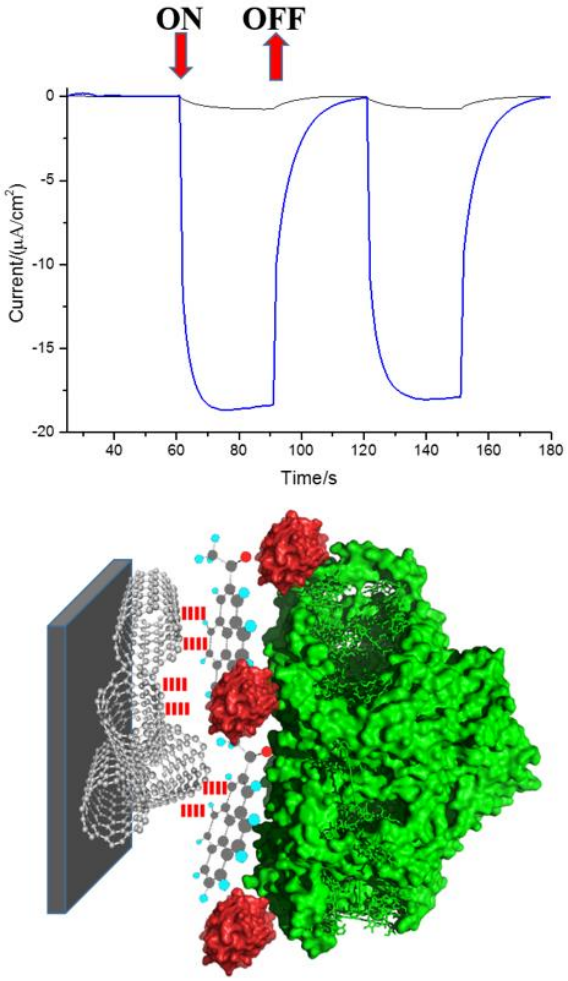

Figure 9. Chronoamperometric measurement of photocurrent response of two different biohybrid electrodes: Black line - PSI/π-pyrene/CNT/GCE, blue line- cyt *c*/PSI/π-pyrene/CNT/GCE. Experimental conditions: U= -100 mV vs. Ag/AgCl, light intensity: 100 mW cm^{-2}, 5 mM KPP, pH 7.

This result suggests that indeed a large amount of PSI has been assembled on the MWCNTs, however, only a small fraction was productively contacted with the electrode. The small redox protein cyt *c* can obviously assemble between MWCNTs and PSI and, thus, is able to accept electrons from the CNTs and transfer them to PSI. Photocurrent densities in this system (18 $\mu A\ cm^{-2}$) are clearly higher than for other systems employing CNT and PSI combination (see Table 1).

Conclusions

In this study we constructed a photobioelectrode based on MWCNTs and cyanobacterial PSI. Our results show that a functional assembly of PSI molecules on the MWCNT surface is possible, but not all PSI molecules on the electrode are electrochemically active. SEM experiments verify the assembly of PSI on MWCNTs. Photoelectrochemical investigations with varying potential demonstrate a dominating cathodic photocurrent generation pointing to a preferred orientation of the connected PSI complexes. The electrode system PSI/π-pyrene/CNT/GCE generates a well-defined photocurrent which is dependent on the light intensity and the wavelength used for excitation. Thus, the functionality of the biohybrid electrode can be clearly attributed to PSI. The system exhibits a rather good stability, which makes it useful for photobioelectrochemical applications. Upon addition of the redox protein cyt *c* the connection between PSI and electrode can be further improved, resulting consequently in much higher photocurrent densities and thus higher light- to-current conversion efficiencies.

Acknowledgements

We gratefully acknowledge financial support of this research by the Bundesministerium für Bildung und Forschung, BMBF, Germany (Biotechnologie 2020+, projects: 031A154A+B). H.L. additionally acknowledges support by the Grant Agency of the Czech Republic, GACR (#P501/12/G055).

Supporting Information

Table S1. MALDI-TOF analysis of trimeric PSI

A 0.5 µl aliquots of PSI solution (2 µM) were mixed with 0.5 µl sinapinic acid (dissolved in 40 % (w/v) acetonitrile and 0.1 % (v/v) TFA). MALDI-TOF spectra were recorded on Burker Microflex spectrometer (Karlsruhe, Germany) in positive-ion mode. The mass spectra were measured in linear mode. All PSI subunits could be determined with exception of PsaA and PsaB, as these are too large for detection with MALDI-TOF.

Subunit	calculated masses $[M+H]^+$ in Da	exp. determined masses in m/z $[M+H]^+$
PsaA	-	-
PsaB	-	-
PsaC	8669.1	8672.2
PsaD	15240.5	15237.4
PsaE	8259.5	8260.4
PsaF	15114.4	15113.8
PsaI	4195.6	4196.2
PsaJ	4796.7	4798.1
PsaK	8390.1	8391.4
PsaL	16118.2	16120.7
PsaM	3424.1	3426.1
PsaX	3969.9	3972.4

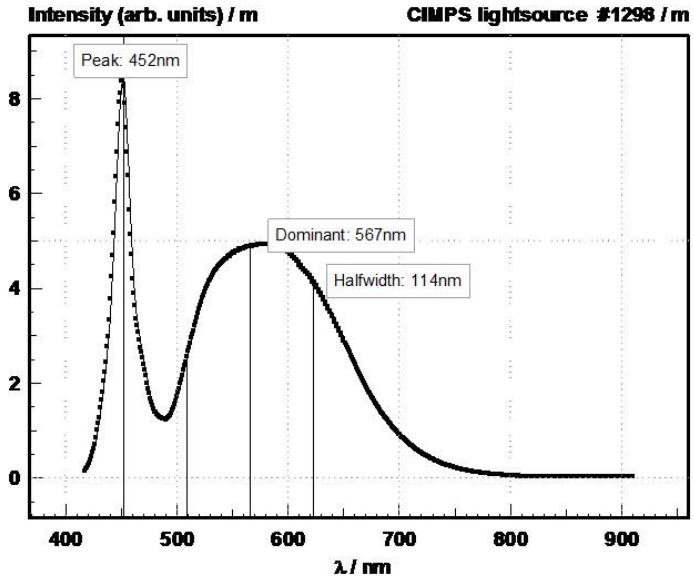

Figure S1. Emission spectrum of the white LED (data from manufacturer) used in photoelectrochemical experiments. Light intensity was continuously monitored due to feedback function of photodiode. In this spectrum a maximum peak intensity is at 452 nm and broad emission is in the region between 500 and 650 nm.

Published in: Journal of American Chemical Society (JACS). Dmitri Ciornii, Marc Riedel, Kai R. Stieger, Sven C. Feifel, Mahdi Hejazi, Heiko Lokstein, Athina Zouni, Fred Lisdat. Bioelectronic circuit on a 3D electrode architecture: Enzymatic catalysis interconnected with photosystem I. J. Am. Chem. Soc. 2017, 139, 46, 16478–16481. **DOI**: 10.1021/jacs.7b10161.

4.2 Bioelectronic circuit on a 3D electrode architecture: Enzymatic catalysis interconnected with photosystem I

Authors: Dmitri Ciornii, Marc Riedel, Kai R. Stieger, Sven C. Feifel, Mahdi Hejazi, Heiko Lokstein, Athina Zouni, Fred Lisdat

Abstract

Inspired by natural photosynthesis, the efficient linking of photoactive protein complexes with light-insensitive biocatalysts is of emerging interest. Such artificial light-driven signal chains are particularly important for the development of systems converting light into current, into chemicals or for light-induced sensing. Here, we report on the construction of an all-protein, light-triggered, catalytic circuit based on photosystem I, cytochrome *c* (cyt *c*) and human sulfite oxidase (hSOx). The defined assembly of all components using a modular design results in an artificial biohybrid electrode architecture, combining the photo-physical features of PSI with the biocatalytic properties of hSOx for advanced light-controlled bioelectronics. The working principle is based on a competitive switch between electron supply from the electrode or by enzymatic substrate conversion.

Introduction

Integration of biomolecules into an electrical circuit in which electrons can be routed in a desirable way represents an interesting topic in biomolecular electronics. It opens new perspectives for practical applications, where desired reactions can be triggered on demand or supplied with the needed energy. The complexity of intermolecular interactions and electronic communication of different biomolecules is by far not trivial, given the fact, that intrinsic features of such biomolecules are very delicate and thus, such molecules are prone to a loss of function under non-physiological conditions.[330] However, designing functional biohybrid architectures on the nanoscale has gained intense research interest over the last decades.[272, 331-336] Such biohybrids are based on an efficient biomolecule-electrode contact. This can be achieved via free or bound redox compounds, shuttling electrons between the electrode and the biocatalytic entity[57, 337] or by direct electron transfer.[95, 338, 339]

However, the efficient wiring of several biocatalysts with the electrode, on the one hand, and with each other, on the other hand, remains a challenging issue. One possibility for communication between multiple enzymes has been exploited by using intermediates of the reaction and establishing enzyme cascades, enzyme competition or recycling schemes on electrodes.[340-342] As a further advancement the concept of metabolic channeling can be considered by constructing multi-enzyme complexes in an artificial way with the aim to reduce the diffusion pathways.[343, 344] Another step in the development of multi-protein biohybrid systems represents the establishment of direct electron exchange between immobilized proteins on electrode surfaces.[345-347] Here, the capability of natural redox proteins to communicate even with non-native partners can be exploited for the design of artificial signal cascades. For example three proteins can be coupled in such a way that the activity of two enzymes (cellobiose dehydrogenase and laccase) can be switched by the redox state of the third protein cyt *c*, allowing the detection of both enzyme substrates by adjusting the electrode potential.[348]

Nonetheless, the successful integration of light-sensitive proteins with biocatalysts is a research target for which only recently first examples have been demonstrated. Biological light-converting complexes such as photosystem I (PSI) have attracted much interest as building blocks in biohybrid systems.[142, 311, 349, 350] The photo-active complex PSI has also been successfully coupled with a hydrogenase via a dithiol-linker allowing a photocatalytically driven electron supply for the enzyme,[137] but here biomolecules have not been immobilized on an electrochemical interface. Following this idea it has been recently shown that hydrogen production and photocurrent production are feasible by combining PSI with a hydrogenase via a redox polymer on an electrode.[351] In a different approach the enzyme glucose oxidase (GOx) has been coupled to an electrode-fixed PSI resulting in enhancement of the anodic photocurrent in the presence of glucose.[352] These developments may illustrate that the combination of biocatalytic conversions with photoactive entities seems to be advantageous in connecting complex redox reactions since light and electrode potential can be used to control the processes.

Encouraged by previous studies on photoelectrodes,[84, 85, 353] we have developed a modular self-driven photobiocatalytic architecture, in which the photo-active unit, photosystem I (PSI), produces a light-induced current, human sulfite oxidase (hSOX) acts as an electron supplier for PSI and cytochrome *c* (cyt *c*) works as a molecular wire between the bio-compounds and also towards the electrode. In our system the assembly of several biomolecules results in an

efficient interprotein electron transfer allowing the establishment of well-defined electron pathways.

For the incorporation of the multi-protein system we have used 3D inverse opal ITO (IO-ITO) electrodes (Fig. S**1**, SI) applying the previously reported template-based preparation procedu-

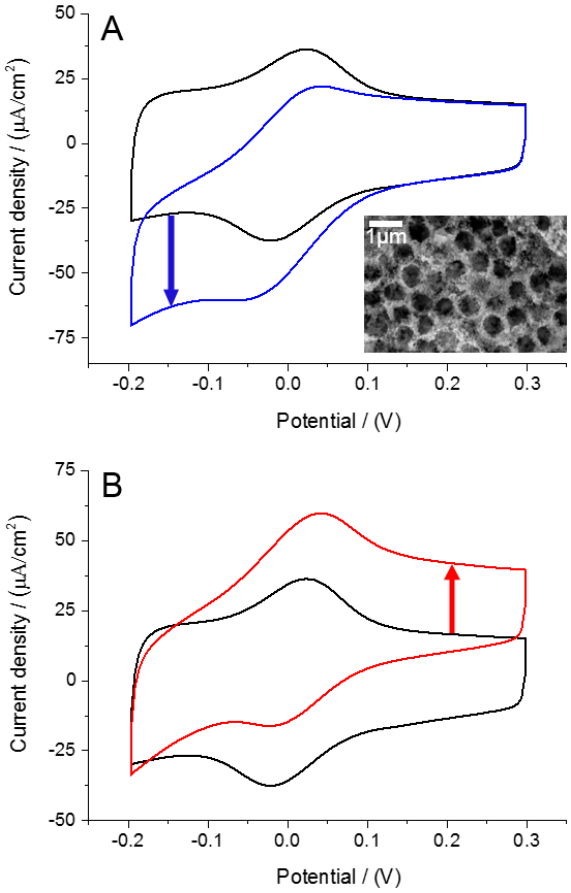

Figure 1. Cyclic voltammetry of IO-ITO•PSI•hSOx•cyt *c* electrode. A – cathodic photocatalysis upon illumination (blue curve). B – enzymatic catalysis upon addition of 1 mM of sulfite (red curve). Inset shows an SEM image of the prepared 3D electrode used for protein incorporation. Cyclic voltammetric measurements have been performed in 5 mM potassium phosphate buffer, pH 7, scan rate 10 mV/s, white light 100 W m^{-2}, reference electrode Ag/AgCl, 1 M KCl.

re.[84] IO-ITO electrodes provide a high surface area, which in turn allows for harboring large amounts of biomolecules. In this system protein binding has been ensured without the need for redox polymers or mediators, but solely by adsorption due to the hydrophilic surface of such IO-ITO structures. Here a sequential procedure starting with PSI and hSOx followed by cyt *c* has been used (see SI for details). In order to verify the successful integration of all components into the IO-ITO structure, firstly, cyclic voltammetric (CV) experiments have been performed. As shown in Fig. **1**, the IO-ITO•PSI•hSOx•cyt *c* electrode exhibits a quasi-

reversible redox behavior of cyt *c* with a formal potential at around 0.02 V *vs.* Ag/AgCl. From these experiments a surface coverage of 17 ± 3 pmol cm^{-2} cyt *c* can be calculated (related to the electrochemically active surface area). The CV experimental results do not only demonstrate the presence of cyt *c*, but also the electro-activity of a large amount of this redox protein, representing one of the pre-conditions for the successful delivery or uptake of electrons for the catalytic units. Upon illumination of the electrode a cathodic photocatalytic current is detected, starting at the redox potential of cyt *c* (Fig. **1, A**). This verifies that PSI can accept electrons from cyt *c* upon illumination – even when another protein is present within the mesoporous electrode structure. In the dark, after addition of the substrate of hSOx, SO_3^{2-}, an anodic bioelectrocatalytic current can be observed (Fig. **1, B**). Here, electrons are collected by the enzyme and further shuttled via cyt *c* to the electrode.

It has to be mentioned here that IO-ITO•hSOx•cyt *c* electrodes, i.e. without PSI, do not show any photocurrent under illumination. Moreover, IO-ITO•PSI•cyt *c* electrodes, i.e. without hSOx, display no anodic response in the presence of SO_3^{2-}.

The quantification of immobilized PSI has been performed by chlorophyll extraction,[354] yielding a PSI coverage of 0.2 ± 0.01 pmol cm^{-2} (again, related to the electrochemically active area). The hSOx coverage has been estimated by eluting the enzyme from the 3D IO-ITO and detecting the enzyme activity as described in the SI. It is in the range of 1.4 ± 0.4 pmol cm^{-2}. The surface coverage data of all three proteins implicate a good coverage of the inner surface with the biomolecules. For PSI and cyt *c* the coverage reaches values in the range of a monolayer. From the catalytic currents and the determined amount of immobilized enzymes additionally the turnover numbers (Tn) of PSI and hSOx within the architecture can be calculated: Tn(PSI) = 16 ± 3 s^{-1} and Tn(hSOx) = 1.6 ± 0.2 s^{-1}. The Tn for PSI is comparable to the value for PSI immobilized on ITO without hSOX and the Tn for hSOx is in the range of values reported in literature (for hSOx 0.85 s^{-1} [277] and for chicken SOX (cSOx) 2-4 s^{-1}).[355] Thus, the turnover numbers from our work are in good agreement with the previously reported data. This indicates that both catalysts react rather undisturbed by the presence of the other biocatalyst. Besides the functional assessment of each biomolecule separately we have further performed photo-chronoamperometric experiments with both catalytic components active. Here, the activity of hSOx is "switched on" by addition of the substrate (SO_3^{2-}) to the solution, whereas the activity of PSI is "switched on" by illumination. When the electrode is polarized at a potential of -0.15 V *vs*. Ag/AgCl a clear cathodic photocurrent is obtained which decreases in the presence of increasing concentrations of SO_3^{2-} (Fig. **2, A**).

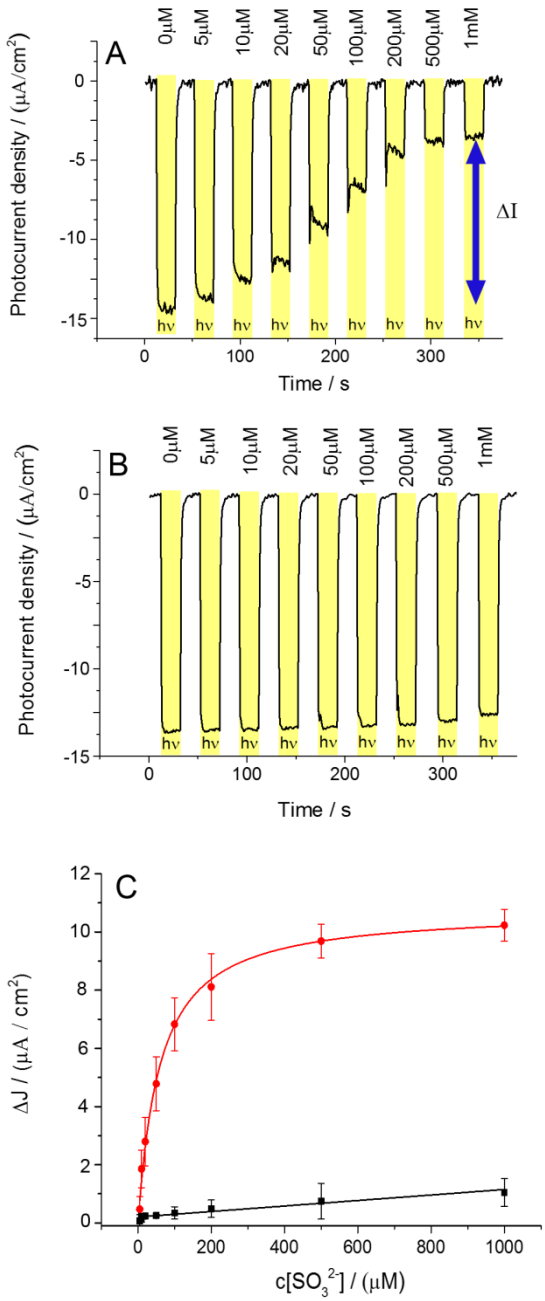

Figure 2. Photocurrent after addition of different concentrations of sulfite in solution for IO-ITO•PSI•hSOx•cyt *c* (A) and for IO-ITO•PSI•cyt *c* (B) electrodes. (C) Plot of the change of the photocurrent density *vs*. the concentration of sulfite for IO-ITO•PSI•hSOx•cyt *c* (red dots) and for IO-ITO•PSI•cyt *c* (black squares). Measurements have been performed under stirring in 5 mM potassium phosphate buffer, pH 7, upon addition of different concentrations of sulfite. Illumination white light 100 W/m^{-2}, at -0.15 V vs Ag/AgCl, 1 M KCl.

When we carry out the same experiment, but with an electrode lacking hSOx, only a slight decrease of the cathodic photocurrent can be detected, which starts at higher sulfite concentrations (Fig. **2, B**). The suppression of the cathodic photocurrent upon addition of sulfite to the IO-ITO•PSI•hSOx•cyt *c* electrode can therefore not simply be explained by

putative side reactions of sulfite with PSI, cyt *c* or the ITO electrode, but has to be driven by the enzymatic reaction of hSOx in the structure. Concluding, there are two competing signal cascades which can be expressed as follows:

(1) Electrode reaction: **Electrode** → cyt *c* → (cyt *c*)$_n$ →PSI → O_2

(2) Enzyme reaction: **SO_3^{2-}**→ hSOx → cyt *c* → (cyt *c*)$_n$ → PSI→ O_2

As depicted in equations (1) and (2) oxidized cyt *c* can receive electrons either from the electrode or from hSOx. If SO_3^{2-} is added, a competing electrical circuit is established, since now the oxidized cyt *c* is not only reduced by the electrode, but is also reduced by the enzyme (pathway 2). This leads to a suppression of the electrode pathway (1) and hence, to a diminished photocurrent. The degree of suppression of the cathodic photocurrent is determined by the efficiency of competition between both pathways and provides a quantitative feedback on the sulfite concentration in solution. By plotting the photocurrent decrease *vs*. the concentration of the added substrate a Michaelis-Menten-type behavior can be observed (Fig. **2, C**); curve fitting gives rise to an apparent K_M value of 59 $\pm$ 5 µM. This value is higher than previously reported for the enzyme in solution (1 µM)[356] but is comparable to values reported for hSOx, immobilized on electrodes (60 µM,[277, 357, 358] 72 ± 14 µM[359]).

These experiments show that the suppression of the photocurrent is of enzymatic origin. The maximum photocurrent suppression reaches ~70 ± 4 % of the initial photocurrent. This may illustrate the rather high efficiency of the established three protein system since pathway 2 can overtake the electron supply by pathway 1 to a very large extent. This also means that the enzyme reaction can "feed" the photoreaction at PSI with electrons. Moreover, the oxidation of sulfite which can lead to an anodic current at higher potentials (Fig. **1, B**) can now be transferred to a cathodic current measurement taking place at negative electrode potentials. It has to be mentioned here that this concept also includes the possibility of cyt *c* - cyt *c* self-exchange and thus, multiple molecules of the redox protein are involved in the electron delivery from the electrode to PSI and also from the enzyme to PSI.[85, 360]

With these functional bio-compounds in the mesoporous electrode we are able to transfer their function into a bio-electronic circuit, whereby the different reactions can be attributed to the following electronic elements: the trigger (sulfite), the detector (electrode), the relay network, which also works as a Nernstian capacitor (cyt *c*) and the photodiode (PSI). The principle including the reaction pathways is illustrated in Fig. **3**.

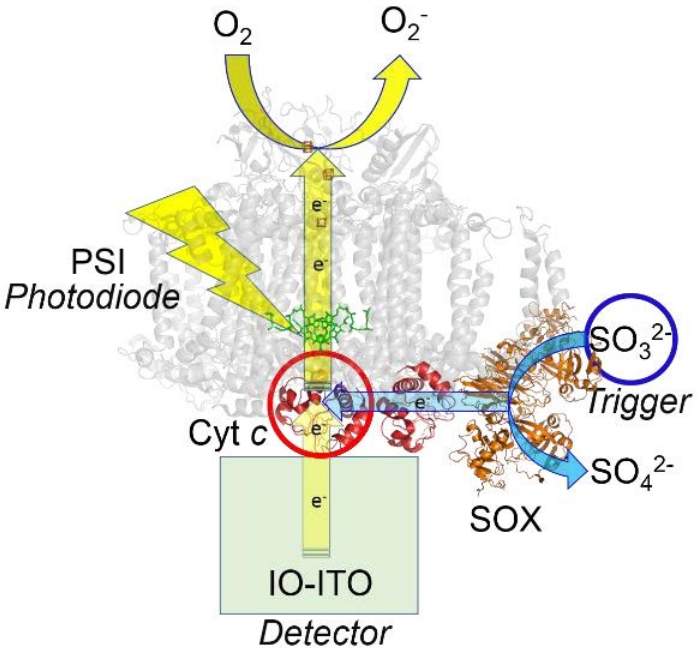

Figure 3. Schematic illustration of electron pathways within the biohybrid architecture upon illumination and addition of sulfite. Yellow arrows represent light-induced electron cascade initiated by the charge separation process within PSI. Blue arrows represent electron pathway during the oxidation of sulfite to sulfate. The enzyme reaction of human sulfite oxidase generates electrons, which reduce oxidized cyt *c* molecules. A "competitive" situation is thus generated at cyt *c* (see red circle), the cathodic photocurrent is suppressed and the degree of competition is detected at the electrode. Crystal structures have been exported for PSI[361], for cyt *c*[362] and for chicken liver SOx[363] and represented in PyMol.

Until now we have described the electron transfer reactions of this bioelectronic system. Nonetheless, the system should be able to operate without any external driving force. In order to test this self-driven modus, open circuit potential (OCP) measurements have been performed. As depicted in Fig. **4**, illumination of the IO-ITO•PSI•hSOx•cyt *c* electrode in the absence of sulfite leads to a slight increase of potential since this is a result of a complete oxidation of cyt *c* molecules by excited PSI (the increase is small since at the start of the measurement a large portion of cyt *c* is already oxidized). By subsequent addition of sulfite in the dark the OCP drops fastly by about 200 mV stabilizing at about -115 mV *vs*. Ag/AgCl (1M). Here, the enzyme reaction is "switched on" and subsequently cyt *c* is reduced. This behaviour is only found for hSOx containing electrodes, not for electrodes where hSOx is absent (Fig. **4**). Here, the OCP stays constant, again demonstrating that the electron supply occurs via the sulfite reaction at the enzyme. If the light is "switched on" again, the OCP increases and stabilizes between the fully oxidized and reduced state of cyt *c*. This steady state depends on the rate of photo-oxidation compared to the rate of enzymatic reduction.

When the biocatalytic electron supply is stopped (by removal of sulfite from the solution) and the electrode is still illuminated, the OCP returns to its initial value, indicating the complete oxidation of cyt *c* by PSI.

These biomolecular reactions can be monitored at the electrode, since the OCP is defined as the ratio of the redox states of cyt *c* (cyt c_{ox} / cyt c_{red}). This is reasonable, since it is the only component which can fastly exchange electrons with the electrode.

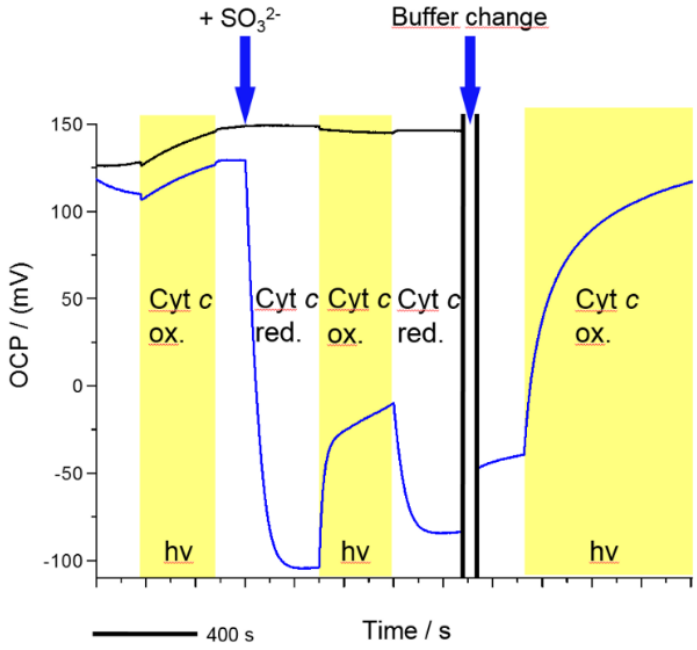

Figure 4. Potentiometric measurements of an IO-ITO•PSI•hSOx•cyt *c* electrode (blue line) and IO-ITO•PSI•cyt *c* electrode (black line). Yellow areas indicate illumination period. Blue arrow indicates addition of sulfite. Measurements have been performed in 5 mM potassium phosphate buffer, at pH 7, 1 mM sulfite. After exchange of the solution with pure buffer the OCP is measured again under illumination (100 W m^{-2}) but without sulfite in solution.

The potential measurements are in agreement with the electron transfer pathways explained in Fig. **3** and confirm the self-driven character of this artificial photobiocatalytic system.

In conclusion, in the present study the design of a multifunctional photobiocatalytic architecture has been shown. This system displays four distinct features: (i) Due to different triggers, such as light, substrate and potential, different reaction pathways can be switched "on" and "off" on demand, (ii) Photo-switchable sensing of sulfite is feasible since the photocurrent follows the sulfite concentration, but can be detected as a cathodic signal at negative polarization.[364] Due to the different reactions in the dark and under illumination the multi-biomolecular unit can be used as a capacitor, which is charged by the biocatalytic

reaction and discharged by the photocatalytic process and (iv) The system demonstrates self-driven character and can be used to surrogate electron delivery to PSI without any external energy source. This tri-protein architecture within a 3D electrode matrix demonstrates that well-defined electron pathways can be generated on an artificial platform. The system works as a bio-circuit and may thus stimulate further developments of smart bioelectronics devices.

ACKNOWLEDGMENTS

We greatfully acknowledge financial support by the BMBF, Germany (Biotechnology 2020+, projects: 031A154A+B). We also greatfully acknowledge Prof. Silke Leimkühler for the supply of the enzyme human sulfite oxidase.

Supporting Information

Preparation of IO-ITO electrodes

ITO slides (20 Ω/sq) have been purchased from Sigma, Germany) and cut into smaller slides 5 x 10 mm. Prior to use these slides have been sonicated in acetone (15 min), followed by a sonication step in isopropanol (15 min) and in ethanol (15 min). After drying in the air ITO slides have been transferred onto a spin coater (SCC-200, KLM). Prior to spin-coating the area of each slide has been isolated with parafilm, leaving a free area of ca. 0.2 cm^2. Next, a mixture of latex beads (LB) of 800 nm (Sigma, Germany) and ITO nanoparticles (ITOnp, 50 nm) (Sigma, Germany) has been prepared according to:[84] A 300 µl (6:1 methanol/water) suspension of 35 mg of ITOnp has been sonicated for 1 h. After this, a methanol suspension of 2.5 % latex beads (LB) has been centrifuged for 10 min at 16 000 rpm (25 000 g). Supernatant has been removed and the pellet has been re-suspended with previously sonicated solution of ITOnp. Such mixture of LB and ITOnp has been again sonicated at 4°C for 5 min. Finally, 4 µl of such LB/ITOnp mixture has been drop-casted on a rotating (60 rps) ITO slide in 3 steps (3 x 4 µl). As prepared ITO slides have been sintered for 2 h at 550° C heat plate.

Preparation of bioelectrodes (IO-ITO•PSI•hSOx•cyt c)

First, PSI solution (2 µl, 20 µM) has been drop-casted on as-prepared inverse opal ITO electrode (IO-ITO) and incubated for 2 min at RT. The IO-ITO•PSI electrode has been gently dipped in 5 mM potassium phosphate buffer, pH 7 for washing away the unbound PSI molecules. In the next step, by the same procedure, hSOx (2 µl, 1 mM) has been immobilized on IO-ITO•PSI electrode. After 2 min of incubation at RT the IO-ITO•PSI•hSOx electrode

has been washed in 5 mM potassium phosphate buffer, pH 7. In the last step, 2 µl of cyt *c* solution (1 mM) has been added (2 min, RT) to the IO-ITO•PSI•hSOx electrode to guarantee for electrical communication of the biomolecules and for the stabilization of the all-protein matrix within the IO-ITO electrode. In order to remove weakly bound proteins the final electrode has been again rinsed with buffered solution (5 mM potassium phosphate buffer, pH 7).

Cyclic voltammetry

All cyclic voltammetry experiments have been performed at Zahner potentiostat (Zahner Zennium, Germany) at scan rate of 10 mV s^{-1}, Pt wire as counter electrode and Ag/AgCl (1 M KCl) as reference electrode. The working buffer in all experiments has been potassium phosphate buffer, pH 7.

Photochronoamperometry

All photochronoamperometric experiments have been performed at Zahner potentiostat (Zahner Zennium, Germany) applied potential -0.15 V vs. Ag/AgCl (1 M KCl) in 5 mM potassium phosphate buffer at pH 7 and under stirring. Light intensity of white LED lamp has been adjusted to 100 W m^{-2}. Light pulses of 20 s have been used.

hSOx activity assay

As-prepared IO-ITO•PSI•hSOx•cyt *c* electrodes have been thoroughly washed in a 500 mM KCl solution to remove the hSOx molecules from the surface for estimation of the amount of fixed enzyme. The so gained hSOx solution has been subjected to the activity assay, as described in.[365] The enzymatic sulfite conversion has been followed by UV-Vis spectroscopy, performed at spectrometer (Evolution 201, Thermo Fisher Scientific, Shanghai) and compared to a calibration measurement.

Determination of PSI concentration

Firstly, the electrodes have been incubated in an acetone/water mix 80 % (v/v) for 1 h to remove Chl *a* molecules from the PSI electrode. Consequently, the as-resulted Chl *a* solution has been subjected to the well-known Chl *a* concentration assay, described in.[366]

Potentiometry

Potentiometric experiments have been performed at Zahner potentiostat (Zahner Zennium, Germany) in OCP modus. Here, zero-current potential deviations have been recorded in the dark and under illumination (100 W m^{-2}, white LED lamp).

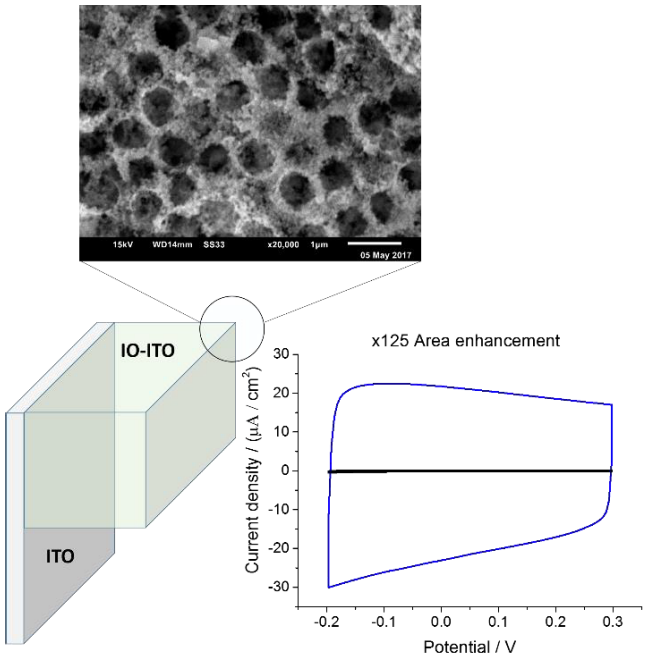

Figure S1. Scheme of the 3D IO-ITO electrode. Zoom in - scanning electron microscopy of the as-prepared 3D IO-ITO electrode. Inset – cyclic voltammetry of the bare ITO slide (black) and 3D IO-ITO (blue), 1 M KCl, scan rate 100 mV s^{-1}.

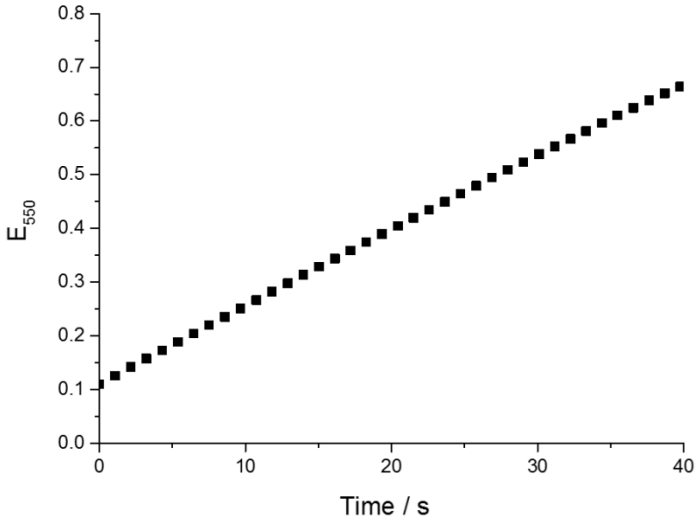

Figure S2. Activity assay of hSOx performed in KPP buffer, 5 mM at pH 7. Black squares: extinction values measured at 550 nm at different timepoints.

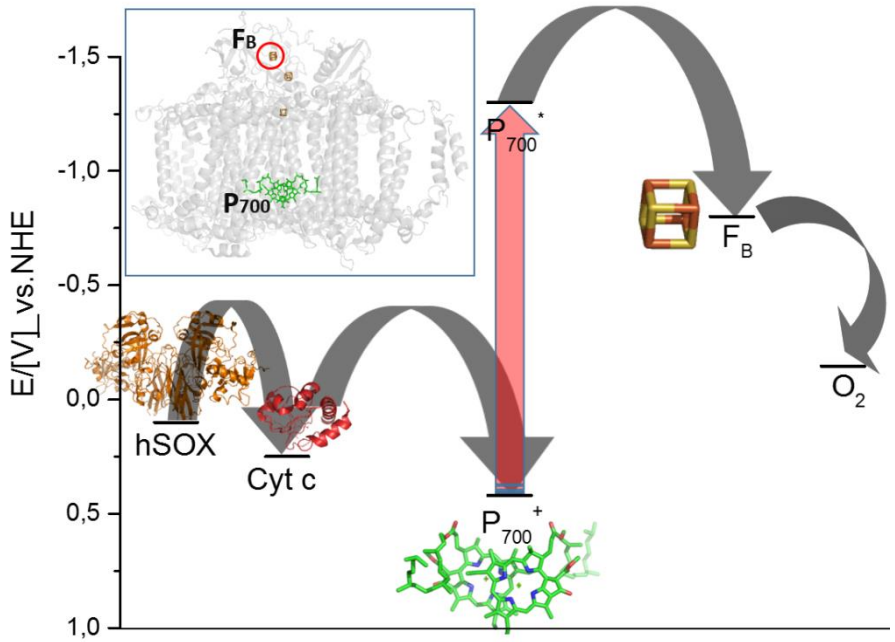

Figure S3. Electron transfer pathway in a hSOx-cyt *c*-PSI-O_2 system. Electrons coming from sulphite oxidation are transferred by the hSOx to the cyt *c*, which in turn transfers electrons to the photo-oxidized P_{700} centre. The in-built intramolecular electron transfer (IET) transports electrons to the oxygen in solution. Inset – position of F_B cluster and P_{700} centre inside PSI molecule.

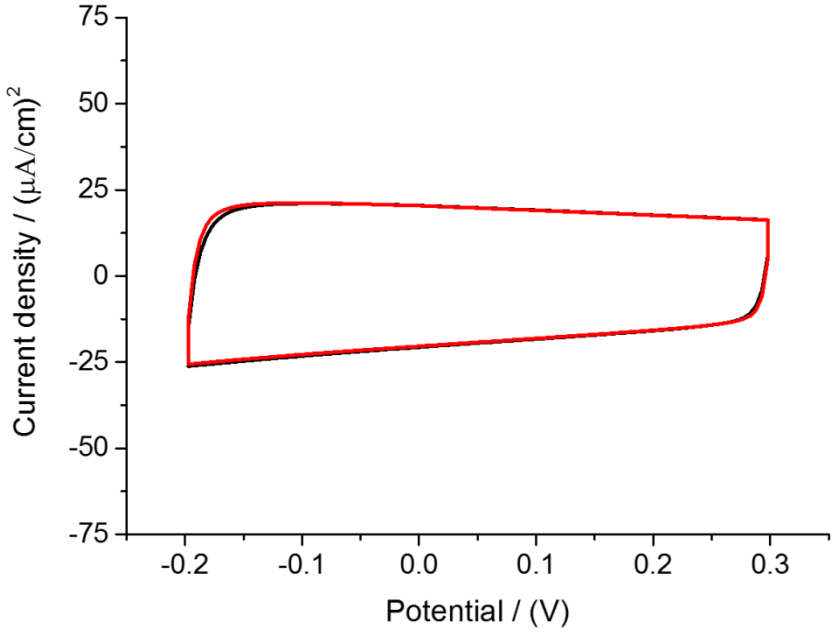

Figure S4. Cyclic voltammetry of bare 3D-IO-ITO electrode (6 layers) with (red curve) and without (black curve) sulphite in solution. Experimental conditions: KPP buffer, 5 mM, pH 7 (with and without 1 mM sulphite). Scan rate 100 mV s^{-1}. Reference electrode Ag/AgCl (1M).

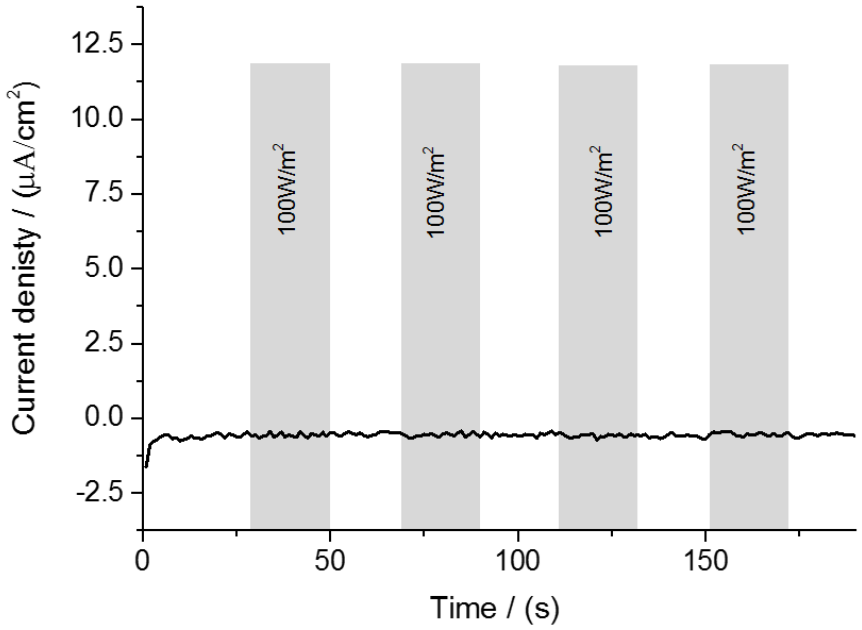

Figure S5. Photoamperometric experiment at 3D-IO-ITO-hSOx-cyt *c* (i.e. lacking PSI) electrode (6 layers). Experimental conditions: KPP buffer, 5 mM, pH 7. Reference electrode Ag/AgCl (1M).

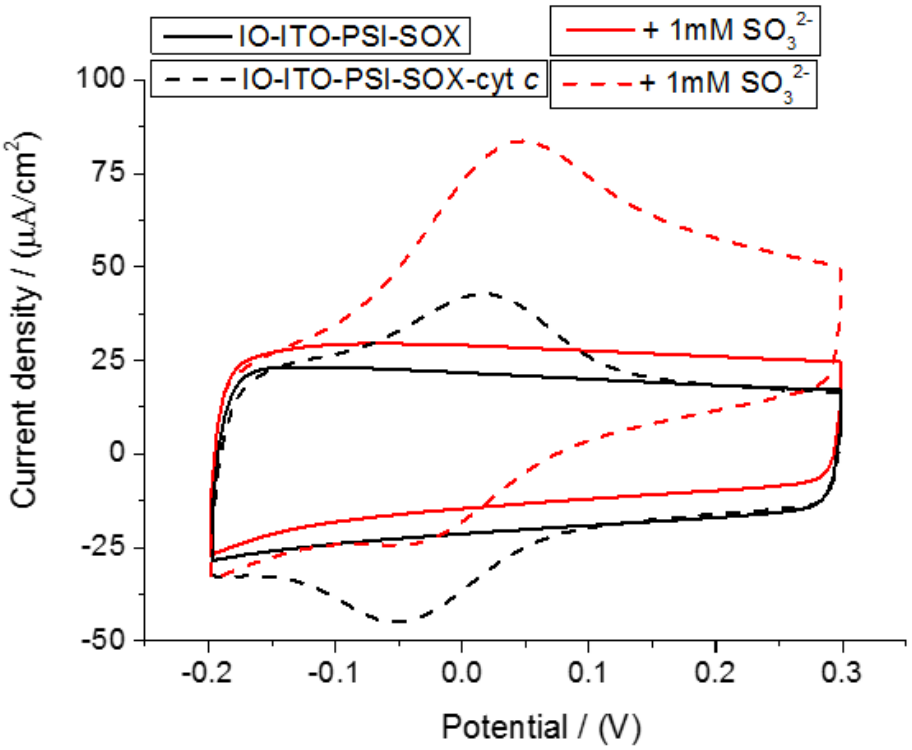

Figure S6. Cyclic voltammetry experiments. Black full curve – IO-ITO-PSI-hSOx (6 layers) in KPP buffer, at pH 7, 5 mM, red full curve - IO-ITO-PSI-hSOx (6 layers) with 1 mM sulphite in solution. Black dashed curve - IO-ITO-PSI-hSOx-cyt *c* (6 layers) in KPP buffer, at pH 7, 5 mM, red dashed curve - IO-ITO-PSI-hSOx-cyt *c* (6 layers) with 1 mM sulphite in solution. Experimental conditions: KPP buffer, 5 mM, pH 7 (with and without 1 mM sulphite). Scan rate 100 mV s^{-1}. Reference electrode Ag/AgCl (1M).

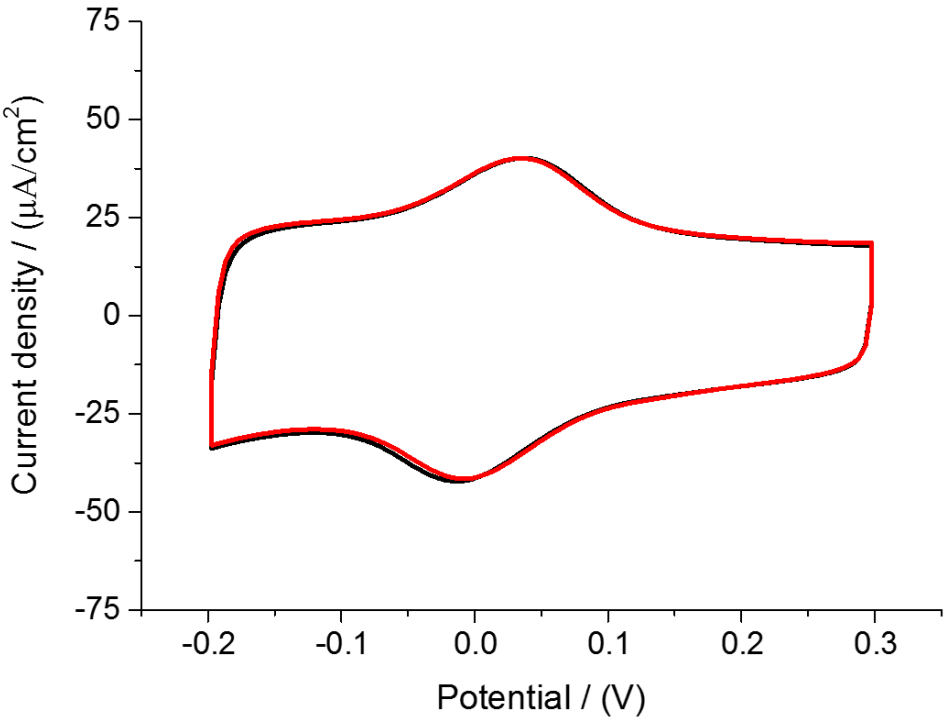

Figure S7. Cyclic voltammetry experiments. Black curve – IO-ITO-PSI-cty *c* (6 layers) in KPP buffer, at pH 7, 5 mM, red curve - IO-ITO-PSI-cty *c* (6 layers) with 1 mM sulphite in solution. Experimental conditions: KPP buffer, 5 mM, pH 7 (with and without 1 mM sulphite). Scan rate 100 mV s^{-1}. Reference electrode Ag/AgCl (1M).

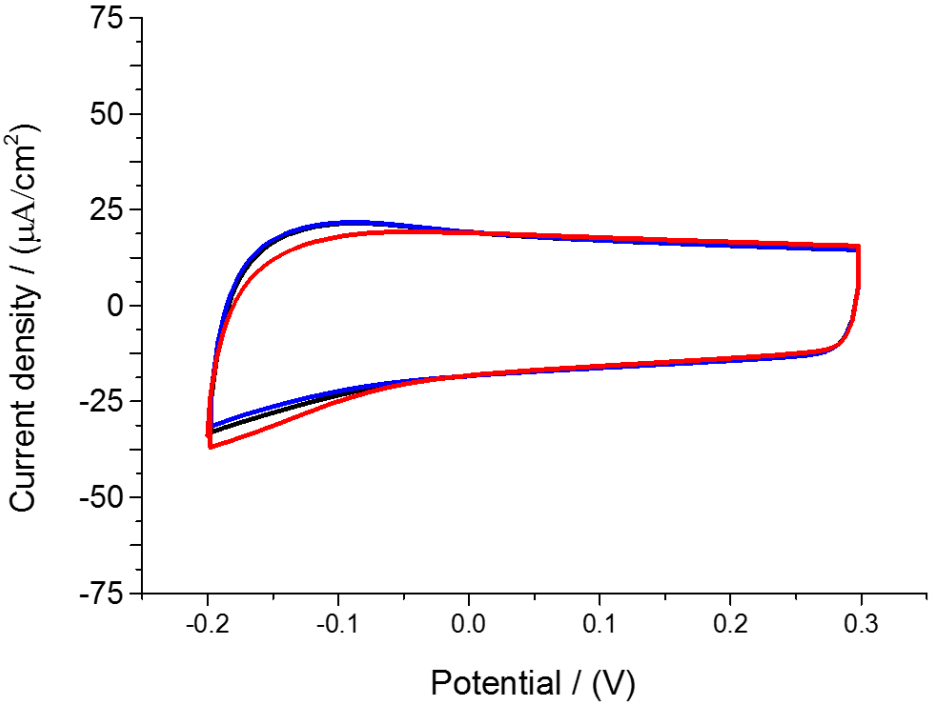

Figure S8. Cyclic voltammetry experiments. Black curve – IO-ITO-PSI-hSOx (6 layers) in KPP buffer, at pH 7, 5 mM, blue curve - IO-ITO-PSI-hSOx (6 layers) under illumination 100 W m^{-2}, red curve - IO-ITO-PSI-hSOx (6 layers) with 1 mM sulphite in solution. Experimental conditions: KPP buffer, 5 mM, pH 7 (with and without 1 mM sulphite). Scan rate 100 mV s^{-1}. Reference electrode Ag/AgCl (1M).

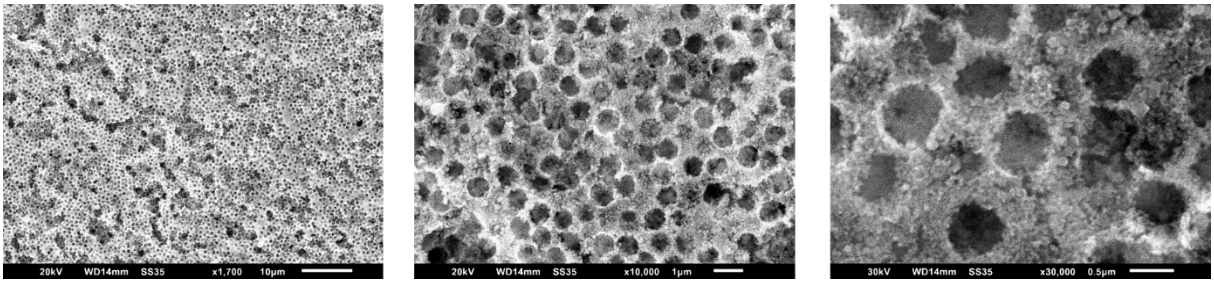

Figure S9. SEM images of as-prepared 3D IO-ITO structures. From left to right: x1700 magnification (scale bar 10 µm), x10 000 magnification (scale bar 1 µm) and x30 000 magnification (scale bar 0.5 µm). Acceleration voltage 20 kV (for the last image 30 kV).

Published in: Electrochimica Acta. Dmitri Ciornii, Adrian Kölsch, Athina Zouni, Fred Lisdat. Exploiting new ways for a more efficient orientation and wiring of PSI to electrodes: A fullerene C70 approach. Electrochimica Acta 2019, 299, 10, 531–539. **DOI**: 10.1016/j.electacta.2019.01.032.

4.3 Exploiting new ways for a more efficient orientation and wiring of PSI to electrodes: A fullerene C70 approach

Authors: Dmitri Ciornii, Adrian Kölsch, Athina Zouni, Fred Lisdat

Abstract

For successful production of photobioelectrodes several aspects have to be addressed: the proper orientation of the photo-active biomolecules on the electrode surface and a good electrical connection with the electrode. In this work a step-by-step procedure for the successful construction of a photosystem I (PSI)-based photobioelectrode is shown. First, the orientation of PSI on a thiol-modified gold surface is improved. Here, positively charged ruthenium hexamine complexes allow for a better and a more directed assembly of PSI with the luminal side to the electrode. In a second step, an improved electrical communication of the PSI reaction center with the electrode is achieved by employing carboxy-modified C_{70}-fullerenes. Due to the outstanding electrical properties of the small fullerene nanoparticles and their accessibility towards the PSI's reaction center and the electrode, the system shows an enhanced magnitude of the cathodic photocurrent (15 µA cm^{-2} at U = - 0.300 V vs. Ag/AgCl (1M)), a positive onset potential of the cathodic photocurrent generation (U_{onset} = + 0.157 V vs. Ag/AgCl(1M)).

Introduction

In recent years, solar-based biotechnology has gained more and more scientific interest, giving rise to several trends in this field: production of solar biofuels,[367-369] photobiovoltaic

cells,[370] biomimetic systems, solar energy storage devices,[2, 371] to name just a few of them. Here, the use of photoactive biomolecules represents an own direction. The prerequisite for an efficient solar-to-electrical energy conversion is the establishment of a functional photobioelectrode. For this, two key parameters are crucial: a) successful integration of functional intact photoactive units in high amounts on the electrode and b) an efficient electric wiring of these molecules to the electrode.[372]

Until now, many successful strategies for construction of such photobioelectrodes have been established.[311, 373-376] The simplest way of integration represents *physical adsorption*. Here, the deposition on a surface is mostly governed by hydrophobic interactions and Van-der-Waals forces. For example, bacterial photosynthetic reaction center (RC from *Rb. sphaeroides*) has been adsorbed on single-walled carbon nanotubes (SWNT) and even bare gold.[377 378] The drawback of such approach is the lack of specificity of interactions, i.e. the attachment of the biomolecule occurs randomly. For a more specific attachment to the electrode the *electrostatic approach* has gained some attention. It has been shown, that deposition of photosystem I (PSI) occurs at carboxy- and hydroxy-terminated thiols.[128, 143, 379] It has been demonstrated that deposition of PSI with the electron-transfer vector pointing away from the electrode, can be achieved at hydroxy-terminated thiols, whereas at amino-terminated thiols the orientation of PSI is rather random.[160] The *covalent approach* has been employed for robust coupling of photo-sensitive compounds to electrodes. Examples here are: PSI covalently attached to TPDA-modified (terephthaldialdahyde) gold[141] or to carbon nanotubes via maleimid-bond,[111] PSI coupled on NHS-pyrene (N-hydroxysuccinimid) ester modified graphene electrode,[304] bacterial reaction center attached to a NHS-PEG-azide (polyethyleneglycol) linker-modified rGO[380] (reduced graphene oxide) or bound to amino-functionalized MWNTs.[381] Other methods for specific assembly of PSI on an electrode are the use of *affinity tags*[382, 383] or *plugging a specific linker* into the photoactive entity.[147, 384] An interesting immobilization strategy for accommodating larger amounts of PSI represents the construction of *multilayers*. Random multilayers, where orientation of photoactive molecules cannot be controlled, are produced by vacuum-assisted deposition[179, 385-387] or by entrapping the molecule of interest in a conductive matrix, like conducting or redox-polymers.[116, 157, 158, 388] Multilayers with some degree of orientation are produced by employing site specific modification, like platinization of the stromal side of PSI,[389] or introduction of a redox molecule cytochrome *c* (cyt *c*) between the layers[150] or even cyt *c*-DNA between PSI layers.[85]

Besides a proper immobilization, electrical communication of the fixed photo-sensitive compound with the electrode is decisive for the performance. Here, mechanisms can be divided in direct electron transfer (DET) or mediated electron transfer (MET). DET between photosynthetic proteins and electrode has been demonstrated at short thiol-modified gold,[128, 143, 160] pyrene-modified graphene,[129] graphene oxide,[167] pyrolytic graphite,[127] ZnO and TiO_2[130] enabling electron tunneling from the electrode to the active site of PSI.[390-392] In contrast, MET is assured by a redox-active shuttle molecule and enables a better access to the active site, therefore many studies have shown successful electric communication between photoactive units and the electrode *via* soluble mediators, like N,N,N',N'-tetramethyl-p-phenylenediamine, DCIP/ascorbate (dichloroindophenol), ferricyanide or quinones.[259, 393, 394] These systems might be complicated since the two redox states of the mediator have different reaction capabilities at the excited photoactive biomolecule and at the electrode.[395] A mediator can also be bound to a polymer backbone (e.g. Osmium-complexes),[116] so that ET takes place by a "hopping" mechanism and becomes highly efficient. In several studies it has been also shown, that small redox protein, cyt *c*, can act also as mediator in mono- or multilayer arrangements.[84, 85, 294, 396-398] Out of the literature analysis it becomes clear that the orientation of PSI binding to surfaces is still poorly understood and controlled. In addition, there are only few successful approaches in electrical contacting PSI with electrodes when soluble shuttle molecules shall be avoided since they can cause unwanted reactions at both electrodes in a cell and the two sides of PSI. For the first issue, i.e. the oriented assembly of PSI, we have investigated how the interaction of PSI with chemisorbed layers on gold can be improved by modifying a thiol layer with an additional component – a ruthenium hexamine complex (ruhex). For the second issue, which is the establishment of an effective electrical contact of PSI with the electrode, we go apart from canonical strategies and have employed for the first time a functionalized fullerene C_{70}. Here, our idea is to integrate conductive fullerene nanoparticles and exploit their small size for electrical wiring of PSI with the electrode resulting in a photobioelectrode which is completely in an immobilized state.

Experimental Section

Materials and Chemicals

Gold electrodes have been purchased from BASi, USA. Ruthenium hexaammine chloride, cis-dichlorobis(2,2'-bipyridyl)ruthenium, mercaptopropanol, mercaptopropionic acid, methyl viologen (MV^{2+}) have been purchased from Sigma Aldrich (Germany). Fullerene tetraglutaric

acid (TGA-C_{70}) have been supplied by SES Research, USA. K_2HPO_4 and KH_2PO_4 have been purchased from ROTH, Germany. In all experiments ultrapure ddH_2O has been used.

Photosystem Preparation

Photosystem I (PSI) has been extracted from *T. elongatus* according to previously described procedure.[328] PSI fraction has been purified by ion exchange columns as previously described.[399] After this, PSI trimers have been crystalized by applying buffer A (5 mM MES-NaOH, pH 6.0 and 0.02 % n-dodecyl-β-maltoside (β-DM), 4 °C). After a concentration of 5 mM $MgSO_4$ has been reached, the crystals have been centrifuged (5 min, 4 °C, 4000 x g) and washed in buffer A. Further, PSI-crystals have been resolubilized in buffer B (5 mM MES-NaOH, 0.02 % β-DM, pH 6.0, 30 mM $MgSO_4$) and recrystalized again. For photoelectrochemical experiments PSI-crystals have been dissolved in 100 mM potassium phosphate (KPP) buffer, pH 8. Functionality of such prepared PSI-crystals has been assessed. Here, a light-driven electron transport from cytochrome *c* (Sigma Aldrich) to methyl viologen (MV^{2+}) has been performed with a Clark-type electrode (Oxygraph, Hansatech, King's Lynn, UK). Oxygen consumption rates were 1640 ± 80 µmol O_2 h^{-1} mg^{-1} Chl *a*.

Electrode preparation

The gold electrodes used in this study have been constructed as follows: first, gold surface has been modified with a self-assembled monolayer of thiols.[400] Here, we have used mercaptopropionic acid (MPA)[401, 402] and mercaptopropanol (MP) (1:3) (1 mM in ethanolic solution, 48 h, 4°C). In a second step, MPA/MP-modified gold electrodes[403] have been either directly used for assembly of PSI (a 0.5 µM PSI solution at pH 8, incubation for 1 h in the dark at 4°C) or additionally modified with a positively charged compound, ruthenium hexaammine, Ruhex, (electrochemistry of ruthenium hexamine has been previously shown on Au-MPA[404]) (10 mM aqueous solution, 1 h in the dark, 4°C). In the last step, Au-MPA/MP-Ruhex-PSI electrodes have been modified by back-filling with a 20 µM of carboxy-functionalized fullerene C_{70} dissolved in 5 mM KPP at pH 7.5. A 1 h incubation followed, in the dark at 4°C.

QCM experiments

QCM measurements have been performed for monitoring and estimation of the deposition process. Here, MPA/MP - and MPA/MP-Ruhex-modified gold surfaces have been tested for

deposition of PSI. For our experiments we have used the Q-Sense device (Vaestra Froelunda, Sweden) and quartz sensor chips previously modified with thiols (ethanolic solution of 1 mM MPA/MP, 48h, 4 °C). Prior to incubation with PSI solution (0.5 µM, pH 8) the sensor chips have been washed with 5 mM potassium phosphate buffer, KPP, pH 8, at 50 µl min^{-1} flow rate. PSI solution has been pumped at 50 µl min^{-1} flow rate for 1 h. Prior to assembly of Ruhex on the MPA/MP-modified gold surface, the sensor chips have been washed with deionized H_2O and then Ruhex (10 mM, aqueous solution) has been pumped at 50 µl min^{-1} flow rate for 1 h. After washing the chip with 5 mM KPP, pH 8, PSI solution has been pumped at 50 µl min^{-1} flow rate for 1 h. In the last step, a fullerene C_{70} solution (20 µM in KPP 7.5) has been pumped over sensor chip at 50 µl min^{-1} flow rate for 1 h.

Electrochemical and photoelectrochemical experiments

All measurements have been performed at the photoelectrochemical workstation, Zennius from Zahner (Germany), in 5 mM KPP buffer at pH 7 in a home-made photoelectrochemical cell.

In chopped light voltammetry experiments the responses of Au-MPA/MP-PSI, Au-MPA/MP-Ruhex-PSI, Au-MPA/MP-Ruhex-PSI-C_{70}, and Au-MPA/MP-Ruhex-C_{70} electrodes have been measured with changing potential (scan rate 2 mV s^{-1}) and light pulses of 5 s and fixed light intensity. Here, a white light source (100 mW cm^{-2}) has been applied.

Photo-action spectra experiments have been employed for detection of wavelength-dependent photo-responses in the range between 400 and 700 nm. These experiments help to assign the origin of the photocurrent.

Light intensity variation: Here white light intensity-dependent photo-responses have been registered. Different white light intensities have been applied, starting from 1 mW cm^{-2} until 100 mW cm^{-2}.

Cyclic voltammetry has been employed for the verification of the assembly of Ruhex on the MPA/MP surface. Here, scan rates have been varied between 10 - 400 mV s^{-1}.

UV-Vis experiments

UV-Vis experiments have been carried out with each compound used for the construction of the electrodes, i.e. PSI (Chl *a*), ruthenium hexamine and Fullerene-C_{70}. Measurements have been performed in a wavelength range between 400 – 700 nm, at UV-Vis spectrometer Varian

(Shanghai). For evaluation of PSI concentration on the electrode chlorophyll extraction has been used with 80% acetone and subsequent absorption measurements.[405] Measurements for ruthenium hexamine (10 mM) and Fullerene-C_{70} (20 µM) have been performed in ddH_2O and in 5 mM KPP buffer at 7.5, respectively.

Atomic force microscopy

AFM experiments have been performed for direct visualization of the PSI layer. The measurements have been taken in QI mode (quantitative imaging) at the atomic force microscope (Nanowizard 3, JPK) with a 0.7 N m^{-1} cantilever (Bruker). As the substrate a cleaned planar gold chip (Xantec) has been employed and all modification steps have been performed accordingly to the electrode preparation procedure (as described in the section "materials and methods: electrode preparation").

Results and discussion

Au-MPA/MP-PSI electrodes

Based on previous reports on PSI assembly on thiol-modified gold electrodes[143, 379, 406-408] we have decided to immobilize PSI on gold, pre-modified with carboxy- and hydroxy-terminated thiols. Here, mercaptopropionic acid and mercaptopropanol have been chosen due to their functional groups and short backbone length. First, for monitoring of the deposition process, we have employed quartz crystal microbalance (QCM).

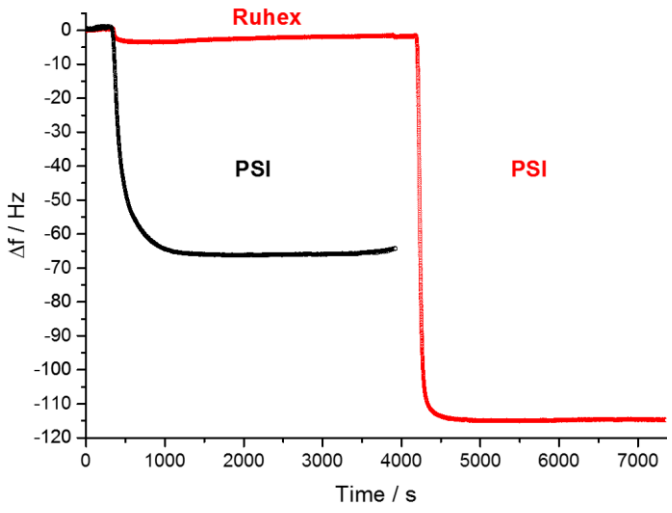

Figure 1. Frequency change (Hz) at a modified quartz chip during the deposition of PSI and Ruhex. Black line: PSI adsorption at Au-MPA/MP (Δf = 65 ± 24 Hz). Red line: adsorption of Ruhex (Δf = 4 ± 1 Hz) and of PSI (Δf = 118 ± 37 Hz) on top of MPA/MP- modified gold. The Ruhex solution (10 mM) and PSI solution (0.5 µM) have been pumped at 50 µl min-1 for 1h.

The frequency shift during the flow of PSI solution over the sensor surface clearly demonstrates the successful immobilization of PSI from solution onto the modified surface (see Figure 1, black line). In our experiments a frequency change of $\Delta f\ cm^{-2} = 65 \pm 24$ Hz has been measured. By assuming a water content of 20 %,[409] a coverage of PSI has been estimated to be 0.10 ± 0.03 pmol cm^{-2}. Chl *a* extraction experiments have revealed a PSI coverage on such electrodes of about 0.09 ± 0.04 pmol cm^{-2}, which is in good agreement with the QCM evaluation. For evaluation of the functional properties of such a simple arrangement we have used chopped light voltammetry

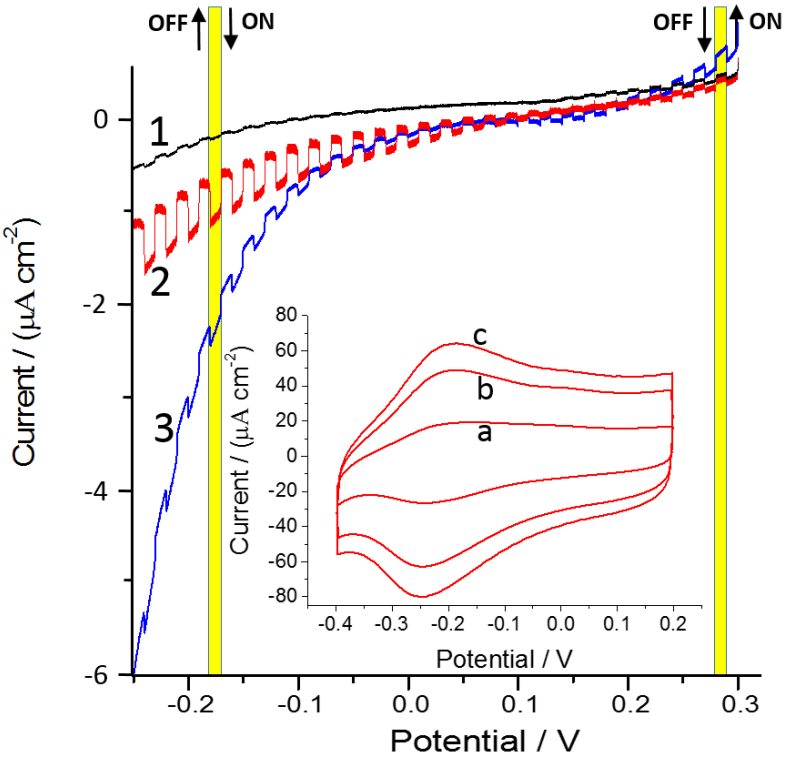

Figure 2. Chopped light voltammetric experiment. 1 – Au-MPA/MP-PSI, 2 – Au-MPA/MP-Ruhex-PSI, 3 – Au-Cysteamine-PSI. Experimental conditions: scan rate 2 mV s^{-1}, light pulses of 5 s, buffer: 5 mM KPP, pH 7, white light lamp: 100 mW cm^{-2}. Inset - cyclic voltammetry of Au-MPA/MP-Ruhex electrode in 5 mM KPP buffer, pH 7. Different scan rates have been applied: a) 10 mV s^{-1}, b) 200 mV s^{-1}, c) 400 mV s^{-1}.

(I-V experiment by alternating light "on" and "off"). The results show that both, cathodic and anodic photocurrents are generated upon illumination (see Figure 2, black line). This means that PSI is assembled randomly on the MPA/MP (mercaptopropanoic acid/mercaptopropanol) surface, resulting in contact of both, the luminal and the stromal sides with the electrode. The onset potential for cathodic photocurrents is rather negative, U_{ONSET} = -150 ± 16 mV vs. Ag/AgCl. This points to a rather heterogeneous distribution of orientations of PSI on the

electrode (with the stromal and luminal side) since here oppositely occurring charge separations will compensate each other to a large extent (see Fig. S1).

The photocurrent magnitude measured for the Au-MPA/MP-PSI system in this work (see Table 1) is rather small, but in good agreement with previously reported values for PSI immobilized on thiol-modified gold electrode.[128, 140, 141, 143, 147]

Table 1. Comparison of the photocurrent density at -270 mV vs. Ag/AgCl and the mass proportional frequency change derived from QCM experiments for the two different surfaces: Au-MPA/MP-PSI vs. Au-MPA/MP-Ruhex-PSI.

	Photocurrent (μA cm^{-2})	Δf (Hz cm^{-2})
MPA/MP-PSI	0.08 ± 0.04	65 ± 24
MPA/MP-Ruhex-PSI	0.37 ± 0.10	118 ± 37

Improvement of the orientation of PSI

To achieve a more oriented assembly of PSI with its luminal side (which is negatively charged) to the surface, we have introduced an additional positively charged component on top of the MPA/MP layer. For this purpose we have chosen the small metal complex, ruthenium hexamine (Ruhex), and adsorbed it on top of MPA/MP before PSI deposition. First, we have verified the immobilization of the redox molecule by cyclic voltammetry (see Figure 2, inset). Here, a coverage of electro-active Ruhex Γ_{Ruhex} = 172 ± 18 pmol cm^{-2} has been elucidated. In order to study the photoelectrochemical properties of PSI on top of this additional Ruhex-layer chopped light voltammetry has been performed. It can be clearly seen that the onset of the cathodic photocurrent for Au-MPA/MP-Ruhex-PSI is shifted to more positive potentials U_{ONSET} = +76 ± 9 mV vs. Ag/AgCl (n=3) (Figure 2, red line). Furthermore, the values of the cathodic photocurrent for these electrodes are higher (I = 0.37 ± 0.10 μA cm^{-2} at -270 mV vs. Ag/AgCl) than for electrodes lacking Ruhex (I = 0.08 ± 0.04 μA cm^{-2} at -270 mV vs. Ag/AgCl) (see Figure 2). In order to analyze the binding behavior of PSI to the new surface design, again, QCM measurements have been performed. The red line in Figure 1 illustrates both, the deposition of Ruhex and the adsorption of PSI. Compared to the MPA/MP only modified gold, here, a higher mass accumulation of PSI has been achieved. The frequency shift can be evaluated as Δf = 118 ± 37 Hz. If we assume a water content of 20 %,[409] a coverage of PSI is estimated to be 0.19 ± 0.06 pmol cm^{-2}. This calculation correlates well with Chl *a* extraction experiments, which reveal a PSI coverage on such electrodes of

0.23 ± 0.10 pmol cm^{-2}. In order to clarify whether the improved photocurrent magnitude has been originated by the amount and/or the orientation of PSI, the photocurrent values have been correlated to the amount of deposited PSI on MPA/MP- and MPA/MP-Ruhex-modified gold electrodes, respectively. Table 1 summarizes the photocurrent values measured at a potential U = -270 mV vs. Ag/AgCl and the frequency changes obtained from QCM. It can be seen that the amount of PSI on the MPA/MP-Ruhex surface is almost twice as much as on the MPA/MP surface, whereas the photocurrent is almost 4 times higher, when assembly takes place on the Ruhex containing surface. This strongly supports the idea that PSI assembles in a more oriented way on the Au-MPA/MP-Ruhex surface (i.e. with a higher fraction of luminally bound PSI – see Figure S1 for visualization). It has to be further noted that at positive potentials, where the onset of cathodic photocurrents has been observed (U_{ONSET} ≈ +76 mV vs. Ag/AgCl) Ruhex cannot withdraw electrons from the electrode (E_0 (Ruhex) = -200 mV vs. Ag/AgCl) and, thus, cannot work as mediator for PSI. This might be another argument for a more preferred orientation of PSI with its luminal side towards the electrode. For comparison to the Au-MPA/MP-Ruhex electrodes, which carry a positively charged metal complex, a positively charged thiol layer on gold - cysteamine - has also been tested (see Figure 2, blue line and Figure S2, red line). Here, the photocurrent is clearly smaller (I = 0.24 ± 0.03 μA cm^{-2} at U = -270 mV vs. Ag/AgCl) as compared to Au-MPA/MP-Ruhex-PSI (I_{U-270} = 0.37 ± 0.10 μA cm^{-2}) and the onset potential for cathodic photocurrents is around 0 mV vs. Ag/AgCl (compared to +76mV vs. Ag/AgCl for Au-MPA/MP-Ruhex-PSI). Taking these results and compare them with the different studies on SAM layers[128, 143, 161, 163, 410-412] it is indicated that the charge is not the only parameter determining the interaction of PSI with the surface.

Electrical wiring of PSI by means of fullerenes

Although photocurrent amplitude and the onset potential have been improved upon introduction of Ruhex in the system, the photocurrent is still relatively tiny. The problem here can be attributed to a poor connection of the reaction center of PSI (P_{700}) with the electrode, i.e. a large part of the immobilized PSI is not taking part in the signal generation. To improve the amount of "well connected" photocatalytic complexes we have exploited the assembly of an additional component between PSI and the electrode surface, a certain type of carbon nanoparticles - fullerenes. Fullerenes are very small (ca. 1 nm) π-conjugated structures and allow electron transfer reactions to occur. A major drawback for interaction with a hydrophilic

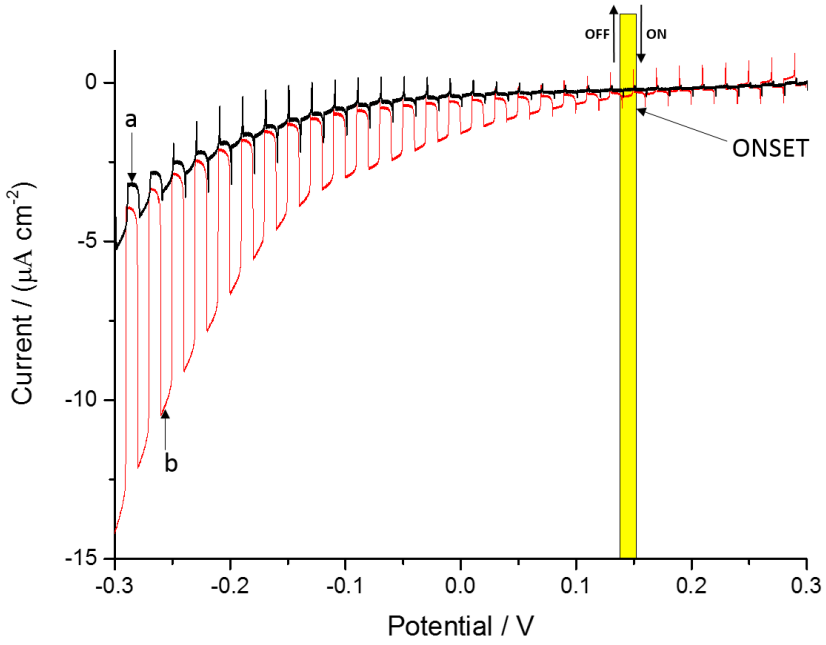

Figure 3. Chopped light voltammetric experiment. Red curve - Au-MPA/MP-Ruhex-PSI-C_{70}, black curve - Au-MPA/MP-Ruhex-C_{70}. Scan rate 2 mV s^{-1}, buffer: 5 mM KPP pH 7, white light lamp 100 mW cm^{-2}.

biomolecule such as PSI and a hydrophilic electrode surface, represents the hydrophobic character of the fullerene. Therefore, in order to achieve a productive connection, a functionalized fullerene is considered to be a better candidate than a pristine one. TGA, tetraglutaric acid C_{70} (Figure S3, SI) has been used within this study. We have introduced TGA in the system as the last step of assembly in order to take benefit of the preferred orientation of PSI achieved on the Au-MPA/MP-Ruhex-electrode. The successful assembly of the fullerene has been monitored during QCM experiments (see Figure S4 and Figure S5, SI). For the characterization of the system we have performed chopped light voltammetry experiments under the same conditions as for Au-MPA/MP-Ruhex-PSI. The cathodic photocurrent shows a significantly larger magnitude and a positively shifted onset potential (Figure 3, U_{ONSET} = +157 ± 9mV vs. Ag/AgCl). Obviously, the conductive properties of the fullerene nanoparticles help to connect PSI complexes with the electrode. Interestingly, it can be observed here, that upon reaching the redox potential of Ruhex, the photocurrent is slightly stronger enhancing its magnitude (Figure 3, red line). This observation might be explained by the participation of Ruhex in electron transfer from electrode towards PSI and hence, by approaching the redox potential of Ruhex electron transfer can additionally proceed via this metal complex. This beneficial effect can also be verified for another redox complex with a higher redox potential, cis-dichlorobis(2,2'-bipyridine)ruthenium(II) (Rubis) (E_0 = +200 mV vs. Ag/AgCl). Here, a very positive onset of

cathodic photocurrent (U_{ONSET} = +290 mV vs. Ag/AgCl) and a complete lack of anodic photocurrents has been observed and thus, the above mentioned explanation on the Ruhex-based system is rather likely. However, it has to be noted here, that the overall magnitude of the photocurrent is much lower for the Rubis-based system (see Figure S6, SI). In control experiments the electrodes have been prepared according to the same stepwise procedure, as explained before, but without PSI. These electrodes also exhibit cathodic photocurrents but of much smaller magnitude. The cathodic photocurrent starts at low potential, U_{ONSET} = -150 ± 16 mV vs. Ag/AgCl (see Figure 3, black curve). In order to further verify that the photocurrents of the Au-MPA/MP-Ruhex-PSI-C_{70} electrode are attributed mainly to the PSI activity, photo-action spectra have been measured. Here, it can clearly be seen that the fullerene electrodes without PSI show a minor photocurrent, which follows the absorption spectrum of the carbon nanoparticles (Figure 4, black line). In contrast, the Au-MPA/MP-Ruhex-PSI-C_{70} electrodes produce much higher photocurrents and in addition, the photo-action spectrum follows the absorption properties of PSI (Figure 4, red line).

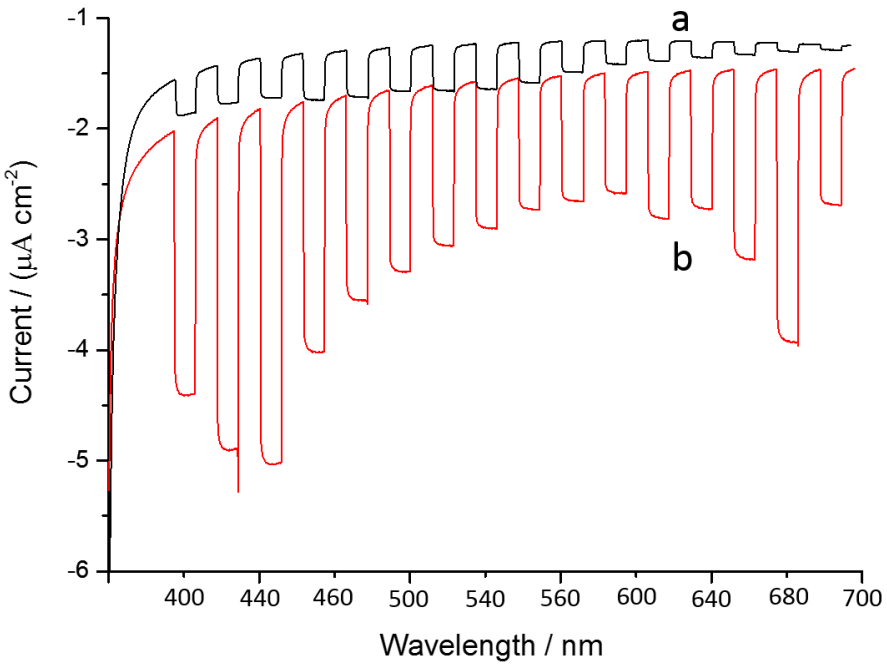

Figure 4. Photo-action spectra of Au-MPA/MP-Ruhex-C_{70} (black line) and Au-MPA/MP-Ruhex-PSI-C_{70} (red line). Applied potential -300 mV vs Ag/AgCl, buffer: 5 mM KPP pH7.

Hence, these experiments demonstrate that most of the measured photocurrent arises from the activity of the PSI. Photoamperometric experiments by varying applied potential have been performed for Au-MPA/MP-Ruhex-PSI- C70 and Au-MPA/MP-Ruhex-C70 electrodes also

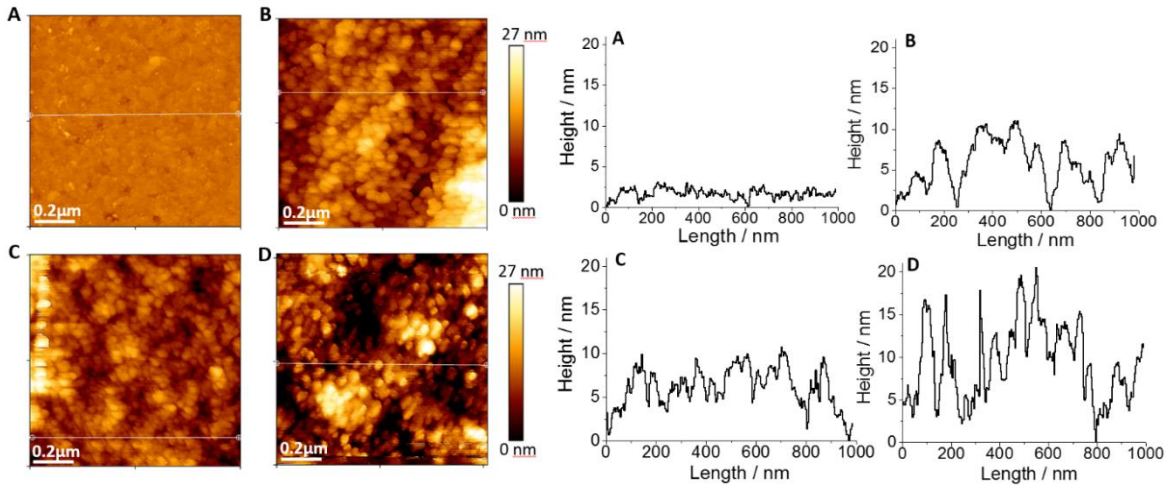

Figure 5. AFM images of PSI assembly on Au-MPA/MP and Au-MPA/MP-Ruhex surfaces. A) Gold surface, B) PSI adsorbed on MPA/MP, C) PSI adsorbed on Au-MPA/MP-Ruhex surface, D) as C) but upon addition of Fullerene C_{70}. A-D at the bottom - corresponding cross-sections.

under red light (680 nm, 9 mW cm^{-2}) illumination (chopped light voltammetry, Figure S7, SI). The curves show clear PSI excitation (red curve) and almost no excitation of the fullerene (black curve). UV-Vis absorption spectra of PSI, C_{70} and Ruhex are shown in Figure S8, SI.

Additional characterization of the photobioelectrode (Au-MPA/MP-Ruhex-PSI)

Atomic force microscopy

For direct visualization of the PSI assembled on the Au-MPA/MP or Au-MPA/MP-Ruhex surface atomic force microscopy measurements have been performed. Here, the surface of the bare gold has also been analyzed and shows only minute roughness, RMS = 0.57 nm (Figure 5, A). PSI molecules on MPA/MP (Figure 5, B) can be observed as a rather uniform layer with a higher degree of roughness, RMS = 2.81 nm. Interestingly, a PSI layer immobilized on Au-MPA/MP-Ruhex surface (Figure 5, C) does not look much different from a PSI layer assembled on Au-MPA/MP surface, RMS = 2.28 nm, although QCM and photoamperometric experiments have indicated a higher PSI amount. It can be explained, that the coverage difference is not obvious enough for a direct visualization by this method. Upon addition of fullerene to the electrode (Figure 5, D) the surface height is slightly increased (Figure 5, D), also roughness is increased, RMS = 4.43 nm, pointing to an immobilization of fullerene not only in between PSI and the electrode but also on top of PSI layer.

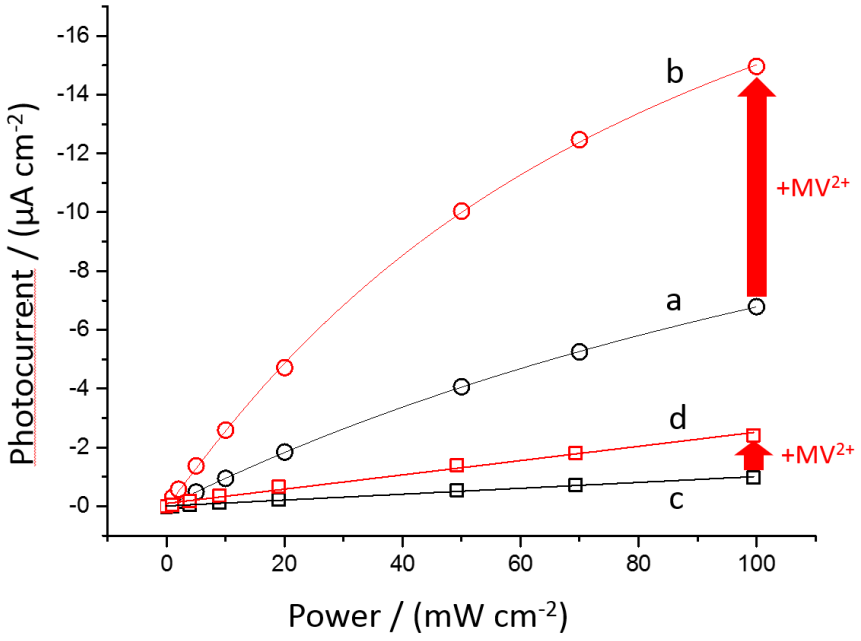

Figure 6. Photoamperometric measurements of an Au-MPA/MP-Ruhex-PSI-C_{70} (a,b) and Au-MPA/MP-Ruhex-C_{70} (c,d) electrode. a) and c) – in 5 mM KPP buffer, pH 7; d) and b) – in 5 mM KPP buffer, pH 7, + 1 mM MV^{2+}. Measurements have been performed at constant applied potential, U= -0.3 V vs. Ag/AgCl with a white light source (20 s pulses) at different intensities (1-100 mW cm^{-2}).

Light intensity variation

We have further investigated the system by evaluating the dependence of the photocurrent on the applied light intensity. The results demonstrate that photocurrent generation starts already at low intensities and that in the range up to 100 mW cm^{-2} no saturation can be observed (Figure 6, a).

Methyl viologen influence

In order to understand whether the photocurrent generation is limited by electron withdrawal at the stromal side of PSI, photocurrent behavior has also been tested upon addition of the well-known electron scavenger, methyl viologen, MV^{2+}. In our system O_2 can accept photo-excited electrons from the F_B cluster of PSI. However, many studies have showed that MV^{2+} can enhance the rate of PSI oxidation at the stromal side.[128, 143, 144, 413] Recently, the mechanism for this process has been discussed and complex intermediates between oxygen and MV^{2+} have been proposed.[134] Upon introduction of MV^{2+} in our system, almost a 100 % enhancement of the cathodic photocurrent can be observed (Figure 6, b). This finding demonstrates that the electric communication between the luminal side of PSI and the electrode surface is not limiting the whole process. Control experiments with methyl viologen

with (Figure 6, *a* and *b*) and without PSI (Figure 6, *c* and *d*) verify again the dominating role of PSI in photocurrent production. Additionally, the influence of methyl viologen on performance in terms of IQE has been verified (Figure S9, SI).

Stability investigation

For stability assessment of the system, photoamperometry at constant potential and prolonged illumination has been employed. Here, after 30 min of continuous illumination with white light (50 mW cm^{-2}) the system retains about 80 % of its original performance (Figure 7). An evaluation of the quality of this performance is not trivial since data in the literature are often not given. For a system based on redox polymers [392, 414] the photocurrent droped to 25 % of the nominal photocurrent magnitude after 30 min of continuous illumination at 40 mW cm^{-2}.

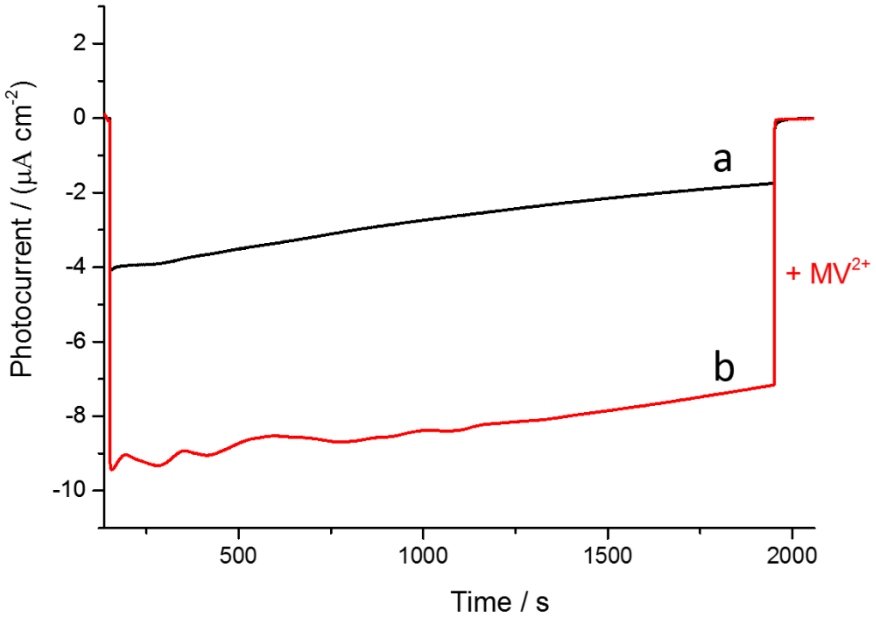

Figure 7. Photoamperometric measurement of an Au-MPA/MP-Ruhex-PSI-C_{70} electrode at constant applied potential, U=-300 mV vs. Ag/AgCl illuminated continuously for 30 min with a white light lamp, 50 mW cm^{-2}. Experimental conditions: 5 mM KPP buffer, pH 7. a) KPP buffer, b) after addition of 1 mM MV^{2+}.

For a photobioelectrode based on cytochrome *c* more than 85 % could be retained after 3min for one configuration and after 30 min for another electrode type (at 20 mW cm^{-2}). In other study [154] photocurrent stability has been assessed also upon illumination period of 30 min (1.4 mW cm^{-2}) and preserved 60 - 70 % of the nominal photocurrent magnitude. Although these data give not a comprehensive picture they may indicate that with the present system a re-sonable stability has been obtained.

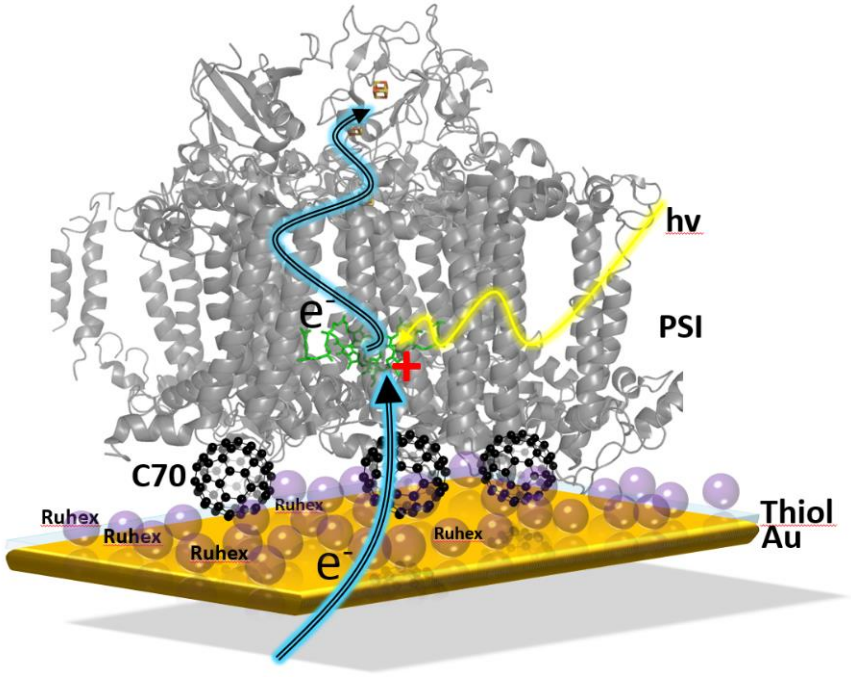

Figure 8. Schematic illustration of the construction of an Au-MPA/MP-Ruhex-PSI-C_{70} electrode and the main electron transfer pathway (blue arrows) from the electrode through the surface modification towards TGA-C_{70} (black) and then to the oxidized reaction center in PSI (green) further through the photoactive complex to the terminal F_B cluster at the stromal side and finally to oxygen in solution. Yellow arrow represents the incoming light, transparent blue layer on Au-plate represents MPA/MP-layer, Ruhex is represented as violet marbles.

Electron transfer pathways

In Figure 8 the suggested electron transfer pathway in our system is illustrated and might be simplified to the following sequence: electrode→C_{70}→P_{700}^+→(intramolecular)F_B→oxygen. First, upon illumination a charge separation occurs in PSI. The generation of a photo-excited electron and a positive hole, P_{700}^+, leads to driving force towards reduction of the hole. Now, the hole in PSI needs to be re-stocked with electrons and this can occur by the electrode via C_{70}, introduced into the system as back-filling material. Since C_{70} is a very small nanoparticle, it can freely accommodate between the PSI and the electrode, and thus, the probability that it comes in close contact to the buried P_{700} – centre on the one hand and the electrode surface on the other, is increased. The P_{700} reduction is followed by subsequent intramolecular ET steps inside the PSI molecule resulting finally in reduction of the stromally-located F_B cluster and subsequently electron transfer to oxygen. It has to be mentioned here that fullerenes can also interact with light resulting in charge carrier formation. However, this process contributes to the photocurrent generation only to a minor extent.

Performance with respect to existing systems

For every new developed system it is important to assign it in the context of already reported electrodes. However, this is not a trivial task, since the reported results have been achieved under various experimental conditions, such as buffer (molarity, kind of ions, pH), electron donors, wavelength of incident light, applied potential, light intensity a.o. Furthermore, experimental details of interest are not always mentioned. In the work of Gunther *et al.*[166] PSI has been immobilized on graphene and produced 550 nA cm^{-2} photocurrent. The onset potential was around 0 mV vs. Ag/AgCl. A very good performance has been achieved in the study of LeBlanc *et al.,*[167] where a mixture of graphene oxide and PSI has been deposited on p-doped silicon. This system produced ca. 150 µA cm^{-2} photocurrent, however, the contribution from Si-GO was ca. 60 µAcm^{-2} and the photocurrents have been generated by applying a rather negative potential. The onset potential was -300 mV vs. Ag/AgCl. A high performance (135 µA cm^{-2}) has also been achieved on modified graphene,[415] where rather negative overpotentials have been applied and the onset potential was around 0 vs. Ag/AgCl. In the work of Efrati *et al.* a redox-active pyrroloquinoline quinone (PQQ)-wired PSI has generated about 20 nA (area n.a.) of cathodic photocurrent.[149] Another approach for wiring of PSI with electrodes has been accomplished by the use of cytochrome *c*. Such electrodes yielded photocurrent of 2 µA cm^{-2}.[150] However, photocurrents of up to 150 µA cm^{-2} have been achieved when this system has been transferred to a 3D electrode, which allows for high loadings with PSI molecules. The photocurrent onset was at around +50 mV vs. Ag/AgCl. In another study large amounts of PSI molecules have been entrapped in conductive polyaniline, thus generating ca. 5.7 µA cm^{-2}.[158] Also Nafion in combination with $Os(bpy)_2Cl_2$ has been used to connect PSI with electrodes[157] and here 2.5 µA cm^{-2} photocurrent has been reported. The onset potential, however, was at around +80mV vs. Ag/AgCl. In another strongly performing system the PSI has been entrapped in an osmium-based hydrogel.[116, 155] Here, photocurrents of ~ 100 µA cm^{-2} at 0 mV vs. Ag/AgCl have been achieved. The onset potential was about +250 mV vs. Ag/AgCl - corresponding to the formal potential of the Os-polymer. In another approach from the same group PSI has been connected to a cross-linked Os-redox polymer and photocurrents of 29 µA cm^{-2} at 0 mV vs. Ag/AgCl have been reported.[153] A more complete list of systems is given in the supporting information (table S2, SI).

Comparing our work with these studies it is obvious that the photocurrent magnitude cannot keep up with the best performing systems previously reported. However, the efficiency parameters such as IQE ~10% (Figure S9, SI) the turnover number at PSI (Te = 228 s^{-1}) and a

positive onset of cathodic photocurrent are pointing to a well performing electrode. Furthermore, the focus of this study was on the adjustment of the surface properties of the electrode in such a way that not only good PSI deposition can be ensured, but also an improved orientation with the luminal side facing the electrode. Thus, compensating photoreactions can be minimized, which results in an attractive feature of a high onset potential of the cathodic photocurrent. The study also demonstrates a new component which can be used as electrical wiring agent for photoactive biomolecules – surface modified fullerenes. Thus, the rather limited portfolio of wiring strategies in photobioelectrodes has been extended.

It has also to be stressed here, that in this study we rely on a monolayer arrangement on the surface. No attempts have been made so far for creating 3D arrangements as it is used for photobioelectrodes with higher photocurrent density reported in the literature. This may indicate that further improvements can be envisaged.

Conclusions

In this study a new strategy for an oriented immobilization of PSI molecules on electrode surfaces has been shown. For this purpose a mixed thiol layer approach has been combined with the deposition of a positively charged metal complex - ruthenium hexamine. This results in photobioelectrodes with a rather high onset potential of the cathodic photocurrent (U_{ONSET} = + 70 mV vs. Ag/AgCl) originating from a higher fraction of PSI complexes oriented with the luminal side towards the electrode. Furthermore, it can be demonstrated that carboxy-modified fullerenes can serve as electrical wiring agents for PSI improving the communication of the reaction center of PSI with electrodes. Thus, the conducting properties as well as the small size of these carbon nanoparticles can be exploited. The onset potential of cathodic photocurrents has been shifted to even more positive values (U = + 0.157 V vs. Ag/AgCl) and photocurrent densities of up to 15 µA cm^{-2} have been achieved – although only a monolayer arrangement has been used. The rather high turnover number at the PSI complex (232 $e^- s^{-1}$) additionally points to the high efficiency of the PSI-electrode contact established.

Applications for such photobioelectrodes can be seen mainly in two directions: i) in the context of solar cells, our system might serve as a cathode, which operates at positive potentials; ii) the electrode can be used as starting point for the coupling to enzymatic reactions making use of the photo-generated electrons for substrate conversion reactions.

Acknowledgements

We gratefully acknowledge the support of this research by the Bundesministerium für Bildung und Forschung BMBF, Germany (Biotechnology 2020+, projects: 03B0557A+B).

Conflicts of interest

There are no conflicts to declare.

Supporting Information

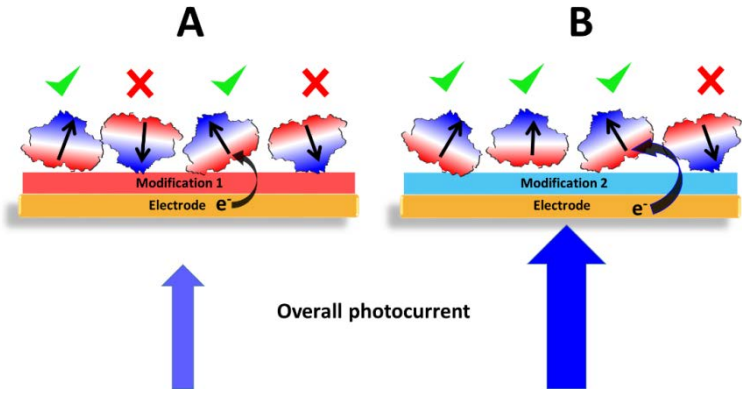

Figure S1. Schematic illustration of two types of electrode assemblies: A – PSI on SAM-modified gold, B – PSI on SAM-Ruhex-modified gold. The orientation on surface (B) is more unidirectional, and thus, leads to an enhanced overall photocurrent, whereas assembly on SAM only leads to a decreased overall photocurrent.

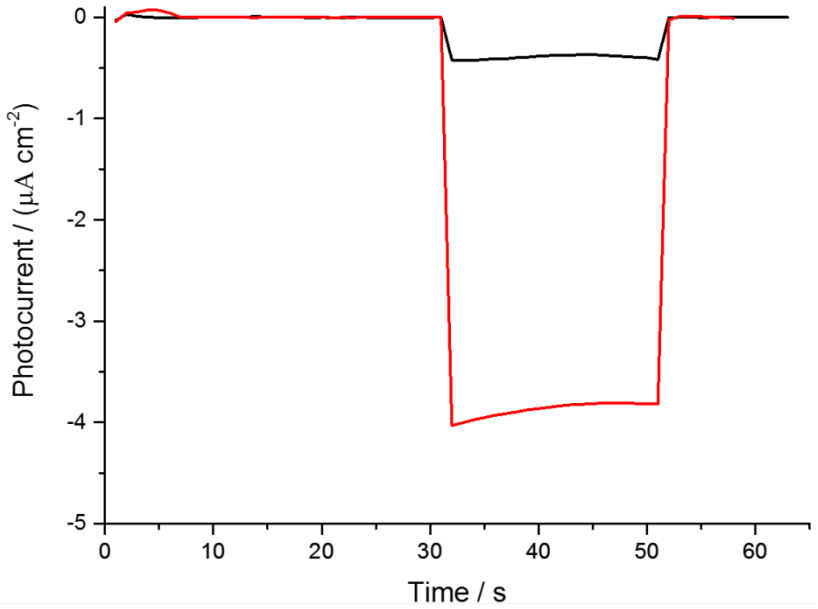

Figure S2. Photochronoamperometric experiment of an Au-Cysteamine-PSI (red) and Au-Cysteamine (black) electrode. Measurements have been performed at applied potential U = - 200 mV vs Ag/AgCl. White light 100 mW cm^{-2} illumination intensity, working buffer 5 mM KPP at pH7.

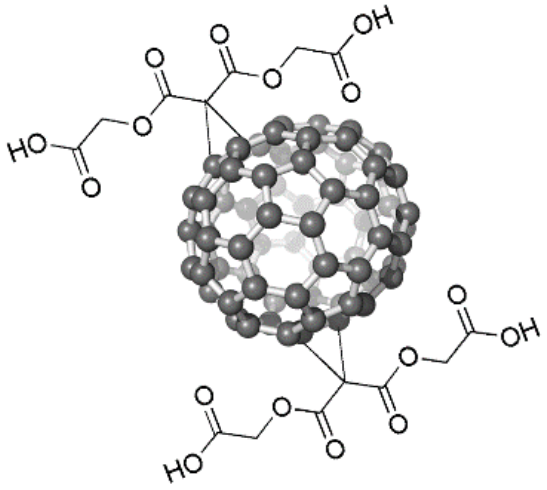

Figure S3. Schematic illustration of fullerene-C_{70}, TGA, generated with PyMol and ChemDraw Ultra 6.0

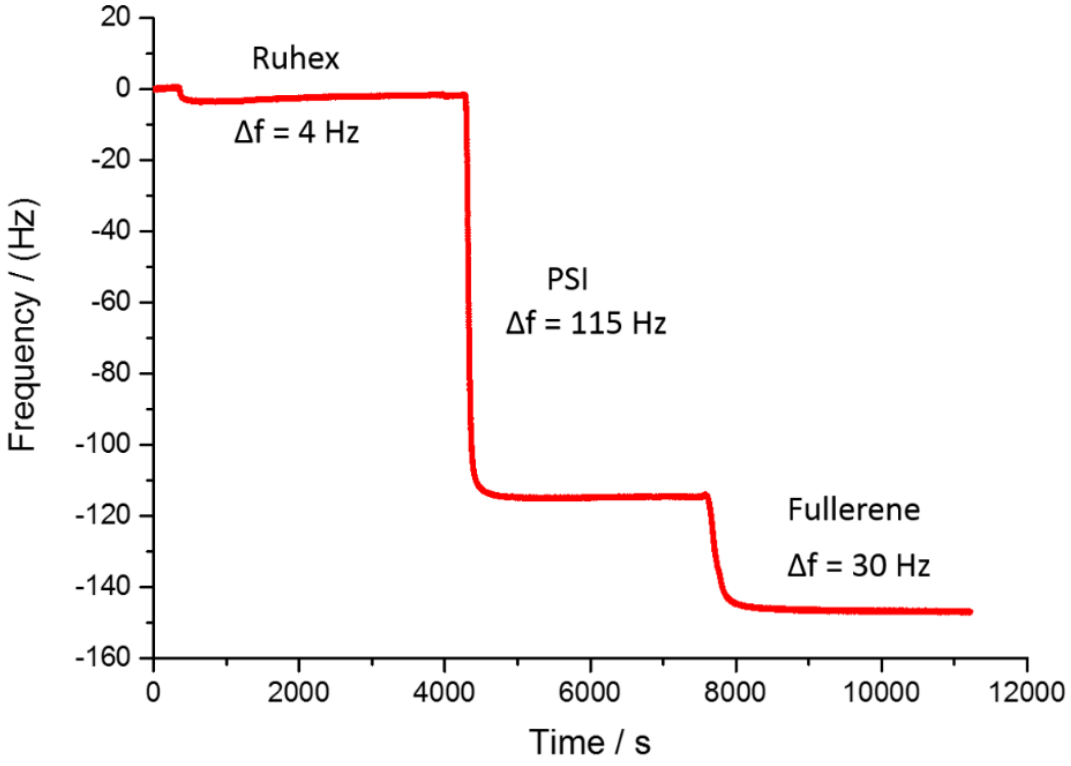

Figure S4. Frequency change (Hz) at a modified quartz chip during the deposition of Ruhex , PSI and subsequently TGA-C_{70}. Δf (Ruhex) = 4 Hz, Δf (PSI) = 115 Hz, Δf (TGA-C_{70}) = 30 Hz. The adsorption of Ruhex, PSI and TGA-C70 has been performed from solution (10 mM, 0.5 µM and 20 µM, respectively, in 5 mM KPP, pH 7.5) at 50 µl min^{-1} for 1h.

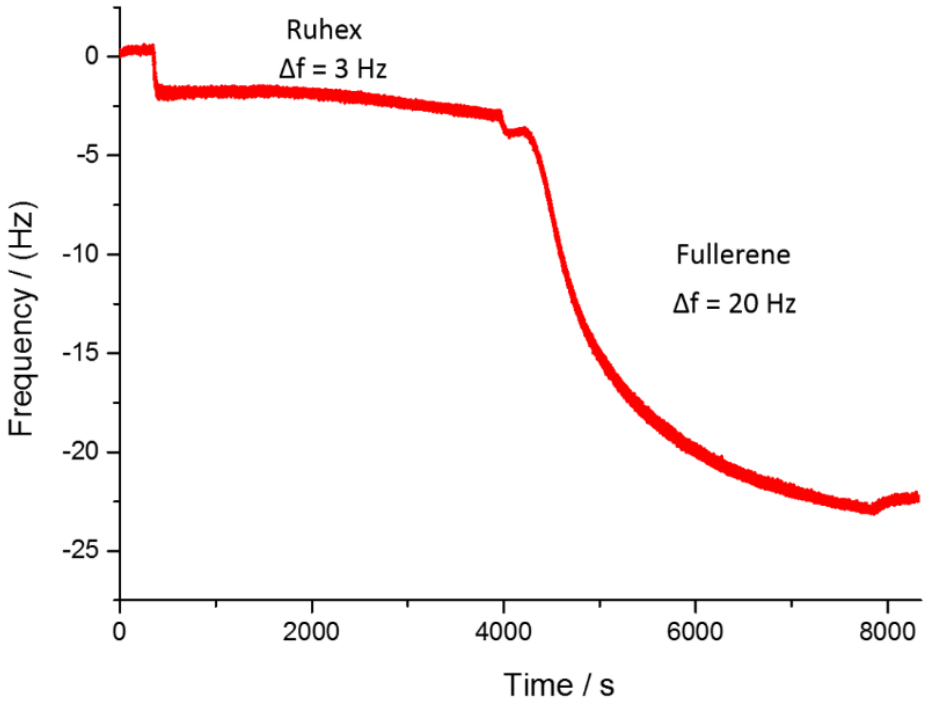

Figure S5. Frequency change (Hz) at a modified quartz chip during the deposition of Ruhex and subsequently TGA-C_{70}. Δf (Ruhex) = 3 Hz, Δf (TGA-C_{70}) = 20 Hz. The adsorption of the Ruhex and TGA-C_{70} has been performed from solution (10 mM and 20 µM respectively, 5 mM KPP, pH 7.5) at 50 µl min^{-1} for 1h.

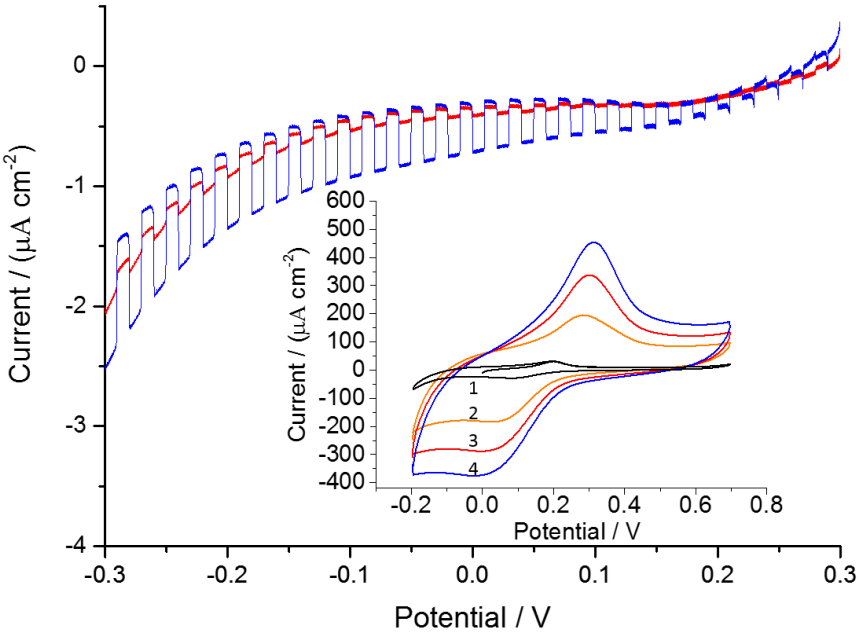

Figure S6. Chopped light experiment of Au-MPA/MP-(cis-2,2'-dichlorobis-Ruthenium)-PSI (red) and Au-MPA/MP-(cis-2,2'-dichlorobis-Ruthenium)-PSI-C_{70} (blue) electrode. Photocurrent onset is about +290 mV vs Ag/AgCl. Scanrate: 2 mV s^{-1}, white light 100 mW cm^{-2} illumination intensity, working buffer 5 mM KPP at pH7, 1 mM MV^{2+}. Inset – cyclic voltammetry of Au-MPA/MP-(cis-2,2'-dichlorobis-Ruthenium) at different scan rates: 1) 10 mV s^{-1}, 2) 100 mV s^{-1} 3) 200 mV s^{-1} 4) 300 mV s^{-1}.

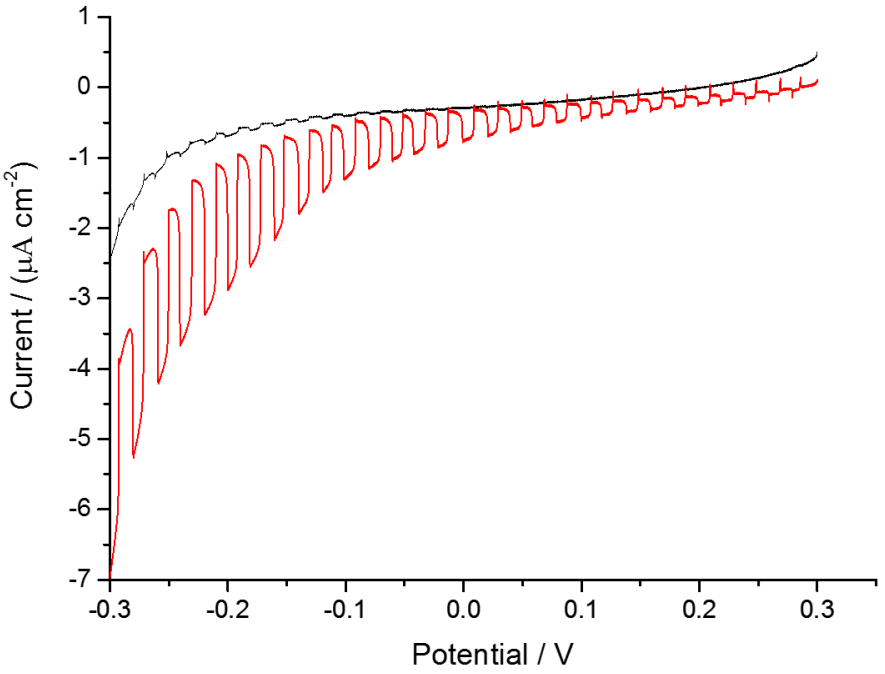

Figure S7. Chopped light experiment of Au-MPA/MP-Ruhex-PSI-C_{70} (red line) and Au-MPA/MP-Ruhex-C_{70} (black line) electrode. Scanrate: 2 mV s^{-1}, red light (680 nm) 9 mW cm^{-2} illumination intensity, working buffer 5 mM KPP at pH7, 1 mM MV^{2+}.

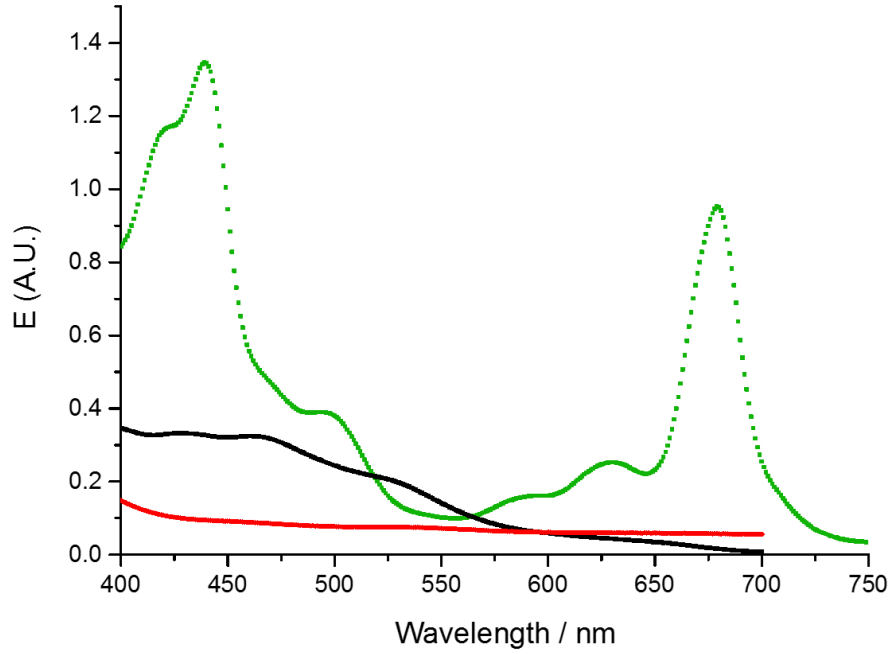

Figure S8. UV-Vis spectra of PSI (green dots), Fulleren C_{70}-TGA (black line) and Ruhex (red line). Measurements have been performed in 5 mM KPP buffer at pH7 (for PSI), ddH_2O (for Ruhex) and 5 mM KPP at pH 7.5 (for FullereneC_{70}-TGA).

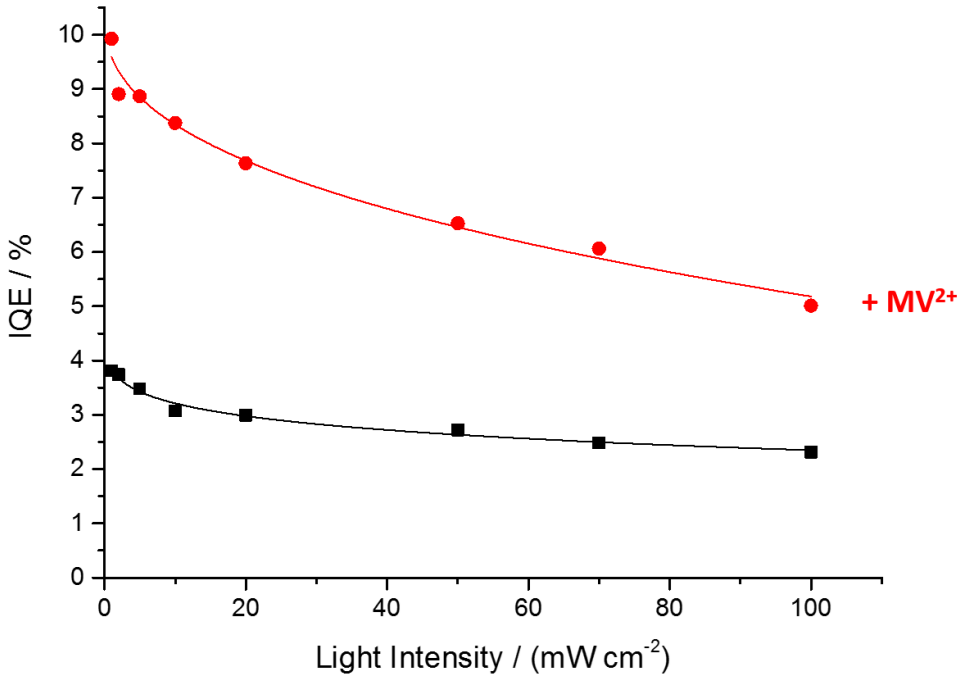

Figure S9. Plot of external quantum efficiency IQE (%) calculated vs. incident light intensity (mW cm^{-2}) for Au-MPA/MP-Ruhex-PSI-C70 system w/wo MV^{2+}.

Published in: Nanoscale. Dmitri Ciornii, Adrian Kölsch, Athina Zouni, Fred Lisdat. Precursor-approach in constructing 3D ITO electrodes for improved performance of PSI-cyt *c* photobioelectrodes. Nanoscale, 2019,11, 15862-15870. **DOI**: 10.1039/C9NR04344F._**Copyright_©_Royal_Society_of_Chemistry_2019._Link:** *https://pubs.rsc.org/en/content/articlelanding/2019/NR/C9NR04344F#!divAbstract*

4.4 Precursor-approach in constructing 3D ITO electrodes for improved performance of PSI-cyt *c* photobioelectrodes

Authors: Dmitri Ciornii, Adrian Kölsch, Athina Zouni, Fred Lisdat

Abstract

In recent years the use of photoelectrodes based on conductive metal oxides has become very popular in the field of photovoltaics. Application of 3D electrodes is holding great promises since they can integrate large amounts of photoactive proteins. In this study photosystem I (PSI) from thermophilic cyanobacterium *Thermosynechococcus elongatus* has been immobilized on 3D ITO electrodes and electrically wired *via* the redox protein cytochrome *c* (cyt *c*). The main goal, however, has been the investigation of construction parameters of such electrodes for achieving a high performance. For this, ITO electrodes have been constructed from liquid precursors resulting in improved transmission compared to previous nanoparticle-based preparation protocols. First, the doping level of Sn has been varied for establishing proper conditions for a fast cyt *c* electrochemistry on such 3D electrodes. In a second step the pore diameter has been varied in order to elucidate optimal conditions. Third, the scalability of the template-based preparation has been studied from 3 to 15 layers during the spin coating and subsequent baking step. In the thickness range from 3 to 17 µm no limitation in the protein immobilization and also in the photocurrent generation has been found. Consequently, photocurrents of about 270 µA cm^{-2} and a turnover number (Te) of 30 e^{-} s^{-1} at the PSI have been achieved. Because of the high current flow the withdrawal of electrons at the stromal side of PSI becomes clearly rate limiting. Here improved transport conditions and alternative electron acceptors have been studied to overcome this limitation.

Introduction

A special merit in photovoltaics can be surely attributed to biophotovoltaics,[416] a relatively new, but very promising emerging field. Much attention has been invested in development of photobiohybrid platforms based on photoactive natural proteins, such as photosystem I (PSI),[130, 175, 394, 417] photosystem II (PSII),[116, 418] bacterial reaction center (bRC),[419-422] but also on whole thylakoid membranes.[423-426] These photosensitive materials are capable of light-

induced charge separation, a process which enables the use of high-energy electrons for synthesis of sugars in nature and production of electric current and/or fuels in biohybrid photovoltaic devices. Particularly the very high quantum efficiency of charge-separation in these photoactive materials makes their application in photobioelectrodes so attractive.

Photosystem I (PSI) from *Thermosynechococcus elongatus* represents a trimeric photosynthetic protein which is characterized by a high theoretical turnover frequency (TOF) 10^6 e^- s^{-1} and high stability in the native system (40 h).[392, 427] This supercomplex can be considered the strongest reductant known in natural biocatalysis (E° = - 1.3 V vs. SHE),[428] however, part of the reductive strength is lost during intramolecular electron transfer across the thylakoid membrane, so that effective electron energy at the final Fe_4-S_4 cluster (F_B) results in -0.58 V vs. SHE. Taking into account, that the hole (P^+_{700}) generated in the charge separation process yields + 0.420 V vs. SHE, a potential difference between P_{700} and F_B of 1 V is produced. The reduction potential (- 0.58 V vs. SHE) is negative enough to reduce protons or CO_2, thus making PSI an attractive tool for light to chemical or light to electrical energy conversions.

Until now many studies have been dealing with the development of PSI-based photobioelectrodes.[311] At its infancy most strategies have relied on 2D arrangements, however, in recent years the expansion in the third dimension in construction of such electrodes has led to considerable enhancement of performance per geometrical area due to higher active surface area and thus, higher protein loadings. Previously several studies have reported on the use of transparent conductive oxides (TCO) for construction of 3D photobioelectrodes,[429] among them are (IO)-ITO,[84, 430-434] IO-ATO,[429, 435, 436] IO-TiO_2.[437-439] High photocurrents have been obtained in a previous study where 3D electrode architectures based on ITO nanoparticles (ITO_{NP}) have been used for integration of PSI. However, such electrodes showed low transparency when several 3D layers have been prepared as electrode.[85]

In this study a new type of 3D electrodes has been used. As basic electrode material we employ again ITO, however, we use here a new preparation procedure, a precursor-based approach, by making use of Indium and Tin precursors for synthesis of 3D-ITO instead of already prepared ITO nanoparticles. The use of liquid precursors is expected to confer more light transmission and allows additionally a fine-tuning of the doping level of ITO. In order to elucidate performance limiting factors, the parameters of the 3D PSI-based photobioelectrodes have been investigated with respect to the Sn doping level of ITO, the

pore diameter of the inverse opal structure and the number of 3D ITO layers as well as the thickness of the individual layers.

Results and discussion

3D-ITO-PSI-cyt *c*

The concept of 3D ITO electrodes with incorporated PSI and cyt *c* (3D-ITO-PSI-cyt *c*) has been developed in a previous study.[84] The system consists of a photobiological entity, PSI, a bioelectrochemical building block, cyt *c* and a signal transduction entity, the 3D-ITO electrode. Upon photoexcitation of the PSI, a hole (P_{700}^{+}) and an excited electron are generated inside PSI. Hereby, cyt *c* is acting as electrical wiring molecule, which exchanges electrons with the electrode and with PSI. The hole is immediately reduced by cyt *c* and subsequently oxidized cyt *c* is re-reduced by the electrode. The excited electron, generated by PSI, can be further transferred to an electron scavenger, e.g. oxygen. The energy diagram (Fig. 1) shows the electron flow pathway in the photobioelectrochemical system.

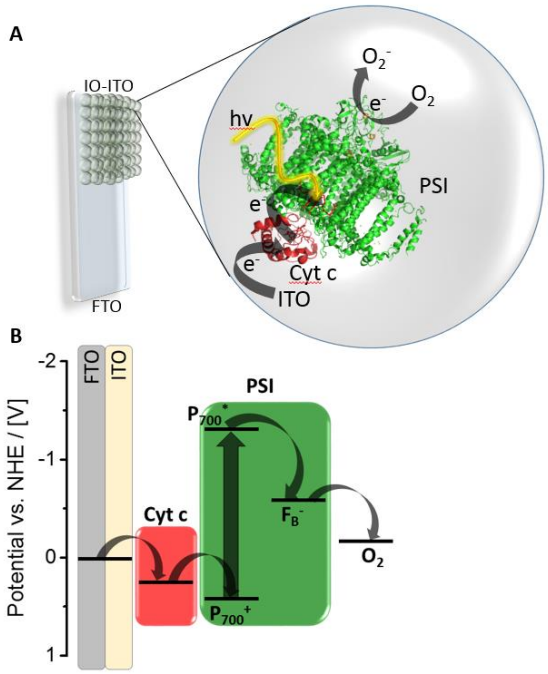

Figure 1. A - Schematic representation of 3D-ITO-PSI-cyt *c* photobioelectrodes, **B** - energy diagram of the electron flow in the system.

3D-ITO electrode preparation – nanoparticle versus liquid precursors

The 3D-ITO electrodes from our previous study were based on ITO nanoparticles.[84] Even though high photocurrents have been achieved (120 µA cm^{-2} for 6x layers of about 30 µm height),[84] limitation can appear by the strongly decreasing transmission with increasing

electrode thickness. Our intention in this study is to use the same biomolecular contact for PSI, but a 3D electrode material with enhanced transparency, higher scalability and a larger surface area per volume. This will be achieved by replacing template-based preparation method. In order to ensure scalability and ease of preparation also in this case a spin-coating procedure has been applied. First results show that 6 layers of a precursors-based electrode (for the same PSI-coverage) generate about 100 µA cm^{-2} photocurrent and are only 6 µm in height. By comparing the efficiency (Eff) of the NP-approach and precursor-approach per unit volume (Eff = I_{ph} cm^{-3}) it is obvious, that the precursor-approach is a more efficient way for photocurrent generation (Eff_{NP} = 40 000 µA cm^{-3} < Eff_{Prec} = 170 000 µA cm^{-3}). Scanning electron microscopy (SEM) investigations show that the new precursor-based approach allows to vary the thickness of the 3D electrode material simply by the number of spin coating steps prior to the thermal decomposition of the template (latex beads). Thus, scalability of the preparation method is indicated (Fig. 2). Furthermore, transmission experiments with protein-free electrodes of different layer thickness of the 3D ITO reveal a high transparency of the precursor-based preparation approach (Fig. 3). Here, even at 15 layers the transparency is still around 12 % at 440 nm and 37 % at 680 nm (relevant for PSI absorption).

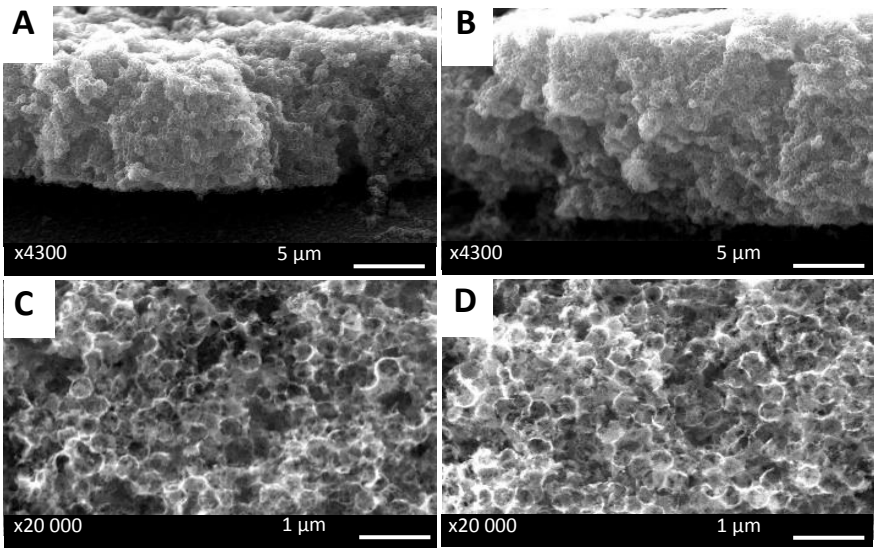

Figure 2. SEM images of as prepared 3D-ITO electrodes. **A, C** – 9x layers and **B,D** – 12x layers. **A,B** - side view and **C**, **D** – top view.

The advantageous behaviour can be even better exemplified when plotting the transmission line of a 3D electrode from the nanoparticle-based preparation protocol for comparison (Figure 4).

Based on this promising results several factors of the electrode preparation have been investigated in order to determine factors which limit overall performance.

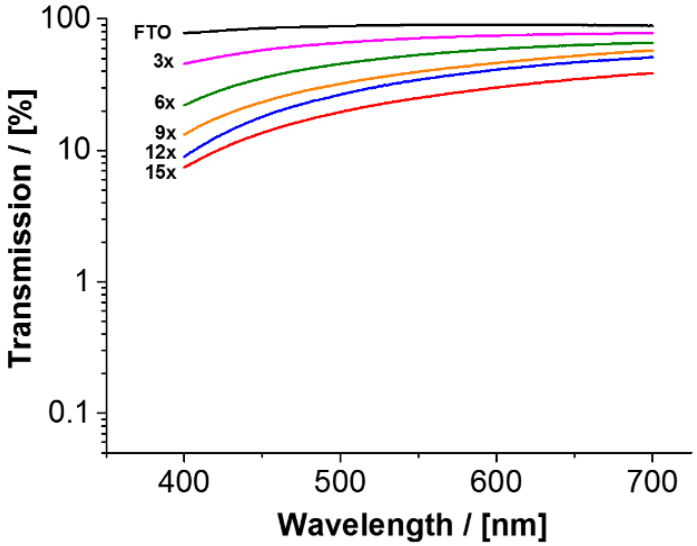

Figure 3. Transmission experiments performed for 3D-ITO electrodes for different numbers of layers (3-15 layers, 0.46 µm, 1.2 % Sn), precursor approach. Experiments have been performed with 5 mM KPP buffer, pH 7.

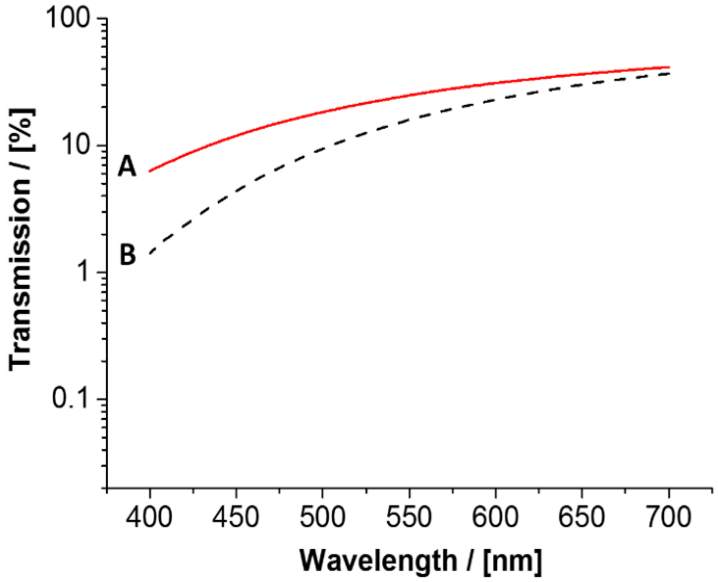

Figure 4. A - Transmission spectrum of a 3D-ITO electrode (9 layers, 0.8 µm latex beads, 10 % Sn, precursor approach, ca. 15 µm height). **B** – Transmission spectrum of 3D-ITO electrode (3 layers, 0.8 µm latex beads, 10 % Sn, nanoparticle approach, ca. 15 µm height). Experiments have been performed in 5 mM KPP buffer, pH 7. The dotted line shows the transmission of a 3D ITO electrode prepared by a nanoparticle approach for comparison according to procedure from Stieger *et al.*[84]

Variation of Sn doping level

A prerequisite for efficient performance of a photobioelectrode is a fast electron transfer between the photoactive compound and the electrode. A particularity of the PSI-cyt *c* system consists in the electron shuttle function of cyt *c*, which enables electrical wiring of the otherwise buried and difficult accessible reaction center of PSI (P_{700}) to the electrode. For maintenance of the electron flow, cyt *c* has to reduce P_{700} on one hand, and be reduced by the electrode on the other hand. The latter reaction, which is the heterogeneous electron transfer (HET) of cyt *c,* can limit the overall current flow. In previous studies it has been found that cyt *c* reacts much slower at ITO than at modified gold electrodes.[440, 441] For the nanoparticle-based ITO a ks-value of 0.5 s^{-1} has been determined.[84] Consequently, it has been first evaluated whether the new ITO preparation procedure will affect the ks value and subsequently whether the rate of HET can be influenced by the composition of the ITO material, i.e. the Sn doping level. For this, different doping levels (1.2 %, 5 % and 10 %) have been tested and corresponding heterogeneous electron transfer rate constants calculated. Fig. S7 illustrates the corresponding CV curves for 1.2 % Sn-doping level. The results summarized in Fig. 5 show a clear increase of ks values compared to the nanoparticle-based preparation (ks = 8.2 ± 2 e^- s^{-1}), however no clear tendency in ks has been observed by varying the Sn amount in the electrode material. Due to the increased ks better conditions for electron flow can be provided by the new approach in 3D electrode preparation.

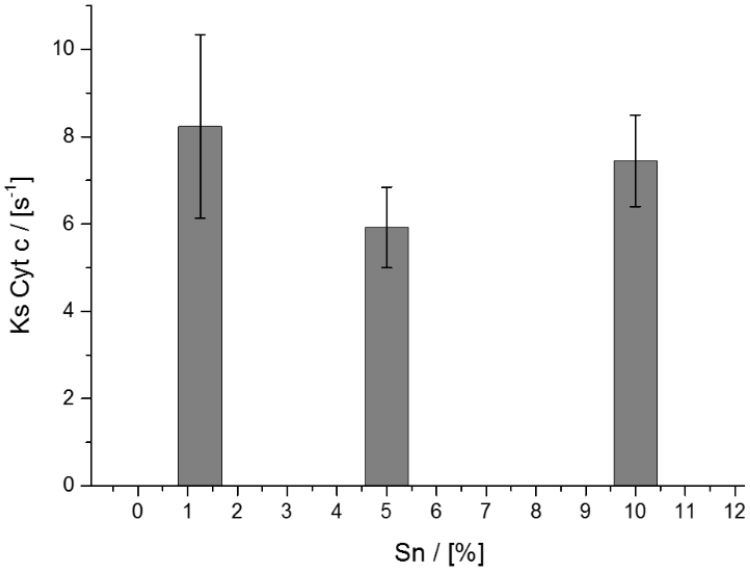

Figure 5. Plot of the heterogeneous electron transfer rate constant *ks* values evaluated for cyt *c* at 3D-ITO electrodes with different Sn doping level (1-10 %, LB diameter 0.8µm) n = 3. Experiments have been performed in 5 mM KPP buffer, pH 7 by analyzing cyclic voltammetry at different scan rates.

The idea of studying different doping levels came from studies demonstrating the influence of the Sn doping on the charge carrier behaviour in the metal oxide electrode material. Here, variations in the range from 0 to 9% were analyzed. [442-445] Most of the reports demo- nstrate good conditions in the range from 0 % - 10%, that is why in this work the adequate range has been chosen.

Cyt *c* electrochemistry is, however, mostly investigated on standard 10 %-doped ITO, thus, it is difficult to evaluate our results with the reports from the literature for each doping level. However, several studies have reported ks values for standard ITO electrodes, planar or porous, or on other conductive oxides. Runge *et al.* reported ks of cyt *c* on planar ITO electrodes ($4.0 \pm 0.5\ s^{-1}$).[446] Highest ks value on planar ITO electrode has been reported in the study of El Kasmi *et al.* ($18\ e^{-}\ s^{-1}$, 10 % Sn-doped planar ITO glass slides, sputter deposited).[447] Several other studies have reported heterogeneous rate constants for other porous conducting metal-oxide materials: ITO ($1.20 \pm 0.02\ s^{-1}$)[448], nano-sized columnar ITO ($12\ s^{-1}$),[449] mesoporous niobium oxide film ($0.28\ s^{-1}$),[450] mesoporous ATO (1.35 and $1.2\ s^{-1}$).[451, 452] Our results are in the range of reported values, but clearly show that not only the material, but also the preparation conditions will influence the actual electrochemical protein behaviour on the interface. This is in correlation with studies showing the effect of diminished charge carrier transport in systems with numerous boundaries between nanoparticles[453] or the effect of rotational mobility of cyt *c* at electrode surfaces for fast heterogeneous electron transfer.[448] Here obviously better conditions can be provided when the electrode is prepared from liquid precursors instead of nanoparticles, but a detailed mechanistic study is beyond the scope of the present investigation.

Variation of LB diameter

As a second parameter the diameter of the latex beads used during the template-based preparation protocol has been varied in order to study the influence of different pore structures on the photoelectro-chemical performance of electrodes with PSI and cyt *c*. Here the focus is on the effect of the cavity diameter on the protein loading and consequently the photocurrent production. We have chosen 0.1, 0.46, 0.8, 1.1 and 3.0 μm diameter LBs and measured photocurrents for a 6 layer arrangement. The range of variation in LB diameter has been intended to provide a macroporous structure, which would allow the trimeric PSI to penetrate into the volume of the electrode body. Based on our previous findings we have proceed with 1.2 % Sn doping for all following experiments. SEM studies show that character

of the 3D structure with different cavity diameter can be retained while varying the LB diameter during the template-based electrode construction (see Fig. S8). Results of the functional characterization of these electrodes clearly verify that the photocurrent amplitude differs for the different preparations and is highest for electrodes built from latex beads with a diameter of Ø = 0.46 µm (Fig. 6, A, black line).

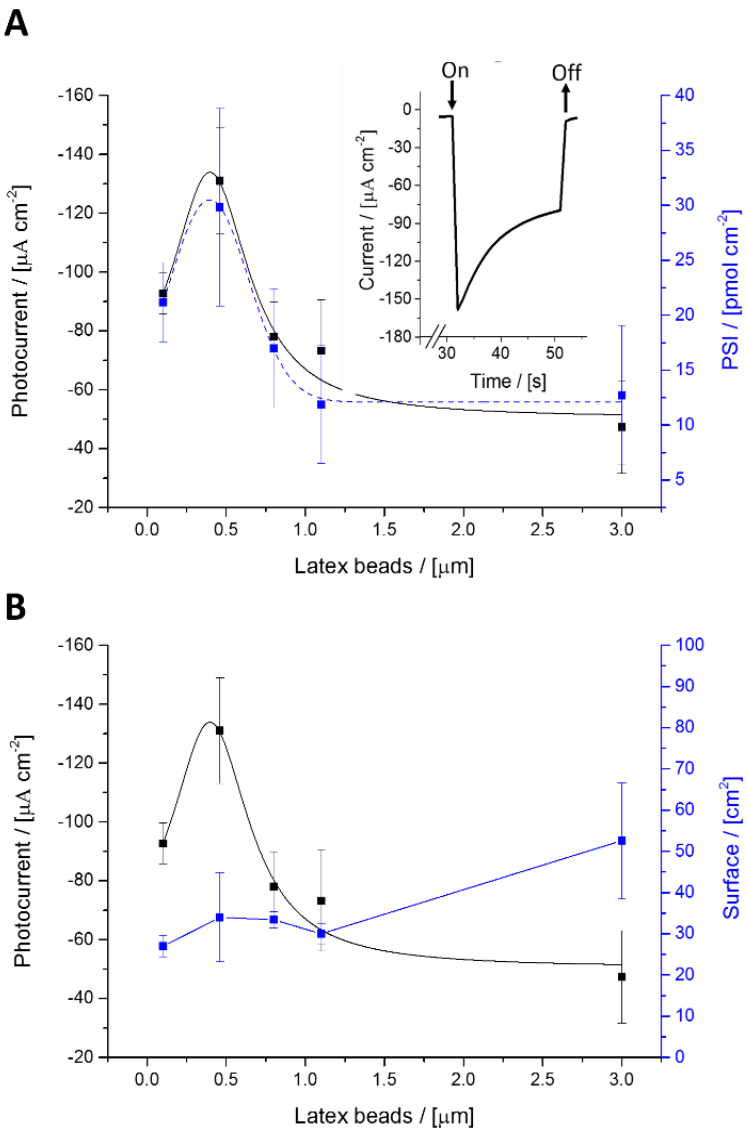

Figure 6. Dependence of parameters of 3D ITO-PSI-cyt *c* electrodes on the diameter of the latex beads used during the preparation of the basic electrode structure. **A**, black line – plot of photocurrent vs LB diameter, blue (dashed line) - correlation between PSI amount and photocurrent for different latex beads diameters. **A**, **inset** - time course of the photocurrent measurement for electrodes prepared with 0.46 µm latex beads. **B** – dependence of the photocurrent and the electro-active area (as analyzed by cyclic voltammetry) on the diameter of latex beads used during the preparation of the 3D ITO (6 layer arrangement), applied potential U= - 0.2 V vs Ag/AgCl, illumination intensity 100 mW cm^{-2}, working buffer: KPP, 5mM at pH 7.

When the amount of immobilized PSI is analyzed for the different electrodes (by extracting PSI with 80 % acetone, according to the Porra protocol),[405] it can be shown that electrodes prepared with 0.46 µm latex beads result in the highest PSI amount. These experiments are suggesting that the higher photocurrents can be attributed to a larger amount of integrated PSI inside the 3D structure (Fig. 6, A, blue dotted line). Surprisingly, there is not a clear tendency when the electro-active electrode area for the different preparations is evaluated from voltammetric scans in buffer (Fig. 6, B, blue line). So the electrode structure prepared from 0.46 µm beads provides better conditions for PSI immobilization compared to smaller and larger bead diameter. Interestingly, in the study of Fang *et al.*, where PSII has been integrated within 3D ITO (10 nm ITO nanoparticles, 3µm latex beads have been compared to 0.75 µm latex beads), higher protein loadings have been achieved for the structures with smaller pore diameter ($\Gamma(PSII)_{0.75\mu m} > \Gamma(PSII)_{3.0\mu m}$). This is in agreement with our study when comparing 3µm with 0.8µm or 0.46µm. The authors postulated that electro-active surface area determined from capacitance measurements "cannot be completely translated into capacity for binding proteins".[433] This postulate can be supported by our study, although the range of the pore structure is different due to the different material (liquid precursors) and different proteins.

Variation of the number of layers

Next, the number of layers deposited by spin coating of the mixture of latex beads and liquid precursors before the final baking step has been varied from 3 to 15 layers. Here, 1.2 % Sn doping and 0.46 µm LBs have been used. Analysis of the structures by means of SEM reveals an increase in height of the 3D structures which follows the number of spin coating steps (Fig. 7, A, blue line). The height of precursor-based structures reaches solely about 17.6 ± 0.3 µm at 15 layers. In contrast, in the NP-based approach 17 µm correspond to about 3.5 layers, underpinning that the new system results in less volume per layer. Investigations of the electro-active surface area of such 3D electrodes show that this area correlates linearly with the height of the structure (Fig. 7, A, black line). This means that with increasing number of layers and height of the structure, the increased electrode surface area is also accessible for the solvent. For the 15-layer arrangement an area of ca. 94 ± 9.5 cm^2 is solvent accessible (Fig. S1, blue dashed line). Photoamperometric experiments with these electrodes of different thickness and incorporated PSI and cyt *c* exhibit a linear correlation of the photocurrent magnitude with the number of layers, which points to a good scalability of the system (Fig. 7,

B). Moreover, the large surface area is available to PSI and cyt *c* molecules. This has been demonstrated by analyzing the amount of integrated proteins (Fig. 7, C, D). Here, the cyt *c* amount has been determined from cyclic voltammetric experiments and the PSI amount by the Chl *a* extraction procedure (*see experimental*). Photocurrents of ca. 270 ± 26 µA cm^{-2} could be achieved by an electrode of 15 layers (corresponding to about 17.6 µm in height). It has to be added here that with a 15-layer electrode also the influence of the PSI concentration used during preparation on the photocurrent output has been analysed.

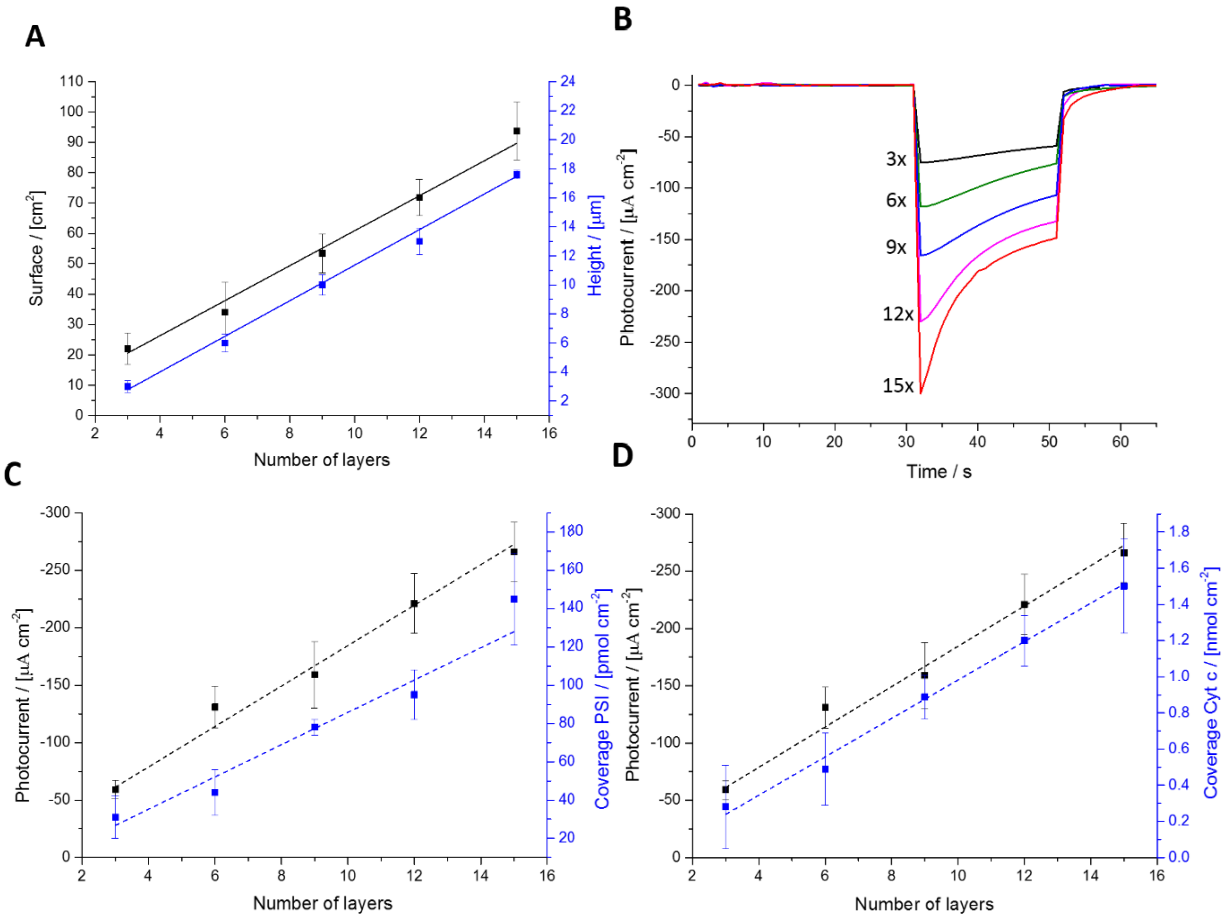

Figure 7. Photocurrents of 3D ITO-PSI-cyt *c* electrodes prepared with varying number of layers during ITO preparation, A – correlation of the surface enlargement (with respect to flat FTO) and height of the structures to the number of layers deposited by spin coating prior to the final baking step, B – photocurrent behaviour of the photobioelectrodes prepared with a different number of spin coating steps, C - correlation between photocurrent and PSI coverage for electrodes prepared with a different number of spin coating steps, D - correlation between photocurrent and cyt *c* coverage for the electrodes prepared with a different number of spin coating steps. (Experimental conditions: 5mM KPP pH7, air saturated, U = - 0.2 V vs Ag/AgCl, illumination intensity 100 mW cm^{-2}).

These results are shown in Fig. S9. It becomes obvious, that higher PSI concentrations are beneficial for higher loading, but at a certain concentration the photocurrent cannot be further enhanced. By following the photocurrent with time during the illumination period it becomes obvious, that a current limiting process occurs. The photocurrents of such electrodes show a depletion behaviour (Fig. 7, B). The effect is more pronounced for thicker electrode structures compared to thinner ones (Fig. 7, B).

However, experiments with a stirred solution during illumination show that the degradation of the photocurrent with time can be almost prevented (Fig. 8, A, dotted line). Although by stirring only the external mass transfer can be improved, this results in much better oxygen availability inside the 3D structure. The enhanced transport conditions for the electron acceptor used so far result in a more stable kinetics of the photocurrent (although disturbances by the stirring can also be seen in the experiment). Oxygen is however, not the best electron acceptor for PSI and in addition, its concentration in an aqueous solution is limited. In order to exploit a better electron uptake from the excited photosystem and subsequently circumvent limitations from the stromal reaction at PSI, several strategies have been developed. For example, quinone molecules can act as reaction partners of bacterial reaction centres.[419, 422] It has also been demonstrated that quinone molecules can serve as electron sink for PSI.[454] In order to show that really the electron withdrawal at the stromal side is an important limiting factor in photocurrent generation, experiments with added water-soluble ubiquinone Q_0 (2,3-dimetoxy-5-methyl-parabenzoquinone) have been performed. Here one can make use of much higher concentrations compared to oxygen (2 mM instead of 220 µM). It has been found that the photocurrent in a non-stirred solution is significantly more stable (Fig. 8, B dashed blue line). The photocurrent, however, is not enhanced by quinone addition which means that now other processes become limiting, but the decrease by the depletion of the electron acceptor can be circumvented in the time frame of the experiment. Almost no reaction of Q_0 at the 3D electrode could be observed in the potential and concentration range used in electrochemical experiments (Fig. S2, red line).

Stability experiments

Stability of bioelectrodes represents a crucial issue, since a system which preserves its functionality during repeated excitation events is of more interest for potential applications. In this study we have investigated the stability of the 3D-ITO-PSI-cyt *c* electrodes during repeated excitation with light pulses. Results show that the system generates higher

photocurrents over 20 short light pulses when an additional electron scavenger Q_0 is present in solution also upon continuous illumination over 30 minutes (Fig. 9). Here photocurrents of

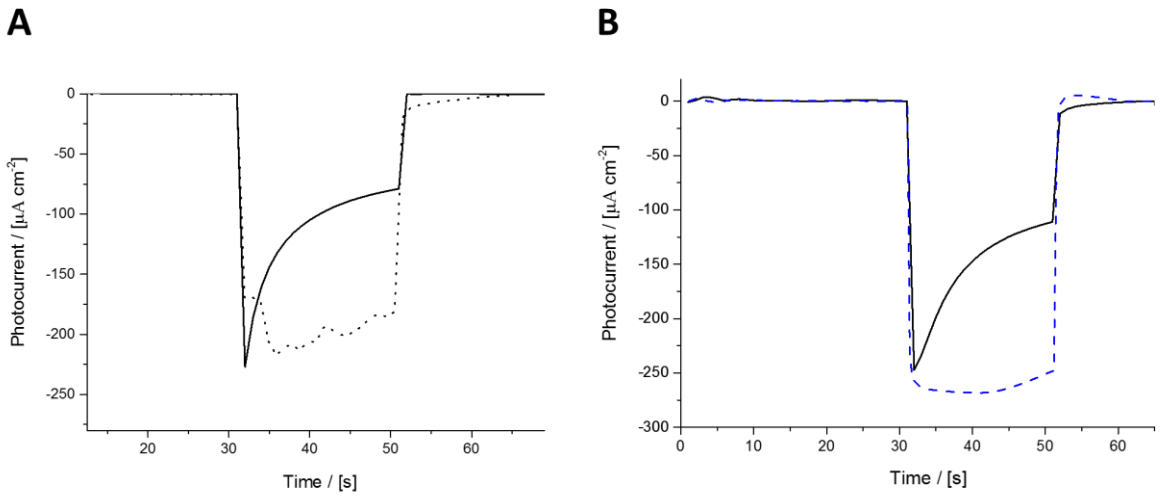

Figure 8. A - Photoamperometric experiment of a 3D-ITO_{12x}-PSI-cyt c electrode. Measurements have been performed in a 5mM KPP buffer, pH7, at applied potential U= - 0.2 V vs Ag/AgCl and an illumination intensity of 100 mW cm^{-2}. The black line shows the result in a non-stirred solution, whereas the dotted line represents the photocurrent of the same electrode in a stirred solution. B - Photoamperometric experiments of a 3D-ITO_{15x}-PSI-cyt c electrode with (blue dotted line) and without Q_0 (black line) in solution. Measurements have been performed in 5mM KPP buffer pH7. Concentration of Q_0 is 2mM, the applied potential U= - 0.15 V vs Ag/AgCl and illumination intensity 100 mW cm^{-2}.

about 100 µA cm^{-2} can be retained. Control experiments without Q_0 reveal a rather fast photocurrent depletion. This is caused by the depletion of oxygen insidethe 3D electrode, but might be also caused by the production of reactive oxygen species upon reduction of molecular oxygen. These species may attack the PSI as discussed in a recent study.[454] Another reason for photocurrent degradation can be seen in the detachment of proteins from the ITO surface during operation. This can be deduced from voltammetric scans evaluating the immobilized electro-active cyt *c*, which show a decrease of about 40 % after such illumination experiments (after 20 pulses). In conse-quence, one can state that more work for the stable integration of proteins into the 3D electrodes seems to be necessary. It can however, also be concluded, that the usage of high energy electrons for oxygen reduction is only an intermittent approach in research of photobioelectrodes and better performance can simply be obtained when these electrons are converted to useful products and thus, degradation reactions by reactive species can be avoided.

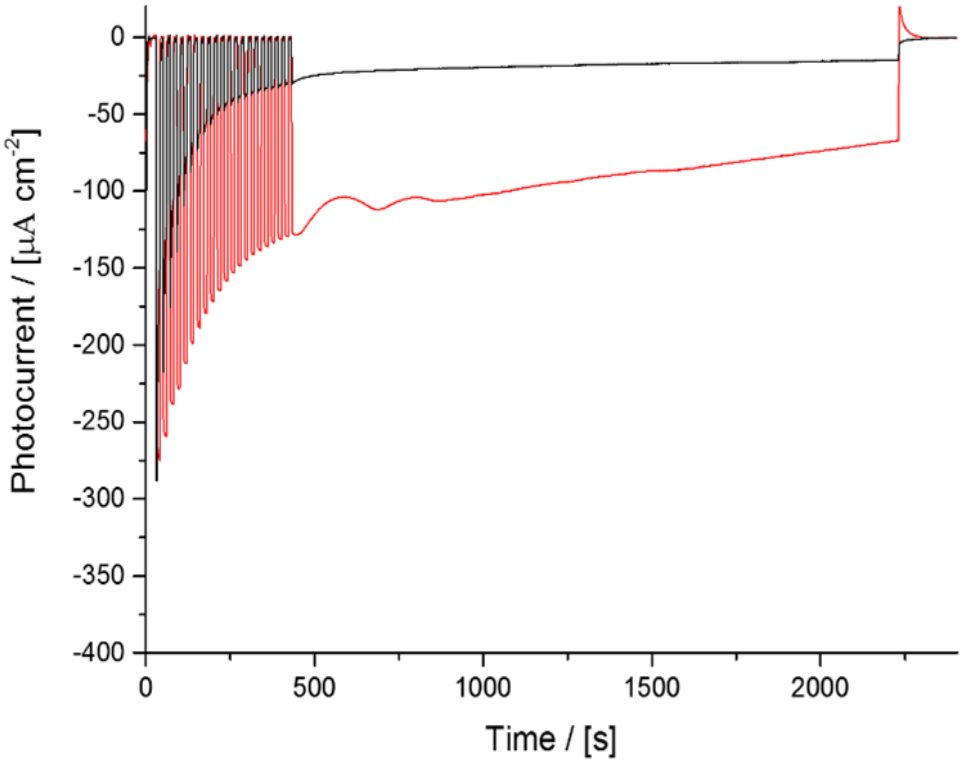

Figure 9. Photoamperometric experiments of a 3D-ITO$_{15x}$-PSI-cyt *c* electrode with repeated short light pulses (20 s) and a continuous illumination for 30 min. The black curve shows the result in air-saturated buffer and the red curve the result with added Q_0 (2 mM). Measurements have been performed in non-stirred 5 mM KPP buffer pH 7 at an applied potential U = - 0.15 V vs Ag/AgCl, and an illumination intensity of 100 mW cm^{-2}.

Conclusions

In this study an improved method for the preparation of 3D ITO electrodes has been investigated with respect to its potential in the photobioelectrochemistry of photosystem I. Here the redox protein cyt *c* has been used as a wiring agent between the electrode surface and PSI. Several parameters of the construction process of 3D ITO- electrodes have been varied and performance parameters of the resulting ITO-PSI-cyt *c* electrodes have been analyzed. The Sn doping level of ITO, the LB diameter and thus, the cavity diameter in the 3D electrodes and finally the electrode thickness have been changed to elucidate limiting factors and establish best conditions for preparation. The results show that highly transparent electrodes with a high surface area can be prepared when liquid precursors are used during the template-based preparation protocol. Higher ks values for the HET of cyt *c* have been found at these electrodes. By varying the cavity diameter of the 3D ITO best conditions for PSI incorporation have been found for latex beads of 0.46 µm diameter. The layer thickness of the electrodes can easily be controlled by the number of spin coating steps of the latex

bead/liquid precursor mixture. By increasing the number of layers the photocurrent can be enhanced without any limitation, thus photocurrent densities of about 270 µA cm^{-2} can be achieved for a 15-layer electrode of about 17.6 µm height. This illustrates the good scalability of the system. Compared to previous approaches with 3D ITO from this study, here a much better efficiency per electrode volume can be achieved. Furthermore, it can be shown that by addition of a non-natural electron scavenger, Q_0, the rate of electron withdrawal from the stromal side of PSI can be enhanced and stability of the photocurrent can be improved.

Experimental

Materials and chemicals

Indium(III) isopropoxide (IIP) (99 % purity, 5 % w/v, in isopropanol solution), Tin(IV) isopropoxide (TIP) (99 %, 10 % w/v), 2,3-dimethoxy-5-methyl-1,4-benzoquinone (Q_0) have been purchased from Alfa Aesar (Germany). Fluorine-doped tin oxide-coated glass slides (FTO, 7 Ω cm), polystyrene latex beads (LB), 10 %, aqueous solution), Methyl Viologen (MV^{2+}) and cytochrome *c* (form horse heart) have been purchased from Sigma Aldrich (Germany). K_2HPO_4 and KH_2PO_4 have been purchased from ROTH, Germany. In all experiments ultrapure H_2O has been used (SG Ultra Clear UV plus, Netherlands).

Isolation of Photosystem I from *T. elongates*

Trimeric photosystem I (PSI) has been extracted and purified from cyanobacterium *T. elongatus* according to previously described procedure.[328] Purification of PSI fraction has been performed by ion exchange columns as previously described.[455]PSI trimers have been crystalized by applying buffer A (5 mM MES- NaOH, pH 6.0 and 0.02 % n-dodecyl-β-maltoside (β-DM), 4 °C). After a concentration of 5 mM $MgSO_4$ has been reached, the crystals have been centrifuged (5 min, 4 °C, 4000 x g) and washed in buffer A. Further, PSI-crystals have been resolubilized in buffer B (5 mM MES-NaOH, 0.02 % β-DM, pH 6.0, 30 mM $MgSO_4$) and recrystalized. For photoelectrochemical experiments PSI-crystals have been washed 4 times in 5mM MES buffer, pH 6, 4°C, at 10 000 rpm, for 3 min and the pellet dissolved in 100 mM potassium phosphate (KPP) buffer, pH 8. Functionality of the as-prepared PSI-crystals has been assessed. Here, a light-driven electron transport from cytochrome *c* (Sigma Aldrich) to methyl viologen Hansatech, King's Lynn, UK). Oxygen consumption rates were 1640 ± 80 µmol O_2 h^{-1} mg^{-1} *Chl a*.

Preparation of 3D-ITO electrodes

FTO slides have been cleaned in acetone, isopropanol and ethanol in an ultrasonication bath for 20 minutes each step. 3D-ITO electrodes with Sn doping level (1.2, 5 or 10 %) have been prepared by spin coating 8 µl per layer of a LB-IIP-TIP-mixture onto FTO slides (rotating velocity 80 rps). The final mixture composition is 50 mg ml^{-1} latex beads, 50 mg ml^{-1} IIP precursors and varying concentration of the doping material, 0.75 to 6 mg ml^{-1} TIP precursors (corresponding to 1.2 to 10 % molar ratio). Before the latex beads have been washed: 100 µl of aqueous solution of latex beads has been incubated with 1 ml ethanol and centrifuged at 16 400 rpm, 4°C for 8 min. The supernatant has been discarded and the pellet resuspended in 1 ml ethanol in the ultrasonication bath. The LB dispersion has been centrifuged again as described above. Finally, the pellet has been resuspended in the isopropanol solution of precursors by ultrasonication for 1 min. The as-prepared LB/IIP/TIP-mixture has been directly used for spin coating. After depositing the desired number of layers the electrodes have been sintered at 535° C for 2 h.

Preparation of 3D ITO-PSI-cyt c electrodes

First, 1 µl of 30 µM PSI solution has been allowed to incubate for 2 min on 3D-ITO electrode (surface area 0.031 cm^2). After careful washing in KPP buffer (5 mM, pH 7) 2 µl of 1 mM cyt *c* solution have been allowed to incubate for 2 min. For the electrodes with increased number of layers, i.e. > 9 layers, 2 µl PSI (90 µM) and 3 µl cyt *c* solution have been used and incubation time has been increased from 2 to 3 minutes, in order to allow a complete penetration of the multi-layered material with biomolecules.

Protein concentration determination

Amount of immobilized PSI has been assessed by a chlorophyll *a* extraction protocol after a previously published procedure.[43] FTO-ITO-PSI-cyt *c* electrodes have been incubated in 1 ml 80 % acetone for 30 min followed by absorption measurements of the supernatant. Measurements have been performed in a wavelength range between 400 – 700 nm, at UV-Vis spectrometer Varian (Shanghai).

Electrochemical and photoelectrochemical experiments

All measurements have been performed at the photoelectrochemical workstation, Zennius from Zahner (Germany), in 5 mM KPP buffer at pH 7, using a Pt counter electrode and an

Ag/AgCl, 1 M KCl reference electrode in a home-made photoelectrochemical cell. Cyclic voltammetry has been employed for the evaluation of cyt *c* coverage (scan rate 0.03 V s^{-1}) and for the determination of *ks* values of cyt *c* (scan rates 0.01 - 1 V s^{-1}) according to the method of Laviron.[456]

Scanning electron microscopy

Scanning electron microscopy experiments have been performed for 3D electrodes with different number of layers (3 – 15 layers) at JSM-6510, JEOL (Japan) by applying 30 kV acceleration voltage.

Conflicts of interest

There are no conflicts to declare.

Acknowledgements

We gratefully acknowledge the support of this research by the Bundesministerium für Bildung und Forschung BMBF, Germany (Biotechnology 2020+, projects: 031B0557A+B).

Supporting Information

Precursor-approach in constructing 3D ITO electrodes for improved performance of Photosystem I-cyt *c* photobioelectrodes

Dmitri Ciornii*, Adrian Kölsch, Athina Zouni, Fred Lisdat*

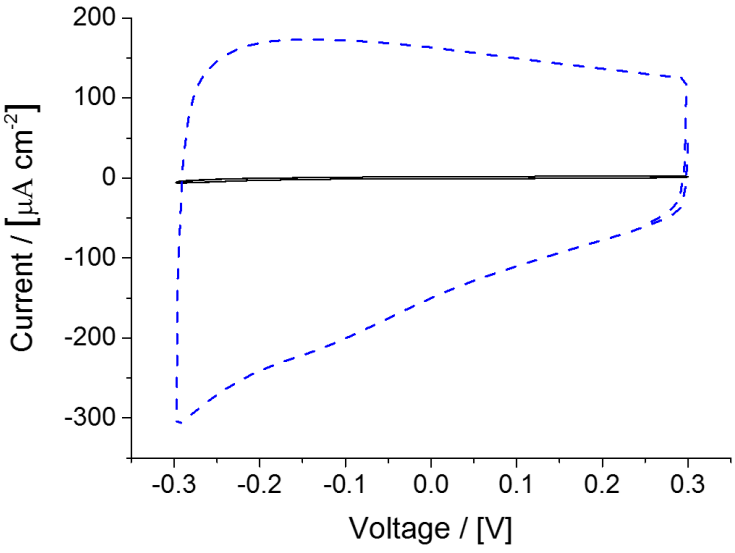

Figure S1. Surface enhancement as determined by cyclic voltammetry. Black line - flat FTO, blue dashed line - 15-layered 3D ITO (0.46 µm latex beads have been used). Scan rate 30 mV s^{-1}, 5 mM KPP, pH 7.

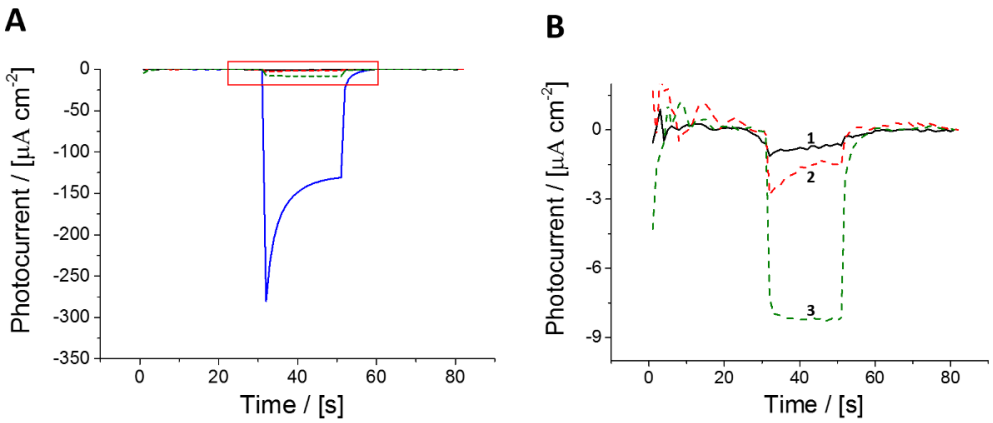

Figure S2. Photoamperometric measuerements at 15-layered 3D ITO electrodes at negative polarisation. **A**: 3D-ITO-PSI-cyt c (blue line). Red square is zoomed in **B**. **B**: 1 – 3D-ITO (black line), 2 - 3D-ITO-cyt c (red dashed line), 3 – 3D-ITO-PSI (green dashed line). Working buffer: KPP, 5 mM, pH 7, applied potential U = -0.2 V vs. Ag/AgCl (1M), light intensity: 100 mW cm^{-2}.

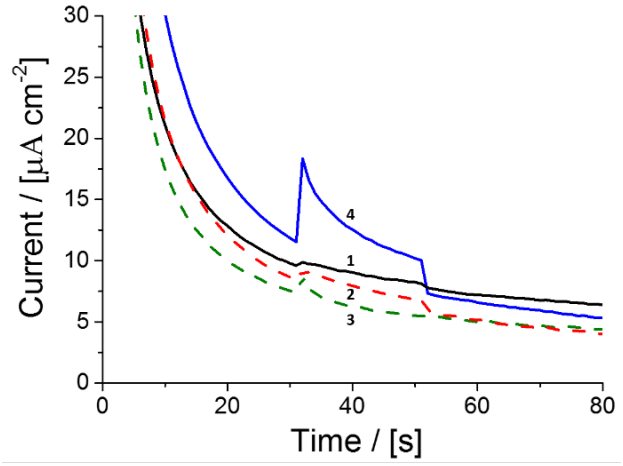

Figure S3. Photoamperometric measurements at 15-layered 3D ITO electrodes at positive polarisation. **1** – 3D-ITO (black line), **2** - 3D-ITO-cyt c (red dashed line), **3** – 3D-ITO-PSI (green dashed line), **4** - 3D-ITO-PSI-cyt c (blue line). Working buffer: KPP, 5 mM, pH 7, applied potential U = +0.2 V vs. Ag/AgCl (1M), light intensity: 100 mWcm^{-2}.

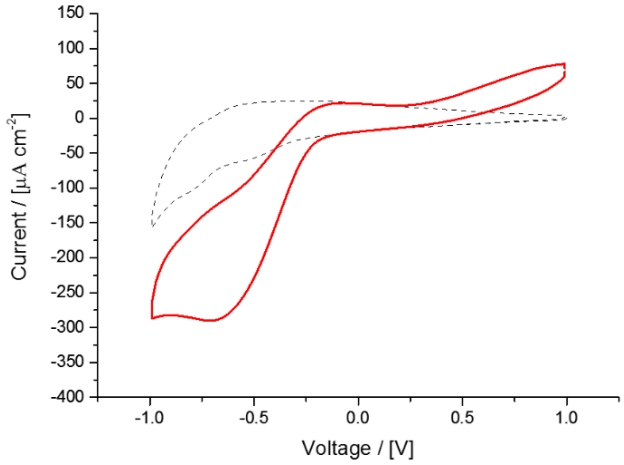

Figure S4. Cyclic voltammetry of 6-layered 3D ITO without (black dashed line) and with (red line) Q_0 (1.5 mM) in working buffer. Scan rate 100 mV s^{-1}, 5 mM KPP, pH 7.

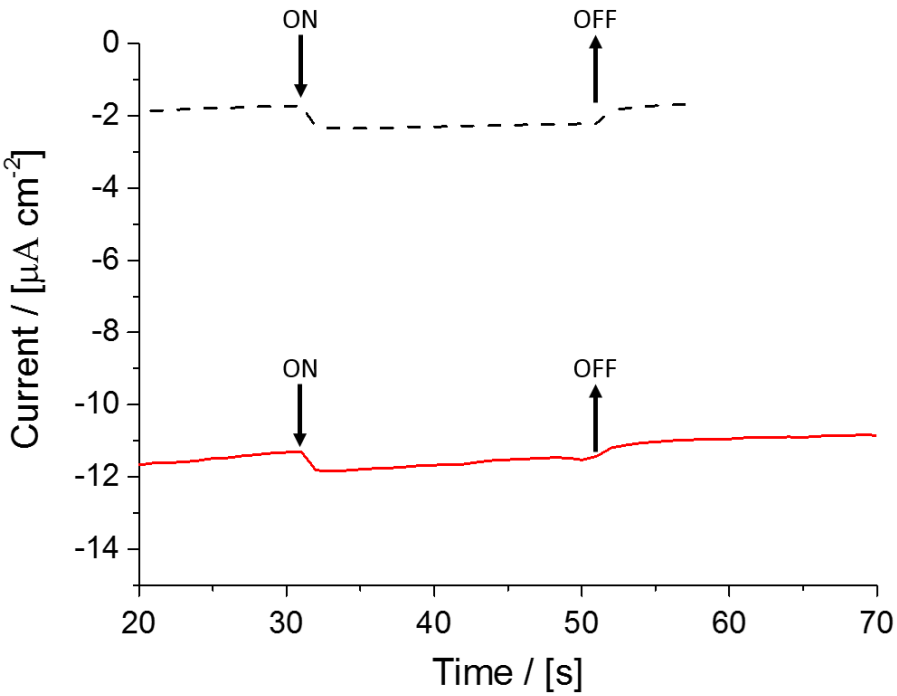

Figure S5. Photoamperometric experiments at 6-layered 3D ITO-PSI electrode prepared without cyt c. Black dashed line - working buffer 5 mM KPP, pH 7. Red line – upon addition of Q_0 (1.5 mM). Illumination with white light was between "On" and "Off" (100 mW cm^{-2}).

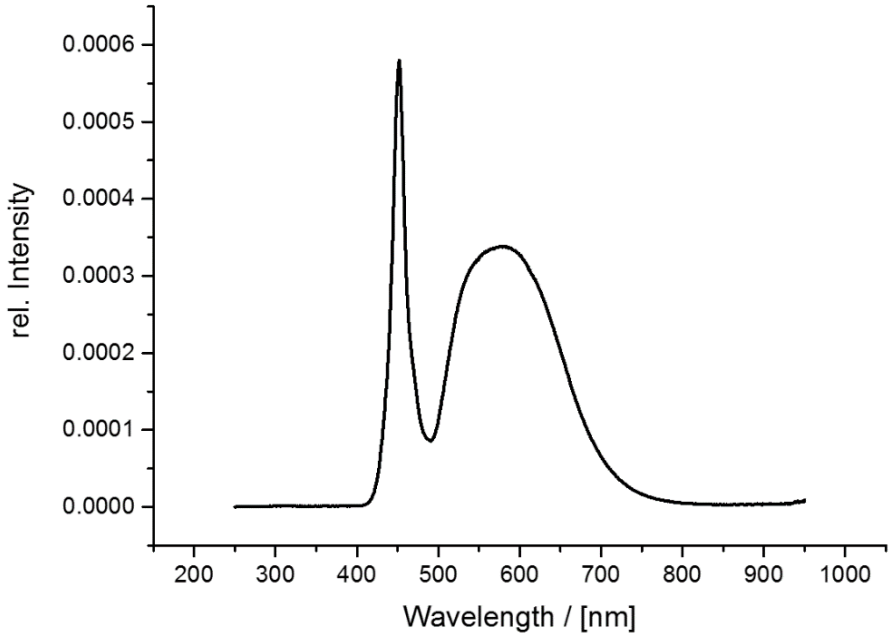

Figure S6. Emission spectrum of white light source used for photoelectrochemical experiments.

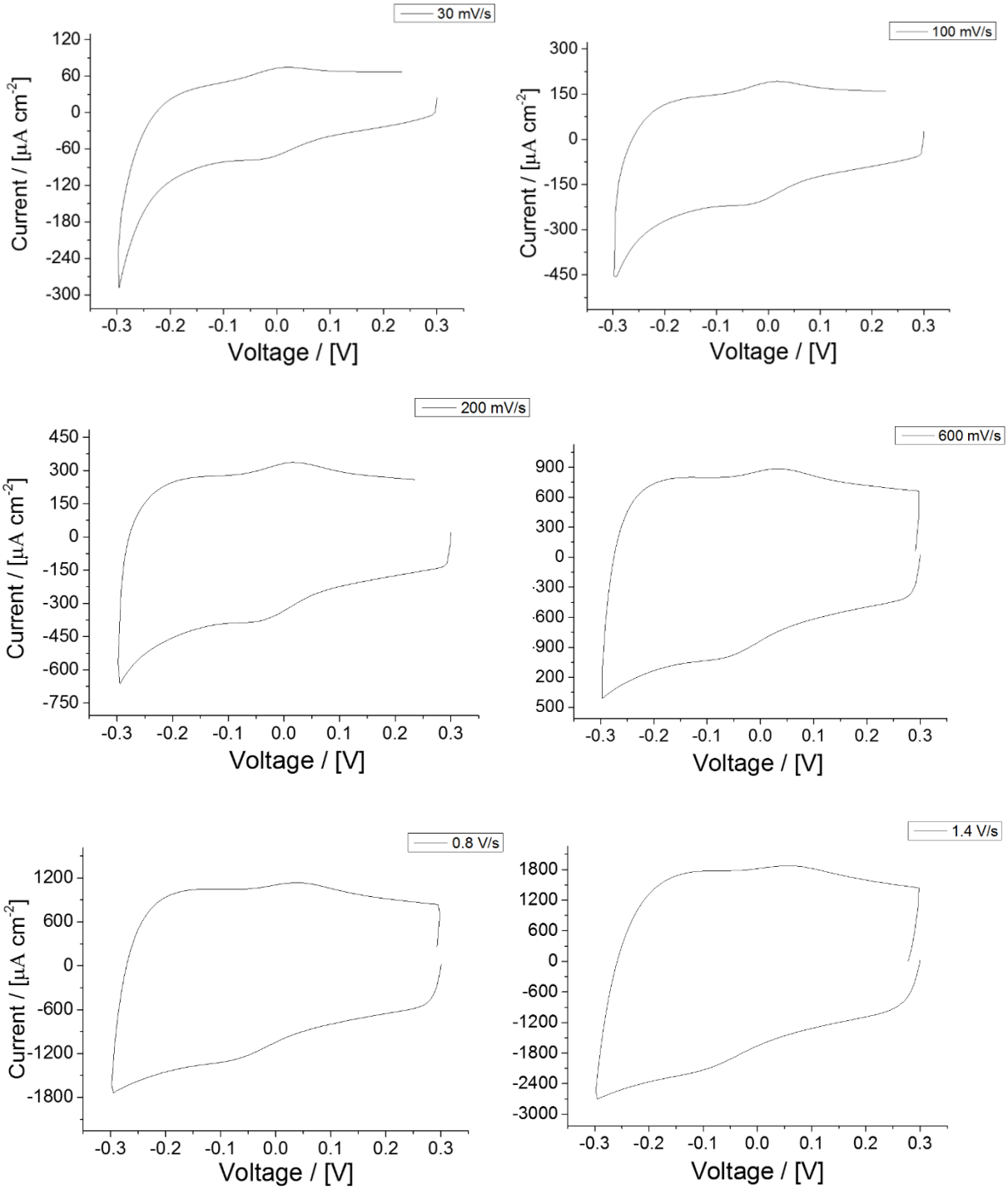

Figure S7. Cyclic voltammetry experiments at 3D-ITO-PSI-cyt *c* (0.8 µm LB, 1.25 % Sn, 3 layer arrangement) and at different scan rates: 30 - 1500 mV s^{-1}. Working buffer: 10 mM KPP, pH 7, reference electrode Ag/AgCl (1M).

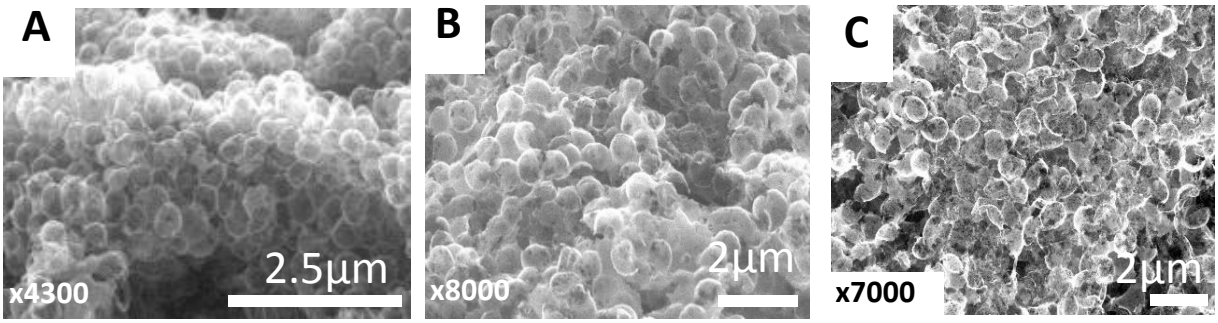

Figure S8. SEM images of as-prepared 3D ITO electrodes by using different Latex Beads diameters. A – 0.46 µm, B – 0.8 µm, C – 1.1 µm Latex Beads. Acceleration voltage 30 kV.

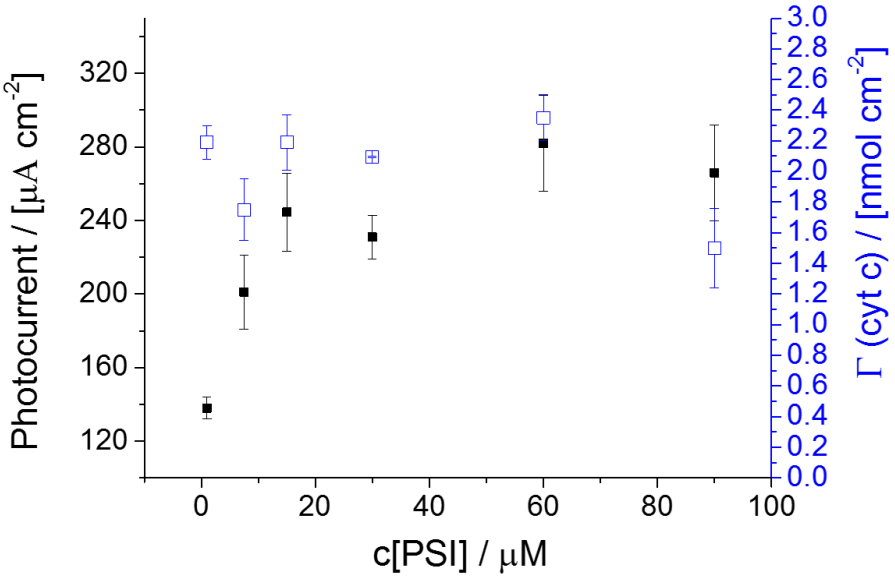

Figure S9. Photocurrents as function of PSI concentration used for preparation of 3D-ITO-PSI-cyt *c* (0.46 µm LB, 1.25 % Sn, 15-layer arrangement, applied potential U= -0.2 vs Ag/AgCl, illumination 100 mW cm^{-2}. Working buffer: 5 mM KPP, pH 7, reference electrode Ag/AgCl (1M). In addition, the surface amount of cyt c is given. Here a slight decrease in photocurrent at high PSI concentration could be observed. This might become a limiting factor since a high amount of cyt c is necessary to wire PSI with the electrode surface.

5. Discussion

In the present thesis following objectives have been addressed:

5.1 Construction of three-dimensional (3D) photobioelectrodes for high performance

- Carbon nanotubes based 3D photobioelectrode (P4.1)
- ITO based 3D electrodes (P4.2 and P4.4)

5.2 Realization of efficient electric wiring of PSI to the electrode (P4.3)

5.3 Establishing electron-supply towards PSI by an enzyme (P4.2)

In this chapter, key features of each system (P4.1-P4.4) will be overviewed and the performances will be compared within this thesis and with other studies as well (Table 1). For objective **1** three different electrode materials have been employed: multi-walled carbon nanotubes (P4.1), tin-doped indium oxide nanoparticles, ITO_{NP} (P4.2), tin-doped indium oxide from liquid precursors, ITO_{prec} (P4.4). For objective **2** a new wiring strategy based on small conductive carbon nanoparticles, fullerenes, has been developed (P4.3). For objective **3** a system based on three proteins (PSI, human sulphite oxidase and cytochrome *c*) has been employed (P4.2).

5.1 Construction of three-dimensional (3D) photobioelectrodes for high performance

5.1.1 Carbon nanotubes based 3D photobioelectrode (P4.1)

In this study edge-carboxylated multi-walled carbon nanotubes (MWNTs-COOH) with diameter of 20-50 nm have been employed as three-dimensional conductive platform for assembly of PSI. Additional pre-modification of MWNTs-COOH with pyrene carboxylic acid has been performed for increasing attachment sites for PSI molecules (for covalent attachment). Such electrode surface is three-dimensional and may allow for high protein loadings. High surface area combined with high conductivity of MWNTs-COOH has been exploited for enzyme electrodes. The photocurrents achieved in this study, however, were rather small (ca. 2 $\mu A\ cm^{-2}$). Since photocurrents are not high, on one hand, and the integrated protein amount is rather high (ca. 4.8 $pmol\ cm^{-2}$), on the other hand, it is to assume that a certain amount of PSI molecules have not been properly electrically wired to the electrode. This might be due to large tunnelling distance between the P_{700} and CNT, thus diminishing the electron transfer rate from CNT towards PSI. A limitation in this system also might be attributed to the insufficient accessibility of the MWNTs surface for the rather large PSI

molecules. Also previous studies have demonstrated that productive connection of such complex biomolecule like PSI or RC on CNTs represents a big challenge, often resulting also in poor electrical connection of photoactive protein with CNT (SWNT/MWNT).[171, 326, 389, 457-459] In order to improve electrical wiring of PSI to the CNT-electrode a small redox-active protein, cytochrome *c*, has been introduced by a back-filling procedure. Interaction between cyt *c* and PSI has been previously extensively studied.[84, 85, 460] Due to its' specific amino acid composition (pI ≈ 9.6), at pH 7 (all experiments have been performed in the working buffer at pH 7) it is positively charged. This enhances probability of electrostatic interactions with the negatively charged luminal side of PSI, where the heme (P_{700} centre) pocket is situated. This situation resembles the natural system where either plastocyanin (PC) or cytochrome *c6* donates electrons to the photo-excited oxidized PSI, however, the interaction of cyt *c* with PSI is a different one as has been elucidated recently.[455] Cyt *c* acted as an electron-shuttle and improved electrical connection of the PSI with the electrode, photocurrent amplitudes have been enhanced (ca. 18 μA cm^{-2} PSI-cyt *c*-MWNTs as compared to 2 μA cm^{-2} for the PSI-MWNTs).

5.1.2 ITO based 3D electrodes (P4.2 and P4.4)

As has been previously shown in this thesis (P4.1) and in the literature three-dimensional electrodes can provide high surface area and make high loadings with proteins possible. In P4.1, despite the larger surface area (ca. 15 fold area enhancement as compared to flat electrode arrangement), the system was limited by low accessibility of proteins towards electrode surface. In order to overcome this limitation tin-doped indium oxide nanoparticles have been used for construction of a macroporous 3D photobioelectrode in P4.2. Since it has been already shown in the literature that such structures can accommodate large amounts of proteins and show certain transparency it has been chosen as electrode material for incorporation of photo-active PSI,[84] wiring compound cytochrome *c* (cyt *c*) (for P4.4) and even a third protein, an enzyme sulphite oxidase (for P4.2). 3D ITO electrodes based on nanoparticle approach (P4.2) provided porous structures of defined height (ca. 5 μm per layer) and a high surface area (ca. 125 fold increased as compared to flat electrode) which is accessible to the proteins, so one limitation in P4.1 has been overcome. Additional transparency property of such structures allowed light transmission even through a 30 μm structures (in P4.2). Photocurrents produced by such electrodes were ca. 30 μA cm^{-2}, which is higher than in P4.1 (18 μA cm^{-2}), although a third protein, hSOx, has been co-integrated in the

3D-ITO structure. The accessible surface area is also larger for 3D ITO structures, leading to the total integrated PSI amount of ca. 19.4 pmol cm^{-2} (in P4.2) vs. 4.8 pmol cm^{-2} (in P4.1). Moving away from the traditional approach for construction of porous 3D ITO electrodes, which is based on ITO nanoparticles (P4.2), a novel liquid precursor-based approach has been introduced in this thesis (P4.4). Results show that the use of precursors instead of nanoparticles leads to a much better electrochemistry of cyt *c* (heterogeneous electron transfer rate constant, $k_s = 7 \pm 1.3$ $e^- s^{-1}$). For comparison, in the nanoparticle-based 3D ITO electrodes developed by Stieger *et al.* (used also in P4.2) k_s values are much lower, $k_s = 0.5 \pm 0.2$ $e^- s^{-1}$.[84] Transparency of such electrodes is even higher than for nanoparticle-based electrodes and thus more light can reach PSI molecules which are integrated inside the 3D structure. Another advantage of such surface (P4.4) is that it can accommodate higher PSI amount (112 pmol cm^{-2}) than a NP-based 3D ITO electrode (ca. 19.4 pmol cm^{-2} in P4.2) and even much higher than at MWNT 3D electrode (ca. 4.8 pmol cm^{-2} in P4.1). Due these new properties compared to nanoparticle-based approach (P4.2) or 3D carbon nanotube-based approach (P4.1) higher photocurrents have been achieved, ca. 270 μA cm^{-2}.(in P4.4) as compared to 30 μA cm^{-2} (P4.2) or 18 μA cm^{-2} (P4.1). Therefore, an overall improvement has been achieved due to a new preparation procedure of 3D ITO electrodes from liquid precursors.

5.2 Realization of an efficient electric wiring of PSI to the electrode (P4.3)

It has been previously demonstrated that the use of small molecules able to exchange electrons (e.g. cyt *c*) can lead to an overall improvement in the performance of the PSI-based photobioelectrode.[84, 85, 460] The question arises, whether even smaller particles can be more efficient in establishing electrical connection between PSI and an electrode.

In P4.3 the electric wiring of PSI with the electrode has been achieved by fullerenes. It is necessary to classify this kind of wiring by comparing several performance parameters of such electrodes with other existing wiring strategies reported in the literature. In the theoretical part of this thesis several PSI wiring approaches have been introduced. Among these noteworthy are Os-polymer wiring, PQQ-wiring, polyaniline wiring (PANI), cyt *c* wiring or pyrene wiring. Photocurrent, however, is not always a helpful tool in assessing efficiency of the system, since one can have inefficient wiring but due to much larger amount of immobilized PSI molecules still reach high photocurrents. Here, molecular efficiency, or turnover frequency, is a more meaningful parameter. With fullerenes in P4.3 a rather high turnover frequency of 232 $e^- s^{-1}$ PSI^{-1} has been achieved. By Os-polymer wiring, for example,

Te values between 3 - 102 $e^- s^{-1} PSI^{-1}$ have been reported.[414] Cyt *c*-based wiring (used also in this thesis in P4.1, P4.2 and P4.4) are moderate and move between 4 – 39 $e^- s^{-1} PSI^{-1}$. PQQ-wiring and PANI-based wiring are not very efficient and Te values are 1.25 $e^- s^{-1} PSI^{-1}$ and 1.4 $e^- s^{-1} PSI^{-1}$ respectively.[149, 158] Thus, one can classify fullerene-based wiring as rather efficient among existing wiring strategies.

5.2.1 Comparison of PSI-based photobioelectrodes

It has to be mentioned that, unfortunately, authors not always provide full information (e.g. height of the electrode structure, area enlargement, PSI coverage or turnover frequency) and a complete comparison with other studies is rather difficult. Moreover, the experimental conditions are rather different, e.g. light intensity, applied potential, molarity and pH of the working buffer.

5.2.1.1 Photocurrent density

Photocurrent densities from this thesis where PSI has been wired *via* cyt *c* have been improved from 18 μA cm^{-2} (P4.1) → 30 μA cm^{-2} (P4.2) → 270 μA cm^{-2} (P4.4). A different wiring strategy developed in P4.3, however, led to 15 μA cm^{-2} (it has to be reminded here, that P4.3 is a 2D system). Therefore, best system from this thesis in terms of photocurrent density is P4.4 and photocurrents reach three-digit value (270 μA cm^{-2}). Interestingly, Feifel *et al.* achieved highest photocurrent for a monolayer of PSI on a flat electrode (135 μA cm^{-2}).[461] Other systems, developed by Zhao and Kothe (140 μA cm^{-2} and 322 μA cm^{-2} respectively)[454, 462] produced also high photocurrents, however, not at monolayer of PSI but due to entrapping of a much larger PSI amount into conductive Os-polymer matrix.

Comparing 3D electrode architectures, the results from P4.4 can compete with previously reported studies on 3D electrode arrangement. However, Mershin,[130] Yu[463] and Shah[132] have reported much higher photocurrents, where PSI has been integrated in a solar cell arrangement in anodic configuration (stromal side, i.e. electron donating side, facing the electrode surface). Other studies where 3D-electrodes have been employed reported photocurrent densities of 1 μA cm^{-2},[141] 1.6 μA cm^{-2},[147] 7.7 μA cm^{-2},[429] 150 μA cm^{-2}.[84]

In Table 1 also other approaches are listed where no wiring *per se* has been used. In such systems electron transfer is assured by tunnelling rather than *via* a molecular wire or by soluble mediators. As can be extracted from Table 1, usually vacuum-assisted approaches to contact PSI with electrode surfaces do not lead to high photocurrents and move in the range

0.1 – 8 μA cm^{-2}. Comparing these reports with photocurrent amplitudes from systems developed in this thesis the photocurrents from P4.1-P4.4 perform well, thus suggesting that a specific wiring (cyt *c* or fullerene) of PSI to the electrode results in higher performance than unspecific vacuum-deposition. Few exceptions, however, exist: in two studies of LeBlanc (2012 and 2014)[131, 167] photocurrents with high magnitudes (625 and 150 μA cm^{-2}) have been reported. In the first system enormous amount of exogeneous soluble mediator methyl viologen (MV^{2+}) has been applied, 100 mM, whereas at smaller concentration of MV^{2+} (20 μM) almost no photocurrent could be produced by PSI. In comparison to this system, in P4.4 ca. 270 μA cm^{-2} could be produced without addition of MV^{2+}, (i.e. under natural oxygen concentration). In the second system of LeBlanc, 150 μA cm^{-2} have been achieved from PSI deposited on reduced graphene oxide (rGO) also by applying vacuum. Here, extremely high PSI amount (20.4 nmol cm^{-2}) on such electrodes has been unspecifically deposited.

5.2.1.2 Turnover frequency

The highest Te in this thesis has been achieved in P4.3 (232 $e^- PSI^{-1} s^{-1}$). This is a rather high value and could be achieved due to fast electron transfer between electrode and PSI mediated by fullerenes. Regarding molecular efficiency, P4.3 can be considered as most efficient system developed in this thesis. In the study of Kothe *et al.* a Te = 102 $e^- s^{-1} PSI^{-1}$ has been achieved when PSI has been entrapped in Os-polymer. The molecular efficiency of the system P4.1, however, is rather moderate (Te = 39 $e^- s^{-1} PSI^{-1}$) but comparable with Stieger's NP-approach (Te = 35 $e^- s^{-1} PSI^{-1}$).[84] In the P4.4 a lower efficiency has been achieved (Te = 25 $e^- s^{-1} PSI^{-1}$), probably because not the whole amount of immobilized PSI could be completely wired by cyt *c*. The photobioelectrode from P4.2, consisting of three proteins, still shows moderate Te (Te = 16 $e^- s^{-1} PSI^{-1}$). Other reported 3D photobioelectrodes showed rather low Te. Calculated Te value for the system developed by LeBlanc (where high photocurrent has been achieved, 625 μA cm^{-2}) was 6.5 $e^- s^{-1} PSI^{-1}$, therefore, comparing molecular efficiency with systems from present thesis (P4.1-P4.4) this system developed by LeBlanc is not very efficient. In another system developed by the same group and mentioned above (150 μA cm^{-2} and 20.4 nmol cm^{-2} PSI content), molecular efficiency was only 0.076 $e^- s^{-1} PSI^{-1}$.

Regarding systems from present thesis, when comparing cyt *c* wiring (P4.1→39 $e^- PSI^{-1} s^{-1}$, P4.2→16 $e^- PSI^{-1} s^{-1}$, P4.4→25 $e^- PSI^{-1} s^{-1}$) with wiring *via* fullerenes (P4.3→232 $e^- PSI^{-1} s^{-1}$), it becomes clear that fullerene-based wiring is more advantageous than cyt *c*-based wiring.

5.2.1.3 The potential which needs to be applied to generate a defined photocurrent

It is also an important parameter, since it reflects how much energy has to be applied in order to extract/inject electrons from/into the electrode. From this point of view, the best system can be considered the one developed by Zhao *et al.* (E_{appl} = + 0.3 vs SHE),[454] followed by Badura and Kothe (E_{appl} = + 0.22 vs SHE).[153, 462] Extraction of electrons from the electrode at such positive applied potentials is possible due to the positive redox potential of Osmium, which lies near the P_{700} midpoint potential (E_0 = + 0.42 vs SHE). From the perspective of applied potential P4.1 is the most energetically useful system (E_{appl} = + 0.12 vs SHE) among other systems in the present thesis. It has to be mentioned here, that in Feifel's work a rather negative potential has been applied (E_{appl} = - 0.34 vs SHE).[464] In contrast, in P4.3 operating potential was more positive (E_{appl} = - 0.08 vs SHE). Other values can be extracted from Table 1.

5.2.1.4 Integrated PSI amount

Analysis of the PSI content integrated in the electrode structure reveals that in P4.4 a rather high amount could be incorporated (112 pmol cm^{-2}). Also NP-based approaches from P4.2 (19.4 pmol cm^{-2}) and Stieger *et al.* (35 pmol cm^{-2})[84] show also rather high PSI loadings. In P4.1, however, much lower PSI content could be integrated (4.8 pmol cm^{-2}). Highest amount of PSI can be accommodated however in a vacuum-deposition procedure or *via* entrapping PSI into a polymer or hydrogel matrix. LeBlanc *et al.* integrated 20 nmol cm^{-2} PSI by applying vacuum, which is the highest reported PSI amount on an electrode. In another work of LeBlanc *et al.* 1 nmol PSI has been integrated by vacuum-procedure. By the PSI entrapment in a polymer matrix (e.g. Os-polymer) usually also rather high PSI loadings can be achieved: Baker *et al.* 104 pmol cm^{-2}, Tapia *et al.* 62 pmol cm^{-2}, Zhao *et al.* 74.5 pmol cm^{-2}, Kothe *et al.* 33 pmol cm^{-2}. Badura *et al.* succeded immobilization of 240 pmol cm^{-2} PSI, which is the highest value without applying vacuum. Most reported systems could not retain a high amount of PSI (or not reported).

5.2.2 Characteristics specific for 3D electrodes

5.2.2.1 Photocurrent per height

The height of the 3D structure represents a separate aspect of 3D electrodes. It is important to obtain efficient photobioelectrode in terms of performance per volume (per height). From this perspective, the system P4.4 ($I_{ph}/\mu m$ = 16) outperforms strongly P4.2 ($I_{ph}/\mu m$ = 1), and

moderately Stieger *et al.* ($I_{ph}/\mu m = 3.8$)[84] and Peters *et al.* ($I_{ph}/\mu m = 4.3$)[429] (both based on NP approach), Ciesielski *et al.* ($I_{ph}/\mu m = 8$), but fails to compete with Mershin,[130] Yu[463] and Shah,[132] which achieved extremely high I_{ph}/height values (95.2, 655 and 1656 respectively). The structure of MWNTs is very heterogeneous and the height in P4.1 cannot be accurately assessed.

5.2.2.2 Photocurrent per real area

Interestingly, when comparing photocurrent per real surface area, the system P4.4 becomes leading even among electrodes producing higher photocurrents. Here, $I_{ph}/A_{real} = 2.7$ μA cm^{-2} and is higher than in Ciesielski's study ($I_{ph}/A_{real} = 0.052$ μA cm^{-2}),[141] Mershin ($I_{ph}/A_{real} = 1.81$ μA cm^{-2}),[130] Stieger ($I_{ph}/A_{real} = 0.68$ μA cm^{-2}).[84] The system P4.1 can be considered moderately performing when real surface area is taken into account ($I_{ph}/A_{real} = 1.2$ μA cm^{-2}). In P4.2 $I_{ph}/A_{real} = 0.24$ μA cm^{-2} and thus, is not very effective in terms of photocurrent performance. Other 3D systems Peters *et al.* and Terasaki *et al.* show lower photocurrent per real area: 0.075 μA cm^{-2} and 0.062 μA cm^{-2} respectively.

5.2.2.3 Area enhancement

Highest achieved area has been reported by Mershin *et al.* for TiO_2 3D electrodes (200 fold).[130] In this thesis, however, 125 fold area enhancement has been achieved by NP-approach (P4.2) and 100 fold enhancement in precursor based approach (P4.4). With MWNT (P4.1) not much area enhancement could be achieved, leading to ca. 15 fold. In Stieger's work, where ITO-NP have been employed, a relatively large surface area could be achieved, ca. 175 fold enhancement.[84] Terasaki *et al.* reported area enhancement of 26 fold and Ciesielski *et al.* a 19 fold enhancement as compared to the flat electrode.

5.2.2.4 Area gain per volume

Evaluating area per volume ($A/V = \mu m^{-1}$) reveals that the surface gain per μm in 3D electrodes constructed in this thesis is not the highest among reported values (e.g. $A/V_{(P4.4)prec} = 5.9$), however, precursor-based approach leads to higher A/V ratio than NP-based approach ($A/V_{(P4.2)NP} = 4.16$, $A/V_{(Stieger)NP} = 5.5$).[84] Despite the fact that highest A/V ratio was achieved by Ciesielski *et al.* ($A/V_{(Ciesielski)} = 152$),[141] such surface lacks transparency, and thus, for thicker gold-leaf structures no light would come through such 3D gold electrode.

Peters *et al.* and Mershin *et al.* have achieved reasonable area gain per volume: A/V= 57.2 and A/V= 52.6 respectively.

Table 1 elucidates reported PSI-based photobioelectrodes. The performance parameters are sorted by the turnover frequency (upper half). The lower part of the listed works are lacking information on turnover frequency or PSI coverage and therefore are sorted by the amplitude of the photocurrent.

5.3 Establishing electron-supply towards PSI by an enzyme (P4.2)

Here, the main aim was to achieve electron supply to PSI by using an enzymatic reaction. There are not many existing systems where biologic photocatalyst is connected with enzymatic conversions, however, the present system (P4.2) can be compared to the few reports in the literature where photo-bioelectrocatalytic electrodes have been developed.

a) Combination of PSI with an enzyme

From the point of view of combining photosystem I with an enzyme, additionally to the systems mentioned above, there are only few publications on combination with hydrogenases (for H_2 production).[135, 137, 465] In these systems PSI donates electrons to an enzyme. Even though such photobiocatalytic systems are designed to perform different tasks (as compared to P4.2) and a comparison is rather difficult, one criterium for comparing efficiency remains the electron transfer rate per PSI molecule. In study of Krassen *et al.* PSI has been genetically fused to the hydrogenase, however, the intermolecular electron flow through both enzymes (from F_B to the H_2-ase) was not very efficient. Electron donor, in contrast to P4.2, has been ensured by a soluble mediator, N-methylphenazonium methyl sulfate (PMS). Here, rather small photocurrents have been recorded (85 nA cm^{-2}). Te from Krassen's system has been calculated to be Te = 0.55 $e^- s^{-1} PSI^{-1}$. In P4.2 the electrons have been transferred directly to the oxygen, electron supply has been achieved either from the electrode or from oxidation of sulphite by the hSOx *via* cyt *c*, Te values were moderate but higher than in Krassen's study, Te=16 $e^- s^{-1} PSI^{-1}$. Lubner *et al.* also wired PSI to a H_2-ase (*via* dithiol linker between F_B and [Fe-Fe]-H_2-ase), however, in contrast to Krassen's system and similarly to P4.2, in this system three proteins have been involved (PSI, cytochrome (cyt *c6*) and an enzyme (H_2-ase)): cyt *c6* acted as an electron donor for P_{700} centre. Here, a low molecular efficiency has been achieved, Te = 4.33 $e^- s^{-1} PSI^{-1}$, which is lower than in P4.2, however, higher than in Krassen's work, since this system was not in an immobilized state on the electrode but in solution. Ihara *et al.* (2006) has wired hydrogenase to PSI *via* cytochrome *c3*.

Substrate	Immobilization	Applied potential (mV vs. SHE)	Light intensity (mW cm^{-2})	Photocurrent (μA cm^{-2})	Turnover number (e$^-$ s^{-1})	PSI content (pmol cm^{-2})	Author
Gold	Electrostatics	+300		0.006			Ciobanu
Gold-lipid layer	adsoprtion	+197	100	0.015			Niroomand
Gold	Vit K-wire	+220	0.32	0.04			Terasaki
Ag-nanopyramids	adsorption		36	0.075			Pamu
Gold	Electrostatics	+120	1.4	0.075	5	0,16	Manocchi
Ag/AgNP/ITO			36	0.09			Niroomand
Gold	Vacuum-assist	+110		0.1			Faulkner
ITO	Electrostatics	-65	0,28	0.15	4	0,39	Efrati
Gold-Os	Electrostatics	+220	280	0.17			Zhao
Gold	Covalent	+170/-80		0.24/0.08	1.25	0,66	Efrati
Graphene	Vacuum-assist	+120	98	0.55			Gunther
Gold	Vacuum	+595	95	0.8			Robinson
3D gold nanoporous	Covalent	+120		1			Ciesielski
TiO2	Adsorption	+485	1	1			Nikandrov
Gold	Covalent/vacuum	+320/+120		1.2/1			Chen
Gold-PEG	Adsorption		55	1			Eßmann
Gold	Os-polymer	+20	1.5	1.2	0.79	15,76	Baker
Gold-thiol	adsorption	+360	95	1.5			Robinson
Gold	Vit K-wire	+220	3.3	1.6			Terasaki
Gold	Electrostatics	+120	20	1.6	10	1,66	Stieger
Gold	Cross-linking	+330	1.13	2	14.8	1,40	Yehezkeli
Gold	Vacuum-assist	+290	95	2			Ciesielski
ITO	Electrostatics	+170	0.28	2.2/1.8	2.5	9,10	Yehezkeli
ITO	Covalent		400	2,2	99	0.23	Efrati
ITO	Covalent	+170	1.92	2.25			Efrati
Gold	Nafion-Os	+70	1.4	4	0.4	103,79	Baker
Gold	PANI	-200	25	5.7	1.4	42,26	Gizzie
Gold	Vacuum-assist	+520	95	8			Ciesielski
macroporous ATO	Vacuum-assist	-80	100	7.7	8.4	9,51	Peters
Gold	Electrostatics	-80	100	15	232	0,67	Ciornii(P4.3)
GCE-MWNT	Covalent	+120	100	18	39	4,79	Ciornii(P4.1)
Au-Os	Electrostatics	+150	400	18	3	62,27	Tapia
ITO	Electrospray	+400	100	20			Shin
IO-ITO	Drop-cast	+20	20	25			Feifel
Gold	Electrostartics	+120	20	25	21	13,00	Stieger
GCE	Os-polymer	+220	1.8	29	1.26	238,87	Badura
3D-ITOnp	Electrostatics	+85	100	30	16	19,46	Ciornii(P4.2)
FTO/Fe2O3	Affinity	+220	100	57			Ocakoglu
GCE	Os-polymer	+170	152	70	24.4	29,77	Zhao
Graphene	Covalent	-340	100	135		0,40	Feifel
Gold	Os-polymer	+300	80	140	19.5	74,51	Zhao
GO-Si/RGO-Si	Vacuum-assist	-112	190	150	0.076	20484,10	LeBlanc
IO-μITO	Drop-cast	+120	20	150	35	35,58	Stieger
ITO-precursors	Electrostatics	+35	100	270	25	112,09	Ciornii(P4.4)
GCE	Os-polymer	+220	40	322	102	32,76	Kothe
mesoTiO2,ZnO NW	Affinity binding		100	362			Mershin
p-doped Silicon	Vacuum-assist	-45	190	625	6.5	997,94	LeBlanc
TiO2	Electrospray	+300	45	2650			Shah

*blue – cathodic, red - anodic

Table 1. Performances of PSI-based photobioelectrodes

b) Electron supply to the PSI by an enzyme

Efrati *et al.* published photonic wiring of an enzyme glucose oxidase (GOx) with the electrode *via* PSI.[177] In this system the oxidation of glucose was coupled to the photocurrent flow through PSI, where GOx served as electron supplier for the oxidized P_{700} centre. In P4.2, in contrast, either electrode or human sulphite oxidase (hSOx) supplied electrons to the PSI *via* cyt *c*, in the latter case electrons were coming from oxidation of sulphite. Glucose photosensing feature has been demonstrated, however, no K_M values have been evaluated. In contrast, in P4.2 the K_M values for sulphite oxidation were 59 μM, being well in agreement with previously reported values for this enzyme in an immobilized state. Additional advantage of the system developed in P4.2 is the electron (energy) storage in cyt *c* layer. In P4.2, in an open circuit potential (OCP) experiment charging and discharging behaviour of such photobioelectrodes has been demonstrated. Unfortunately, in Efrati's work no such behaviour has been investigated. The overall photocurrent in Efrati's work was 2.2 μA cm^{-2}, whereas in P4.2 30 μA cm^{-2} have been achieved. However, the system developed in Efrati's work is more efficient on molecular level, which means that efficiency per PSI molecule is much higher than in P4.2 (Te = 99 $e^- s^{-1}$ PSI^{-1} vs. Te = 16 $e^- s^{-1}$ PSI^{-1} in P4.2).

c) Sulphite bio-sensing feature

P4.2 has also sulphite sensing property. Here, concentration of sulphite can be evaluated from the decrease of the photocurrent (as has been explained in P4.2). In the Table 2 the sensing properties are compared with existing SOx-based sulphite sensors.[466-475] As can be extracted form Table 2, the sensing properties of P4.2 are in the range of existing hSOx-based biosensors. The detection of sulphite in P4.2 is at low potentials (which is an advantage over most existing systems), the sensitivity, however, lays is in the middle range (0.2 μA μM^{-1}). The apparent Michaelis constant, is however, not always reported (in P4.2 K_M^{app} = 59 μM). On top of that, P4.2 provides additionally also other features, mentioned in P4.2 publication.

From perspective of sulphite photo-detection a work by Zeng *et al.*[476] can be compared with P4.2. Here, however, instead of PSI the quantum dots (QDs) have been employed as photoactive entity. Substrate conversion kinetics has been investigated at 0.220 V vs. SHE (in P4.2 at U_{appl} = + 0.07 V vs SHE). The maximal catalytic current has been 1 μA cm^{-2} (at U_{appl} = + 0.22 V vs SHE) whereas in P4.2 ca. 10 μA cm^{-2} (at U_{appl} = + 0.07 V vs SHE) for the same amount of substrate (200 μM SO_3^{2-}), which can be attributed to a much higher active surface area and therefore higher amount of hSOx (ca. 140 pmol cm^{-2} in P4.2 vs. 4.2 pmol cm^{-2} in

Zeng's work). The catalytic activity of hSOx in Zeng's study was, however, higher (k_{cat} = 3.17 s^{-1}) than in P4.2 (k_{cat} = 1.6 s^{-1}). The authors stated that the accessibility of substrate towards enzyme's active site is rather good, which is reflected in low K_M^{app} = 20 µM (in P4.2 for comparison K_M^{app} = 59 µM).

Support for immobilization	Mediator	Sox immobilization	Working potential vs SHE	Calibration range	Sensitivity	Km	Ref
MTF_on_vitreous carbon		Adsorption	-5 mV	200-2800 µM			32
Fe_3O_4@GNPs/Au		Covalent	+420 mV	0.5–1000 uM			33
PBNPs/PPy/Au		Adsorption	+620 mV	0.5–1000 uM			34
SPCEs	TTF	Cross-linking	+420 mV	9.9–82.6 µM	0,054 µA $µM^{-1}$		35
Vitreous carbon	TCNQ/TTF	Encapsulation by dialysis membrane	+220 mV	0–500 µM	0,0015 µA $µM^{-1}$		36
SPCEs	Os-polymer	Cross-linking	+120 mV	0.5–100 uM	0,72 nA $µM^{-1}$		37
Platinized glassy carbon with polytyramine	–	Covalent	+720 mV	2–300 µM			38
PASA modified Au	Cyt *c*	Adsorption	+220 mV	1–60 µM	2,2 µA $µM^{-1}$	77 µM	39
AuNPs/CHIT/MWCNT/PANI/Au		Covalent	+820 mV	0.75–400 uM			40
PBNPs/PPy/ITO		Adsorption	+520	0.5–1000 uM			41
ITO-NP	**Cyt *c***	**Adsorption**	**+70 mV**	**5-500 µM**	**0,2 µA $µM^{-1}$**	**59 µM**	**Ciornii P4.2**

Table 2. hSOx-based biosensors

SPCE - screen printed carbon electrode

MTF - mercury thin film

PASA - polyanyline sulfonic acid

PANI - polyaniline

CHIT - chitosan

PBNP - prussian blue nanoparticles

PPy - polypyrrole

Fe_3O_4@GNPs - gold coated magnetic nanoparticles

TCNQ – tetracyanoquinodimethane

TTF - tetrathiafulvalene

6. Summary

Efficient harvesting of light energy represents one of the most actual directions in todays' bioenergetics worldwide. It is worth to develop and optimize biomolecule-based devices for light-to-current or light-to-chemical conversion. This aspiration has been the motivation of the author of this thesis. In this connection major focus was applied on comprehensive study of energy harnessing from the photoactive protein photosystem I (PSI). One of the possibilities to harness the energy from PSI may be realized by the construction of PSI-based photoelectrode which can produce light-dependent electron flow, also called photocurrent. If high amount of PSI molecules can be integrated on an electrode the photocurrent production will be increased. Therefore, in this thesis the construction of three-dimensional (3D) photobioelectrodes for high performance has been desired and achieved (P4.1, P4.4). For effective light-to-current conversion one needs to establish efficient electric wiring of PSI to the electrode, which has been addressed and realized in the present thesis (P4.3). Another important issue for productive functioning of the PSI-based photobioelectrodes is realization of electron supply to the PSI and has also been addressed and successfully realized in the present work. Here, the electron-supply system towards PSI has been developed by using an enzyme (P4.2).

In **P4.1** the focus has been set on the construction of a 3D electrode architecture based on conductive nanomaterial (multi-walled carbon nanotubes, MWNTs). Here, electric connection could not be completely realized with MWNTs alone. However, after adding a small redox-active protein, cyt *c*, a good electron transfer (ET) between the electrode and the PSI could be established (I_{ph} = 18 μA cm^{-2} for PSI-cyt *c*-MWNTs compared to 2 μA cm^{-2} for PSI-MWNTs). Turnover frequency, Te, values achieved in this system were 39 $e^- s^{-1}$, already approaching Te in natural photosynthesis, 47 $e^- s^{-1}$. The system has, however, a limitation regarding accessibility of the PSI towards the MWNT. Thus this system may be considered as moderately efficient.

In **P4.2** and **P4.4** the PSI-cyt *c* system has been translated on a transparent conductive oxide 3D electrode (**P4.2** – ITO nanoparticles, **P4.4** - ITO from liquid precursors). The slow electron exchange rate between cyt *c* and the electrode (the limitation in a nanoparticle-based approach, **P4.2**) could be overcome in **P4.4**, thus, heterogeneous electron transfer rates (HET) of cyt *c* could be improved (k_s = 7 $e^- s^{-1}$ vs. 0.5 $e^- s^{-1}$), which led to an overall higher

photocurrent amplitudes (270 μA cm^{-2}) as compared to the previous 3D ITO electrodes from P4.2 (30 μA cm^{-2}) and reported in the literature (150 μA cm^{-2}).[84] The transparency of the electrode (**P4.4**) has been improved as compared to nanoparticle-based approach (12 % at 440 nm for precursor-based approach (P4.4) vs. 4 % at 440 nm from NP-based approach).[84] The scalability of the system has been demonstrated by means of solvent-accessible surface area, integrated PSI and cyt *c* amount and photocurrent amplitudes (3 to 15 layers). Therefore, 112 pmol cm^{-2} of PSI could be integrated in 3D structure based on precursors as compared to 19.4 pmol cm^{-2} (in P4.2) or 35.6 pmol cm^{-2} PSI in NP-based approach by Stieger *et al.*[84] Photocurrent limitation by the hampered oxygen diffusion could be overcome to a certain degree by stirring and by addition of an exogeneous electron scavenger ubiquinone Q_0. The system P4.4 may be considered as the most effective system developed in this thesis from the point of view of photocurrent production.

The **P4.3** has been dedicated to optimization of ET between PSI and electrode by developing a new approach. Here, first, the orientation of PSI on the electrode has been addressed by exploiting the advantages of the PSI' dipole character. Targeted design of the electrode surface has been adjusted for assembly of PSI preferentially with its luminal side towards the electrode. Here, a positively charge metal complex, ruthenium hexamine has been combined with a thiol-modification step for creating a charged surface for PSI deposition. The assembly of PSI on such a surface yielded a positive onset of cathodic photocurrent, suggesting a more preferred orientation, which also has been desired. QCM experiments showed that more amount of PSI could be deposited on the thiol-ruhex modified electrode as compared to the electrode surface lacking ruhex (thiol only) thus suggesting a more specific interaction between PSI molecules and charged ruhex surface. Onset of cathodic photocurrent has been improved on thiol-ruhex surface as compared to thiol surface only (U_{onset}(ruhex-thiol) = +0.330 vs SHE vs. U_{onset}(thiol) = +0.09 vs SHE). Photocurrent magnitude could be enhanced 4 fold when PSI was assembled on ruhex-thiol surface (I_{ph}= 0.37 μA cm^{-2}) as compared to the thiol surface only (I_{ph}= 0.08 μA cm^{-2}). After deposition of PSI in a more directed manner, the electric wiring has been achieved by a new approach developed in this thesis. For this small conductive carbon nanoparticles, the carboxy-modified fullerenes have been added to the system. Since **P4.1** has demonstrated, that back-filling approach might be beneficial for establishing efficient ET between PSI and electrode, the aim here was to further improve ET rates. Results demonstrate an improvement of Te over five-fold as compared to P4.1 (Te = 39

$e^- s^{-1} PSI^{-1}$), reaching 232 $e^- s^{-1}$. Therefore, in this thesis the system P4.3 is the most efficient system on molecular level.

In **P4.2** an alternative electron supply for PSI has been investigated. Usually, the electrode accomplishes this function. In this thesis the role of an enzyme, human sulphite oxidase (hSOx), as an alternative biological electron supplier has been demonstrated. The cyt *c* acted in this system as the "relay" between two ET pathways – the photocatalytic ET and the bio-enzymatic ET and as an electron storage module. Interesting features could be gained from this all-protein architecture: i) capacitive-like character of the system, ii) sulphite photo-sensing (sulphite detection could be accomplished at rather low applied potential), iii) switchability of the system, light and sulphite could be used as triggers of photocatalytic and bioenzymatic electron pathways, respectively, iv) self-sustaining character of the system (no energy input is needed, except light and sulphite). This system showed that photocatalytic electron transfer pathway (electrode→cyt *c*→PSI) may be combined with bio-enzymatic electron transfer pathway (SO_3^{2-}→hSOx→ cyt *c*) where a third protein, a small redox-active cytochrome *c* accomplished relay function for both, PSI and hSOx.

Since PSI represents a very promising candidate for light-to-energy conversion reactions it is highly desirable to continue further search for efficient electron extraction from or electron supply to this outstandingly efficient biomolecule. The results from this thesis provide more insights into interaction between PSI and enzymes, demonstrate new strategies for a more efficient photocurrent production and offer strategy for alternative electron supply towards PSI. These might be only small steps in the development of efficient photobiodevices, but hopefully they contribute to a better understanding of such super-complex biological machineries and facilitate the future developments in photobioenergetics along with other interesting and helpful studies on PSI.

7. References

1. G. W. Crabtree and N. S. Lewis, *Physics Today*, 2007, **60**, 37-42.

2. N. S. Lewis and D. G. Nocera, *Proceedings of the National Academy of Sciences*, 2006, **103**, 15729-15735.

3. J. Whitmarsh and Govindjee, in *Concepts in Photobiology: Photosynthesis and Photomorphogenesis*, eds. G. S. Singhal, G. Renger, S. K. Sopory, K. D. Irrgang and Govindjee, Springer Netherlands, Dordrecht, 1999, DOI: 10.1007/978-94-011-4832-0_2, pp. 11-51.

4. A. Zouni, H.-T. Witt, J. Kern, P. Fromme, N. Krauss, W. Saenger and P. Orth, *Nature*, 2001, **409**, 739.

5. W. A. Cramer, G. M. Soriano, M. Ponomarev, D. Huang, H. Zhang, S. E. Martinez and J. L. Smith, *Annual Review of Plant Physiology and Plant Molecular Biology*, 1996, **47**, 477-508.

6. W. A. Cramer, H. Zhang, J. Yan, G. Kurisu and J. L. Smith, *Annual Review of Biochemistry*, 2006, **75**, 769-790.

7. J. M. Anderson, *Photosynthesis Research*, 1992, **34**, 341-357.

8. Y. Munekage, M. Hashimoto, C. Miyake, K.-I. Tomizawa, T. Endo, M. Tasaka and T. Shikanai, *Nature*, 2004, **429**, 579.

9. J. F. Allen, *Cell*, 2002, **110**, 273-276.

10. A. Díaz-Quintana, J. A. Navarro, M. Hervás, F. P. Molina-Heredia, B. De la Cerda and M. A. De la Rosa, *Photosynthesis Research*, 2003, **75**, 97-110.

11. M. A. De la Rosa, J. A. Navarro, A. Díaz-Quintana, B. De la Cerda, F. P. Molina-Heredia, A. Balme, P. d. S. Murdoch, I. Díaz-Moreno, R. V. Durán and M. Hervás, *Bioelectrochemistry*, 2002, **55**, 41-45.

12. R. V. Durán, M. Hervás, M. A. De la Rosa and J. A. Navarro, *Journal of Biological Chemistry*, 2004, **279**, 7229-7233.

13. P. Joliot and A. Joliot, *Biochemistry*, 1999, **38**, 11130-11136.

14. K. Brettel and W. Leibl, *Biochimica et Biophysica Acta (BBA) - Bioenergetics*, 2001, **1507**, 100-114.

15. M. Guergova-Kuras, B. Boudreaux, A. Joliot, P. Joliot and K. Redding, *Proceedings of the National Academy of Sciences*, 2001, **98**, 4437-4442.

16. G. Kurisu, M. Kusunoki, E. Katoh, T. Yamazaki, K. Teshima, Y. Onda, Y. Kimata-Ariga and T. Hase, *Nature Structural Biology*, 2001, **8**, 117.

17. C. J. Batie and H. Kamin, *Journal of Biological Chemistry*, 1984, **259**, 11976-11985.

18. M. Calvin, *Angewandte Chemie*, 1956, **68**, 253-264.

19. D. Stock, A. G. W. Leslie and J. E. Walker, *Science*, 1999, **286**, 1700-1705.

20. P. D. Boyer, *Annual Review of Biochemistry*, 1997, **66**, 717-749.

21. T. J. Berg JM, Stryer L. , *Book*, 2002, **5th edition**, Berg JM, Tymoczko JL, Stryer L. Biochemistry. 5th edition. New York: W H Freeman; 2002. Section 2019.2004, A Proton Gradient Across the Thylakoid Membrane Drives ATP Synthesis. Available from: https://www.ncbi.nlm.nih.gov/books/NBK22519/.

22. D. I. Arnon, M. B. Allen and F. R. Whatley, *Biochimica et Biophysica Acta*, 1956, **20**, 449-461.

23. J. F. Allen, *Nature*, 1975, **256**, 599.

24. A. E. Senior, S. Nadanaciva and J. Weber, *Biochimica et Biophysica Acta (BBA) - Bioenergetics*, 2002, **1553**, 188-211.

25. W. Iwanzik, M. Tevini, G. Dohnt, M. Voss, W. Weiss, P. Gräber and G. Renger, *Physiologia Plantarum*, 1983, **58**, 401-407.

26. P. Jordan, P. Fromme, H. T. Witt, O. Klukas, W. Saenger and N. Krauß, *Nature*, 2001, **411**, 909.

27. S. Santabarbara, P. Heathcote and M. C. W. Evans, *Biochimica et Biophysica Acta (BBA) - Bioenergetics*, 2005, **1708**, 283-310.

28. I. P. Muhiuddin, P. Heathcote, S. Carter, S. Purton, S. E. J. Rigby and M. C. W. Evans, *FEBS Letters*, 2001, **503**, 56-60.

29. P. Fromme, H. T. Witt, W.-D. Schubert, O. Klukas, W. Saenger and N. Krauβ, *Biochimica et Biophysica Acta (BBA) - Bioenergetics*, 1996, **1275**, 76-83.

30. V. P. Chitnis and P. R. Chitnis, *FEBS Letters*, 1993, **336**, 330-334.

31. Q. Xu, D. Hoppe, V. P. Chitnis, W. R. Odom, J. A. Guikema and P. R. Chitnis, *Journal of Biological Chemistry*, 1995, **270**, 16243-16250.

32. P. Fromme, P. Jordan and N. Krauß, *Biochimica et Biophysica Acta (BBA) - Bioenergetics*, 2001, **1507**, 5-31.

33. S. Naithani, J.-M. Hou and P. R. Chitnis, *Photosynthesis Research*, 2000, **63**, 225-236.

34. P. R. Chitnis, *Plant Physiology*, 1996, **111**, 661-669.

35. N. Li, J. Zhao, P. V. Warren, J. T. Warden, D. A. Bryant and J. H. Golbeck, *Biochemistry*, 1991, **30**, 7863-7872.

36. G. Zanetti and G. Merati, *European Journal of Biochemistry*, 1987, **169**, 143-146.

37. J. Kruip, P. R. Chitnis, B. Lagoutte, M. Rögner and E. J. Boekema, *Journal of Biological Chemistry*, 1997, **272**, 17061-17069.

38. Q. Xu, Y. S. Jung, V. P. Chitnis, J. A. Guikema, J. H. Golbeck and P. R. Chitnis, *Journal of Biological Chemistry*, 1994, **269**, 21512-21518.

39. F. Rousseau, P. Sétif and B. Lagoutte, *The EMBO Journal*, 1993, **12**, 1755-1765.

40. N. Fischer, M. Hippler, P. Sétif, J. P. Jacquot and J. D. Rochaix, *The EMBO Journal*, 1998, **17**, 849-858.

41. P. Fromme, A. Melkozernov, P. Jordan and N. Krauss, *FEBS Letters*, 2003, **555**, 40-44.

42. G. Panitchayangkoon, D. Hayes, K. A. Fransted, J. R. Caram, E. Harel, J. Wen, R. E. Blankenship and G. S. Engel, *Proceedings of the National Academy of Sciences*, 2010, **107**, 12766.

43. A. N. Webber and W. Lubitz, *Biochimica et Biophysica Acta (BBA) - Bioenergetics*, 2001, **1507**, 61-79.

44. A. W. Rutherford and P. Sétif, *Biochimica et Biophysica Acta (BBA) - Bioenergetics*, 1990, **1019**, 128-132.

45. A. Nakamura, T. Suzawa, Y. Kato and T. Watanabe, *Plant and Cell Physiology*, 2011, **52**, 815-823.

46. N. Nelson and A. Ben-Shem, *The complex architecture of oxygenic photosynthesis*, 2005.

47. J. H. Golbeck, *Photosynthesis Research*, 1999, **61**, 107-144.

48. N. Fischer, P. Sétif and J.-D. Rochaix, *Biochemistry*, 1997, **36**, 93-102.

49. I. R. Vassiliev, Y.-S. Jung, F. Yang and J. H. Golbeck, *Biophysical Journal*, 1998, **74**, 2029-2035.

50. N. Fischer, P. Sétif and J.-D. Rochaix, *Journal of Biological Chemistry*, 1999, **274**, 23333-23340.

51. J. Zhao, N. Li, P. V. Warren, J. H. Golbeck and D. A. Bryant, *Biochemistry*, 1992, **31**, 5093-5099.

52. M. L. Antonkine, E. M. Maes, R. S. Czernuszewicz, C. Breitenstein, E. Bill, C. J. Falzone, R. Balasubramanian, C. Lubner, D. A. Bryant and J. H. Golbeck, *Biochimica et Biophysica Acta (BBA) - Bioenergetics*, 2007, **1767**, 712-724.

53. P. Sétif, N. Fischer, B. Lagoutte, H. Bottin and J.-D. Rochaix, *Biochimica et Biophysica Acta (BBA) - Bioenergetics*, 2002, **1555**, 204-209.

54. P. Sétif, *Biochimica et Biophysica Acta (BBA) - Bioenergetics*, 2001, **1507**, 161-179.

55. M. El-Khouly, E. El-Mohsnawy and S. Fukuzumi, *Solar energy conversion: From natural to artificial photosynthesis*, 2017.

56. P. R. Chitnis, *Annual Review of Plant Physiology and Plant Molecular Biology*, 2001, **52**, 593-626.

57. J. E. Frew and H. A. O. Hill, *European Journal of Biochemistry*, 1988, **172**, 261-269.

58. A. G. Sykes, *Advances in Inorganic Chemistry*, Elsevier Science, 1991.

59. W. R. Heineman, B. J. Norris and J. F. Goelz, *Analytical Chemistry*, 1975, **47**, 79-84.

60. T. Kôno and S. Nakamura, *Bulletin of the Agricultural Chemical Society of Japan*, 1958, **22**, 399-403.

61. F. Scheller, M. Jänchen, J. Lampe, H. J. Prümke, J. Blanck and E. Palecek, *Biochimica et Biophysica Acta (BBA) - Protein Structure*, 1975, **412**, 157-167.

62. T. M. Cotton, S. G. Schultz and R. P. Van Duyne, *Journal of the American Chemical Society*, 1980, **102**, 7960-7962.

63. N. S. Lewis and M. S. Wrighton, *Science*, 1981, **211**, 944.

64. M. J. Eddowes and H. A. O. Hill, *Journal of the Chemical Society, Chemical Communications*, 1977, DOI: 10.1039/C3977000771B, 771b-772.

65. P. Yeh and T. Kuwana, *Reversible Electrode-Reaction of Cytochrome c*, 1977.

66. P. M. Allen, H. Allen, O. Hill and N. J. Walton, *Journal of Electroanalytical Chemistry and Interfacial Electrochemistry*, 1984, **178**, 69-86.

67. N. S. Hush, *Coordination Chemistry Reviews*, 1985, **64**, 135-157.

68. C. E. D. Chidsey, *Science*, 1991, **251**, 919.

69. N. P. Mongwaketsi, L. Kotsedi, Z. Y. Nuru, R. Sparrow, G. Garab and M. Maaza, *J Porph Phtalloc*, 2014, **18**.

70. R. Marcus and N. Sutin, *Electron transfers in chemistry and biology*, 1985.

71. R. A. Marcus, *Electrochimica Acta*, 1968, **13**, 995-1004.

72. T. T. T. Li and M. J. Weaver, *Journal of the American Chemical Society*, 1984, **106**, 6107-6108.

73. R. A. Marcus and N. Sutin, *Biochimica et Biophysica Acta (BBA) - Reviews on Bioenergetics*, 1985, **811**, 265-322.

74. K. V. Mikkelsen and M. A. Ratner, *Chemical Reviews*, 1987, **87**, 113-153.

75. Q. Chi, J. Zhang, J. U. Nielsen, E. P. Friis, I. Chorkendorff, G. W. Canters, J. E. T. Andersen and J. Ulstrup, *Journal of the American Chemical Society*, 2000, **122**, 4047-4055.

76. S. Shleev, J. Tkac, A. Christenson, T. Ruzgas, A. I. Yaropolov, J. W. Whittaker and L. Gorton, *Biosensors and Bioelectronics*, 2005, **20**, 2517-2554.

77. P. Yang, J. You, F. Li, J. Fei, B. Feng, X. He and J. Zhou, *Analytical Methods*, 2013, **5**, 3168-3171.

78. H. Allen, O. Hill, D. J. Page, N. J. Walton and D. Whitford, *Journal of Electroanalytical Chemistry and Interfacial Electrochemistry*, 1985, **187**, 315-324.

79. L. Wang and E. Wang, *Electrochemistry Communications*, 2004, **6**, 49-54.

80. J.-F. Wu, M.-Q. Xu and G.-C. Zhao, *Electrochemistry Communications*, 2010, **12**, 175-177.

81. D. E. Reed and F. M. Hawkridge, *Analytical Chemistry*, 1987, **59**, 2334-2339.

82. F. M. Hawkridge and I. Taniguchi, *Comments on Inorganic Chemistry*, 1995, **17**, 163-187.

83. K. R. Stieger, S. C. Feifel, H. Lokstein and F. Lisdat, *Physical Chemistry Chemical Physics*, 2014, **16**, 15667-15674.

84. K. R. Stieger, S. C. Feifel, H. Lokstein, M. Hejazi, A. Zouni and F. Lisdat, *Journal of Materials Chemistry A*, 2016, **4**, 17009-17017.

85. K. R. Stieger, D. Ciornii, A. Kölsch, M. Hejazi, H. Lokstein, S. C. Feifel, A. Zouni and F. Lisdat, *Nanoscale*, 2016, **8**, 10695-10705.

86. F. A. Armstrong, H. A. O. Hill and N. J. Walton, *FEBS Letters*, 1982, **145**, 241-244.

87. K. Nishiyama, H. Ishida and I. Taniguchi, *Journal of Electroanalytical Chemistry*, 1994, **373**, 255-258.

88. Y. M. Lvov, Z. Lu, J. B. Schenkman, X. Zu and J. F. Rusling, *Journal of the American Chemical Society*, 1998, **120**, 4073-4080.

89. J. F. Rusling, *Accounts of Chemical Research*, 1998, **31**, 363-369.

90. H.-Y. Gu, A.-M. Yu and H.-Y. Chen, *Journal of Electroanalytical Chemistry*, 2001, **516**, 119-126.

91. C. Cai and J. Chen, *Analytical Biochemistry*, 2004, **325**, 285-292.

92. E. E. Ferapontova, T. Ruzgas and L. Gorton, *Analytical Chemistry*, 2003, **75**, 4841-4850.

93. V. J. Razumas, A. V. Gudavičius and J. J. Kulys, *Journal of Electroanalytical Chemistry and Interfacial Electrochemistry*, 1983, **151**, 311-315.

94. V. J. Razumas, A. V. Gudavičius and J. J. Kulys, *Journal of Electroanalytical Chemistry and Interfacial Electrochemistry*, 1986, **198**, 81-87.

95. P. Ramírez, N. Mano, R. Andreu, T. Ruzgas, A. Heller, L. Gorton and S. Shleev, *Biochimica et Biophysica Acta (BBA) - Bioenergetics*, 2008, **1777**, 1364-1369.

96. G. Gupta, C. Lau, V. Rajendran, F. Colon, B. Branch, D. Ivnitski and P. Atanassov, *Electrochemistry Communications*, 2011, **13**, 247-249.

97. S. Shleev, A. Jarosz-Wilkolazka, A. Khalunina, O. Morozova, A. Yaropolov, T. Ruzgas and L. Gorton, *Bioelectrochemistry*, 2005, **67**, 115-124.

98. C. Baffert, K. Sybirna, P. Ezanno, T. Lautier, V. Hajj, I. Meynial-Salles, P. Soucaille, H. Bottin and C. Léger, *Analytical Chemistry*, 2012, **84**, 7999-8005.

99. C. Gutiérrez-Sánchez, D. Olea, M. Marques, V. M. Fernández, I. A. C. Pereira, M. Vélez and A. L. De Lacey, *Langmuir*, 2011, **27**, 6449-6457.

100. A. Sucheta, R. Cammack, J. Weiner and F. A. Armstrong, *Biochemistry*, 1993, **32**, 5455-5465.

101. J. Hirst, A. Sucheta, B. A. C. Ackrell and F. A. Armstrong, *Journal of the American Chemical Society*, 1996, **118**, 5031-5038.

102. H. A. O. Hill, *Journal*, 1987, **59**, 743.

103. I. W. Schubart, G. Göbel and F. Lisdat, *Electrochimica Acta*, 2012, **82**, 224-232.

104. G. Göbel, I. W. Schubart, V. Scherbahn and F. Lisdat, *Electrochemistry Communications*, 2011, **13**, 1240-1243.

105. C. Tanne, G. Göbel and F. Lisdat, *Biosensors and Bioelectronics*, 2010, **26**, 530-535.

106. A. Guiseppi-Elie, C. Lei and R. H. Baughman, *Nanotechnology*, 2002, **13**, 559-564.

107. C. Cai and J. Chen, *Analytical Biochemistry*, 2004, **332**, 75-83.

108. F. Tasca, L. Gorton, W. Harreither, D. Haltrich, R. Ludwig and G. Nöll, *The Journal of Physical Chemistry C*, 2008, **112**, 9956-9961.

109. F. Tasca, L. Gorton, W. Harreither, D. Haltrich, R. Ludwig and G. Nöll, *The Journal of Physical Chemistry C*, 2008, **112**, 9956-9961.

110. L. Ghindilis Andrey, P. Atanasov and E. Wilkins, *Electroanalysis*, 2005, **9**, 661-674.

111. S. Kaniber, L. Frolov, F. Simmel, A. Holleitner, C. Carmeli and I. Carmeli, *arXiv preprint arXiv:0902.4359*, 2009.

112. B. Albinsson, M. P. Eng, K. Pettersson and M. U. Winters, *Physical Chemistry Chemical Physics*, 2007, **9**, 5847-5864.

113. A. Troisi, *Molecular Simulation*, 2006, **32**, 707-716.

114. A. Heller, *Electron-Conducting Redox Hydrogels: Design, Characteristics and Synthesis*, 2007.

115. N. A. Peppas, J. Z. Hilt, A. Khademhosseini and R. Langer, *Advanced Materials*, 2006, **18**, 1345-1360.

116. T. Kothe, S. Pöller, F. Zhao, P. Fortgang, M. Rögner, W. Schuhmann and N. Plumeré, *Chemistry – A European Journal*, 2014, **20**, 11029-11034.

117. T. J. Ohara, R. Rajagopalan and A. Heller, *Wired" Enzyme Electrodes for Amperometric Determination of Glucose or Lactate in the Presence of Interfering Substances*, 1994.

118. T. J. Ohara, R. Rajagopalan and A. Heller, *Analytical Chemistry*, 1994, **66**, 2451-2457.

119. A. Zebda, C. Gondran, A. Le Goff, M. Holzinger, P. Cinquin and S. Cosnier, *Nature Communications*, 2011, **2**, 370.

120. Y. Okawa, M. Nagano, S. Hirota, H. Kobayashi, T. Ohno and M. Watanabe, *Biosensors and Bioelectronics*, 1999, **14**, 229-235.

121. I. Willner, V. Heleg-Shabtai, R. Blonder, E. Katz, G. Tao, A. F. Bückmann and A. Heller, *Journal of the American Chemical Society*, 1996, **118**, 10321-10322.

122. R. G. Nuzzo, B. R. Zegarski and L. H. Dubois, *Journal of the American Chemical Society*, 1987, **109**, 733-740.

123. A. Ulman, *Chemical Reviews*, 1996, **96**, 1533-1554.

124. M. K. Beyer, *The Journal of Chemical Physics*, 2000, **112**, 7307-7312.

125. K. Exner and P. v. R. Schleyer, *The Journal of Physical Chemistry A*, 2001, **105**, 3407-3416.

126. O. Kievit and G. W. Brudvig, *Journal of Electroanalytical Chemistry*, 2001, **497**, 139-149.

127. B. Munge, S. K. Das, R. Ilagan, Z. Pendon, J. Yang, H. A. Frank and J. F. Rusling, *Journal of the American Chemical Society*, 2003, **125**, 12457-12463.

128. M. Ciobanu, H. A. Kincaid, V. Lo, A. D. Dukes, G. Kane Jennings and D. E. Cliffel, *Journal of Electroanalytical Chemistry*, 2007, **599**, 72-78.

129. S. C. Feifel, K. R. Stieger, H. Lokstein, H. Lux and F. Lisdat, *Journal of Materials Chemistry A*, 2015, **3**, 12188-12196.

130. A. Mershin, K. Matsumoto, L. Kaiser, D. Yu, M. Vaughn, M. K. Nazeeruddin, B. D. Bruce, M. Graetzel and S. Zhang, *Scientific Reports*, 2012, **2**, 234.

131. G. LeBlanc, G. Chen, E. A. Gizzie, G. K. Jennings and D. E. Cliffel, *Advanced Materials*, 2012, **24**, 5959-5962.

132. V. B. Shah, W. R. Henson, T. S. Chadha, G. Lakin, H. Liu, R. E. Blankenship and P. Biswas, *Langmuir*, 2015, **31**, 1675-1682.

133. G. Chen, G. LeBlanc, G. K. Jennings and D. E. Cliffel, *Journal of The Electrochemical Society*, 2013, **160**, H315-H320.

134. T. Bennett, H. Niroomand, R. Pamu, I. Ivanov, D. Mukherjee and B. Khomami, *Physical Chemistry Chemical Physics*, 2016, **18**, 8512-8521.

135. H. Krassen, A. Schwarze, B. Friedrich, K. Ataka, O. Lenz and J. Heberle, *ACS Nano*, 2009, **3**, 4055-4061.

136. M. Ihara, H. Nishihara, K.-S. Yoon, O. Lenz, B. Friedrich, H. Nakamoto, K. Kojima, D. Honma, T. Kamachi and I. Okura, *Photochemistry and Photobiology*, 2006, **82**, 676-682.

137. C. E. Lubner, P. Knörzer, P. J. N. Silva, K. A. Vincent, T. Happe, D. A. Bryant and J. H. Golbeck, *Biochemistry*, 2010, **49**, 10264-10266.

138. J. F. Millsaps, B. D. Bruce, J. W. Lee and E. Greenbaum, *Photochemistry and Photobiology*, 2001, **73**, 630-635.

139. L. M. Utschig, N. M. Dimitrijevic, O. G. Poluektov, S. D. Chemerisov, K. L. Mulfort and D. M. Tiede, *The Journal of Physical Chemistry Letters*, 2011, **2**, 236-241.

140. C. J. Faulkner, S. Lees, P. N. Ciesielski, D. E. Cliffel and G. K. Jennings, *Langmuir*, 2008, **24**, 8409-8412.

141. P. N. Ciesielski, A. M. Scott, C. J. Faulkner, B. J. Berron, D. E. Cliffel and G. K. Jennings, *ACS Nano*, 2008, **2**, 2465-2472.

142. P. N. Ciesielski, F. M. Hijazi, A. M. Scott, C. J. Faulkner, L. Beard, K. Emmett, S. J. Rosenthal, D. Cliffel and G. Kane Jennings, *Bioresource Technology*, 2010, **101**, 3047-3053.

143. A. K. Manocchi, D. R. Baker, S. S. Pendley, K. Nguyen, M. M. Hurley, B. D. Bruce, J. J. Sumner and C. A. Lundgren, *Langmuir*, 2013, **29**, 2412-2419.

144. G. Chen, G. LeBlanc, G. K. Jennings and D. E. Cliffel, *Journal of The Electrochemical Society*, 2013, **160**, H315-H320.

145. H. Niroomand, R. Pamu, D. Mukherjee and B. Khomami, *MRS Communications*, 2018, DOI: 10.1557/mrc.2018.83, 1-7.

146. R. Pamu, V. P. Sandireddy, R. Kalyanaraman, B. Khomami and D. Mukherjee, *The Journal of Physical Chemistry Letters*, 2018, **9**, 970-977.

147. N. Terasaki, N. Yamamoto, T. Hiraga, Y. Yamanoi, T. Yonezawa, H. Nishihara, T. Ohmori, M. Sakai, M. Fujii, A. Tohri, M. Iwai, Y. Inoue, S. Yoneyama, M. Minakata and I. Enami, *Angewandte Chemie*, 2009, **121**, 1613-1615.

148. O. Yehezkeli, O. I. Wilner, R. Tel-Vered, D. Roizman-Sade, R. Nechushtai and I. Willner, *The Journal of Physical Chemistry B*, 2010, **114**, 14383-14388.

149. A. Efrati, O. Yehezkeli, R. Tel-Vered, D. Michaeli, R. Nechushtai and I. Willner, *ACS Nano*, 2012, **6**, 9258-9266.

150. K. R. Stieger, S. C. Feifel, H. Lokstein and F. Lisdat, *Physical Chemistry Chemical Physics*, 2014, **16**, 15667-15674.

151. K. R. Stieger, S. C. Feifel, H. Lokstein and F. Lisdat, *Physical Chemistry Chemical Physics*, 2014, **16**, 15667-15674.

152. S. C. Feifel, K. R. Stieger, M. Hejazi, X. Wang, M. Ilbert, A. Zouni, E. Lojou and F. Lisdat, *Electrochemistry Communications*, 2018, **91**, 49-53.

153. A. Badura, D. Guschin, T. Kothe, M. J. Kopczak, W. Schuhmann and M. Rogner, *Energy & Environmental Science*, 2011, **4**, 2435-2440.

154. D. R. Baker, A. K. Manocchi, M. L. Lamicq, M. Li, K. Nguyen, J. J. Sumner, B. D. Bruce and C. A. Lundgren, *The Journal of Physical Chemistry B*, 2014, **118**, 2703-2711.

155. F. Zhao, K. Sliozberg, M. Rögner, N. Plumeré and W. Schuhmann, *Journal of The Electrochemical Society*, 2014, **161**, H3035-H3041.

156. T. Kothe, S. Pöller, F. Zhao, P. Fortgang, M. Rögner, W. Schuhmann and N. Plumeré, *Chemistry – A European Journal*, 2014, **20**, 11029-11034.

157. D. R. Baker, R. F. Simmerman, J. J. Sumner, B. D. Bruce and C. A. Lundgren, *Langmuir*, 2014, **30**, 13650-13655.

158. E. A. Gizzie, G. LeBlanc, G. K. Jennings and D. E. Cliffel, *ACS Applied Materials & Interfaces*, 2015, **7**, 9328-9335.

159. F. Zhao, S. Hardt, V. Hartmann, H. Zhang, M. M. Nowaczyk, M. Rögner, N. Plumeré, W. Schuhmann and F. Conzuelo, *Nature Communications*, 2018, **9**, 1973.

160. I. Lee, J. W. Lee and E. Greenbaum, *Physical Review Letters*, 1997, **79**, 3294-3297.

161. D. Mukherjee, M. Vaughn, B. Khomami and B. D. Bruce, *Colloids and Surfaces B: Biointerfaces*, 2011, **88**, 181-190.

162. L. Frolov, Y. Rosenwaks, C. Carmeli and I. Carmeli, *Advanced Materials*, 2005, **17**, 2434-2437.

163. H. A. Kincaid, T. Niedringhaus, M. Ciobanu, D. E. Cliffel and G. K. Jennings, *Langmuir*, 2006, **22**, 8114-8120.

164. N. Terasaki, N. Yamamoto, T. Hiraga, I. Sato, Y. Inoue and S. Yamada, *Thin Solid Films*, 2006, **499**, 153-156.

165. C. Tapia, R. D. Milton, G. Pankratova, S. D. Minteer, H.-E. Åkerlund, D. Leech, A. L. De Lacey, M. Pita and L. Gorton, *ChemElectroChem*, 2016, **4**, 90-95.

166. D. Gunther, G. LeBlanc, D. Prasai, J. R. Zhang, D. E. Cliffel, K. I. Bolotin and G. K. Jennings, *Langmuir*, 2013, **29**, 4177-4180.

167. G. LeBlanc, K. M. Winter, W. B. Crosby, G. K. Jennings and D. E. Cliffel, *Advanced Energy Materials*, 2014, **4**, 1301953-n/a.

168. I. Carmeli, M. Mangold, L. Frolov, B. Zebli, C. Carmeli, S. Richter and A. W. Holleitner, *Advanced Materials*, 2007, **19**, 3901-3905.

169. S. M. Kaniber, F. C. Simmel, A. W. Holleitner and I. Carmeli, *Nanotechnology*, 2009, **20**, 345701.

170. S. M. Kaniber, M. Brandstetter, F. C. Simmel, I. Carmeli and A. W. Holleitner, *J Am Chem Soc*, 2010, **132**, 2872-2873.

171. D. Nii, M. Miyachi, Y. Shimada, Y. Nozawa, M. Ito, Y. Homma, S. Ikehira, Y. Yamanoi, H. Nishihara and T. Tomo, *Photosynthesis Research*, 2017, **133**, 155-162.

172. L. Frolov, Y. Rosenwaks, S. Richter, C. Carmeli and I. Carmeli, *The Journal of Physical Chemistry C*, 2008, **112**, 13426-13430.

173. V. V. Nikandrov, Y. V. Borisova, E. A. Bocharov, M. A. Usachev, G. V. Nizova, V. A. Nadtochenko, E. P. Lukashev, B. V. Trubitsin, A. N. Tikhonov, V. N. Kurashov, M. D. Mamedov and A. Y. Semenov, *High Energy Chemistry*, 2012, **46**, 200-205.

174. O. Yehezkeli, R. Tel-Vered, D. Michaeli, R. Nechushtai and I. Willner, *Small*, 2013, **9**, 2970-2978.

175. K. Ocakoglu, T. Krupnik, B. van den Bosch, E. Harputlu, M. P. Gullo, J. D. J. Olmos, S. Yildirimcan, R. K. Gupta, F. Yakuphanoglu, A. Barbieri, J. N. H. Reek and J. Kargul, *Advanced Functional Materials*, 2014, **24**, 7467-7477.

176. E. A. Gizzie, J. Scott Niezgoda, M. T. Robinson, A. G. Harris, G. Kane Jennings, S. J. Rosenthal and D. E. Cliffel, *Energy & Environmental Science*, 2015, **8**, 3572-3576.

177. A. Efrati, C.-H. Lu, D. Michaeli, R. Nechushtai, S. Alsaoub, W. Schuhmann and I. Willner, *Nature Energy*, 2016, **1**, 15021.

178. K. Peters, H. N. Lokupitiya, D. Sarauli, M. Labs, M. Pribil, J. Rathouský, A. Kuhn, D. Leister, M. Stefik and D. Fattakhova-Rohlfing, *Advanced Functional Materials*, 2016, **26**, 6682-6692.

179. P. N. Ciesielski, C. J. Faulkner, M. T. Irwin, J. M. Gregory, N. H. Tolk, D. E. Cliffel and G. K. Jennings, *Advanced Functional Materials*, 2010, **20**, 4048-4054.

180. S. Iijima and T. Ichihashi, *Nature*, 1993, **363**, 603.

181. D. S. Bethune, C. H. Kiang, M. S. de Vries, G. Gorman, R. Savoy, J. Vazquez and R. Beyers, *Nature*, 1993, **363**, 605.

182. S. Iijima, *Nature*, 1991, **354**, 56.

183. S. Iijima, *Physica B: Condensed Matter*, 2002, **323**, 1-5.

184. R. S. Ruoff and D. C. Lorents, *Carbon*, 1995, **33**, 925-930.

185. R. S. Ruoff, D. Qian and W. K. Liu, *Comptes Rendus Physique*, 2003, **4**, 993-1008.

186. Z. K. Tang, L. Zhang, N. Wang, X. X. Zhang, G. H. Wen, G. D. Li, J. N. Wang, C. T. Chan and P. Sheng, *Science*, 2001, **292**, 2462.

187. M. S. Dresselhaus, G. Dresselhaus and R. Saito, *Carbon*, 1995, **33**, 883-891.

188. W.-K. Tse, E. H. Hwang and S. Das Sarma, *Applied Physics Letters*, 2008, **93**, 023128.

189. J. Baringhaus, M. Ruan, F. Edler, A. Tejeda, M. Sicot, A. Taleb-Ibrahimi, A.-P. Li, Z. Jiang, E. H. Conrad, C. Berger, C. Tegenkamp and W. A. de Heer, *Nature*, 2014, **506**, 349.

190. S. Hong and S. Myung, *Nature Nanotechnology*, 2007, **2**, 207.

191. M. Pumera, *Chemistry – A European Journal*, 2009, **15**, 4970-4978.

192. C. E. Banks, R. R. Moore, T. J. Davies and R. G. Compton, *Chemical Communications*, 2004, DOI: 10.1039/B406174H, 1804-1805.

193. C. E. Banks, T. J. Davies, G. G. Wildgoose and R. G. Compton, *Chemical Communications*, 2005, DOI: 10.1039/B413177K, 829-841.

194. R. H. Baughman, A. A. Zakhidov and W. A. de Heer, *Science*, 2002, **297**, 787-792.

195. M. F. L. De Volder, S. H. Tawfick, R. H. Baughman and A. J. Hart, *Science*, 2013, **339**, 535-539.

196. J. Li, H. T. Ng, A. Cassell, W. Fan, H. Chen, Q. Ye, J. Koehne, J. Han and M. Meyyappan, *Nano Letters*, 2003, **3**, 597-602.

197. Z. Zhu, L. Garcia-Gancedo, A. J. Flewitt, H. Xie, F. Moussy and W. I. Milne, *Sensors*, 2012, **12**.

198. Y. Lin, F. Lu, Y. Tu and Z. Ren, *Nano Letters*, 2004, **4**, 191-195.

199. S. Roy, H. Vedala and W. Choi, *Nanotechnology*, 2006, **17**, S14-S18.

200. A. Wisitsoraat, C. Karuwan, K. Wong-ek, D. Phokharatkul, P. Sritongkham and A. Tuantranont, *Sensors*, 2009, **9**.

201. M.-L. Ye, B. Xu and W.-D. Zhang, *Microchimica Acta*, 2011, **172**, 439-446.

202. R. Devasenathipathy, C. Karuppiah, S.-M. Chen, V. Mani, V. S. Vasantha and S. Ramaraj, *Microchimica Acta*, 2015, **182**, 727-735.

203. G. Yang, Y. Chen, L. Li and Y. Yang, *Clinica Chimica Acta*, 2011, **412**, 1544-1549.

204. L.-C. Jiang and W.-D. Zhang, *Electroanalysis*, 2009, **21**, 1811-1815.

205. H.-F. Cui, Y.-H. Cui, Y.-L. Sun, K. Zhang and W.-D. Zhang, *Enhancement of dopamine sensing by layer-by-layer assembly of PVI–dmeOs and Nafion on carbon nanotubes*, 2010.

206. A. C. Dillon, K. M. Jones, T. A. Bekkedahl, C. H. Kiang, D. S. Bethune and M. J. Heben, *Nature*, 1997, **386**, 377.

207. C. Liu, Y. Y. Fan, M. Liu, H. T. Cong, H. M. Cheng and M. S. Dresselhaus, *Science*, 1999, **286**, 1127-1129.

208. S. M. Lee and Y. H. Lee, *Applied Physics Letters*, 2000, **76**, 2877-2879.

209. H.-M. Cheng, Q.-H. Yang and C. Liu, *Carbon*, 2001, **39**, 1447-1454.

210. K. Gong, F. Du, Z. Xia, M. Durstock and L. Dai, *Science*, 2009, **323**, 760-764.

211. M. Holzinger, A. Le Goff and S. Cosnier, *Electrochimica Acta*, 2012, **82**, 179-190.

212. V. Scherbahn, M. T. Putze, B. Dietzel, T. Heinlein, J. J. Schneider and F. Lisdat, *Biosensors and Bioelectronics*, 2014, **61**, 631-638.

213. L. Hussein, G. Urban and M. Krüger, *Physical Chemistry Chemical Physics*, 2011, **13**, 5831-5839.

214. C. Bunte, L. Hussein and G. A. Urban, *Journal of Power Sources*, 2014, **247**, 579-586.

215. K. Elouarzaki, M. Bourourou, M. Holzinger, A. Le Goff, R. S. Marks and S. Cosnier, *Energy & Environmental Science*, 2015, **8**, 2069-2074.

216. A. Le Goff, M. Holzinger and S. Cosnier, *Cellular and Molecular Life Sciences*, 2015, **72**, 941-952.

217. Y.-P. Sun, K. Fu, Y. Lin and W. Huang, *Accounts of Chemical Research*, 2002, **35**, 1096-1104.

218. E. Katz and I. Willner, *Angewandte Chemie International Edition*, 2004, **43**, 6042-6108.

219. J. Wang, M. Musameh and Y. Lin, *Journal of the American Chemical Society*, 2003, **125**, 2408-2409.

220. M. J. O'Connell, P. Boul, L. M. Ericson, C. Huffman, Y. Wang, E. Haroz, C. Kuper, J. Tour, K. D. Ausman and R. E. Smalley, *Chemical Physics Letters*, 2001, **342**, 265-271.

221. E. P. Dillon, C. A. Crouse and A. R. Barron, *ACS Nano*, 2008, **2**, 156-164.

222. H. Hu, Y. Ni, S. K. Mandal, V. Montana, B. Zhao, R. C. Haddon and V. Parpura, *The Journal of Physical Chemistry B*, 2005, **109**, 4285-4289.

223. A. Star, J. F. Stoddart, D. Steuerman, M. Diehl, A. Boukai, W. Wong Eric, X. Yang, S.-W. Chung, H. Choi and R. Heath James, *Angewandte Chemie*, 2001, **113**, 1771-1775.

224. F. Lisdat, D. Sarauli, V. Scherbahn, G. Göbel, M. Putze, T. Heinlein and J. J. Schneider, *Meeting Abstracts*, 2014, **MA2014-01**, 974.

225. G. Göbel, V. Scherbahn, M. Putze, B. Dietzel, T. Heinlein, J. J. Schneider and F. Lisdat, *Meeting Abstracts*, 2015, **MA2015-02**, 1198.

226. G. Fusco, G. Göbel, R. Zanoni, E. Kornejew, G. Favero, F. Mazzei and F. Lisdat, *Electrochimica Acta*, 2017, **248**, 64-74.

227. G. Fusco, G. Göbel, R. Zanoni, M. P. Bracciale, G. Favero, F. Mazzei and F. Lisdat, *Biosensors and Bioelectronics*, 2018, **112**, 8-17.

228. J. Cami, J. Bernard-Salas, E. Peeters and S. E. Malek, *Science*, 2010, **329**, 1180.

229. P. Ehrenfreund and B. H. Foing, *Science*, 2010, **329**, 1159.

230. H. W. Kroto, J. R. Heath, S. C. O'Brien, R. F. Curl and R. E. Smalley, *Nature*, 1985, **318**, 162.

231. K. Paneer Selvam, A. L Himaja and S. Singh, *Carbon-allotropes: Synthesis methods, applications and future perspectives*, 2014.

232. P. W. Fowler and A. Ceulemans, *The Journal of Physical Chemistry*, 1995, **99**, 508-510.

233. P. C. Eklund, A. M. Rao, Y. Wang, P. Zhou, K.-A. Wang, J. M. Holden, M. S. Dresselhaus and G. Dresselhaus, *Thin Solid Films*, 1995, **257**, 211-232.

234. R. Hesper, L. H. Tjeng and G. A. Sawatzky, *EPL (Europhysics Letters)*, 1997, **40**, 177.

235. W. Andreoni, F. Gygi and M. Parrinello, *Chemical Physics Letters*, 1992, **190**, 159-162.

236. K. Harigaya, *Chemical Physics Letters*, 1992, **189**, 79-83.

237. S. Saito and A. Oshiyama, *Physical Review B*, 1991, **44**, 11532-11535.

238. L. Echegoyen and L. E. Echegoyen, *Accounts of Chemical Research*, 1998, **31**, 593-601.

239. F. Zhou, C. Jehoulet and A. J. Bard, *Journal of the American Chemical Society*, 1992, **114**, 11004-11006.

240. Q. Xie, E. Perez-Cordero and L. Echegoyen, *Journal of the American Chemical Society*, 1992, **114**, 3978-3980.

241. D. Dubois, G. Moninot, W. Kutner, M. T. Jones and K. M. Kadish, *The Journal of Physical Chemistry*, 1992, **96**, 7137-7145.

242. J. Chlistunoff, D. Cliffel and A. J. Bard, *Thin Solid Films*, 1995, **257**, 166-184.

243. A. Szücs, M. Tölgyesi, E. Szücs, J. B. Nagy and M. Novák, *Journal of Electroanalytical Chemistry*, 1997, **429**, 27-35.

244. Á. Szűcs, M. Tölgyesi, M. Csiszár, J. B. Nagy and M. Novák, *Electrochimica Acta*, 1998, **44**, 613-621.

245. C.-H. Chen, H.-W. Chang and J.-S. Shih, *Sensors and Actuators B: Chemical*, 2007, **123**, 1025-1033.

246. V. G. Gavalas and N. A. Chaniotakis, *Analytica Chimica Acta*, 2000, **409**, 131-135.

247. L.-H. Lin and J.-S. Shih, *Journal of the Chinese Chemical Society*, 2011, **58**, 228-235.

248. M. Cassell Alan, A. Scrivens Walter and M. Tour James, *Angewandte Chemie International Edition*, 1998, **37**, 1528-1531.

249. D.-W. Pang, Y.-D. Zhao, P.-F. Fang, J.-K. Cheng, Y.-Y. Chen, Y.-P. Qi and H. D. Abruña, *Journal of Electroanalytical Chemistry*, 2004, **567**, 339-349.

250. K. Saeedfar, Y. L. Heng, L. T. Ling and M. Rezayi, *Sensors*, 2013, **13**.

251. Y.-F. Gao, T. Yang, X.-L. Yang, Y.-S. Zhang, B.-L. Xiao, J. Hong, N. Sheibani, H. Ghourchian, T. Hong and A. A. Moosavi-Movahedi, *Biosensors and Bioelectronics*, 2014, **60**, 30-34.

252. F. Patolsky, G. Tao, E. Katz and I. Willner, *Journal of Electroanalytical Chemistry*, 1998, **454**, 9-13.

253. C.-W. Chuang and J.-S. Shih, *Sensors and Actuators B: Chemical*, 2001, **81**, 1-8.

254. L.-H. Lin and J.-S. Shih, *Journal of the Chinese Chemical Society*, 2011, **58**, 228-235.

255. A. Kurz, C. M. Halliwell, J. J. Davis, H. Allen O. Hill, A. Kurz and G. W. Canters, *Chemical Communications*, 1998, DOI: 10.1039/A708026C, 433-434.

256. M. Csiszár, Á. Szűcs, M. Tölgyesi, Á. Mechler, J. B. Nagy and M. Novák, *Journal of Electroanalytical Chemistry*, 2001, **497**, 69-74.

257. M. Braun, S. Atalick, M. Guldi Dirk, H. Lanig, M. Brettreich, S. Burghardt, M. Hatzimarinaki, E. Ravanelli, M. Prato, R. van Eldik and A. Hirsch, *Chemistry – A European Journal*, 2003, **9**, 3867-3875.

258. F. D'Souza, L. M. Rogers, E. S. O'Dell, A. Kochman and W. Kutner, *Bioelectrochemistry*, 2005, **66**, 35-40.

259. J. Z. Zhang, K. P. Sokol, N. Paul, E. Romero, R. van Grondelle and E. Reisner, *Nature chemical biology*, 2016, **12**, 1046-1052.

260. C. Kisker, H. Schindelin, A. Pacheco, W. A. Wehbi, R. M. Garrett, K. V. Rajagopalan, J. H. Enemark and D. C. Rees, *Cell*, 1997, **91**, 973-983.

261. H. J. Cohen, I. Fridovich and K. V. Rajagopalan, *Journal of Biological Chemistry*, 1971, **246**, 374-382.

262. H. J. Cohen, R. T. Drew, J. L. Johnson and K. V. Rajagopalan, *Proceedings of the National Academy of Sciences*, 1973, **70**, 3655.

263. J. L. Johnson and K. V. Rajagopalan, *The Journal of Clinical Investigation*, 1976, **58**, 543-550.

264. K. V. Rajagopalan, in *Molybdenum and Molybdenum-Containing Enzymes*, Pergamon, 1980, DOI: https://doi.org/10.1016/B978-0-08-024398-6.50012-2, pp. 241-272.

265. L. G. Howell and I. Fridovich, *Journal of Biological Chemistry*, 1968, **243**, 5941-5947.

266. S. J. Elliott, A. E. McElhaney, C. Feng, J. H. Enemark and F. A. Armstrong, *Journal of the American Chemical Society*, 2002, **124**, 11612-11613.

267. E. E. Ferapontova and L. Gorton, *Bioelectrochemistry*, 2005, **66**, 55-63.

268. S. Frasca, O. Rojas, J. Salewski, B. Neumann, K. Stiba, I. M. Weidinger, B. Tiersch, S. Leimkühler, J. Koetz and U. Wollenberger, *Bioelectrochemistry*, 2012, **87**, 33-41.

269. T. Zeng, S. Leimkühler, J. Koetz and U. Wollenberger, *ACS Applied Materials & Interfaces*, 2015, **7**, 21487-21494.

270. L. A. Coury, R. W. Murray, J. L. Johnson and K. V. Rajagopalan, *The Journal of Physical Chemistry*, 1991, **95**, 6034-6040.

271. L. A. Coury, L. Yang and R. W. Murray, *Analytical Chemistry*, 1993, **65**, 242-246.

272. R. Dronov, D. G. Kurth, H. Möhwald, R. Spricigo, S. Leimkühler, U. Wollenberger, K. V. Rajagopalan, F. W. Scheller and F. Lisdat, *Journal of the American Chemical Society*, 2008, **130**, 1122-1123.

273. R. Spricigo, R. Dronov, K. V. Rajagopalan, F. Lisdat, S. Leimkühler, F. W. Scheller and U. Wollenberger, *Soft Matter*, 2008, **4**, 972-978.

274. A. K. Abass, J. P. Hart and D. Cowell, *Sensors and Actuators B: Chemical*, 2000, **62**, 148-153.

275. R. Dronov, D. G. Kurth, H. Möhwald, F. W. Scheller and F. Lisdat, *Angew Chem*, 2008, **120**.

276. R. Spricigo, R. Dronov, K. V. Rajagolan, F. Lisdat, S. Leimkühler, F. W. Scheller and U. Wollenberger, *Soft Matter*, 2008, **4**.

277. M. Sezer, R. Spricigo, T. Utesch, D. Millo, S. Leimkuehler, M. A. Mroginski, U. Wollenberger, P. Hildebrandt and I. M. Weidinger, *Physical Chemistry Chemical Physics*, 2010, **12**, 7894-7903.

278. B. Bahmani, F. Moztarzadeh, M. Rabiee and M. Tahriri, *Synthetic Metals*, 2010, **160**, 2653-2657.

279. M. Mann, C. K. Meng and J. B. Fenn, *Analytical Chemistry*, 1989, **61**, 1702-1708.

280. R. E. Dickerson, M. L. Kopka, C. L. Borders, J. Varnum, J. E. Weinzierl and E. Margoliash, *Journal of molecular biology*, 1967, **29**, 77-95.

281. G. W. Bushnell, G. V. Louie and G. D. Brayer, *Journal of molecular biology*, 1990, **214**, 585-595.

282. T. M. Nahir and E. F. Bowden, *Journal of Electroanalytical Chemistry*, 1996, **410**, 9-13.

283. M. C. Leopold and E. F. Bowden, *Langmuir*, 2002, **18**, 2239-2245.

284. K. Nakano, T. Yoshitake, Y. Yamashita and E. F. Bowden, *Langmuir*, 2007, **23**, 6270-6275.

285. T. Liu, J. Zhong, X. Gan, C. Fan, G. Li and N. Matsuda, *ChemPhysChem*, 2003, **4**, 1364-1366.

286. D. Millo, A. Ranieri, W. Koot, C. Gooijer and G. van der Zwan, *Analytical Chemistry*, 2006, **78**, 5622-5625.

287. O. Ikeda, M. Ohtani, T. Yamaguchi and A. Komura, *Electrochimica Acta*, 1998, **43**, 833-839.

288. J. Wang, M. Li, Z. Shi, N. Li and Z. Gu, *Analytical Chemistry*, 2002, **74**, 1993-1997.

289. J. Wang, M. Li, Z. Shi, N. Li and Z. Gu, *Analytical Chemistry*, 2002, **74**, 1993-1997.

290. G.-C. Zhao, Z.-Z. Yin, L. Zhang and X.-W. Wei, *Electrochemistry Communications*, 2005, **7**, 256-260.

291. F. D'Souza, L. M. Rogers, E. S. O'Dell, A. Kochman and W. Kutner, *Bioelectrochemistry*, 2005, **66**, 35-40.

292. A. El Kasmi, M. C. Leopold, R. Galligan, R. T. Robertson, S. S. Saavedra, K. El Kacemi and E. F. Bowden, *Electrochemistry Communications*, 2002, **4**, 177-181.

293. X. Jiang, L. Zhang and S. Dong, *Electrochemistry Communications*, 2006, **8**, 1137-1141.

294. K. R. Stieger, S. C. Feifel, H. Lokstein and F. Lisdat, *Physical Chemistry Chemical Physics*, 2014, **16**, 15667-15674.

295. C. Wettstein, H. Möhwald and F. Lisdat, *Bioelectrochemistry*, 2012, **88**, 97-102.

296. C. Wettstein, C. Kyne, A. M. Doolan, H. Mohwald, P. B. Crowley and F. Lisdat, *Nanoscale*, 2014, **6**, 13779-13786.

297. A. Kölsch, H. Mahdi, K. Stieger, S. Feifel, J. Kern, F. Müh, F. Lisdat, H. Lokstein and A. Zouni, *Insights into the binding behavior of native and non-native cytochromes to Photosystem I from Thermosynechococcus elongatus*, 2018.

298. C. Feifel Sven, A. Kapp, R. Ludwig and F. Lisdat, *Angewandte Chemie International Edition*, 2014, **53**, 5676-5679.

299. R. Spricigo, R. Dronov, F. Lisdat, S. Leimkühler, F. W. Scheller and U. Wollenberger, *Analytical and Bioanalytical Chemistry*, 2009, **393**, 225-233.

300. D. Ciornii, S. C. Feifel, M. Hejazi, A. Kölsch, H. Lokstein, A. Zouni and F. Lisdat, *physica status solidi (a)*, 2017, **214**, 1700017-n/a.

301. F. Wegerich, P. Turano, M. Allegrozzi, H. Möhwald and F. Lisdat, *Langmuir*, 2011, **27**, 4202-4211.

302. C. Wettstein, K. Kano, D. Schäfer, U. Wollenberger and F. Lisdat, *Analytical Chemistry*, 2016, **88**, 6382-6389.

303. J. Lee, J. Im and S. Kim, *Bioelectrochemistry*, 2016, **108**, 21-27.

304. S. C. Feifel, H. Lokstein, M. Hejazi, A. Zouni and F. Lisdat, *Langmuir*, 2015, **31**, 10590-10598.

305. Y. Zhang, N. M. Magdaong, M. Shen, H. A. Frank and J. F. Rusling, *ChemistryOpen*, 2015, **4**, 111-114.

306. M. Byrdin, P. Jordan, N. Krauss, P. Fromme, D. Stehlik and E. Schlodder, *Biophysical Journal*, 2002, **83**, 433-457.

307. J. O. Calkins, Y. Umasankar, H. O'Neill and R. P. Ramasamy, *Energy & Environmental Science*, 2013, **6**, 1891-1900.

308. L. Nagy, M. Magyar, T. Szabó, K. Hajdu, L. Giotta, M. Dorogi and F. Milano, *Current Protein & Peptide Science*, 2014, **15**, 363-373.

309. N. Sekar and R. P. Ramasamy, *Journal of Photochemistry and Photobiology C: Photochemistry Reviews*, 2015, **22**, 19-33.

310. N. Sekar and R. P. Ramasamy, *Journal of Photochemistry and Photobiology C: Photochemistry Reviews*, 2015, **22**, 19-33.

311. K. Nguyen and B. D. Bruce, *Biochimica et Biophysica Acta (BBA) - Bioenergetics*, 2014, **1837**, 1553-1566.

312. A. T. Brunger, P. D. Adams, P. Fromme, R. Fromme, M. Levitt and G. F. Schröder, *Structure (London, England : 1993)*, 2012, **20**, 957-966.

313. M. J. Holst and F. Saied, *Journal of Computational Chemistry*, 1995, **16**, 337-364.

314. T. W. Ebbesen, H. J. Lezec, H. Hiura, J. W. Bennett, H. F. Ghaemi and T. Thio, *Nature*, 1996, **382**, 54-56.

315. J. W. G. Wilder, L. C. Venema, A. G. Rinzler, R. E. Smalley and C. Dekker, *Nature*, 1998, **391**, 59-62.

316. T. W. Odom, J.-L. Huang, P. Kim and C. M. Lieber, *Nature*, 1998, **391**, 62-64.

317. A. Peigney, C. Laurent, E. Flahaut, R. R. Bacsa and A. Rousset, *Carbon*, 2001, **39**, 507-514.

318. P. Serp, M. Corrias and P. Kalck, *Applied Catalysis A: General*, 2003, **253**, 337-358.

319. D. Ivnitski, K. Artyushkova, R. A. Rincón, P. Atanassov, H. R. Luckarift and G. R. Johnson, *Small*, 2008, **4**, 357-364.

320. W. Feng and P. Ji, *Biotechnology Advances*, 2011, **29**, 889-895.

321. B. Munge, G. Liu, G. Collins and J. Wang, *Analytical Chemistry*, 2005, **77**, 4662-4666.

322. A. Modi, N. Koratkar, E. Lass, B. Wei and P. M. Ajayan, *Nature*, 2003, **424**, 171-174.

323. S. Chopra, A. Pham, J. Gaillard, A. Parker and A. M. Rao, *Applied Physics Letters*, 2002, **80**, 4632-4634.

324. A. Star, V. Joshi, S. Skarupo, D. Thomas and J.-C. P. Gabriel, *The Journal of Physical Chemistry B*, 2006, **110**, 21014-21020.

325. M.-H. Ham, J. H. Choi, A. A. Boghossian, E. S. Jeng, R. A. Graff, D. A. Heller, A. C. Chang, A. Mattis, T. H. Bayburt, Y. V. Grinkova, A. S. Zeiger, K. J. Van Vliet, E. K. Hobbie, S. G. Sligar, C. A. Wraight and M. S. Strano, *Nat Chem*, 2010, **2**, 929-936.

326. T. Szabó, M. Magyar, K. Hajdu, M. Dorogi, E. Nyerki, T. Tóth, M. Lingvay, G. Garab, K. Hernádi and L. Nagy, *Nanoscale Research Letters*, 2015, **10**, 458.

327. N. Lebedev, S. A. Trammell, S. Tsoi, A. Spano, J. H. Kim, J. Xu, M. E. Twigg and J. M. Schnur, *Langmuir*, 2008, **24**, 8871-8876.

328. J. Kern, B. Loll, C. Lüneberg, D. DiFiore, J. Biesiadka, K. D. Irrgang and A. Zouni, *Biochimica et Biophysica Acta (BBA) - Bioenergetics*, 2005, **1706**, 147-157.

329. H. K. Lichtenthaler, in *Methods in Enzymology*, Academic Press, 1987, vol. Volume 148, pp. 350-382.

330. P. V. Iyer and L. Ananthanarayan, *Process Biochemistry*, 2008, **43**, 1019-1032.

331. B. Willner, E. Katz and I. Willner, *Current Opinion in Biotechnology*, 2006, **17**, 589-596.

332. E. Katz, A. F. Bückmann and I. Willner, *Journal of the American Chemical Society*, 2001, **123**, 10752-10753.

333. N. Mano, F. Mao and A. Heller, *Journal of the American Chemical Society*, 2002, **124**, 12962-12963.

334. A. Bachmeier, V. C. C. Wang, T. W. Woolerton, S. Bell, J. C. Fontecilla-Camps, M. Can, S. W. Ragsdale, Y. S. Chaudhary and F. A. Armstrong, *Journal of the American Chemical Society*, 2013, **135**, 15026-15032.

335. E. Reisner, D. J. Powell, C. Cavazza, J. C. Fontecilla-Camps and F. A. Armstrong, *Journal of the American Chemical Society*, 2009, **131**, 18457-18466.

336. A. Bassegoda, C. Madden, D. W. Wakerley, E. Reisner and J. Hirst, *Journal of the American Chemical Society*, 2014, **136**, 15473-15476.

337. K. Habermüller, M. Mosbach and W. Schuhmann, *Fresenius' Journal of Analytical Chemistry*, 2000, **366**, 560-568.

338. Y. Wu and S. Hu, *Microchimica Acta*, 2007, **159**, 1-17.

339. M. Kato, T. Cardona, A. W. Rutherford and E. Reisner, *Journal of the American Chemical Society*, 2012, **134**, 8332-8335.

340. U. Wollenberger, F. Schubert, D. Pfeiffer and F. W. Scheller, *Trends in Biotechnology*, 1993, **11**, 255-262.

341. D. P. Hickey, M. S. McCammant, F. Giroud, M. S. Sigman and S. D. Minteer, *Journal of the American Chemical Society*, 2014, **136**, 15917-15920.

342. A. Yarman, C. Schulz, C. Sygmund, R. Ludwig, L. Gorton, U. Wollenberger and F. W. Scheller, *Electroanalysis*, 2014, **26**, 2043-2048.

343. S. Schoffelen and J. C. M. van Hest, *Soft Matter*, 2012, **8**, 1736-1746.

344. B. Bulutoglu, K. E. Garcia, F. Wu, S. D. Minteer and S. Banta, *ACS Chemical Biology*, 2016, **11**, 2847-2853.

345. E. Katz and I. Willner, *Journal of the American Chemical Society*, 2003, **125**, 6803-6813.

346. M. K. Beissenhirtz, F. W. Scheller, W. F. M. Stöcklein, D. G. Kurth, H. Möhwald and F. Lisdat, *Angewandte Chemie International Edition*, 2004, **43**, 4357-4360.

347. C.-Y. Lee, B. Reuillard, K. P. Sokol, T. Laftsoglou, C. W. J. Lockwood, S. F. Rowe, E. T. Hwang, J. C. Fontecilla-Camps, L. J. C. Jeuken, J. N. Butt and E. Reisner, *Chemical Communications*, 2016, **52**, 7390-7393.

348. S. C. Feifel, A. Kapp, R. Ludwig and F. Lisdat, *Angewandte Chemie International Edition*, 2014, **53**, 5676-5679.

349. L. M. Utschig, S. R. Soltau and D. M. Tiede, *Current Opinion in Chemical Biology*, 2015, **25**, 1-8.

350. R. A. Voloshin, V. D. Kreslavski, S. K. Zharmukhamedov, V. S. Bedbenov, S. Ramakrishna and S. I. Allakhverdiev, *Biofuel Research Journal*, 2015, **2**, 227-235.

351. C. Tapia, R. D. Milton, G. Pankratova, S. D. Minteer, H.-E. Åkerlund, D. Leech, A. L. De Lacey, M. Pita and L. Gorton, *ChemElectroChem*, 2017, **4**, 90-95.

352. A. Efrati, C.-H. Lu, D. Michaeli, R. Nechushtai, S. Alsaoub, W. Schuhmann and I. Willner, *Nature Energy*, 2016, **1**, 15021.

353. M. Kato, J. Z. Zhang, N. Paul and E. Reisner, *Chemical Society Reviews*, 2014, **43**, 6485-6497.

354. F. Müh and A. Zouni, *Biochimica et Biophysica Acta (BBA) - Biomembranes*, 2008, **1778**, 2298-2307.

355. S. J. Elliott, A. E. McElhaney, C. Feng, J. H. Enemark and F. A. Armstrong, *Journal of the American Chemical Society*, 2002, **124**, 11612-11613.

356. R. Spricigo, R. Dronov, F. Lisdat, S. Leimkühler, F. W. Scheller and U. Wollenberger, *Analytical and Bioanalytical Chemistry*, 2009, **393**, 225-233.

357. M. Sezer, R. Spricigo, T. Utesch, D. Millo, S. Leimkuehler, M. A. Mroginski, U. Wollenberger, P. Hildebrandt and I. M. Weidinger, *Physical Chemistry Chemical Physics*, 2010, **12**, 7894-7903.

358. M. Sezer, R. Spricigo, T. Utesch, D. Millo, S. Leimkuehler, M. A. Mroginski, U. Wollenberger, P. Hildebrandt and I. M. Weidinger, *Physical Chemistry Chemical Physics*, 2010, **12**, 7894-7903.

359. S. Frasca, O. Rojas, J. Salewski, B. Neumann, K. Stiba, I. M. Weidinger, B. Tiersch, S. Leimkühler, J. Koetz and U. Wollenberger, *Bioelectrochemistry*, 2012, **87**, 33-41.

360. S. C. Feifel, K. R. Stieger, A. Kapp, D. Weber, M. Allegrozzi, M. Piccioli, P. Turano and F. Lisdat, *ACS Omega*, 2016, **1**, 1058-1066.

361. A. T. Brunger, P. D. Adams, P. Fromme, R. Fromme, M. Levitt and G. F. Schroder, *Structure*, 2012, **20**, 957-966.

362. T. Takano and R. E. Dickerson, *Proc Natl Acad Sci U S A*, 1980, **77**, 6371-6375.

363. C. Kisker, H. Schindelin, A. Pacheco, W. A. Wehbi, R. M. Garrett, K. V. Rajagopalan, J. H. Enemark and D. C. Rees, *Cell*, 1997, **91**, 973-983.

364. C. Jianwei, Ç. Tahir and A. G. William, III, *Nanotechnology*, 2000, **11**, 65.

365. H. J. Cohen and I. Fridovich, *Journal of Biological Chemistry*, 1971, **246**, 359-366.

366. H. K. Lichtenthaler, *Methods in Enzymology*, 1987, **148**, 350-382.

367. E.-M. Aro, *Ambio*, 2016, **45**, 24-31.

368. R. Agrawal and N. R. Singh, *Annual Review of Chemical and Biomolecular Engineering*, 2010, **1**, 343-364.

369. P. C. Hallenbeck, M. Grogger, M. Mraz and D. Veverka, *Applied Energy*, 2016, **179**, 136-145.

370. R. Höfer and J. Bigorra, *Green Chemistry Letters and Reviews*, 2008, **1**, 79-97.

371. M. Kenisarin and K. Mahkamov, *Renewable and Sustainable Energy Reviews*, 2007, **11**, 1913-1965.

372. E. Y. Katz and A. A. Solov'ev, *Analytica Chimica Acta*, 1992, **266**, 97-106.

373. K. Younghye, S. Seon Ae, L. Jaehun, Y. Ki Dong and N. Ki Tae, *Nanotechnology*, 2014, **25**, 342001.

374. S. K. Ravi and S. C. Tan, *Energy & Environmental Science*, 2015, **8**, 2551-2573.

375. N. Terasaki, in *Solar to Chemical Energy Conversion: Theory and Application*, eds. M. Sugiyama, K. Fujii and S. Nakamura, Springer International Publishing, Cham, 2016, DOI: 10.1007/978-3-319-25400-5_25, pp. 419-435.

376. V. M. Friebe and R. N. Frese, *Current Opinion in Electrochemistry*, 2017, **5**, 126-134.

377. M. Dorogi, Z. Balint, C. Miko, B. Vileno, M. Milas, K. Hernadi, L. Forro, G. Varo and L. Nagy, *The journal of physical chemistry. B*, 2006, **110**, 21473-21479.

378. M. J. Hollander, J. G. Magis, P. Fuchsenberger, T. J. Aartsma, M. R. Jones and R. N. Frese, *Langmuir*, 2011, **27**.

379. I. Lee, J. W. Lee and E. Greenbaum, *Physical Review Letters*, 1997, **79**, 3294-3297.

380. R. R. Tangorra, A. Antonucci, F. Milano, A. Operamolla, F. Italiano, R. Ragni, O. H. Omar, P. Salice, S. Silvestrini, E. Menna, M. Maggini, A. Agostiano, M. Trotta and G. M. Farinola, *MRS Proceedings*, 2015, **1717**.

381. K. Hajdu, T. Szabó, M. Magyar, G. Bencsik, Z. Németh, K. Nagy, A. Magrez, L. Forró, G. Váró, K. Hernádi and L. Nagy, *Phys Status Solidi B*, 2011, **248**.

382. N. Terasaki, M. Iwai, N. Yamamoto, T. Hiraga, S. Yamada and Y. Inoue, *Thin Solid Films*, 2008, **516**, 2553-2557.

383. C. Ley, D. Holtmann, K.-M. Mangold and J. Schrader, *Colloids and Surfaces B: Biointerfaces*, 2011, **88**, 539-551.

384. N. Terasaki, N. Yamamoto, K. Tamada, M. Hattori, T. Hiraga, A. Tohri, I. Sato, M. Iwai, M. Iwai, S. Taguchi, I. Enami, Y. Inoue, Y. Yamanoi, T. Yonezawa, K. Mizuno, M. Murata, H. Nishihara, S. Yoneyama, M. Minakata, T. Ohmori, M. Sakai and M. Fujii, *Biochimica et Biophysica Acta (BBA) - Bioenergetics*, 2007, **1767**, 653-659.

385. E. Darby, G. LeBlanc, E. A. Gizzie, K. M. Winter, G. K. Jennings and D. E. Cliffel, *Langmuir*, 2014, **30**, 8990-8994.

386. M. T. Robinson, M. E. Armbruster, A. Gargye, D. E. Cliffel and G. K. Jennings, *ACS Applied Energy Materials*, 2018, DOI: 10.1021/acsaem.7b00230.

387. G. Chen, F. M. Hijazi, G. LeBlanc, G. Kane Jennings and D. E. Cliffel, *ECS Electrochemistry Letters*, 2013, **2**, H59-H62.

388. K. Hasan, H. Bekir Yildiz, E. Sperling, P. O Conghaile, M. A. Packer, D. Leech, C. Hagerhall and L. Gorton, *Physical Chemistry Chemical Physics*, 2014, **16**, 24676-24680.

389. L. Frolov, O. Wilner, C. Carmeli and I. Carmeli, *Advanced Materials*, 2008, **20**, 263-266.

390. A. Badura, T. Kothe, W. Schuhmann and M. Rogner, *Energy & Environmental Science*, 2011, **4**, 3263-3274.

391. R. Tel-Vered and I. Willner, *ChemElectroChem*, 2014, **1**, 1778-1797.

392. N. Plumeré and M. M. Nowaczyk, in *Biophotoelectrochemistry: From Bioelectrochemistry to Biophotovoltaics*, ed. L. J. C. Jeuken, Springer International Publishing, Cham, 2016, DOI: 10.1007/10_2016_7, pp. 111-136.

393. S. C. Tan, L. I. Crouch, M. R. Jones and M. Welland, *Angewandte Chemie International Edition*, 2012, **51**, 6667-6671.

394. M. T. Robinson, E. A. Gizzie, F. Mwambutsa, D. E. Cliffel and G. K. Jennings, *Current Opinion in Electrochemistry*, 2017, **5**, 211-217.

395. N. Plumeré, O. Rüdiger, A. A. Oughli, R. Williams, J. Vivekananthan, S. Pöller, W. Schuhmann and W. Lubitz, *Nature Chemistry*, 2014, **6**, 822.

396. A. Efrati, R. Tel-Vered, D. Michaeli, R. Nechushtai and I. Willner, *Energy & Environmental Science*, 2013, **6**, 2950-2956.

397. V. M. Friebe, J. D. Delgado, D. J. K. Swainsbury, J. M. Gruber, A. Chanaewa, R. van Grondelle, E. von Hauff, D. Millo, M. R. Jones and R. N. Frese, *Advanced Functional Materials*, 2016, **26**, 285-292.

398. V. M. Friebe, D. Millo, D. J. K. Swainsbury, M. R. Jones and R. N. Frese, *ACS Applied Materials & Interfaces*, 2017, **9**, 23379-23388.

399. A. Kölsch, M. Hejazi, K. R. Stieger, S. C. Feifel, J. F. Kern, F. Müh, F. Lisdat, H. Lokstein and A. Zouni, *Journal of Biological Chemistry*, 2018, **293**, 9090-9100.

400. R. Woods, in *Modern Aspects of Electrochemistry*, eds. J. O. M. Bockris, B. E. Conway and R. E. White, Springer US, Boston, MA, 1996, DOI: 10.1007/978-1-4613-0327-5_5, pp. 401-453.

401. S. Chah, J. Yi, C. M. Pettit, D. Roy and J. H. Fendler, *Langmuir*, 2002, **18**, 314-318.

402. L. Jiang, A. Glidle, C. J. McNeil and J. M. Cooper, *Biosensors and Bioelectronics*, 1997, **12**, 1143-1155.

403. K. V. Gobi, Y. Sato and F. Mizutani, *Electroanalysis*, 2001, **13**, 397-403.

404. S. Berchmans, R. G. Nirmal, G. Prabaharan, A. K. Mishra and V. Yegnaraman, *Journal of Solid State Electrochemistry*, 2005, **10**, 439.

405. R. J. Porra, *Biochimica et Biophysica Acta (BBA) - Bioenergetics*, 1990, **1019**, 137-141.

406. J. Zhao, B. Liu, Y. Zou, C. Xu and J. Kong, *Electrochimica Acta*, 2002, **47**, 2013-2017.

407. D. Mukherjee, M. May, M. Vaughn, B. D. Bruce and B. Khomami, *Langmuir*, 2010, **26**, 16048-16054.

408. M. Giustini, M. Autullo, M. Mennuni, G. Palazzo and A. Mallardi, *Sensors and Actuators B: Chemical*, 2012, **163**, 69-75.

409. D. E. K. Felix Haurowitz, *Journal*, 2018, 02.14, 6-7.

410. B. S. Ko, B. Babcock, G. K. Jennings, S. G. Tilden, R. R. Peterson, D. Cliffel and E. Greenbaum, *Langmuir*, 2004, **20**, 4033-4038.

411. D. Mukherjee, M. May, M. Vaughn, B. D. Bruce and B. Khomami, *Langmuir*, 2010, **26**, 16048-16054.

412. M. Ciobanu, H. A. Kincaid, G. K. Jennings and D. E. Cliffel, *Langmuir*, 2005, **21**, 692-698.

413. Y. Yamanoi, N. Terasaki, M. Miyachi, Y. Inoue and H. Nishihara, *Thin Solid Films*, 2012, **520**, 5123-5127.

414. T. Kothe, S. Pöller, F. Zhao, P. Fortgang, M. Rögner, W. Schuhmann and N. Plumeré, *Chemistry – A European Journal*, 2014, **20**, 11029-11034.

415. S. C. Feifel, H. Lokstein, M. Hejazi, A. Zouni and F. Lisdat, *Langmuir*, 2015, **31**, 10590-10598.

416. A. J. McCormick, P. Bombelli, R. W. Bradley, R. Thorne, T. Wenzel and C. J. Howe, *Energy & Environmental Science*, 2015, **8**, 1092-1109.

417. P. I. Gordiichuk, G.-J. A. H. Wetzelaer, D. Rimmerman, A. Gruszka, J. W. de Vries, M. Saller, D. A. Gautier, S. Catarci, D. Pesce, S. Richter, P. W. M. Blom and A. Herrmann, *Advanced Materials*, 2014, **26**, 4863-4869.

418. V. Hartmann, V. T. Kothe, S. Poller, E. El-Mohsnawy, M. M. Nowaczyk, N. Plumere, W. Schuhmann and M. Rogner, *Chem Phys*, 2014, **16**.

419. E. Y. Katz, A. Y. Shkuropatov and V. A. Shuvalov, *Journal of Electroanalytical Chemistry and Interfacial Electrochemistry*, 1990, **298**, 239-247.

420. E. Katz, *Journal of Electroanalytical Chemistry*, 1994, **365**, 157-164.

421. E. Y. Katz, A. Y. Shkuropatov, O. I. Vagabova and V. A. Shuvalov, *Biochimica et Biophysica Acta (BBA) - Bioenergetics*, 1989, **976**, 121-128.

422. V. M. Friebe, D. J. K. Swainsbury, P. K. Fyfe, W. van der Heijden, M. R. Jones and R. N. Frese, *Biochimica et Biophysica Acta (BBA) - Bioenergetics*, 2016, **1857**, 1925-1934.

423. J. Lee, J. Im and S. Kim, *Bioelectrochemistry*, 2016, **108**, 21-27.

424. D. C. Goetze and R. Carpentier, *Journal of Photochemistry and Photobiology B: Biology*, 1990, **8**, 17-26.

425. H. Hamidi, K. Hasan, S. C. Emek, Y. Dilgin, H.-E. Åkerlund, P.-Å. Albertsson, D. Leech and L. Gorton, *ChemSusChem*, 2015, **8**, 990-993.

426. J. Lee and S. Kim, *Electrochemistry Communications*, 2014, **49**, 55-59.

427. D. C. I. Yao, D. C. Brune and W. F. J. Vermaas, *FEBS Letters*, 2012, **586**, 169-173.

428. H. T. Witt, *Berichte der Bunsengesellschaft für physikalische Chemie*, 1996, **100**, 1923-1942.

429. K. Peters, H. N. Lokupitiya, D. Sarauli, M. Labs, M. Pribil, J. Rathouský, A. Kuhn, D. Leister, M. Stefik and D. Fattakhova-Rohlfing, *Advanced Functional Materials*, 2016, **26**, 6682-6692.

430. T. Minami, *Transparent Conducting Oxide Semiconductors for Transparent Electrodes*, 2005.

431. B. Reuillard, K. H. Ly, P. Hildebrandt, L. J. C. Jeuken, J. N. Butt and E. Reisner, *Journal of the American Chemical Society*, 2017, **139**, 3324-3327.

432. M. Kato, T. Cardona, A. W. Rutherford and E. Reisner, *Journal of the American Chemical Society*, 2012, **134**, 8332-8335.

433. X. Fang, K. P. Sokol, N. Heidary, T. A. Kandiel, J. Z. Zhang and E. Reisner, *Nano Letters*, 2019, **19**, 1844-1850.

434. P. G. Hoertz, Z. Chen, C. A. Kent and T. J. Meyer, *Inorganic Chemistry*, 2010, **49**, 8179-8181.

435. M. Riedel, J. Wersig, A. Ruff, W. Schuhmann, A. Zouni and F. Lisdat, *Angewandte Chemie International Edition*, 2019, **58**, 801-805.

436. E. Arsenault, N. Soheilnia and G. A. Ozin, *ACS Nano*, 2011, **5**, 2984-2988.

437. Z. Wang, X. Li, H. Ling, C. K. Tan, L. P. Yeo, A. C. Grimsdale and A. I. Y. Tok, *Small*, 2018, **14**, 1800395.

438. T. Hitosugi, N. Yamada, S. Nakao, Y. Hirose and T. Hasegawa, *physica status solidi (a)*, 2010, **207**, 1529-1537.

439. M. Wang, J. Bai, F. Le Formal, S.-J. Moon, L. Cevey-Ha, R. Humphry-Baker, C. Grätzel, S. M. Zakeeruddin and M. Grätzel, *The Journal of Physical Chemistry C*, 2012, **116**, 3266-3273.

440. B. Ge and F. Lisdat, *Analytica Chimica Acta*, 2002, **454**, 53-64.

441. J. Wei, H. Liu, A. R. Dick, H. Yamamoto, Y. He and D. H. Waldeck, *Journal of the American Chemical Society*, 2002, **124**, 9591-9599.

442. K. Song, Y. Jung, Y. Kim, A. Kim, J. K. Hwang, M. M. Sung and J. Moon, *Journal of Materials Chemistry*, 2011, **21**, 14646-14654.

443. G. Frank and H. Köstlin, *Applied Physics A*, 1982, **27**, 197-206.

444. R. Bel Hadj Tahar, T. Ban, Y. Ohya and Y. Takahashi, *Journal of Applied Physics*, 1998, **83**, 2631-2645.

445. K. Y. Kim and S. B. Park, *Materials Chemistry and Physics*, 2004, **86**, 210-221.

446. A. F. Runge and S. S. Saavedra, *Langmuir*, 2003, **19**, 9418-9424.

447. A. El Kasmi, M. C. Leopold, R. Galligan, R. T. Robertson, S. S. Saavedra, K. El Kacemi and E. F. Bowden, *Electrochemistry Communications*, 2002, **4**, 177-181.

448. S. Frasca, T. von Graberg, J.-J. Feng, A. Thomas, B. M. Smarsly, I. M. Weidinger, F. W. Scheller, P. Hildebrandt and U. Wollenberger, *ChemCatChem*, 2010, **2**, 839-845.

449. D. Schaming, C. Renault, R. T. Tucker, S. Lau-Truong, J. Aubard, M. J. Brett, V. Balland and B. Limoges, *Langmuir*, 2012, **28**, 14065-14072.

450. A. Bandyopadhyay and A. J. Pal, *Advanced Materials*, 2003, **15**, 1949-1952.

451. P. Kwan, D. Schmitt, A. M. Volosin, C. L. McIntosh, D.-K. Seo and A. K. Jones, *Chemical Communications*, 2011, **47**, 12367-12369.

452. V. Müller, J. Rathousky and D. Fattakhova-Rohlfing, *Electrochimica Acta*, 2014, **116**, 1-8.

453. J. Li and N. Wu, *Catalysis Science & Technology*, 2015, **5**, 1360-1384.

454. F. Zhao, A. Ruff, M. Rögner, W. Schuhmann and F. Conzuelo, *Journal of the American Chemical Society*, 2019, DOI: 10.1021/jacs.8b13869.

455. A. Kölsch, M. Hejazi, K. R. Stieger, S. C. Feifel, J. F. Kern, F. Müh, F. Lisdat, H. Lokstein and A. Zouni, *Journal of Biological Chemistry*, 2018, **293**, 9090-9100.

456. E. Laviron, *Journal of Electroanalytical Chemistry and Interfacial Electrochemistry*, 1979, **101**, 19-28.

457. I. Carmeli, L. Frolov, C. Carmeli and S. Richter, *Journal of the American Chemical Society*, 2007, **129**, 12352-12353.

458. M.-H. Ham, J. H. Choi, A. A. Boghossian, E. S. Jeng, R. A. Graff, D. A. Heller, A. C. Chang, A. Mattis, T. H. Bayburt, Y. V. Grinkova, A. S. Zeiger, K. J. Van Vliet, E. K. Hobbie, S. G. Sligar, C. A. Wraight and M. S. Strano, *Nature chemistry*, 2010, **2**, 929-936.

459. N. Lebedev, S. A. Trammell, S. Tsoi, A. Spano, J. H. Kim, J. Xu, M. E. Twigg and J. M. Schnur, *Langmuir*, 2008, **24**, 8871-8876.

460. K. R. Stieger, S. C. Feifel, H. Lokstein and F. Lisdat, *Physical Chemistry Chemical Physics*, 2014, **16**, 15667-15674.

461. S. C. Feifel, K. R. Stieger, H. Lokstein, H. Lux and F. Lisdat, *Journal of Materials Chemistry A*, 2015, **3**, 12188-12196.

462. T. Kothe, S. Pöller, F. Zhao, P. Fortgang, M. Rögner, W. Schuhmann and N. Plumeré, *Chemistry – A European Journal*, 2014, **20**, 11029-11034.

463. D. Yu, M. Wang, G. Zhu, B. Ge, S. Liu and F. Huang, *Scientific reports*, 2015, **5**, 9375-9375.

464. S. C. Feifel, K. R. Stieger, H. Lokstein, H. Lux and F. Lisdat, *Journal of Materials Chemistry A*, 2015, **3**, 12188-12196.

465. M. Ihara, H. Nakamoto, T. Kamachi, I. Okura and M. Maedal, *Photochemistry and Photobiology*, 2006, **82**, 1677-1685.

466. E. Dinçkaya, M. K. Sezgintürk, E. Akyılmaz and F. N. Ertaş, *Food Chemistry*, 2007, **101**, 1540-1544.

467. R. Rawal, S. Chawla and C. S. Pundir, *Biosensors and Bioelectronics*, 2012, **31**, 144-150.

468. R. Rawal and C. S. Pundir, *Biochemical Engineering Journal*, 2013, **71**, 30-37.

469. B. Molinero-Abad, M. A. Alonso-Lomillo, O. Domínguez-Renedo and M. J. Arcos-Martínez, *Analytica Chimica Acta*, 2014, **812**, 41-44.

470. C. A. Groom, J. H. T. Luong and C. Masson, *Journal of Biotechnology*, 1993, **27**, 117-127.

471. R. Spricigo, C. Richter, S. Leimkühler, L. Gorton, F. W. Scheller and U. Wollenberger, *Colloids and Surfaces A: Physicochemical and Engineering Aspects*, 2010, **354**, 314-319.

472. M. Situmorang, D. Brynn Hibbert, J. Justin Gooding and D. Barnett, *Analyst*, 1999, **124**, 1775-1779.

473. R. Spricigo, R. Dronov, F. Lisdat, S. Leimkühler, F. W. Scheller and U. Wollenberger, *Analytical and Bioanalytical Chemistry*, 2009, **393**, 225-233.

474. R. Rawal, S. Chawla, T. Dahiya and C. S. Pundir, *Analytical and Bioanalytical Chemistry*, 2011, **401**, 2599-2608.

475. R. Rawal and C. S. Pundir, *International Journal of Biological Macromolecules*, 2012, **51**, 449-455.

476. T. Zeng, S. Leimkühler, J. Koetz and U. Wollenberger, *ACS Applied Materials & Interfaces*, 2015, **7**, 21487-21494.

Danksagung

Ich möchte mich bei den folgenden Personen für ihren vielfältigen Beitrag zu meiner Doktorarbeit bedanken:

- **Prof. Dr. Fred Lisdat** für seine kompetente und fachliche Unterstützung, für die große Geduld und sein Verständnis, für die intensive Betreuung, für die Möglichkeit an nationalen und internationalen Konferenzen meine Arbeit präsentieren zu dürfen, für das Glauben an mich und für die finanzielle Unterstützung, für die hilfreichen Diskussionen, für die investierte Zeit, für die gemeinsamen Publikationen und gute Ideen und Ratschläge.
- **Prof. Dr. Athina Zouni** für ihre fachliche und kompetente Hilfe in jeder Frage, für unsere produktive Zusammenarbeit und gemeinsam erzielten Erfolge, für die sehr netten Gespräche und Aufmunterung, für ihre Offenheit und Hilfsbereitschaft.
- **Dr. Marc Riedel** für die sehr zahlreichen und sehr hilfreichen Diskussionen, Ideen, Gespräche, (und nicht nur wissenschaftlich), für die schöne gemeinsame Zeit außer Labor, für die permanente Aufmunterung, Hilfsbereitschaft, sehr netten und freundlichen Umgang.
- **Dr. Sven Feifel** für seine enorme Unterstützung, zahlreiche Gespräche über jedes Thema, Hilfsbereitschaft und die netten Gespräche in der Küche beim Kaffetrinken, für sein zauberhaftes Lächeln und eine sehr gute freundschaftliche Atmosphäre die einem den Arbeitsalltag verschönerte.
- **Dr. Kai Stieger** für seine umfassendsten Gespräche und unglaublichen Kompetenzen in jedem denkbaren Bereich, für seine sehr interessanten Ideen und große Unterstützung im Labor sowie bei der Einarbeitung am Zahner, für die netten Diskussionen in der Küche und außer Labor.
- **Andreas Kapp** (Kappi) für seine einzigartige Art, für sein freundschaftliches Verhältnis, Hilfsbereitschaft und sehr viel lustige Momente im Alltag. Ohne Dich, Kappi, wäre mein Arbeitsalltag nicht so bunt!
- **Gero Göbel** für seine ständige Unterstützung in jedem denkbaren Bereich, für die netten langen Gespräche, für die schönen Erzählungen von Urlauben und ein sehr nettes freundschaftliches Verhältnis, für die Erklärungen vieler wissenschaftlicher

Zusammenhänge und natürlich für die Einarbeitung an mein Lieblingsgerät, das Raster Elektron Mikroskop (REM).

- **Daniel Schäfer** für seine permanente Hilfsbereitschaft, für die große kompetente Unterstützung, Aufmunterung, den sehr netten Umgang und die schönen Momente außer Büro.
- **Dr. Anita Wesolowski** für ihre nette Art, immer offenes Ohr und sehr freundschaftliches Verhältnis, für ihre Hilfsbereitschaft und die zahlreichen privaten Gespräche.
- **Julian Autrata** für die schöne gemeinsame Zeit außer Labor, für sein energisches Auftreten und sein freundschaftliches Verhältnis, für seine übertragbare gute Laune die den langen Alltag sehr kurz erscheinen lässt.
- Meiner Freundin **Maria Hoffmann**, für ihre enorme Unterstützung, Aufmerksamkeit, ihr Verständnis und ihre Geduld, für die schöne Zeit, die wir gemeinsam verbracht haben und die Bereicherung in allen Bereichen meines Lebens. Ich danke Dir für die eiserne Motivation weiter durchzuziehen, die Aufmunterung und für deinen großen Glauben an mich.
- Besonderen Dank drücke ich meiner Familie aus, die stets hinter mir gewesen ist und mich sehr unterstützt hat.

Ehrenwörtliche Erklärung

Hiermit erkläre ich ausdrücklich, dass ich die Dissertation selbstständig und nur unter Verwendung der angegebenen Quellen und zulässigen Hilfsmittel geschrieben habe. Ich versichere außerdem, dass ich die beigefügte Dissertation nur in diesem und keinem anderen Promotionsverfahren eingereicht habe und, dass diesem Promotionsverfahren keine endgültig gescheiterten Promotionsverfahren vorausgegangen sind. Ich habe mich nicht anderwärts um einen Doktorgrad beworben und besitze keinen Doktorgrad. Ich habe die Promotionsordnung der Lebenswissenschaftlichen Fakultät der Humboldt-Universität zu Berlin vom 5. März 2015 der das Promotionsverfahren zugrunde liegt, zur Kenntnis genommen. Außerdem erkläre ich, dass die Grundsätze der Humboldt-Universität zu Berlin zur Sicherung guter wissenschaftlicher Praxis eingehalten wurden und keine Zusammenarbeit mit gewerblichen Promotionsberaterinnen/rn stattgefunden hat.